Single-molecule analysis of transcription initiation in archaea and eukaryotes

Dissertation

zur Erlangung des Doktorgrades der Naturwissenschaften (Dr. rer. nat.)
der Fakultät für Biologie und Vorklinische Medizin
der Universität Regensburg

Vorgelegt von

Kevin Oliver Kramm

aus

Peine

Regensburg im September 2020

Das Promotionsgesuch wurde eingereicht am:
18.09.2020

Die Arbeit wurde angeleitet von:
Prof. Dr. Dina Grohmann

Unterschrift:

Parts of this thesis have been published in the following articles:

K. Kramm, T. Schröder, J. Gouge, A.M. Vera, K. Gupta, F.B. Heiss, T. Liedl, C. Engel, I. Berger, A. Vannini, P. Tinnefeld, D. Grohmann, DNA origami-based single-molecule force spectroscopy elucidates RNA Polymerase III pre-initiation complex stability., Nat. Commun. 11 (2020) 2828.

K. Kramm, C. Engel, D. Grohmann, Transcription initiation factor TBP: old friend new questions., Biochem. Soc. Trans. 47 (2019) 411–423.

K. Kramm, U. Endesfelder, D. Grohmann, A Single-Molecule View of Archaeal Transcription, J. Mol. Biol. 431 (2019) 4116–4131.

J. Gouge, N. Guthertz, K. Kramm, O. Dergai, G. Abascal-Palacios, K. Satia, P. Cousin, N. Hernandez, D. Grohmann, A. Vannini, Molecular mechanisms of Bdp1 in TFIIIB assembly and RNA polymerase III transcription initiation, Nat. Commun. 8 (2017) 130.

Contributions to other publications:

R.J. Buckley, K. Kramm, C.D.O. Cooper, D. Grohmann, E.L. Bolt, Mechanistic insights into Lhr helicase function in DNA repair, Biochem. J. 477 (2020) 2935–2947.

L. Jakob, T. Treiber, N. Treiber, A. Gust, K. Kramm, K. Hansen, M. Stotz, L. Wankerl, F. Herzog, S. Hannus, D. Grohmann, G. Meister, Structural and functional insights into the fly microRNA biogenesis factor Loquacious., RNA. 22 (2016) 383–96.

S. Schulz, K. Kramm, F. Werner, D. Grohmann, Fluorescently labeled recombinant RNAP system to probe archaeal transcription initiation, Methods. 86 (2015) 10–18.

Table of Contents

Abstract **11**

Zusammenfassung **13**

1 Introduction **15**

2 Single-molecule measurements **18**
2.1 Single-molecule fluorescence measurements 18
2.1.1 Photophysics of organic fluorophores 18
2.1.2 Förster resonance energy transfer 20
2.1.3 Total internal reflection fluorescence microscopy 23
2.1.4 Confocal fluorescence microscopy 25
2.2 Single-molecule force measurements 26
2.2.1 DNA origami-based single-molecule force spectroscopy 27

3 Transcription initiation **30**
3.1 The TATA-binding protein 33
3.1.1 Analysis of TBP-DNA interactions with single-molecule FRET 35
3.2 TFIIB-like factors 35
3.2.1 Analysis of TFIIB-like factor mechanisms with single-molecule FRET 37
3.3 The central RNA polymerase III initiation factor TFIIIB 37
3.4 Mechanisms of transcriptional regulation in archaea 38
3.5 Influence of DNA strain and compaction on transcription 39

4 Objectives **43**

5 Materials **44**
5.1 Chemicals and reagents 44
5.2 Buffers 45
5.3 Proteins 48
5.4 DNA oligonucleotides 49
5.5 Expendable items 50
5.6 Devices 51
5.7 Microscope components 52
5.8 Software 54

6 Methods **55**
6.1 Annealing of DNA oligonucleotides 55
6.2 Absorption spectroscopy 55
6.3 Preparation of DNA origami force clamps 55
6.3.1 Preparation of doubly labelled promoter DNA 55
6.3.2 Restriction digestion of origami scaffolds 57
6.3.3 Thermal annealing and purification 57
6.4 Calculation of forces for DNA origami force clamps 58
6.5 Transmission electron microscopy 61
6.6 Confocal single-molecule fluorescence microscopy experiments 62
6.6.1 Pulsed Interleaved Excitation 63
6.6.2 Diffusion-based single-molecule FRET measurements 63

6.7 Data analysis for confocal fluorescence microscopy experiments 64
6.7.1 Calculation of correction factors 66
6.7.2 Calculation of FRET efficiency histograms 67
6.7.3 TBP-induced bending probability 67
6.7.4 Dwell time calculation for diffusion-based experiments 68
6.7.5 FRET-2CDE filter 69
6.7.6 Fluorescence correlation spectroscopy 71
6.8 TIRF microscopy experiments 71
6.8.1 Alternating laser excitation 73
6.8.2 Passivation of microscope slides 73
6.8.3 Flow chamber preparation 73
6.8.4 Photo-stabilization 74
6.8.5 Surface-based single-molecule FRET measurements 76
6.9 Data analysis for TIRF microscopy experiments 77
6.9.1 Calculation of correction factors 77
6.9.2 Calculation of FRET efficiency histograms 79
6.9.3 Dwell time calculation from FRET efficiency-time traces 79
6.10 Construction of a prism-type TIRF microscope 81
6.10.1 Laser-combining unit 82
6.10.2 Illumination unit 84
6.10.3 Detection unit 86
6.10.4 Control of electronic devices 88

7 Results 89
7.1 Conformational dynamics of DNA Holliday junctions 89
7.1.1 Magnesium-dependent conformational dynamics of DNA Holliday junctions 90
7.1.2 Kinetics of isoform I–isoform II conformational dynamics 92
7.1.3 Role of the open conformation in Holliday junction dynamics 94
7.2 Assembly of human TFIIIB at the U6 snRNA promoter 97
7.2.1 Assembly of TFIIIB subcomplexes under equilibrium conditions 100
7.2.2 Stability of TFIIIB subcomplexes after depletion of unbound proteins 102
7.2.3 Dynamics of HsTBP-induced promoter DNA bending 105
7.3 Force-dependency of DNA binding by RNAP II and III transcription factors 108
7.3.1 Force dependency of human TBP-induced promoter DNA bending 112
7.3.2 Influence of RNAP II and III transcription factors on TBP-induced DNA bending 112
7.3.3 Influence of mechanical strain on DNA bending kinetics 116
7.4 Mechanisms of transcriptional regulation in archaea 121
7.4.1 The role of *Sulfolobus acidocaldarius* TFB2 in transcription initiation 121
7.4.2 Analysis of *Pyrococcus furiosus* TFB RF1-assisted transcription initiation 124
7.4.3 Force-dependency of DNA bending induced by archaeal transcription factors 128

8 Discussion 131
8.1 Influence of individual subunits on TFIIIB assembly 131
8.1.1 Influence of DNA sequence on HsTBP-induced DNA bending dynamics 131
8.1.2 Different DNA bending angles for U6 promoter and MLP complexes 133
8.1.3 Stabilization of the U6 promoter-TBP complex by Brf2 135

8.1.4 Stabilization of the U6 promoter-TBP-Brf2 complex by Bdp1 135
8.1.5 Bending-angle differences between TIRF and confocal microscopy experiments 138
8.2 Comparison of force-dependent DNA binding by human RNAP II and III transcription factors 139
8.2.1 Influence of mechanical strain on TBP-induced DNA bending dynamics 139
8.2.2 Stability of ternary U6 promoter and MLP complexes 141
8.2.3 Stability of quarternary U6 promoter and MLP complexes 142
8.2.4 The central FRET efficiency population in FC experiments 145
8.2.5 Comparison of experimental and theoretical DNA bending probabilities 147
8.3 The role of TFB2 in transcription initiation 150
8.4 Mechanism of TFB-RF1-mediated TFB recruitment 153
8.5 Influence of force on DNA bending induced by archaeal transcription factors 155
8.6 Conclusion and outlook 157

9 References 159

Danksagung 185

List of abbreviations 186

List of figures 188

List of tables 191

Appendix 192
A Protein sequences 192
B DNA origami scaffolds 195
C Extended data 197
C.1 Measurements with DNA Holliday junctions 197
C.2 Analysis of human TFIIIB with TIRF microscopy 198
C.3 Force measurements with human RNAP II and III transcription factors 200
C.4 Measurements with *Sulfolobus acidocaldarius* transcription factors 204
C.5 Measurements with *Pyrococcus furiosus* transcription factors 205
C.6 Force measurements with archaeal transcription factors 206

Abstract

Transcription is the transfer of information stored in the DNA genome into RNA and an essential process for cellular life. In all three domains of life, transcription is carried out by structurally conserved RNA polymerases (RNAP). archaea employ only a single RNAP while eukaryotes have evolved three functionally distinct variants, RNAP I, II and III. Transcription is a cyclic process divided into initiation, elongation and termination phases. During transcription initiation, RNAPs are recruited to the promoter region of their target genes by transcription factors (TF) that recognize sequence elements in the promoter DNA, leading to formation of a pre-initiation complex (PIC). In archaeal and all eukaryotic transcription systems, initiation relies on the TATA-binding protein (TBP) and a TFIIB-like factor.

TFIIIB, the central initiation factor of the human RNAP III system is composed of TBP, the TFIIB-related factors Brf1 or Brf2 and the RNAP III-specific factor Bdp1. At TATA-box-containing promoters, TFIIIB alone can recruit RNAP III. In contrast, RNAP II recruitment can be achieved by TBP and TFIIB. How TFIIIB dynamically assembles at the promoter and the role of Bdp1 as an additional required factor are still not well understood. Furthermore, TFIIIB forms highly stable complexes on DNA that can persist for multiple rounds of transcription. How transcription factors are affected by mechanical forces exerted on DNA by cellular processes like transcription and DNA compaction is mostly unexplored. The archaeal transcription machinery resembles the eukaryotic RNAP II system, but gene regulation is performed by Bacteria-like transcriptional regulators. In *Pyrococcus furiosus*, the TFB recruitment factor 1 (TFB-RF1) can recruit TFB to promoters with a weak B recognition element (BRE) by binding to a conserved upstream promoter element. The molecular mechanism and potential conformational changes in the DNA are still elusive. Many archaea evolved paralogs of TBP and TFB that are involved in stress response. In *Sulfolobus acidocaldarius*, TFB2, a paralog of TFB is expressed in a cell cycle dependent manner. However, its function in the context of transcription is still unexplored.

Assembly of TFs at the promoters is highly dynamic and involves TBP-induced bending of the promoter DNA by approximately 90°. This conformational change can be detected by Förster resonance energy transfer (FRET), a distance-dependent non-radiative process that can report on distance changes in the 1–10 nm regime with high time resolution. In this work, FRET measurements are performed at the single-molecule level, which allows direct observation of different conformational states of individual initiation complexes in real-time. Furthermore, force measurements were performed with a DNA origami-based nanodevice that can exert constant force in the piconewton range on a double stranded DNA fragment. To facilitate FRET experiments, a total internal reflection fluorescence (TIRF) microscope was constructed. In this work, TIRF and confocal fluorescence microscopy were used to study the molecular mechanisms underlying human and archaeal transcription initiation.

The stepwise assembly of TFIIIB at the U6 snRNA promoter was monitored, revealing transient DNA binding of TBP on the millisecond timescale. Addition of Brf2 and Bdp1 stabilized dynamic DNA/TBP complexes. Force measurements revealed that binding of human TFs to DNA under mechanical strain is impaired. The complete TFIIIB complex can bind to DNA at forces up to 6.3 pN,

whereas binding of TBP and TBP/Brf2 was strongly reduced at 2.6 pN and 6.3 pN, respectively. A comparison with the RNAP II-specific TFIIB and TFIIA provides evidence that the cage-like structure of TFIIIB confers superior resistance to mechanical force.

S. acidocaldarius TFB2 cannot stabilize a bent promoter DNA/TBP complex and is thus not functional as a transcription initiation factor. Instead, six-fold molar excess of TFB2 could destabilize a DNA-bound TBP/TFB complex, suggesting a regulatory role for TFB2.

TFB-RF1 can enhance TFB recruitment at promoters with weak or consensus BREs to similar degree without inducing conformational changes in the DNA. However, formation of a bent promoter DNA complex is slower at promoters with a consensus BRE. TFB-RF1 likely acts as a secondary binding site for TFB.

DNA origami-based force spectroscopy further demonstrated force-dependent DNA bending of archaeal TFs. *Methanocaldococcus jannaschii* TBP can bend DNA alone whereas *P. furiosus* requires TBP and TFB. For both systems, low DNA bending efficiency was observed at 6.2 pN force.

Taken together, this work highlights conserved mechanisms employed by archaeal and eukaryotic transcription systems to modulate the stability of the TBP/TFIIB-like factor complex that nucleates PIC formation, thereby enabling control over transcription initiation.

Zusammenfassung

Transkription ist der Transfer von im DNA-Genom gespeicherten Informationen in RNA und daher ein wichtiger Prozess für zelluläres Leben. Transkription erfolgt in allen drei Domänen des Lebens durch strukturell konservierte RNA-Polymerasen (RNAPs). Archaeen verwenden nur eine einzige RNAP, während Eukaryoten drei funktionell unterschiedliche Varianten entwickelt haben, RNAP I, II und III. Transkription ist ein zyklischer Prozess, der in Initiations-, Elongations- und Terminationsphasen unterteilt ist. Während der Transkriptionsinitiation wird die RNAP durch Transkriptionsfaktoren (TFs), die Sequenzelemente in der Promotor-DNA erkennen, in die Promotorregion ihrer Zielgene rekrutiert. Dies führt zur Formierung eine Prä-Initiationskomplexes (engl.: pre-initiation complex, PIC). Im archaeellen und allen eukaryotischen Transkriptionssystemen bilden das TATA-bindende Protein (TBP) und ein TFIIB-ähnlicher Faktor die Kernkomponenten der Initiation.

TFIIIB, der zentrale Initiationsfaktor des humanen RNAP III-Systems, besteht aus TBP, dem TFIIB-ähnlichen Faktor Brf1 oder Brf2 und dem RNAP III-spezifischen Faktor Bdp1. Die Rekrutierung von RNAP III kann an Promotoren mit einem TATA-box Element allein durch TFIIIB erfolgen. Im Gegensatz dazu kann die Rekrutierung von RNAP II durch TBP und TFIIB erreicht werden. Der dynamische Assemblierungsprozess von TFIIIB auf der Promotor DNA, sowie die Rolle von Bdp1 als zusätzlich erforderlichem Faktor im RNAP III System, sind noch nicht gut untersucht. Darüber hinaus bildet TFIIIB extrem stabile Komplexe mit DNA, die für mehrere Transkriptionszyklen bestehen bleiben können. Wie Transkriptionsfaktoren durch mechanische Kräfte beeinflusst werden, die durch zelluläre Prozesse wie Transkription und DNA-Kompaktierung auf die DNA ausgeübt werden, ist weitgehend unerforscht. Die archaeelle Transkriptionsmaschinerie ähnelt dem eukaryotischen RNAP II System, aber Genregulation erfolgt durch Transkriptionsregulatoren, die denen in Bakterien ähneln. Im Archaeon *Pyrococcus furiosus* kann TFB an Promotoren mit einem schwachen B-Erkennungselement (engl.: B recognition element, BRE) durch den TFB-Rekrutierungsfaktor 1 (TFB-RF1) stimuliert werden, der an ein konserviertes Promotorelement stromaufwärts des BRE bindet. Der molekulare Mechanismus und mögliche Konformationsänderungen der DNA sind noch nicht bekannt. Viele Archaeen haben Paraloga von TBP und TFB evolviert, die an Genregulation in Reaktion auf Stressbedingungen beteiligt sind. In *Sulfolobus acidocaldarius* wird TFB2, ein Paralog von TFB, zellzyklusabhängig exprimiert. Welche Funktion TFB2 im Rahmen der Transkriptionsinitiation spielt ist jedoch noch unerforscht.

Die Assemblierung von TFs an der Promotor-DNA ist dynamisch und eine wichtige Konformationsänderung bei diesem Prozess ist eine durch TBP induzierte Biegung der DNA um circa 90°. Diese Konformationsänderung kann durch Förster-Resonanzenergietransfer (FRET) detektiert werden. FRET ist ein abstandsabhängiger, strahlungsfreier Prozess, mit dem Abstandsänderungen im Bereich von 1–10 nm mit hoher zeitlicher Auflösung gemessen werden können. In dieser Arbeit werden FRET-Messungen auf Einzelmolekülebene durchgeführt, wodurch die direkte Beobachtung verschiedener Konformationszustände einzelner Initiationskomplexe in Echtzeit möglich ist. Darüber hinaus wurden Kraftmessungen mit einem DNA Origami-basierten Nanogerät durchgeführt, das eine konstante Kraft im Piconewton-Bereich auf ein

doppelsträngiges DNA-Fragment ausüben kann. Für FRET-Experimente wurde ein internes Totalreflektionsfluoreszenzmikroskop (engl.: total internal reflection fluorescence, TIRF) konstruiert. In dieser Arbeit wurden TIRF und konfokale Fluoreszenzmikroskopie eingesetzt um die molekularen Mechanismen der Transkription in archaeellen und eukaryotischen Transkriptionssystemen zu erforschen.

Die Untersuchung der schrittweisen Assemblierung des TFIIIB-Komplexes am U6 snRNA-Promotor zeigte, dass TBP-induzierte DNA-Biegung transient erfolgt, mit Bindungszeiten im Millisekundenbereich. Brf2 und Bdp1 können dynamische DNA/TBP-Komplexe stabilisieren. Kraftspektroskopiemessungen ergaben, dass die DNA-Bindung humaner TFs beeinträchtigt ist, wenn mechanische Kraft auf die DNA einwirkt. Der vollständige TFIIIB-Komplex kann bei Kräften bis zu 6,3 pN an DNA binden, während die Bindung von TBP und TBP/Brf2 bei 2,6 pN bzw. 6,3 pN stark reduziert war. Ein Vergleich mit den RNAP II-spezifischen Faktoren TFIIB und TFIIA liefert Hinweise darauf, dass die käfigartige Struktur des TFIIIB-Komplexes eine hohe Beständigkeit gegen mechanische Kräfte vermittelt.

Der *S. acidocaldarius* Faktor TFB2 trägt nicht zur Stabilisierung eines Promotor-DNA/TBP-Komplex bei und ist daher keine funktionsfähiger Transkriptionsinitiationsfaktor. Stattdessen konnte ein sechsfacher molarer Überschuss an TFB2 einen DNA-gebundenen TBP/TFB-Komplex destabilisieren, was auf eine regulatorische Rolle für TFB2 hindeutet.

TFB-RF1 kann die TFB-Rekrutierung sowohl an Promotoren mit schwachen als auch consensus BREs in ähnlichem Maße verbessern. Dabei wurden keine Konformationsänderungen der DNA beobachtet. Die Formierung eines gebogenen Promotor-DNA-Komplexes erfolgte jedoch bei Promotoren mit consensus BRE langsamer. Es ist anzunehmen, dass TFB-RF1 als eine sekundäre Bindungsstelle für TFB am Promotor fungiert.

DNA-Origami-basierte Kraftspektroskopie zeigte ferner, dass DNA-Biegung durch archaeelle Transkriptionsfaktoren kraftabhängig ist. *Methanocaldococcus jannaschii* TBP kann DNA allein biegen, während im *P. furiosus* Transkriptionssystem TBP und TFB benötigt werden. Für beide Systeme war bei einer an der DNA anliegenden Kraft von 6,2 pN die Effizienz der DNA-Biegung stark reduziert.

Zusammengenommen beleuchtet diese Arbeit konservierte Mechanismen, die von archaeellen und eukaryotischen Transkriptionssystemen genutzt werden um die Stabilität des TBP/TFIIB-ähnlichen Faktor-Komplexes zu modulieren, der den Kern des PIC bildet, wodurch Kontrolle über die Transkriptionsinitiation ermöglicht wird.

1 Introduction

Single-molecule techniques have reshaped our view on cellular life over the last decades. The molecular machines that perform the most fundamental processes within living cells such as DNA replication, transcription and translation are highly dynamic by nature. Just as in large scale machines, movement of individual components – domains and subunits – are critical to their functionality and understanding the underlying molecular mechanism is the key to understanding cellular life itself (reviewed in [1–3]). The concept of interrogating such complex systems one molecule at a time presents unique advantages over classical ensemble approaches:

Probing individual molecules provides information on the distribution of values for a given property, e.g. structural conformation, whereas averaging over an ensemble only reflects the mean value of the observed parameter. Thus, single-molecule approaches can reveal molecular heterogeneity, which is an intrinsic feature of biological systems. A theoretical example for this is provided by a protein that can exist in two different conformational states that differ in the distance between two domains (Figure 1a). In an ensemble experiment, only the mean distance can be measured. This value does not correspond to either conformation and only reflects the relative fraction of each conformer in the heterogeneous ensemble. On the other hand, probing individual molecules also yields the relative fraction of each conformer, but more importantly provides information on the mean distance and its variance for each separate conformational state. If the state of each molecule remains constant over the timespan of the observation, such a system displays static heterogeneity.

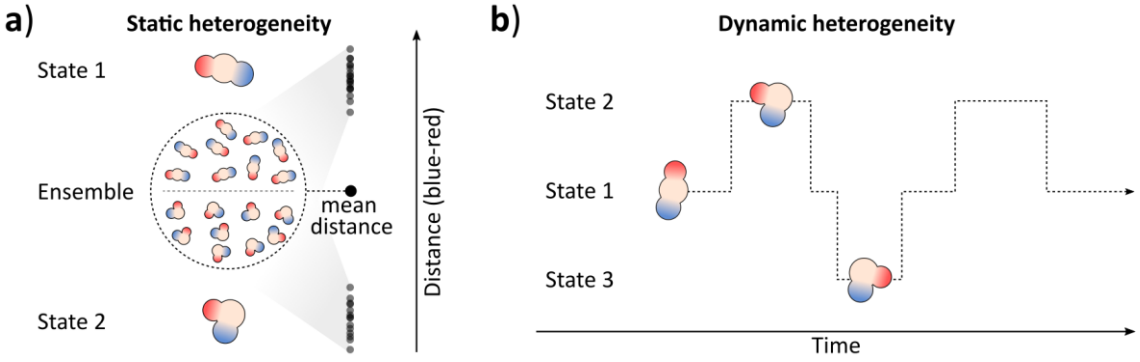

Figure 1: Concepts of molecular heterogeneity. a) Static heterogeneity is observed in a sample by probing the conformational state (distance between red and blue domain) of individual molecules. This approach captures the distribution of distance values in a sample. In contrast, measuring the sample in an ensemble approach only recovers the mean distance resulting from the relative fraction of each conformer in the ensemble (here 1:1). **b)** Dynamic heterogeneity is observed for a molecule that fluctuates between three conformational states in a stochastic manner.

In contrast, dynamic heterogeneity is observed if the conformation of the molecules can change over the timespan of the observation. Conformational transitions can be divided into two categories. The first are unidirectional transitions, e.g. the unfolding of a single protein [4]. These changes are per se also accessible to ensemble methods as they can in some instances be synchronized, i.e. the initial and final state are respectively identical for each molecule in the ensemble. The second category are recurring transitions that occur in a stochastic manner and are thus inherently non-synchronizable (Figure 1b). These processes are generally inaccessible to

ensemble methods but constitute the majority of biomolecular motions [5]. By employing a single-molecule approach, the conformational transitions in a molecule can be followed in real-time providing information on the order and relative occurrence of individual steps as well as the dwell time of the molecule in each specific state (Figure 1b). In this manner, rare subpopulations of molecules can be discovered and interrogated [6]. Consequently, molecules can be further sorted to focus downstream data analysis on only on relevant subpopulations. Hence, single-molecule methods provide a wealth of information and enable unique strategies to approach biochemical and biophysical questions.

The detection of single molecules can be achieved by several means (reviewed in [7]): changes in electrical current (patch clamp and nanopore DNA sequencing [8]), local differences in electronic transmittance (electron microscopy) or exerted forces (atomic force microscopy (AFM), optical and magnetic tweezers [9,10]). But for biological applications, optical detection schemes have proven to be the most versatile (reviewed in [11]). In particular fluorescence provides a readout parameter well suited for biological samples as fluorescent proteins can be genetically fused to a protein of interest in living cells [12,13]. Organic fluorophores, on the other hand, can be covalently attached to proteins and nucleic acids through a plethora of chemical reactions, many of which are suitable for application in living cells [14,15] (reviewed in [11,16,17]).

Single-molecule fluorescence experiments involving biological samples encounter two main challenges (reviewed in [11,16,18]). First, sensitivity to the fluorescence emission of a single molecule must be achieved. Autofluorescence and light scattering within the sample can cause significant background signals that can dominate the combined signal [19]. Thus, reliable detection of single molecules depends on either signal amplification [20,21] or background reduction [22–25]. The most commonly utilized methods for single-molecule fluorescence experiments are confocal [22,26] and total internal reflection fluorescence (TIRF) microscopy [25,27], which both rely on limiting the detection volume and thereby reducing the contribution of background signal. Secondly, single-molecule methods generally operate at extremely low concentrations (picomolar to nanomolar) to achieve spatial separation between particles [18]. However, many biological systems often have considerably higher dissociation constants (K_D) [18]. This concentration barrier dictates that only biological interaction of labeled reactants with K_D values below 50 nM are accessible to single-molecule techniques [16].

As stated above, the detection of conformational changes in individual biological complexes is one of the main aims of single-molecule approaches in life sciences. Distance information in the biologically relevant regime of 1–10 nm can be obtained in single-molecule fluorescence measurements by exploiting a phenomenon termed Förster resonance energy transfer (FRET) [28,29]. FRET is a form of non-radiative energy transfer from a fluorescent donor molecule to an acceptor. The efficiency of this process is highly distance-dependent and requires donor and acceptor to be in close proximity (1–10 nm). By measuring the FRET efficiency between two strategically placed fluorophores within a biomolecular complex, distances and distance changes can be monitored [30,31]. Hence, single-molecule FRET experiments (smFRET) can identify distinct structural states of a biological macromolecule and detect transient or rare species. In contrast to classical structural biology methods such as x-ray crystallography or cryo-electron microscopy,

these data are attainable at high time-resolution, allowing real-time observation of entire conformational cycles (reviewed in [2,32–35]).

SmFRET experiments have been variously applied to study the molecular mechanism of cellular processes such as DNA replication [36–39] and mRNA translation [40–43]. In this work, the focus is set on transcription, the transfer of the genetic information encoded in the DNA genome into RNA. Transcription is the first step in gene expression and this task is carried out by structurally conserved multisubunit RNA polymerases (RNAPs) in all three domains of life – Bacteria, Archaea and Eukarya [44]. While bacteria and archaea rely on a single RNAP, eukaryotes have evolved three functionally distinct variants, RNAP I, II and III. RNAP I exclusively synthesizes ribosomal RNA (rRNA), performing the bulk of transcription activity in dividing cells [45]. RNAP II primarily produces messenger RNAs (mRNA) that are translated into proteins, as well as regulatory RNAs and small nuclear RNAs (snRNA). RNAP III transcribes short structured RNAs such as transfer RNAs (tRNA), the 5S rRNA and the U6 snRNAs. These molecular machines consist of an evolutionary conserved five-subunit core complex that harbors the catalytic center of the RNAP. In archaea and eukaryotes, this core complex is extended by additional 7–12 subunits that share functional and structural features (reviewed in [44,46]).

Transcription is a cyclic process that can be divided into the initiation, elongation and termination phases. During the initiation phase, the RNAP binds the promoter DNA upstream of a target gene and separates the DNA duplex. In the elongation phase, the RNAP translates along the gene body and synthesizes an RNA complementary to the DNA matrix via nucleoside triphosphate hydrolysis. In the termination phase, the RNAP releases the transcribed RNA and disengages the DNA. These steps are supported by a multitude of accessory proteins dynamically associating with the promoter DNA and RNAP to induce conformational changes that are critical for RNAP functionality and progression through the transcription cycle (reviewed in [47]).

During the initiation phase, the RNAP must bind to the promoter region of a gene, separate (“melt”) the DNA duplex and position the transcription start site (TSS) in the active center. To achieve this, RNAPs are aided by transcription factors (TFs) that assist in promoter recognition, precise RNAP positioning and DNA melting. In Bacteria, σ factors bind to the RNAP in solution to form a holo-enzyme. This complex can bind to different target promoters depending on the bound σ factor (reviewed in [48–50]). The core initiation Complex in archaea and eukaryotes constitutes the TATA-binding protein (TBP) that binds to the TATA-box element of the promoter, thereby inducing a sharp bent in the DNA and a TFIIB-like factor that recruits the RNAP to the promoter, forming a pre-initiation complex (PIC) [51–53]. This core arrangement is generally conserved and expanded by additional RNAP-specific factors (reviewed in [46,54]).

While snapshots of these intermediate assemblies have been attained by classical structural biology approaches (reviewed in [55,56]), real time-observation provides a more nuanced picture of this highly dynamic process. Hence, single-molecule experiments are the preferred choice to unravel the molecular mechanisms underlying transcription that have expanded our knowledge over the past decades (reviewed in [57–60]). In this work, several aspects surrounding the mechanisms of transcription initiation in eukaryotes and archaea will be addressed by harnessing the power of the single-molecule FRET toolbox.

2 Single-molecule measurements

2.1 Single-molecule fluorescence measurements

Optical single-molecule measurements can provide detailed insights into biological processes. Fluorescence serves as a sensitive reporter that provides information on changes in the environment of the fluorophore such as pH value [61], temperature [62], viscosity, and the vicinity of other molecules (e.g. FRET [28] (Chapter 2.1.2), protein induced fluorescence enhancement [63]) or surface proximity (metal induced energy transfer [64]). In this section, a theoretical background on the single-molecule fluorescence microscopy methods applied in this work is provided.

2.1.1 Photophysics of organic fluorophores

Fluorophores are molecules that contain delocalized π-electrons, which can absorb light with a wavelength λ in the ultraviolet to near infrared spectrum. The energy E_{photon} of absorbed photons is described by:

$$E_{\mathrm{photon}} = h \cdot \frac{c}{\lambda} \qquad \textbf{Equation 1}$$

where h is the Planck constant and c is the speed of light in vacuum. The absorbed energy can then be released via emission of light, which is termed luminescence. The processes that occur between the absorption and emission of light by fluorophores, and their respective rates k, are usually visualized in a Jablonski diagram (Figure 2).

Initially, the fluorophore is in the singlet ground state S_0. Upon absorption of a photon with an energy equal or higher than the energy barrier of the first (S_1) or second excited singlet state (S_2), the fluorophore is shifted to the respective state. The transition is near instantaneous ($k_{abs} \approx 10^{15}$ s^{-1}), and the excited electron is usually shifted to a higher vibrational level of the S_1 or S_2 state, where it is spin-paired with the electron in the S_0 state. From there, the molecule quickly transitions to the lowest vibrational level of that state by vibrational relaxation under dissipation of heat ($k_{VR} \approx 10^{12}$ s^{-1}). If overlap exists between the vibrational levels of two electronic states, the molecule can relax to the lower state in a process termed internal conversion ($k_{IC} = 10^{9}$–10^{12} s^{-1}). Internal conversion is more likely to occur in the S_2–S_1 transition than the S_1–S_0 transition due to the larger energy difference of the latter. From the relaxed S_1 state, further relaxation to S_0 can occur via emission of a photon as fluorescence, a subtype of luminescence. This transition is spin allowed and can therefore proceed rapidly ($k_{fl} \approx 10^{8}$ s^{-1}). Alternatively, excited electrons in the S_1 state can undergo spin-conversion to the first excited triplet state T_1 in a process called inter system crossing ($k_{ISC} = 10^{8}$ s^{-1}). From this state, the molecule can also radiatively return to S_0 by emitting phosphorescence. This transition is spin-forbidden and is several orders of magnitude slower than fluorescence ($k_{pho} \approx 10^{-2}$–10^{2} s^{-1}). Additional non-radiative relaxation pathways exist, such as collision quenching, complex formation and resonance energy transfer [65,66] (Chapter 2.1.2). Both radiative relaxation processes usually lead to a decay to a higher vibrational level of S_0. From there, excess energy is dissipated via vibrational relaxation.

The energy losses incurred from intermediate relaxation pathways decrease the energy available for radiative relaxation. Thus, fluorescence and phosphorescence occur at a longer wavelength than the absorbed light, an effect termed Stokes shift. This phenomenon can be exploited in technical applications to achieve spectral separation of excitation and emission photons.

The number of photons emitted as fluorescence versus the total amount of absorbed photons (or the total amount of deexcitation events) is defined as the fluorescence quantum yield Φ_{fl}.

$$\Phi_{fl} = \frac{k_{fl}}{k_{fl} + k_{nr}} \qquad \textbf{Equation 2}$$

where k_{nr} is the sum of all non-radiative rates competing for S_1 depopulation. Conversely, the average time a molecule spends in the excited state prior to fluorescence emission is defined as the fluorescence lifetime τ_{fl} of the fluorophore:

$$\tau_{fl} = \frac{1}{k_{fl} + k_{nr}} \qquad \textbf{Equation 3}$$

Fluorescence lifetimes are usually in the range of 1–10 ns. Fluorescence emission is a stochastic process, that can be described by an exponential decay model:

$$N_{F*}(t) = N_{F*,0} \cdot e^{-\frac{t}{\tau_{fl}}} \qquad \textbf{Equation 4}$$

where $N_{F*}(t)$ is the number of excited state fluorophores at time point t after excitation and $N_{F*,0}(t)$ is the total number of excited fluorophores. Thus, at $t = \tau_{fl,}$ on average, 63% of all fluorophores in a simultaneously excited ensemble have returned to the ground state.

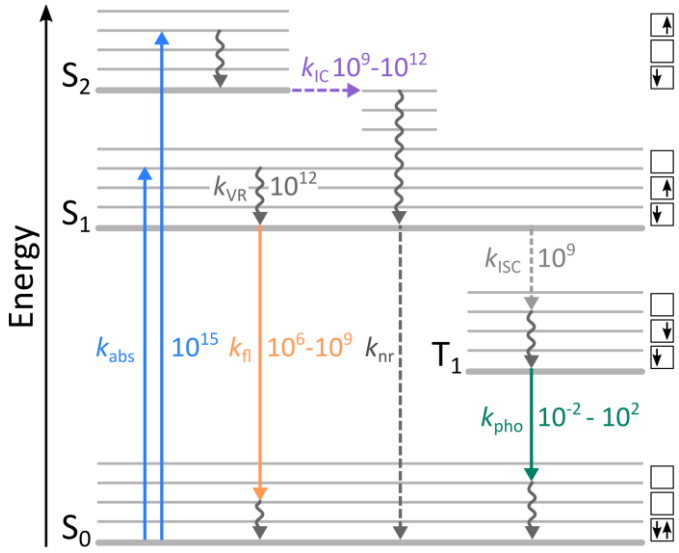

Figure 2: Simplified Jablonski diagram. A fluorophore in the electronic ground state S_0 is excited to the first (S_1) or second (S_2) excited singlet state via absorption (k_{abs}) of a photon. The molecule relaxes to the lowest excited vibrational level by vibrational relaxation (k_{VR}). From there, the molecule can relax radiatively via emission of fluorescence (k_{fl}). Overlapping vibrational levels (thin gray lines) and electronic states (thick gray lines) allow the molecule to relax non radiatively via internal conversion (k_{IC}). Alternatively, the molecule can undergo inter system crossing (k_{ICS}) to the first triplet state T_1 and radiatively relax by emission of phosphorescence (k_{pho}). Additional non-radiative relaxation pathways are included in k_{nr}. The electron spin configuration of the ground state, first and second excited states (bottom to top) are indicated by boxed arrows. Rates are given in s^{-1}.

2.1.2 Förster resonance energy transfer

An alternative route for excited state depopulation is Förster resonance energy transfer, named after Theodor Förster who developed the theoretical framework around this photophysical phenomenon [28,67,68]. FRET is a non-radiative transfer of energy from an excited state donor fluorophore to a ground state acceptor molecule via dipole-dipole interaction [28]. For FRET to occur, several conditions must be fulfilled [69]:

1) Donor and acceptor must be in close, but not too close, vicinity (1–10 nm).
At closer distances, contact-based energy transfer mechanisms become prevalent such as collision quenching and complex formation between donor and acceptor [70]. It must be noted that for biological applications, fluorophores are generally attached to flexible linkers, around 1–1.5 nm in length. In praxis, inter-fluorophore contacts can already occur in the 0–3 nm distance regime [71]. At greater distances, reabsorption can be observed, wherein a photon emitted by the donor is subsequently absorb by the acceptor and elicits acceptor fluorescence. Depending on the experimental setup, the above phenomena can macroscopically be interpreted as FRET but operate through entirely different mechanisms [70].

2) Spectral overlap is required between the donor emission the acceptor absorption.
As a simplification, donor and acceptor fluorophores can be visualized as groups of electrical oscillators, each consisting of a stationary nucleus and an electron that can oscillate along one direction. The donor and acceptor transition dipole moments each point from the center of the respective molecule along its positive-negative charge gradient generated by the sum of all internal oscillators [72]. Spectral overlap includes that the donor emission dipole moment and acceptor absorption dipole moment oscillate at wavelengths that can resonate with each other. This can be visualized by the intersection of the respective spectra (Figure 3). The spectral overlap is defined as the overlap integral J (Figure 3):

$$J = \int f_{\mathrm{D}}(\lambda) \cdot \varepsilon_{\mathrm{A}}(\lambda) \cdot \lambda^4 \, \mathrm{d}\lambda \qquad \textbf{Equation 5}$$

where $f_{\mathrm{D}}(\lambda)$ is the area-normalized donor fluorescence spectrum, and $\varepsilon_{\mathrm{A}}(\lambda)$ is the molar extinction spectrum of the acceptor (in $\mathrm{M^{-1}cm^{-1}}$) integrated over the spectral range.

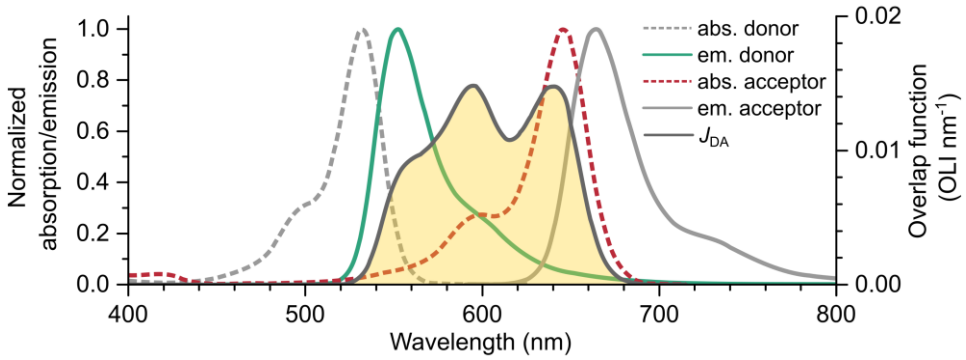

Figure 3: The spectral overlap integral *J*. Absorption (abs.) and emission spectra (em.) of the FRET donor-acceptor fluorophore pair ATTO 532 and ATTO 647N, normalized to 1. The area shaded in yellow is the overlap integral J_{DA} as a function of the wavelength. OLI: overlap integral units (10^{-14} $\mathrm{mol^{-1}}$ $\mathrm{dm^3}$ $\mathrm{cm^3}$).

3) Donor and acceptor dipoles must be in suitable alignment to each other.
In addition to spectral overlap, resonance between both dipole moments is dependent on their angular relation, defined as the orientation factor κ^2:

$$\kappa^2 = (\cos\theta_T - 3\cos\theta_D \cdot \cos\theta_A)^2 \qquad \textbf{Equation 6}$$

where θ_D is the angle between the donor emission transition dipole moment and the donor-acceptor connection line, θ_A is the angle between the acceptor absorption transition dipole moment and the donor-acceptor connection line and θ_T is the angle between the transition dipole moments of donor emission and acceptor absorption (Figure 4). Extreme values of κ^2 can be observed for collinear orientation of both transition dipole moments ($\theta_D = \theta_A = \theta_T = 0°$), where κ^2 becomes 4 and orthogonal orientation ($\theta_D = \theta_T = 90°$, $\theta_A = 0°$), where κ^2 becomes 0. Averaging θ_A and θ_D over all possible orientations yields $\kappa^2 = 2/3$ (Figure 4). This approximation requires both fluorophores to be in isotropic rotation at a rate much faster than the rate of energy transfer[69]. When one of the dipoles is fixed in a static orientation while the other can freely rotate, κ^2 takes on values from 1/4 to 3/4, which is still reasonably approximated by 2/3 in most cases.

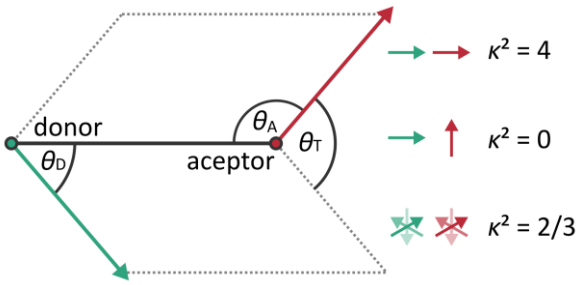

Figure 4: The orientation factor κ^2. θ_D and θ_A are the angles between the donor-acceptor connection line (black) and the donor emission transition dipole moment (green arrow) or acceptor absorption transition dipole moment (red arrow). θ_T is the angle between the planes defined by θ_D and θ_A (gray dashed line). The extrema of κ^2 for collinear (top) and orthogonal (middle) orientation of the dipole moments, as well as the average obtained for fast isotropic rotation of fluorophores (bottom) are depicted.

If the above conditions are fulfilled, a donor residing in the S_1 excited state can transfer its energy to the acceptor, thereby returning to the ground state. Simultaneously, the acceptor is excited to the S_1 state and can return to S_0 either non-radiatively or via emission of fluorescence (Figure 5a). Thus, acceptor emission upon donor excitation can be observed. The efficiency of the energy transfer E is defined as:

$$E = \frac{k_T}{k_T + \tau_{fl,D}^{-1}} = \frac{R_0^6}{R_0^6 + r_{DA}^6} \qquad \textbf{Equation 7}$$

Where k_T is the energy transfer rate, $\tau_{fl,D}$ is the fluorescence lifetime of the donor fluorophore, r_{DA} is the distance between the donor and acceptor. R_0 is the Förster radius, at which the energy transfer efficiency is exactly 0.5. R_0 contains the spectral overlap and orientation conditions as:

$$R_0 = \frac{9(\ln 10) \cdot \kappa^2 \cdot \phi_D \cdot J}{128\pi^5 \cdot N_A \cdot n^4} \qquad \textbf{Equation 8}$$

where N_A is the Avogadro constant and n is the refractive index of the medium. Due to the r_{DA}^{-6} dependence of E, FRET is highly sensitive to distance changes in the $0.5R_0$–$1.5R_0$ regime (Figure 5b). Values for R_0 are typically between 3–6 nm (see [69] for a comprehensive list), which

is ideal to study protein and nucleic acid structures. Hence, FRET is often used as a "molecular ruler" to measure inter- and intra-molecular distances in biomolecular complexes [73].

Experimentally, measuring FRET can be approached by multiple strategies that all employ common basic principles.

i) FRET is detectable as change in τ_{fl}. Since FRET provides an additional pathway for excited state depopulation, the donor fluorescence lifetime in the presence of an acceptor $\tau_{fl,DA}$ is reduced compared to the isolated donor $\tau_{fl,D}$, which can be exploited to calculate E as:

$$E = 1 - \frac{\tau_{\mathrm{fl,DA}}}{\tau_{\mathrm{fl,D}}} \qquad \textbf{Equation 9}$$

ii) Alternatively, using fluorescence intensity as a readout parameter, FRET is detected as quenching of donor fluorescence in the presence of an acceptor compared to the isolated donor.

iii) The emission of acceptor fluorescence upon donor excitation (acceptor sensitization) measured in the presence or absence of a donor provides information on E. The first and second approach offer the flexibility of using a non-fluorescent quencher as acceptor [74]. However, numerous deexcitation processes can lead to quenching of donor fluorescence lifetime or intensity, making this readout alone unreliable if the presence of an acceptor cannot be confirmed. Thus, in praxis, a combination of all the above principles is favored. The single-molecule techniques employed in this work offer the unique advantage of measuring all the above quantities simultaneously whilst also confirming the presence of an acceptor via direct excitation. Thus, all parameters for accurate calculation of E can be obtained from a single experiment (Chapters 6.6.1 and 6.8.1).

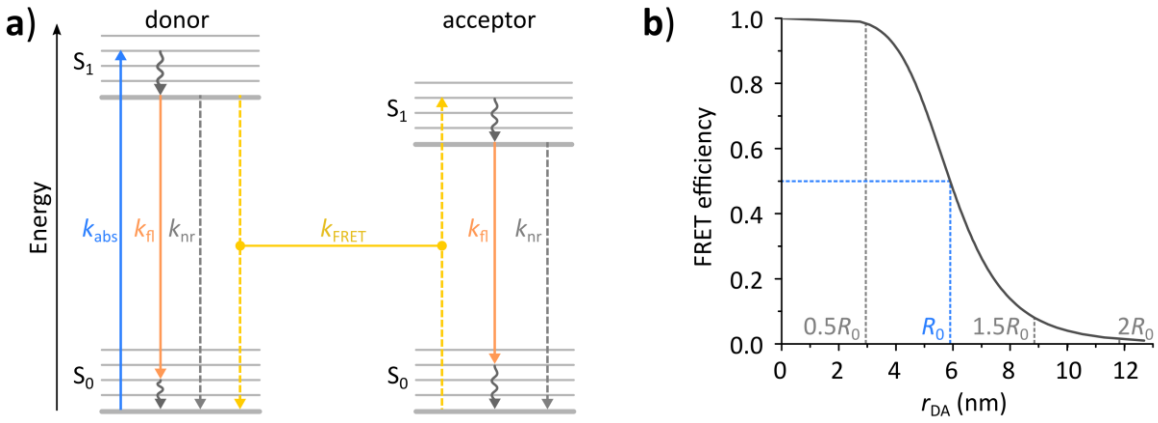

Figure 5: Principles of Förster resonance energy transfer. Simplified Jablonski diagram representing the excitation of a donor fluorophore from the electronic ground state S_0 upon absorption of a photon (k_{abs}) to the first excited singlet state S_1, followed by internal conversion to the lowest vibrational level of S_1 (black dashed arrow). Relaxation to S_0 can occur via emission of fluorescence (k_{fl}), non-radiative decay (k_{nr}, Figure 3) or Förster resonance energy transfer (k_{FRET}). For FRET to occur, the energy difference of the donor S_1–S_0 transition must be equal to the S_0–S_1 transition of the acceptor (depicted as connected yellow arrows). After FRET, the acceptor is in the excited state and can relax via emission of fluorescence or non-radiative decay. **b)** FRET efficiency as a function of donor-acceptor distance r_{DA} (donor: ATTO 532, acceptor: ATTO 647N). R_0 is the Förster radius at which the FRET efficiency is 0.5 ($R_{0,\ \mathrm{ATTO\ 532–ATTO\ 647N}}$ = 5.9 nm). FRET is sensitive to distance changes in the $0.5R_0$-$2R_0$ range (modified from [69]).

2.1.3 Total internal reflection fluorescence microscopy

A powerful technique to realize single-molecule observation is total internal reflection fluorescence (TIRF) microscopy, that provides a high signal-to-background ratio by limiting excitation to a 100–300 nm section of the sample. This selective illumination is achieved by the total internal reflection of the incident excitation laser beam at the sample interface which creates an evanescent light field.

Light striking the *xy* interface plane ($z = 0$) of two transparent, optically isotropic media of refractive indices n_1 and n_2 at an incidence angle θ_1 is refracted at an angle θ_2 following Snell's law:

$$n_1 \sin\theta_1 = n_2 \sin\theta_2 \qquad \textbf{Equation 10}$$

When transitioning into a medium of lower refractive index ($n_1 > n_2$), light is refracted towards the boundary. At a certain incidence angle, termed critical angle θ_{crit} (Equation 11), θ_2 reaches the maximum value of 90°. For incidence angles larger θ_{crit}, refraction no longer occurs and light is instead totally internally reflected (Figure 6a).

$$\theta_{crit} = \arcsin\frac{n_2}{n_1} \qquad \textbf{Equation 11}$$

Simultaneously, an evanescent wave forms at the interface and propagates along the boundary in the relative direction the incident beam. The evanescent field intensity *I* decays exponentially with increasing distance *z* from the interface plane (Figure 6b) according to:

$$I(z) = I_0 \cdot e^{-\frac{z}{d}} \qquad \textbf{Equation 12}$$

where I_0 is the intensity of the evanescent field at z = 0, and *d* is the penetration depth given by:

$$d = \frac{\lambda}{4\pi} \cdot \sqrt{n_1^2 \cdot (\sin\theta_1)^2 - n_2^2} \qquad \textbf{Equation 13}$$

d decreases as θ_1 increases and is dependent on the wavelength of the excitation beam, e.g. for light striking a quartz/water interface ($n_{quartz} = 1.46$, $n_{water} = 1.33$) at an incident angle of 72°, the resulting penetration depth is $d = 109$ nm for 532 nm excitation and $d = 131$ nm for 637 nm excitation (Figure 6c). I_0 depends on the incidence angle and the polarization of the excitation beam $I_1^{\parallel,\perp}$,with the p-polarized components $I_1^{\parallel}$ and the s-polarized component $I_1^{\perp}$, according to:

$$I_0^{\parallel} = I_1^{\parallel} \frac{4\cos^2\theta_1 \left(2\sin^2\theta_1 - \frac{n_2^2}{n_1^2}\right)}{\frac{n_2^4}{n_1^4}\cos^2\theta_1 + \sin^2\theta_1 - \frac{n_2^2}{n_1^2}} \qquad \textbf{Equation 14}$$

$$I_0^{\perp} = I_1^{\perp} \frac{4\cos^2\theta_1}{1 - \frac{n_2^2}{n_1^2}} \qquad \textbf{Equation 15}$$

Equation 14 and Equation 15, plotted for the above quartz/water example in Figure 6d, illustrate that the evanescent field intensity can be 4–5 times stronger than the excitation wave for incidence angles close to as θ_{crit}.

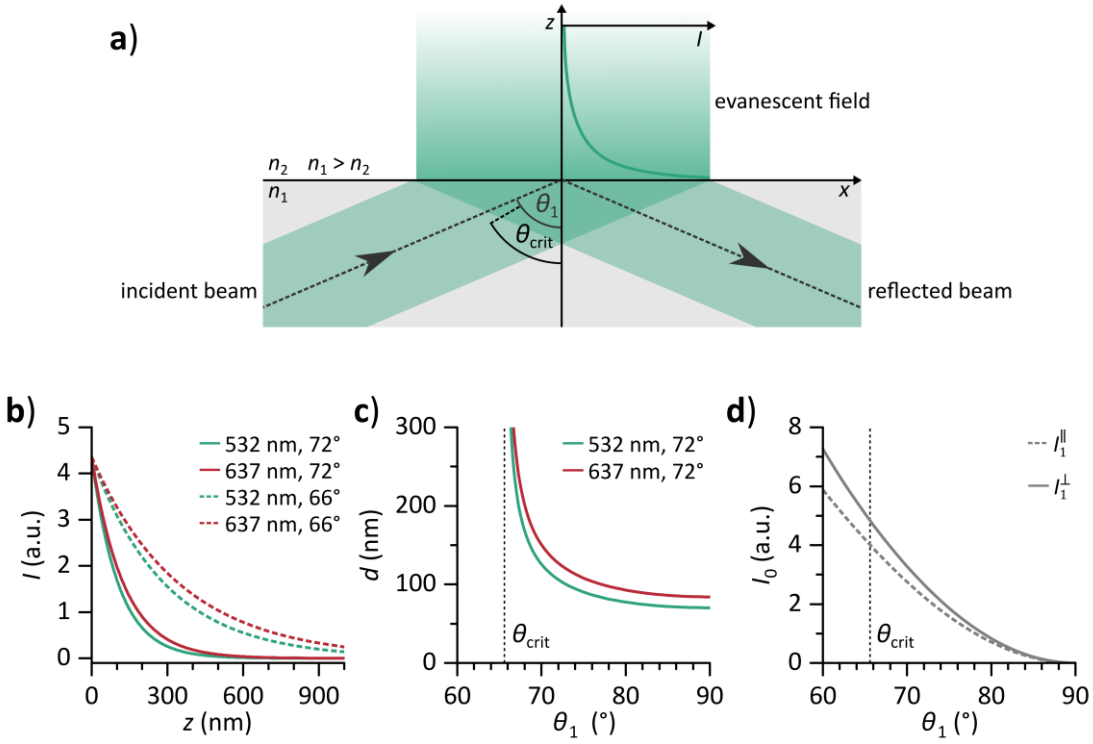

Figure 6: Principles of total internal reflection fluorescence microscopy. a) Light striking the interface of two media with refractive index n is totally internally reflected if the angle of incidence θ_1 is larger than the critical angle for total internal reflection θ_{crit}. The resulting evanescent field intensity decays with increasing distance z along the z-axis (green curve). **b)** Evanescent field intensity I as a function of z compared for different excitation wavelengths and incidence angles. **c)** Penetration depth d as a function of θ_1. **d)** Evanescent field intensity at the boundary I_0 as a function of θ_1 for p- ($I_1^{\parallel}$) and s-polarized ($I_1^{\perp}$) excitation. Arbitrary units (a.u.) are multiples of incident beam intensity I_1. Interface media: $n_{1,quartz} = 1.46$, $n_{2,water} = 1.33$)

In a TIRF microscope, an evanescent field is created at the boundary of the microscope slide (or cover glass) and the sample phase, usually an aqueous buffer, to selectively excite a thin (100–300 nm) section of the sample close to the phase boundary. Compared to epi-fluorescence microscopy, where the entire sample volume (10–100 µm) is excited and emits fluorescence, this improves the signal-to-background ratio by a factor of 100–1000. In a sufficiently diluted sample, only molecules tethered directly to the surface of the microscope slide are excited, allowing the observation individual particles. With this technique, immobilized particles can be monitored over extended periods of time. TIRF microscopy is realized by two main approaches to evanescent field geometry: one is objective-based, and one is prism-based.

In objective based TIRF microscopes, light is directed to the sample and collected from it by the objective lens. To achieve total internal reflection, the excitation light must exit the objective at an angle θ_1 from the optical axis larger than θ_{crit} as a parallel beam, allowing uniform reflection. For this, the excitation laser is focused at the back focal plane of the objective and displaced parallel to the microscope's optical axis. Thus, the beam strikes the edge of the objective and is refracted at an angle determined by the numerical aperture *NA,* that defines the maximum half-angle α at which the objective can receive, or in this case, transmit light as:

$$NA = n \sin \alpha$$ **Equation 16**

To achieve an incidence angle suitable for total internal reflection, a high *NA* objective, typically *NA* ≥ 1.45, is required. A disadvantage of this configuration is that in addition to the fluorescence from the sample, the reflected excitation beam is also efficiently collected by the objective and must be removed using suitable filters. This reduces the emission photon yield which can be problematic for weakly fluorescent samples.

In prism based TIRF microscopy, the excitation beam is directed towards the interface through a prism connected to the microscope slide by a medium of similar refractive index, e.g. immersion oil or glycerol. This configuration, introduced by Daniel Axelrod in 1981 [27], allows for a large incidence angle, resulting in a thin evanescent field (Equation 12) and consequently a high signal-to-background ratio. Emitted fluorescence is subsequently collected by an objective opposite of the excitation field. Thus, the reflected beam is excluded from the detection path. For cell and tissue imaging, this poses a disadvantage due to the need to focus trough the specimen, leading to spherical aberrations caused by diffraction within the sample. Single-molecule application are largely unaffected by this, as the sample volume is usually an isotropic aqueous phase, and the benefit of reduced background signal is appreciated. Compared to the objective-based approach, access to the sample, sandwiched between objective and prism, is limited and a specialized sample chamber is required to adjust buffer conditions during the experiment (Chapter 6.8.3).

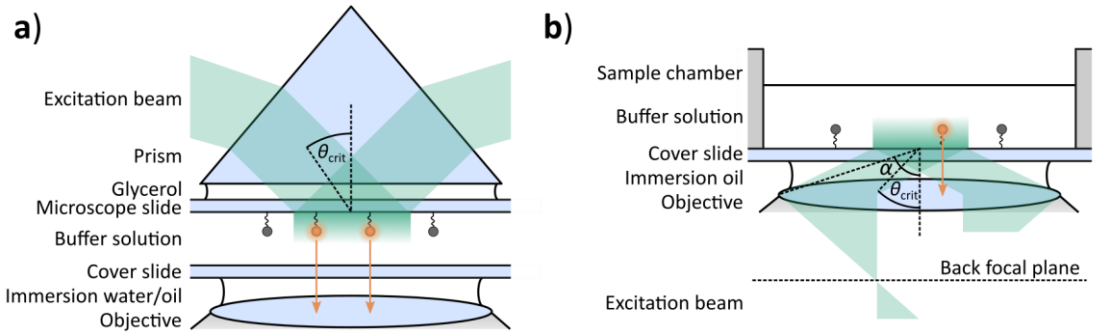

Figure 7: Comparison of TIRF microscope geometries. In a prism-based TIRF microscope, the excitation beam is directed to the sample by a prism and totally internally reflected, if the angle of incidence is greater than the critical angle θ_{crit}. The angle of incidence can have any value between θ_{crit} and 180°. Fluorescence emitted by surface tethered fluorescent molecules (orange arrow) is collected by the objective opposite of the prism. **b)** In an objective-based TIRF microscope, the excitation beam is focused through the back focal plane and refracted by an objective with a high numerical aperture ($NA = n \cdot \sin \alpha$). The range of incidence angles is limited to values between θ_{crit}.to α. The emitted fluorescence is collected on the same side as the excitation field (adapted from [75]).

2.1.4 Confocal fluorescence microscopy

Confocal fluorescence microscopy achieves a high signal-to-background ratio by axial confinement of the excitation beam and by blocking out-of-focus emission [22,26]. To achieve the first, the excitation laser beam is focused through the objective to a diffraction-limited spot in the sample plane. The focused beam penetrates the entire sample along the z-axis and the emitted fluorescence is collected by the same objective and focused on a micrometer-sized pinhole. By this, out-of-focus emission is physically blocked. Depending on the wavelength of the excitation

laser and diameter of the pinhole the resulting confocal observation volume can be limited to approximately one femtoliter (Figure 8).

Confocal microscopy is suitable for single-molecule experiments with samples immobilized to a surface or freely diffusing particles in solution. The latter requires a sufficiently low sample concentration (1–100 pM) to ensure that the confocal volume is only ever occupied by a single particle. This approach offers the advantage of removing potential interactions of the charged glass surface with proteins and nucleic acids. Depending on diffusion speed of the sample, the transit time through the confocal volume is approximately 0.5–5 ms. During its transit, a fluorescent particle is continuously excited and emits photons (10^2–10^3) that are detected as a "burst" in signal intensity by an avalanche photo diode (APD). These devices are characterized by high time resolution (on average 200 ps) high photon detection efficiency (on average 70%) and offer single-photon sensitivity.

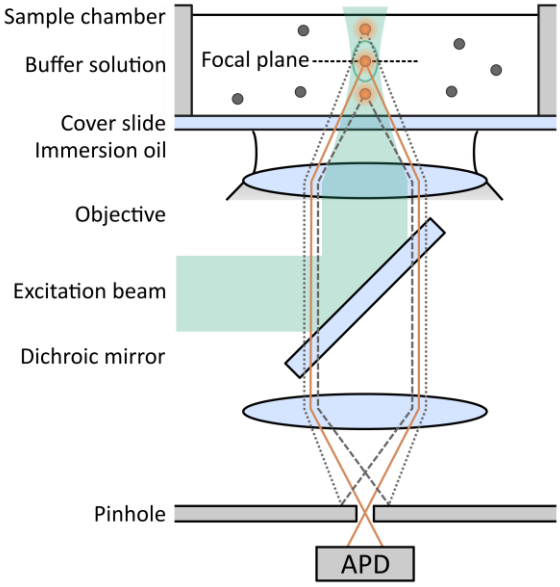

Figure 8: Principles of confocal fluorescence microscopy. The excitation beam is focused through the objective into a diffraction limited spot. Diffusing molecules (gray spheres) transitioning through the excitation beam emit fluorescence (orange spheres). Emission is collected by the same objective and focused on a pinhole that block out-of-focus emission (dotted and dashed gray line). Only emission close to the focal plane (orange line) can reach the avalanche photodiode (APD), creating a confocal volume (green circle) defined by the excitation beam width and the pinhole diameter.

2.2 Single-molecule force measurements

Forces play a fundamental role in cellular processes like transcription [76–78], DNA replication [79,80] and translation [42,81] as well as mechanisms of DNA compaction [82–85]. The most widely employed methods for force application and sensing in biological systems are optical and magnetic tweezers as well as AFM (reviewed in [86]). In magnetic tweezer measurements, the molecule of interest is tethered to a surface on one end and to a magnetic particle (0.5–5 µm) on the other. Force is applied by an electromagnet positioned above the sample [87]. Similarly, optical tweezers trap a dielectric particle in the diffraction limited spot of a focused laser beam [10]. The molecule of interest is tethered to the trapped particle on one end and either to a surface or another trapped particle on the other end [88–90]. Displacement of the particle from the laser focus exerts a restoring force that pulls the particle towards the focus [10]. In AFM experiments, force sensing and application is facilitated by a cantilever equipped with a monomolecular tip. This

requires the molecule of interest to be tethered to the cantilever and a surface while force is applied by displacing the sample relative to the cantilever, e.g. via a piezoelectric stage [9].
These methods fill specific niches depending on the required temporal, spatial and force resolution. AFM provides high spatial resolution (approximate 1 nm) but is limited in force resolution below 10 pN, which is relevant for many biological processes (Chapter 3.5). While optical tweezers can, in principle, resolve single base pair steps in RNAP transcription (< 0.5 nm) [91], they can only measure few molecules at once, limiting experimental throughput [92]. Magnetic tweezers, on the other hand, are both force sensitive and multiple immobilized complexes can be imaged at once, but their spatial resolution is limited to approximately 5 nm. Additionally, long linkers are usually required in the above techniques that connect the system of interest to a surface or large particle, thereby introducing considerable noise and drift [93]. Moreover, surface connectors do not permit *in vivo* applications. To circumvent these limitations, force application and sensing devices that are not connected to the macroscopic world have been constructed by exploiting DNA nanotechnology [94–97].

2.2.1 DNA origami-based single-molecule force spectroscopy

In DNA nanotechnology, DNA is repurposed from a carrier of genetic information to a building material for the construction of nanometer scale structures [98]. This can be realized by the DNA origami technique that was introduced 2006 by Paul Rothemund and named in analogy to origami, the art of folding a sheet of paper into a two- or three-dimensional structure [99]. Likewise, DNA origami is the process of molecular self-folding of a prescribed structure using a long, circular ssDNA (scaffold) and hundreds of short single-stranded DNA (ssDNA) oligonucleotides. These so-called staple strands, typically 20–60 bp long, are designed to bind to complementary regions of the scaffold DNA, thereby connecting (“staple”) distal parts into an organized structure. (Figure 9a). DNA presents in ideal construction material due to the inherent complementarity of Watson-Crick base pairing, which allows self-assembly of origami structures. Hence, all necessary components can be combined in a single reaction.

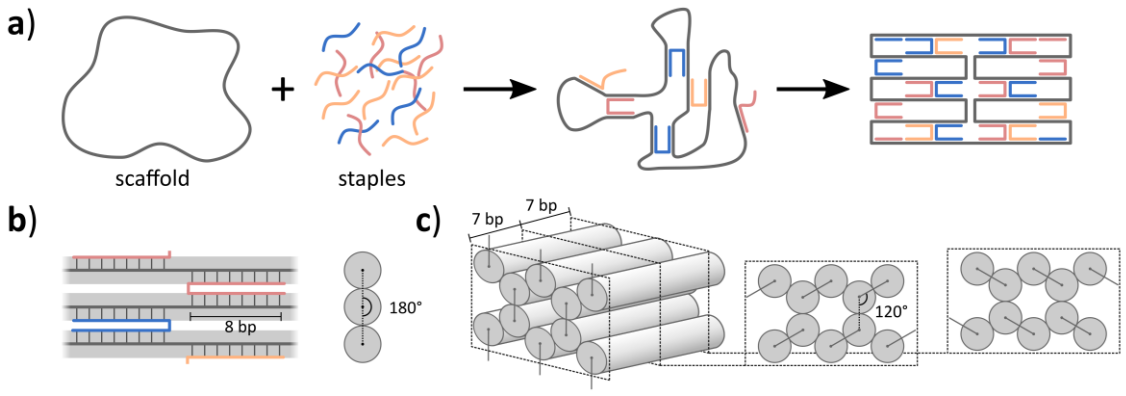

Figure 9: Principles of DNA origami. a) Self-folding of a DNA origami structure from a circular ssDNA scaffold and 20-60 nt complementary staple strands. **b)** Schematic representation of strand cross-over in planar helix monolayers. Watson-Crick base-pairings are indicated as connecting lines between scaffold and staples; DNA helices are depicted as gray cylinders. **c)** Honeycomb structure of three-dimensional DNA origami constructs. Strand crossovers are indicated by connected dots. Slices represent possible combinations of interconnection with a 21 bp periodicity (adapted from [100,101]).

After heating, the origami anneals ("folds") based on thermodynamic stability of individual base pairings. Thus, staple strands can be added in high excess, as strands that are only partially complementary to a scaffold region will be displaced by the correct strand during the cooling process. This enables a high yield of fully folded DNA origami structures and simplifies downstream processing.

The first DNA origami structures utilized the circular single-stranded M13mp18 phage genome (7249 nt) as a scaffold [99]. The design principle of these constructs was to connect neighboring helices via strand cross-overs every 8 bp, resulting in a 180° angle between helices (Figure 9b). These helix monolayers were relatively flexible and only allowed construction of two-dimensional structures. In order to realize three dimensional objects, Douglas *et al*. introduced a honeycomb structure, wherein each helix is connected to three adjacent ones at a 120° angle every 7 bp (Figure 9c). Due to the tight packing of negatively charged phosphates in the DNA backbone, these DNA origami structures require high concentrations of Mg^{2+} ions to remain stable.

A great advantage of DNA origami is that every position in the scaffold can be specifically addressed by base complementarity. Thus, chemical modifications such as fluorophores or biotins, covalently linked to staple strands, can be precisely positioned within a structure. This enables the construction of functional nanometer scale devices (reviewed in [102]).

This technique was utilized recently to construct nanoscale structures that enable force application to biological samples [94,95]. Force measurements on DNA/protein complexes performed in this works were conducted using a DNA origami-based nanodevice designed by Nickels *et al.* [94]. This construct exploits the entropic force generated by a constrained ssDNA chain to exert a constant force in the piconewton range on a system of interest fixed within the spring. In convention with other constant force application techniques this device is termed DNA origami force clamp (FC). The FC has already been applied to study the force-dependency of conformational fluctuations in small DNA structures as well as DNA bending by TBP [94].

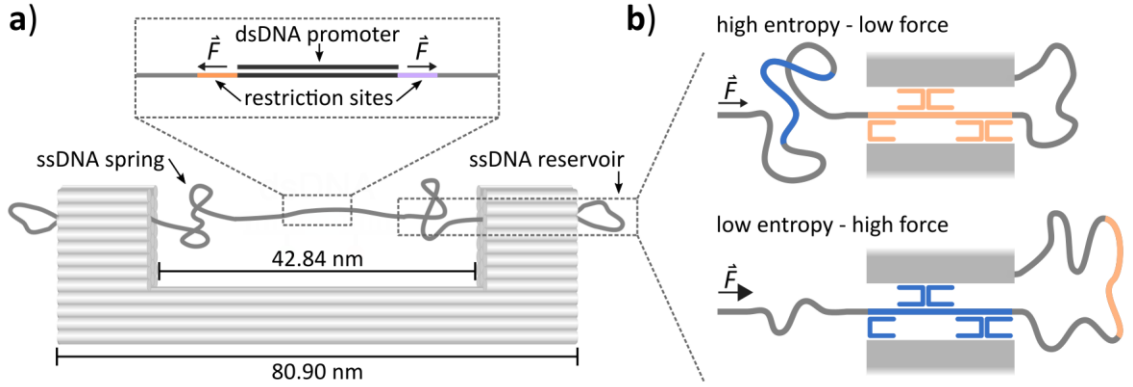

Figure 10: The DNA origami force clamp. a) Schematic depiction of the DNA origami force clamp structure. Gray cylinders represent DNA helices. The inset shows the multiple cloning site of the M13mp18 phage scaffold with a cloned target sequence (here: promoter sequence) annealed to a complementary strand to form a dsDNA probe segment that is under constant force *F* applied by the entropic ssDNA spring. **b)** The force of the entropic spring is tuned by using different sets of ten staple strands (five per post) that distribute ssDNA between the spring and the outer reservoir segment. Increasing the spring length raises the entropy of the system, resulting in a lower entropic force, whereas shortening the spring has the opposite effect.

The FC structure consists of a rigid, bracket-like frame of horizontally aligned helix-bundles in a honeycomb configuration. This frame has an outer diameter of 80.90 nm and the opening formed by the outer posts has a diameter of 42.84 nm (Figure 10a). The scaffold (M13mp18 phage genome, 7249 nt) runs through the entire structure and emerges from the posts to span the opening as ssDNA. The fixed anchor points limit the conformational freedom of this ssDNA segment and as a result, it acts as an entropic spring that exerts constant force inversely proportional to its length (Chapter 6.4). Lowering the length of the spring reduces the conformational freedom and entropy of the system, resulting in higher forces. The length of the ssDNA within the spring region can be adjusted by using different sets of ten staple strands that bind to the scaffold in defined regions and allocate scaffold DNA between the ssDNA spring and the outer ssDNA reservoir sections (Figure 10b). Using a specific set of staples in the folding reaction yields DNA origami structures with a fixed spring length and force that cannot be adjusted afterwards. To utilize this force experimentally, different target sequences can be placed within the spring using the multiple cloning site of the M13mp18 scaffold, which is centered in the spring segment. In the context of this work, archaeal und eukaryotic promoter sequences were inserted into the scaffold. Annealing a complementary strand to this target sequence creates a double-stranded DNA (dsDNA) segment, which is under strain applied by the surrounding spring DNA (Figure 10a). Conformational changes in the DNA such as TBP-induced DNA bending have to occur in opposition to the applied force.

3 Transcription initiation

The primary goal during the transcription initiation phase is the specific recruitment of the RNAP to the promoter region of a gene, leading to the formation a closed PIC. Subsequently, the DNA duplex is melted to form an open PIC. This includes the accurate positioning of the TS in the active center of the RNAP. Afterwards, the RNAP repeatedly starts to synthesize and release small RNA transcripts in a process termed abortive initiation, which eventually results in the RNAP escaping from the promoter to enters the processive elongation phase (reviewed in [47]). Bacteria, archaea and eukaryotes have evolved characteristic mechanisms to realize the individual steps of transcription initiation and a selection of the involved factors and structures will be highlighted in the following section.

In Bacteria, the RNAP binds to one of several σ-factors, the most common being the housekeeping factor σ70, to form an RNAP holo-enzyme [103,104]. The bacterial core promoter features five sequence elements: the -35 motif, extended -10 motif, -10 motif, discriminator and the core recognition element (CRE) [105]. The -35, extended -10 and -10 motif as well as the discriminator sequence are each recognized by the σ4, σ3, σ2 and σ1.2 domains of σ70, while the RNAP contacts the CRE surrounding the TSS (Figure 11a). Following DNA binding, the σ2 domain promotes DNA melting by flipping and trapping the -11 and -7 nucleotides of the NTS and thus destabilizes the DNA duplex [105]. The RNAP then proceeds into abortive initiation [106], transcribing and releasing short RNA transcripts in a DNA scrunching mechanism [107,108]. Upon synthesis of a sufficiently long transcript (approximately 7–11 nt), the RNAP can break the strong interactions with the σ factor and escapes into productive elongation [109].

Archaea and eukaryotes display much higher structural homology amongst their transcription machineries as compared to the bacterial system and do not contain a homolog of σ factors. Instead, the archaeal RNAP utilizes TBP, TFB and TFE that are homologous to eukaryotic TBP and the RNAP II specific factors TFIIB and TFIIE [110–117], respectively (reviewed in [44,118,119]). TBP (Chapter 3.1) and an RNAP-specific TFIIB-like factor (Chapter 3.2) bind to the promoter DNA upstream of the TSS and subsequently recruit their cognate RNAP.

The archaeal transcription machinery is often described as a simplified version of the eukaryotic RNAP II system. Hence, transcription initiation in archaea only requires a minimal amount of factors (reviewed in [44,118–120]) (Figure 11b). In archaea, TBP binds the TATA-box around position -24 relative to the TSS and induces a sharp kink in the DNA [121–125]. The TFIIB-like factor TFB contacts the BRE around position -32, establishing DNA contacts upstream and downstream of the TATA-box thereby stabilizing the bent promoter DNA/TBP complex in the correct orientation [121,123,124,126]. TFB then recruits the RNAP resulting in the formation of the closed PIC [127]. This minimal factor combination is sufficient to support transcription initiation [111,112,128,129] as the TBP-induced bent conformation destabilizes the DNA duplex and assist in formation of a transcription bubble spanning the -7 to +1 region [53]. The initiation factor TFE supports DNA melting and transition into the elongation phase [129–131]. After binding, the RNAP engages in abortive initiation and escapes the promoter upon synthesis of a 10–14 nt transcript, breaking contacts with TFB [132].

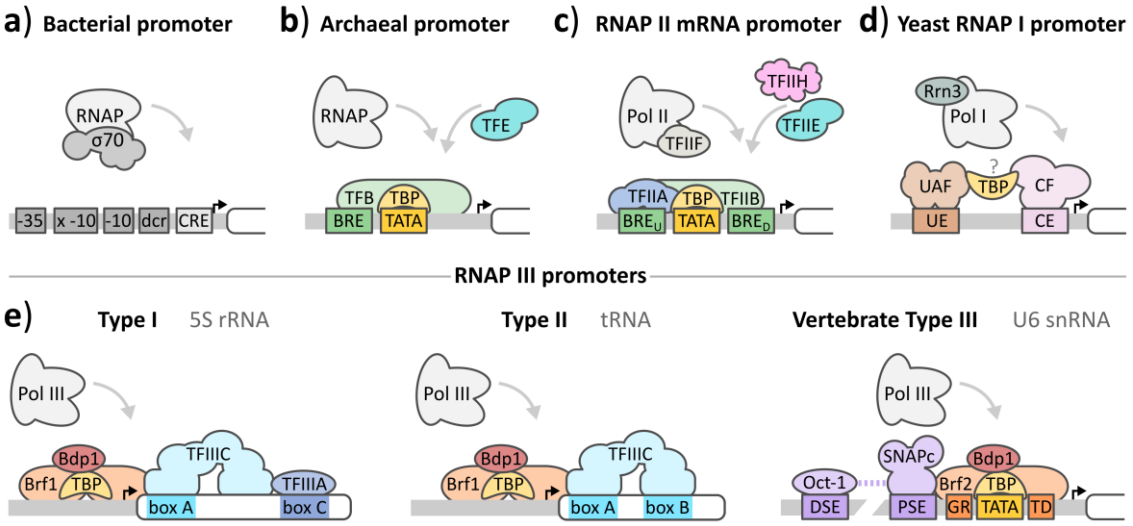

Figure 11: Transcription initiation complex assembly in bacteria, archaea and eukaryotes. a) Model of a bacterial core promoter containing the -35, extended -10 (x -10), -10, discriminator (dcr) that are bound by σ70 domains and core recognition element (CRE) bound by the RNAP. **b)** Model of an archaeal promoter. The TATA box is bound by TBP and the upstream BRE bound by TFB, which recruits the RNAP. The optional factor TFE then binds to the RNAP. **c)** Model of an exemplary RNAP II mRNA promoter. The TATA box promoter element is bound by the TBP and the flanking upstream (U) and downstream (D) BREs are bound by TFIIB which contributes to Pol II recruitment. TFIIA binds the DNA upstream of the TATA-box thereby stabilizing TBP. Binding of TFIIE and TFIIH completes the PIC. **d)** Model of an *S. cerevisiae* rDNA promoter: an upstream element (UE) is bound by the UAF which then positions the core factor (CF) at the core element (CE) with the help of TBP (?: positioning unresolved in structures), allowing for the recruitment of the RNAP I-Rrn3 complex. **e)** Three types of Pol III promoters. Type I promoters contain the gene-internal element 'box C' bound by TFIIIA and the 'box A' element bound by TFIIIC that recruits. Together with the TFIIIB complex (TBP, Brf1 and Bdp1), they co-operate to recruit RNAP III. Type II promoters contain a 'box A' and a 'box B', both bound by TFIIIC, which interacts with TFIIIB to recruit RNAP III. A vertebrate-specific type III promoter consists of a distal sequence element (DSE) and proximal sequence element (PSE) in addition to a mandatory TATA-box flanked by the GR and TD motif. The DSE is bound by Oct-1 that supports SNAPc binding of the PSE. Together they recruit a specific TFIIIB version which contains Brf2 instead of Brf1. The DNA is shown as a gray bar, the transcription start site is indicated by an arrow. The gene body is shown as a white box. Dark and light colors denote associated factors/sequence elements (adapted from [54]).

TBP and TFIIB-like factors are conserved in all three eukaryotic transcription systems [133]. Highly regulated RNAP II promoters are structurally similar to archaeal core promoters, featuring a TATA-box around position -24 to -31 relative to the TSS [134] and an upstream and downstream BRE flanking the TATA-box around position -32 to -38 and -17 to -23 respectively [135,136] (reviewed in [137]). These motifs are recognized by TBP and TFIIB that form a bent promoter complex structurally similar to its archaeal counterpart [127,138,139]. The initial step of TBP binding can be stimulated by the RNAP II-specific factor TFIIA that is not required for RNAP II transcription *in vitro* [140–142]. TFIIA is composed of two subunits and binds the DNA immediately upstream of the TATA-box, stabilizing the bent DNA/TBP complex [140–142]. RNAP II is recruited into the complex via interaction with N-terminal zinc-ribbon of TFIIB [143,144]. This complex can be joined by the dimeric factor TFIIE [145–148], the eukaryotic homolog of TFE and TFIIF [148–151] that stabilize the PIC and support open complex formation [51,152,153]. RNAP II relies on the ATP-dependent DNA translocase activity of TFIIH, which is recruited by TFIIE [154], to facilitate melting of the DNA downstream of the TSS [155–157] (Figure 11c). Promoter clearance depends on

abortive initiation coupled to TFIIB ejection upon synthesis of a 7-9 nt RNA [158]. RNAP I exclusively transcribes rDNA promoters and differs the most from the archaeal/RNAP II initiation mode (reviewed in [159]). RNAP I initiation in *Saccharomyces cerevisiae* relies on the core factor (CF) or selectivity factor 1 (SL1) in mammals, which binds to the upstream core element and includes the TFIIB-like subunit Rrn7 (TAF1B in mammals) [133,160–162]. The CF can subsequently recruit RNAP I in complex with Rrn3, forming a basal PIC [163–165]. The upstream activating factor (UAF) can stimulate CF recruitment via interaction with TBP, that does not bind a TATA-box like sequence on the DNA and instead is predicted to bridge UAF and CF [166–168] without inducing the characteristic kink in the DNA [169–171] (Figure 11d). Open complex formation and promoter escape do not require additional factors [172]. It is noteworthy that *in vitro*, basal RNAP I initiation rates can be reconstructed in a system that lacks TBP [163,173].

RNAP III and its accompanying transcription initiation factors share a high similarity to the RNAP II system (reviewed in [133,174]). A distinct difference is the stable incorporation of TFIIE- and TFIIF-like subunits into the RNAP III (reviewed in [133,174]). The C37/C53 dimer functionally corresponds to TFIIF [175,176], whereas the subunits C31/C34/C82 are structurally similar to TFIIE [176,177]. Transcription by RNAP III proceeds from three different promoter classes that contain different promoter elements and require corresponding factors for initiation (reviewed in [178]). The only common factor required for transcription from all three promoter classes is TFIIIB, a complex consisting of TBP, the TFIIB-related factor 1 (Brf1) [179–181] and Bdp1 (B-double prime, B'') [181–183] (Chapter 3.3). Vertebrates additionally employ a TFIIIB variant in which Brf1 is replaced by Brf2 [183–185]. Both factors are structurally similar, but Brf2 association to the DNA/TBP complex is regulated by the redox state of the cell [186]. The Brf2 containing variant of TFIIIB is required for transcription from type III promoters (e.g. U6 snRNA and selenocystein tRNA), whereas type I and II promoters utilize the Brf1 containing variant [187,188].

In most organisms, only type III promoters contain a canonical TATA box that is recognized by the TBP subunit of TFIIIB [189]. In vertebrates, type III promoters additionally feature a proximal sequence element (PSE) and distal sequence element (DSE) -50 and -240 bp relative to the TSS, respectively [190]. These are bound by SNAPc and Oct-1, respectively. Type I and II promoter typically do not contain a canonical TATA box [190]. Hence, initiation from type I and type II promoters requires additional factors to accurately position TFIIIB [191]. Type II promoters (most tRNAs) contain gene internal A and B box promoter elements that are both bound by the multisubunit factor TFIIIC to recruit and deposit TFIIIB upstream of the TSS via a direct interaction with TBP [191,192]. The 5S rRNA promoter is the only type I promoter and further requires TFIIIA for TFIIIC binding and subsequent TFIIIB recruitment (reviewed in [193]). TFIIIB is sufficient to recruit RNAP III and to initiate transcription *in vitro* (Figure 11e). Promoter melting is facilitated by the RNAP III subunit C34, which is structurally similar to TFIIE, and Bdp1 [194–196]. RNAP III also engages in abortive initiation for fewer cycles than RNAP II or bacterial RNAP before promoter clearance [197].

3.1 The TATA-binding protein

TBP is the pivotal initiation factor in archaeal and eukaryotic transcription initiation, and highly conserved in both, structure and function (reviewed in [54,198,199]) (Figure 12a) and is necessary to achieve high rates of transcription of archaeal RNAP and all three eukaryotic RNAPs. TBP consists of a conserved 180 amino acid core that is formed by two symmetrical TBP domains each consisting of approximately 60 residues arranged in a five-stranded, antiparallel β-sheets and two α-helices (Figure 12b). The symmetry relates to the evolutionary origin of TBP as a result of gene duplication of the bacterial RNase HIII [198,200]. The β-sheets form a concave, hydrophobic surface, which tightly binds the minor groove of the DNA double helix while the two α-helices form a convex surface on the opposite side, resulting in an overall saddle-shaped structure. This analogy is furthered by two "stirrup" loops emerging between the outer β-strands which each contain a conserved phenylalanine [200]. A second conserved phenylalanine is located at the end of strand 4 of either lobe (Figure 12c). The core structure is evolutionary highly conserved (Figure 12d). Additionally, some TBP proteins, mainly in eukaryotes, possess an N-terminal extension that varies in length, sequence and functionality, but is generally enriched in glutamic acid residues. Likewise, archaeal TBPs often contain a short N-terminal extension enriched in glutamines (Figure 12a).

TBP shows a high affinity for the TATA-box sequence element found in archaeal and eukaryotic core promoters (consensus sequence TATAWAWR [201]; W = T/A; R = G/A). TBP binds to this sequence with its concave side by forming hydrophobic interactions with the nucleobases and simultaneously inserts the conserved phenylalanines between bases 1/2 and 7/8 of the TATA-box to induces a sharp, approximately 90° bent in the DNA that also results in a widening of the major groove [121,123,202–204]. This function had been predicted based on gel assays [122] and was later confirmed by the crystal structures of a DNA/TBP complex [202,203]. The TA-rich TATA sequence is well suited for bending due to the low energy cost of inserting phenylalanines between base pairs TA:AT and AT:GC [205,206]. Changes in the sequence can severely affect TBP binding affinity [207,208]. Even though TBP shows a high degree of internal symmetry, hydrophobic residues that form direct interactions with DNA bases are placed in an asymmetric fashion, allowing for a unidirectional orientation of TBP on the consensus TATA sequence [202,209]. Stopped-flow experiments revealed that binding and bending by TBP occur simultaneously [210]. An analysis of the underlying kinetics suggested a three-step binding model, proceeding through two DNA-bound intermediates before reaching a stable complex. All intermediates varied in DNA bending time but showed identical bending angle [211–213].

As the central initiation factor, TBP dynamically interacts with a variety of other transcription factors and regulators (reviewed in [214]). The most critical is the interaction with RNAP-specific TFIIB-like factors, that primarily contact the N-terminal lobe of TBP [200] and act as adapters to bridge the RNAP to the promoter [123,138,162,215] (Chapter 3.2). In contrast, the C-terminal lobe of eukaryotic TBPs is targeted by regulatory proteins that either stabilize the DNA/TBP complex such as the RNAP II specific factor TFIIA or destabilize it such as BTAF1/Mot1 and NC2 that can actively evict TBP from the promoter [216–218].

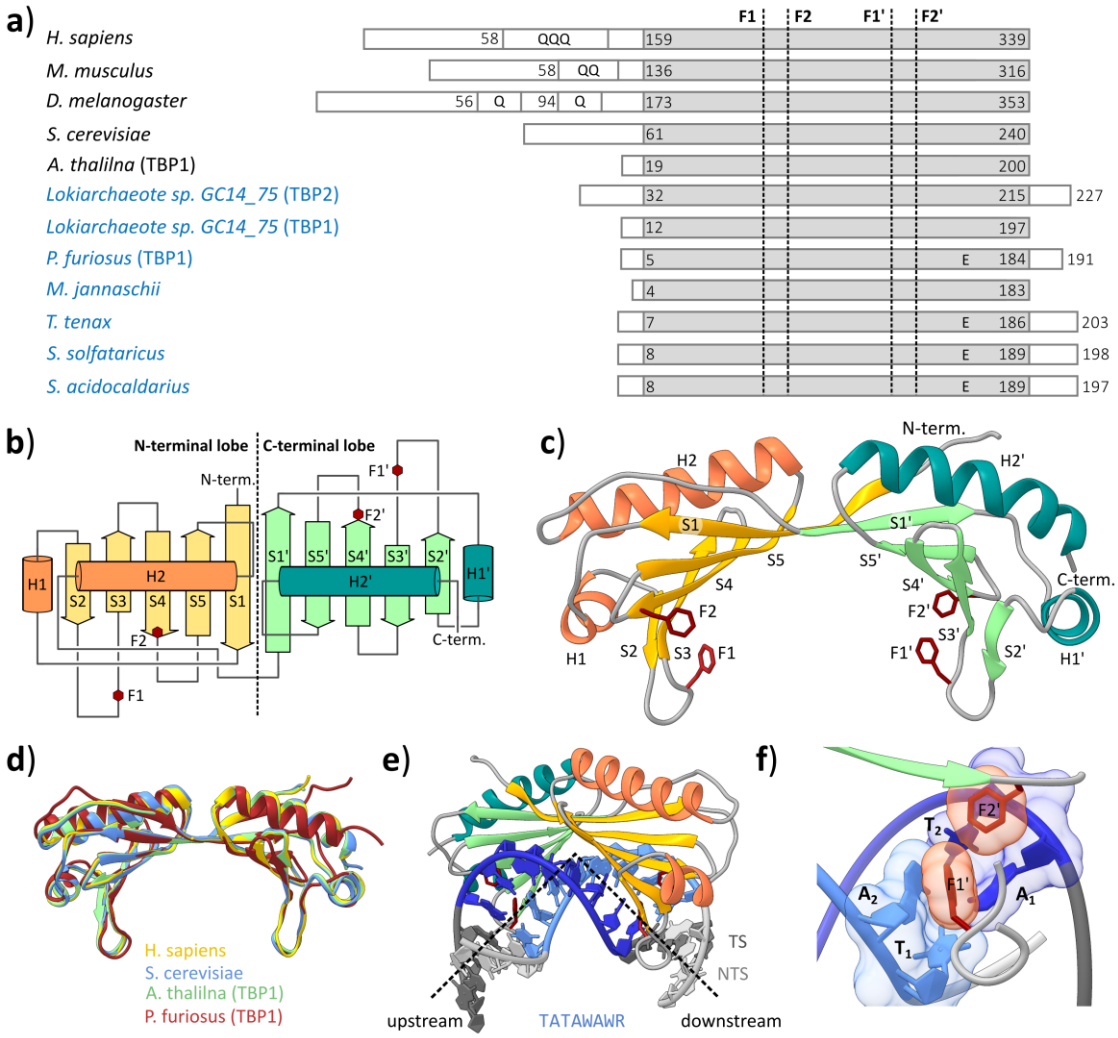

Figure 12: Structural conservation of TBP. a) Comparison of eukaryotic (black) and archaeal (blue) TBP amino acid sequences highlighting the positions of the conserved 180 amino acid core region (gray box) that contains the phenylalanines (F1, F2, F1', F2'), the 5–38 glutamine stretches (indicates as Q–QQQ) in the N-terminal extension of eukaryotic TBPs and the 4–8 glutamic acid residues (E) in the short C-terminal tail of archaeal TBPs. **b)** Schematic overview of the symmetric secondary structure organization of core TBP: β-strand (S), α-helix (H). **c)** X-ray crystal structure of human core TBP (PDB 1CDW) colored according to (b); **d)** Structure alignment of eukaryotic and archaeal core TBPs. **e)** Bending of the promoter DNA by TBP bound to the TATA-box sequence (blue). The bending angle of the DNA is highlighted as black dashed line (PDB 1CDW). The human consensus TATA-box sequence on the NTS is shown. **f)** Close-up of a set of phenylalanines intercalating between the bases 1 (T_1/A_1) and 2 (T_2/A_2) of the TATA box; parts of the structure were cut to improve visibility. (adapted from [54])

In Archaea, TBP and TFB are necessary and sufficient for PIC formation and promoter dependent transcription *in vitro* [111,112,128]. This holds true for the closely related RNAP II system for TATA-box containing promoters if the DNA around the TSS is naturally susceptible to melting [153,219]. However, isolated eukaryotic TBP is insufficient *in vivo* [220,221], as well as for transcription from promoters without a TATA box [222], which constitute the majority of eukaryotic promoters. [223]. For initiation at RNAP II transcribed TATA-less promoters, correct TBP binding and positioning require higher order complexes such as TFIID [224,225] or SAGA [226,227] that are centered around TBP and encompass several TBP-associated factors (TAFs). These TAFs facilitate recognition of core promoter elements to accurately position TBP, and thus the TSS, on all types

of promoters [220,228]. TFIID has also been implied to facilitate reallocation of TBP between initiation complexes [229]. TBP also interacts with the 25 subunit Mediator coactivator complex [230], which is required for initiation of most genes *in vivo* (reviewed in [231]).

3.1.1 Analysis of TBP-DNA interactions with single-molecule FRET

TBP-induced DNA bending in the absence of additional factors is a dynamic process that occurs in a stochastic manner. Hence, DNA/TBP-interaction have been studied using smFRET approaches to unravel intermediate steps of DNA binding and bending.

Time-resolved smFRET experiments using TIRF microscopy demonstrated that DNA bending in archaea occurs in a single step from the unbent to the fully bent complex with dwell times in both states in the millisecond range [232]. Furthermore, TBP from the euryarchaeon *M. jannaschii* can bend the DNA without further factors, whereas TBP from the crenarchaeon *S. acidocaldarius* strictly relies on interaction with TFB to bend the DNA [232]. The requirement for both, TBP and TFB has also been shown in confocal smFRET experiments for the euryarchaeal *P. furiosus* transcription system [232,233].

For *S. cerevisiae* TBP, a three-step mechanism proceeding through a TBP-bound unbent state, a partially bent state and a final fully bent state has been demonstrated [232]. *S. cerevisiae* TBP has also been show to bind DNA in a reverse orientation (C-terminal lobe facing downstream), in particular in the absence of additional factors such as TFIIA and TFIIB [234]. This has received further confirmation by smFRET experiments utilizing fluorescently labeled *S. cerevisiae* TBP, which also showed that TFIIA assists in positioning TBP in the correct orientation [217]. The *S. cerevisiae* DNA/TBP complex is highly stable with DNA binding times of several minutes [217,218,232]. TBP binding can be regulated by NC2 that causes DNA unbending and slides TBP off the TATA-box [218].

Time resolved smFRET experiments using human TBP revealed two kinetically distinct populations of DNA bound TBP with average bent state dwell times of 5 s and 50 s, that showed identical bending angles [235]. DNA bending also occurs in a single transition from unbent to fully bent state without partially bent intermediates [235]. The bending angle of human DNA/TBP complexes has also been reported to be independent of the TATA box sequence [235,236].

3.2 TFIIB-like factors

The other essential initiation factor crucially involved in PIC formation is a TFIIB-like factor that binds to the DNA/TBP complex and selectively recruits its cognate RNAP to the promoter. This family of proteins is named after the RNAP II specific factor, which was the first to be discovered and is the best characterized [127,237,238]. In Archaea, TFB fulfills an identical role [112,129,239]. The eukaryotic RNAP III relies on Brf1 for most transcription [179–181], but in vertebrates, transcription of type III promoters requires Brf2 [183–185]. The TFIIB-like factor corresponding to RNAP I was identified through sequence homology prediction as the subunit Rrn7 of the CF in yeast and TAF1B of the human SL1 [160–162].

All TFIIB-like factor share a common core domain organization (Figure 13a), consisting of an N-terminal zinc-ribbon (B-ribbon) that is connected via a reader (B-reader) and linker domain

(B-linker) to two C-terminal cyclin fold domains, each consisting of five α-helices [127,240–242] (Figure 13c). Brf1 and Brf2 additionally feature a C-terminal extension that wraps around TBP and in Brf2 additionally confers redox sensitivity [186,215]. An extended C-terminal domain is also featured in the RNAP I factors Rrn7 and TAF1B [161,162] (Figure 13a). The cyclin domains bind the DNA/TBP complex by specific recognition of the BRE upstream of the TATA-box [139,243] to stabilizing the bent DNA/TBP complex in the correct orientation [124,139,234,244] (Figure 13c). The zinc-ribbon is an essential domain for RNAP recruitment [127,143,245]. Interestingly, the zinc-ribbon of Brf1 is not strictly required to recruit RNAP III [246]. After RNAP recruitment, the N-terminal domain motif assists in TSS selection via its B-reader helix [242,245,247,248] and with the help of the B-linker contributes to promoter melting [52,127,249]. Additionally, the B-reader also interacts with the emerging RNA transcript, which triggers ejection of TFB/TFIIB and promoter escape by the RNAP after synthesis of a sufficiently long transcript [132,158]. The B-linker domains are functionally interchangeable for all eukaryotic TFIIB-like factors, whereas the B-reader confers RNAP-specificity [161,162].

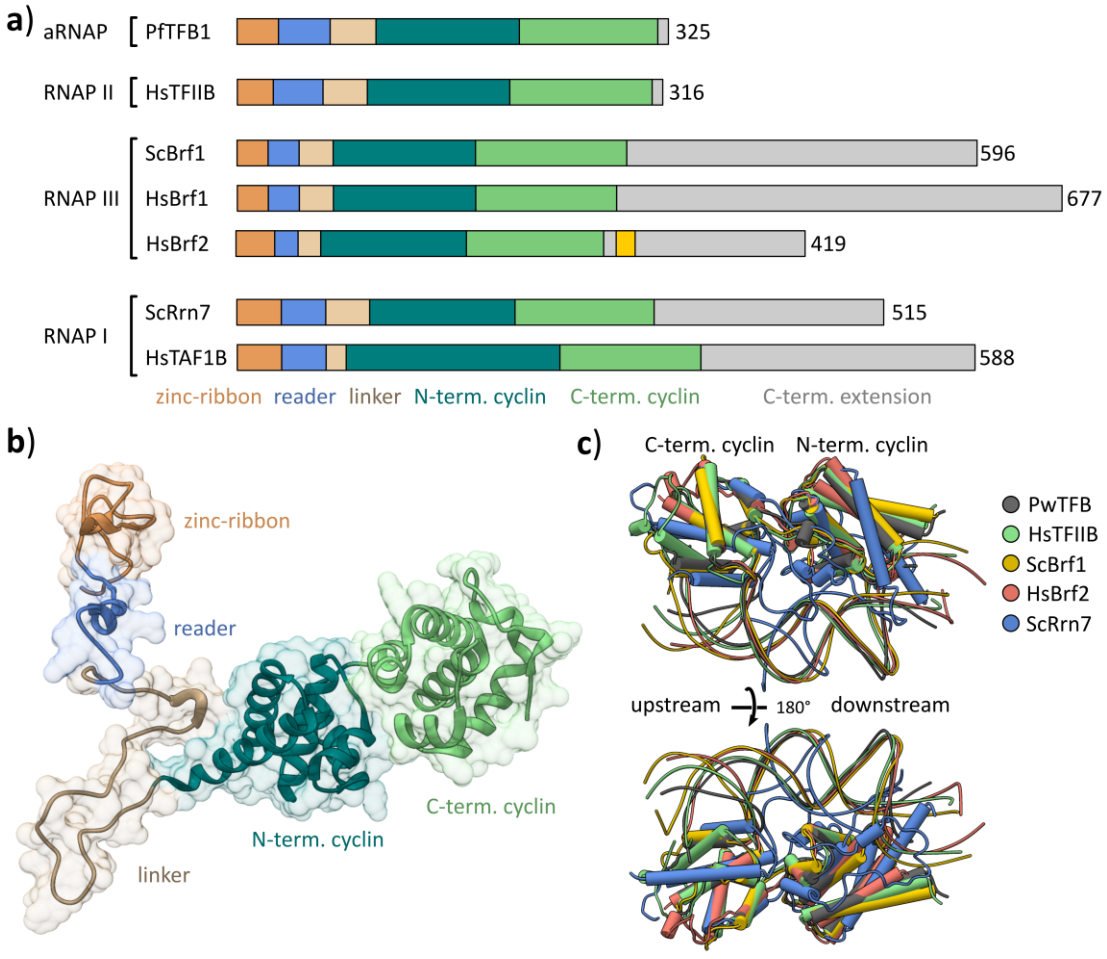

Figure 13: Structural conservation of TFIIB-like factors. a) Comparison of domain organization in eukaryotic RNAP I, II and III as well as archaeal RNAP (aRNAP) specific TFIIB-like factors. The redox sensing molecular pin structure in the vertebrate-specific Brf2 is highlighted in yellow (adapted from [162]). **b)** Structure model of human TFIIB (PDB 5IYB). **c)** Structure alignment of the core cyclin fold domains and upstream promoter DNA for *P. woesei* TFB (PDB 1D3U), *H. sapiens* TFIIB (PDB 5IYB), *S. cerevisiae* Brf1 (PDB 6F40), *H. sapiens* Brf2 (PDB 4ROC) and *S. cerevisiae* Rrn7 (PDB 6TPS). The upstream DNA is not fully resolved in the Rrn7 structure.

3.2.1 Analysis of TFIIB-like factor mechanisms with single-molecule FRET

The interactions of archaeal TFB have been subject to analysis using smFRET experiments to unravel the interactions of the flexible N-terminal domains with the RNAP during transcription initiation. In the *M. jannaschii* transcription system, the TFB B-linker and B-reader domains move along with the clamp domain of the RNAP. This flexible domain can adopt several conformations over the course of the transcription cycle [250]. Addition of TFE has been demonstrated to further open the clamp in the open PIC [250], a movement that is also reflected by the linker and reader domain of TFB [132].

In the human RNAP II transcription system, smFRET experiments revealed that the majority of RNAPs that escape into productive elongation can release TFIIB at two distinct trigger points, upon transcription of a 7 nt and 9 nt RNAP transcript. TFIIB releases was demonstrated to occur at a similar kinetic rate after either checkpoint [158].

3.3 The central RNA polymerase III initiation factor TFIIIB

The mechanisms of transcription have been studied in detail for the eukaryotic RNAP II system (reviewed in [251,252]), while knowledge on the mechanisms and, in particular, structures of RNAP I and III has only improved in recent years, despite their critical role in cell functionality [164,169,172,194–196,253] (reviewed in [159,174]). Transcription by RNAP I and III is crucially linked to cellular growth and proliferation as their gene products (rRNA and tRNA) are directly involved in protein synthesis.

Transcription initiation by RNAP III is strictly dependent on the heterotrimeric factor TFIIIB, both *in vivo* [254] and *in vitro* [189,191]. For transcription initiation at type III promoters like the U6 snRNA promoter, TFIIIB is the only required basal factor in *S. cerevisiae* [255]. In vertebrates, type III promoters additionally require SNAPc to recruit TFIIIB, as well as Oct-1 which enhances recruitment of SNAPc [256–259]. SNAPc acts as a selectivity factor that coordinates RNAP III initiation at TATA-containing snRNA promoter and RNAP II initiation at TATA-less snRNA promoters [260] (reviewed in [261]).

The first step in U6 promoter dependent transcription initiation, the TATA box of the promoter is specifically recognized and bound by TBP, inducing a sharp bend of the DNA [186]. This complex is joined by Brf2 that recognizes the GR and TD motifs adjacent to the TATA-box [186]. A key difference of both, Brf1 and Brf2, to their RNAP II homolog TFIIB is an extended C-terminal domain that binds along the convex surface of TBP and enables stable binding of TBP in the absence of DNA [186,262,263]. The C-terminal domain of Brf2 harbors a unique structural element termed “molecular pin” which confers redox-sensing capability by impairing Brf2 binding to a DNA/TBP complex in an oxidized state [186]. The Bdp1 subunit of TFIIIB is unique to the RNAP III system and no paralog in the RNAP I or II system has been identified. Structurally, all Bdp1 proteins contain an N-terminal core of approximately 500 amino acids featuring a conserved SANT domain (SWI3, ADA2, N-CoR, and TFIIIB B’’) which constitutes the primary interaction hub with the DNA/TBP/Brf1(2) complex [183,264,265] and together with the N-terminal linker and C-terminal flanking regions is necessary for transcription [264–266]. Bdp1 only weakly associates with the TBP/Brf1(2) complex in absence of DNA [246] but allows formation of an extremely stable

TFIIIB/DNA complex [183,263,267,268] [189,191,269,270] with complex lifetimes of 95 min reported for *S. cerevisiae* DNA/TFIIIB complex [271]. Consequently, TFIIIB can act as genomic roadblock. Furthermore, Bdp1 interacts with SNAPc to ensure selective initiation of RNAP III at the U6 promoter [272]. Interaction between *S. cerevisiae* Brf1 and the RNAP III subunits C34 and C17 are important for RNAP recruitment [273–275]. Post recruitment, Bdp1 supports DNA opening by stabilizing the C34 subunit of RNAP III [194–196]. Together, TFIIIB and SNAPc constitute the minimal factor combination required for U6 promoter directed transcription initiation by human RNAP III [276]. Several key functions of TFIIIB have been discovered by biochemical approaches, however, structural information, in particular for the human complex, have only recently been uncovered [186,277].

3.4 Mechanisms of transcriptional regulation in archaea

Accurate regulation of gene expression is critical for the fitness of any living organism. The domain of archaea in particular contains a high number of extremophiles that thrive in habitats characterized by fluctuating environmental conditions such as extreme temperature [278], acidity [279] and salinity [280]. Consequently, archaeal organisms must precisely tune transcriptional output levels in response to these changes. Genetic regulation in archaea presents an interesting mosaic of both, eukaryotes and bacteria, with a core transcription machinery that resembles a simplified eukaryotic RNAP II system (reviewed in [44,118–120]). In contrast, regulatory factors such as activators and repressors bear greater similarity to those of Bacteria in terms of operation mode and domain composition (reviewed in [119,281,282]). Genome-wide analyses determined that structurally, most archaeal transcription factors include a helix-turn-helix (HTH), winged HTH, or ribbon-helix-helix domains, that also constitute the most prevalent DNA-binding domains in Bacteria [283].

Prokaryotic transcriptional regulators affect their target genes or operons by binding specific sequence elements close to the core promoter with a DNA binding domain. This binding activity can additionally be modulated by a sensor domain [281]. In Archaea, activators typically bind upstream of the TATA-box and the BRE to stabilize TBP and/or TFB through direct protein-protein contacts at the promoter and thereby enhance PIC formation [284–286]. Repressors, in contrast, bind either overlapping with these critical sequence elements, sterically blocking initiation factors from assembling at the promoter, or binding downstream preventing recruitment of the RNAP [281,283]. However, alternative modes of operation have been reported [287].

The *P. furiosus* transcriptional regulator TFB recruitment factor 1 (PfTFB-RF1) stimulates recruitment of TFB to promoters with weak BREs like the *pf1089* locus upstream of its own gene, as well as the *pf1011/pf1012* operon [285,288]. The gene products of the latter were identified as components of an ABC transporter system by bioinformatic analysis that also predicted four transmembrane domains for PF1089, indicating a potential connection for all PfTFB-RF1 regulated genes [288]. TFB-RF1 likely binds a homodimer [289] to a conserved recognition sequence upstream of its target genes [285,288]. Biochemical analysis revealed that TFB-RF1 binding resulted in a seven-fold increase in transcription from the *pf1089* promoter [285]. In contrast, introduction of a strong consensus BRE at the *pf1089* promoter yielded only two-fold activation.

Gel shift experiments indicate that TFB-RF1 solely interacts with TFB and not with TBP, whereas TFB1 and TFB-RF1 cooperatively bind the promoter [285]. However, the exact molecular mechanism of recruitment and potential conformational changes in the promoter DNA could so far not be determined.

In addition to Bacteria-like transcriptional regulators, many archaeal organisms have evolved different paralogs of the basal transcription factors TBP and TFB (reviewed in [290]). Genome analyses revealed that approximately 70% of archaea encode at least two copies of TBP and/or TFB [283,291]. So far, only few of these paralogs and their function have been characterized in detail but they generally seem to play role in stress response and the regulation of differential gene expression. For example, the genome of *P. furiosus* encodes one TBP and two TFBs that are both transcriptionally active [292]. Under heat shock conditions, the expression of TFB2 is increased, suggesting a stress response function [292]. Similarly, *Thermococcus kodakarensis* encodes two TFB paralogs. TFB1 controls the expression of genes essential for motility/adhesion, while TFB2 initiates transcription at genes involved in mevalonate/lipid biosynthesis [293]. A complex system of six TBP and seven TFB paralogs, enabling 42 different TBP/TFB combinations, is present in the halophilic archaeon *Halobacterium salinarum*. It has been demonstrated that specific TBP/TFB combinations recognize different promoter classes involved in heat shock response, oxidative stress and adaptation to low temperatures [291,294]. A computational analysis of sequence motifs revealed that slight variations in the BRE sequences determine which of the seven TFBs recognizes a specific promoter [295].

The genomes of *S. acidocaldarius* and the related *Saccharolobus solfataricus* encode three TFB paralogs, TFB1, TFB2 and TFB3 [296,297]. Under standard growth conditions, the transcription machinery of *S. acidocaldaris* utilizes TBP and TFB1 to direct PIC assembly [298]. SaTFB3 is a shortened TFB variant that lacks both cyclin domains and instead features a coiled coil-domain. Additionally, SaTFB3 contains a canonical Zn-ribbon domain with four cysteine residues that bind a Zn^{2+} ion, whereas in SaTFB1 and SaTFB2, only two cysteines are present [299]. Multiple studies demonstrated that SaTFB3 regulates the expression of genes that encode factors involved in UV-induced DNA damage repair [299–301] and that the above structural features are essential for this function [299]. In contrast, the functional role of TFB2 is still unexplored. A study on cell-cycle specific gene expression in *S. acidocaldarius* demonstrated a cyclic increase of SaTFB2 mRNA levels, peaking at the G_1/S phase transition. Additionally, SaTFB2 expression is increased upon nutrient depletion [302,303]. Evidence from both studies suggests a regulatory role for TFB2, but its function as an initiation factor or transcriptional regular has so far not been analyzed.

3.5 Influence of DNA strain and compaction on transcription

Most *in vitro* studies in transcription analysis are performed using short naked DNAs. This, however, diverges completely from the *in vivo* situation, where transcription occurs in the context of a highly organized three-dimensional chromatin structure (reviewed in [304]). The fundamental organizing unit of eukaryotic chromatin is the nucleosome formed by histone octamers comprising two copies each of the canonical histones: H3, H4, H2A and H2B that are wrapped by approximately 146 bp of DNA [305–307]. The individual histone proteins feature N-terminal tails

that can be post-transcriptionally modified with a variety of chemical groups [308–310]. Multiple nucleosomes can form higher-order structures such as tetranucleosome units [311], which can be further extended into compact fibers [312].

These structures give rise to a complex, three-dimensional genome architecture that affects gene regulation on multiple levels. First, compartmentalization of transcriptionally active euchromatin and inactive heterochromatin, which are marked by histone modifications and allow wide-ranging control of gene expression [313]. At the megabase-level, organization of DNA into topology associated domains [314–316] creates intricate networks of gene-enhancer interactions. These large-scale organizational domains are formed and maintained by DNA binding proteins such as cohesin and the CCCTC-binding factor that modulate the three-dimensional chromatin structure [304,314,317,318]. The nucleosome decoration of individual promoters and adjoining DNA regions can vary for different promoter classes (reviewed in [319]) and has been demonstrated to impact transcriptional efficiency [320,321].

An often overlooked aspect in the analysis of transcriptional regulation is that in the context of the chromatin superstructure, DNA is subject to mechanical force (reviewed in [322,323]). Flexural and torsional tension in the range of $1–30$ pN can be induced by a number of intracellular processes including transcription [76–78], DNA replication [79,80], and chromatin compaction [82–84]. Furthermore, extracellular forces transmitted to the nucleus via lamins were shown to affect gene expression (reviewed in [324].

Due to the nanomechanical properties of the DNA fiber, this strain can be transferred over the distance of several kilobases [325,326]. Experiments using optical tweezers demonstrated that transcribing *Escherichia coli* RNAP can generate forces up to 15–30 pN [76,77,327]. In contrast, elongating *S. cerevisiae* RNAP II is stalled by pulling forces of 7.5 pN or 16.9 pN in complex with the elongation factor TFIIS [78]. Transcription by RNAPs also generates positive supercoiling in the downstream DNA and negative supercoiling in the trailing upstream DNA [328]. Excessive supercoiling of the DNA duplex through repeated rounds of transcription can stall elongation [304,329,330]. The accumulated torsional stress, if not relieved by enzymatic activity such as topoisomerases, can propagate along the DNA helix [325,326,331].

The chromatin structure itself can also exhibit structural dynamics on various timescales (reviewed in [323]). These dynamics are controlled by various factors like post-transcriptional modifications of histones [332,333], proteins that recognize or modify histone post-transcriptional modifications [310,334], chromatin binding proteins like linker histone H1 [335] and ATP dependent chromatin remodelers [334,336]. Stacking interactions within tetranucleosomes can resist forces up to 4 pN [337]. Force-clamp measurements at 3 pN revealed H1-induced conformational dynamic on the second timescale resulting from transient loss of stacking interactions [338]. Histone tails have been reported to engage dynamic inter-molecular contacts on a microsecond time scale [339] that can exert forces on their coupled DNA [95]. These influxes of force are contained and accumulate within topologically constraint regions and can in return inhibit or enhance transcription on a larger scale (reviewed in [340]). As a result, force generation and management are inextricably linked to transcriptional activity. Transcription initiation factors must accommodate this by either

confining their binding to low-force environment such as nucleosome depleted regions or by adapting to resist mechanical stress.

In this regard, the eukaryotic RNAP III transcription machinery present a particularly interesting case. High transcriptional throughput of RNAP III-transcribed genes is suggested to be achieved through the recycling of RNAPs [341–343]. This in turn requires TFIIIB complexes that remain bound to the DNA for multiple rounds of initiation [191,344,345]. Coherent with this, TFIIIB has been described as highly resistant to both, ionic stress and heparin competition [189,191,269,270]. The ability of Bdp1 to form roadblocks on DNA is also abolished upon depletion of Bdp1, indicating a crucial role for this RNAP III specific factor in complex stabilization [346]. Moreover, an RNAP III-transcribed tRNA gene and its associated factor decoration can prevent the spreading of heterochromatin into neighboring euchromatin [347]. Activated transcription of human U6 snRNA genes requires Oct-1 in addition to SNAPc for TFIIIB recruitment, which binds cooperatively with SNAPc [256–258]. Cooperative binding is dependent on a positioned nucleosome between the PSE and DSE that brings the two factors into interaction range [258]. As a result, SNAPc and TFIIIB are in immediate proximity to the nucleosome and likely subjected to force. Taken together, these factors suggest an increased stress tolerance of the RNAP III transcription machinery. In contrast, RNAP II transcription initiation predominantly occurs in nucleosome depleted regions, which implies a higher sensitivity to mechanical strain [348,349].

Similar to eukaryotes, many archaeal species structurally organize their genomes into chromatin and employ two distinct strategies to compact their DNA. Most euryarchaeal species encode histone proteins that mimic the core eukaryotic histone fold [306,350–352].

Archaeal histones generally lack the N-terminal tail structures found in eukaryotic histones which critically interact with chromatin remodeling factors [353]. Thus, archaeal chromatin serves primarily as an architectural tool without the additional layer of information that histone tail modifications provide in eukaryotes [308]. The absence of histone tails in archaeal histone proteins allows for tight interactions between individual nucleosomes, which can lead to formation of extended nucleosome stacks resulting in a continuous helical ramp of histone dimers [350,351] up to 300 bp in length [350].

In contrast, most crenarchaeal species are reliant on small nucleoid-associated proteins (NAPs) to organize their genomes [354,355]. The best studied example being Alba, an Sac10b family protein [356–359]. However, several other like Sul7, Cren7, CC1 and TrmBl2 have been identified [85,360–362] (reviewed in [363,364]). Sac10b-type proteins are found in most archaeal species, even those that additionally encode histones [364]. Alba binds to ssDNA and dsDNA without sequence specificity and possesses trimethylation-regulated DNA binding affinity [356,359,365]. Generally, one or two isoforms of Alba are expressed that can bind DNA in homo- or heterodimeric manner. Homodimers form DNA loops by bridging distant DNA region which causes genome compaction at low Alba concentrations [357,366] similar to eukaryotic cohesion [318]. At higher concentrations, rigid linear DNA-protein complexes can be formed [357]. Heterodimers also contribute to loop formation at low protein concentration [367], whereas at high concentration, highly compacted DNA structures are formed [357]. In contrast to archaeal histones, post translational modifications have been described for Alba [356].

While chromatin dynamics in eukaryotes have been subject to rigorous study over the past decades, relatively little is known about its role in archaea (reviewed in [119,363,364]). However, archaeal chromatin has been reported to impact transcriptional activity during initiation [368] and elongation [369–371]. While some studies characterized the core promoters in archaea to be generally devoid of organized chromatin structures [372,373], in *Methanocaldococcus jannaschii*, histone assembly upstream of the *rb2* gene has been shown to block formation of PICs and thereby reduce transcription rates [374]. In *P. furiosus*, reduced transcriptional activity of histone bound DNA templates has been reported. The diminishing effect was greater for circular than for linear templates, suggesting that topological changes introduced by nucleosome assembly accumulate in constraint DNA regions [371]. How mechanical strain interacts with the transcriptional machinery has so far mostly been studied in Bacteria and eukaryotes, whereas almost nothing is known about its influence on transcription in archaea. This is especially of interest, since the bacterial RNAP has generally been described to generate higher forces than its eukaryotic ortholog [322]. This, in turn should be reflected in the accompanying transcription factors. Since archaea use both, a eukaryote-like RNAP and basal TFs in combination with bacterial-like transcriptional regulators, much can be learned by studying the effects of force on archaeal transcription. In contrast to most eukaryotic transcription systems, where TBP is sufficient to bend the promoter DNA, several archaea require both, TBP and TFB for this critical assembly step [232,233]. In this context, it is interesting to study how promoter strain affects a system that is strictly dependent on the interaction of two factors.

4 Objectives

Transcription initiation in archaea and eukaryotes is a highly dynamic process and many of its underlying molecular details are still unknown. In this work, smFRET experiments coupled with DNA origami-based force spectroscopy will be applied to analyze the assembly of the human TFIIIB complex at the U6 snRNA promoter. For further comparison, the human RNAP II specific initiation factors TFIIA and TFIIB will be examined in single-molecule force measurements. For archaeal transcription systems, these techniques will be applied to examine different strategies to regulate transcription initiation.

- As an initial step to facilitate smFRET experiments, instrumentation for time-resolved single-molecule fluorescence detection was implemented in the form of a prism-based TIRF microscope and tested using a standard model system.
- The stepwise assembly of the human TFIIIB complex from its subunits TBP, Brf2 and Bdp1 was analyzed with smFRET measurements to determine binding dynamics of individual factors and assembly hierarchy.
- The ability of transcription initiation factors to stably bind DNA under mechanical strain is analyzed for the human TFIIIB complex and compared to factors specific to the human RNAP II transcription system (TFIIB, TFIIA) by employing the DNA origami-based force clamp.
- The interaction of the *S. acidocaldarius* TFB paralog TFB2 with the canonical transcription initiation factors TBP and TFB1 is analyzed to test whether TFB2 can substitute TFB1 as an initiation factors or can modulate the assembly of a DNA/TBP/TFB1 complex.
- The TFB-RF1-mediated recruitment of *P. furiosus* TFB to the promoter is analyzed with smFRET to monitor conformational changes in the DNA and the rate of factor assembly to the promoter.
- The effect of DNA strain on formation of a bent promoter DNA complex is further analyzed for the *M. jannaschii* transcription system that only requires TBP for this initiation step and the *P. furiosus* system, where TBP and TFB are mandatory.

5 Materials

5.1 Chemicals and reagents

Table 1: List of chemicals and reagents. Items are listed in alphabetical order.

Reagent	Supplier
40% acrylamide/bisacrylamide solution (19:1)	Roth-Chemie, Karlsruhe
Acetic acid, p.a. ≥ 99.8%	Merck, Darmstadt
Agarose LE	Biozyme, St. Joseph (MO, USA)
Ammonium acetate	Merck, Darmstadt
Ammonium persulfate (APS)	Roth-Chemie, Karlsruhe
Biotin-PEG	Laysan Bio, Arab (AL, USA)
Boric acid	Merck, Darmstadt
Bovine serum albumin (BSA)	Sigma-Aldrich, St. Louis (MS, USA)
Bromophenol blue	AppliChem, Karlsruhe
Catalase from bovine liver	Sigma-Aldrich, St. Louis (MS, USA)
Dimethyl Sulfoxide (DMSO)	Sigma-Aldrich, St. Louis (MS, USA)
Dithiothreitol (DTT)	Roth-Chemie, Karlsruhe
Ethanol, p.a. ≥ 99.8%	Sigma-Aldrich, St. Louis (MS, USA)
Ethanol, technical 99%	J.T. Baker, Deventer (NL)
Ethylenediaminetetraacetic acid (EDTA, Titriplex III)	Merck, Darmstadt
FastDigest BamHI	ThermoFisher Scientific, Waltham (MS, USA)
FastDigest Green buffer	ThermoFisher Scientific, Waltham (MS, USA)
GeneRuler 1 kb Plus DNA Ladder	ThermoFisher Scientific, Waltham (MS, USA)
α-D-Glucose monohydrate	Merck, Darmstadt
Glucose oxidase type VII	Sigma-Aldrich, St. Louis (MS, USA)
Glycerol 99%, Ph.Eur.	Roth-Chemie, Karlsruhe
Hellmanex	Hellma, Müllheim
Heparin sodium salt	Sigma-Aldrich, St. Louis (MS, USA)
Hydrochloric acid 37%	Merck, Darmstadt
Hydrogen peroxide solution 34.5-36.5%	Sigma-Aldrich, St. Louis (MS, USA)
4-(2-hydroxyethyl)-1-piperazineethanesulfonic acid (HEPES)	Roth-Chemie, Karlsruhe
6-Hydroxy-2,5,7,8-tetramethylchroman-2-carboxylic acid (Trolox)	Sigma-Aldrich, St. Louis (MS, USA)
Magnesium acetate,	Merck, Darmstadt
Magnesium chloride hexahydrate	Merck, Darmstadt
Magnesium sulfate	Merck, Darmstadt
2-Mercaptoethanol	Roth-Chemie, Karlsruhe
Methanol, p.a. ≥ 99.8%	Merck, Darmstadt
Methoxy-polyethylene glycol-succinimidyl valerate 5000 (mPEG)	Laysan Bio, Arab (AL, USA)
Midori Green Direct DNA stain	Nippon Genetics Europe, Düren
NeutrAvidin	ThermoFisher Scientific, Waltham (MS, USA)
PEG-8000	Sigma-Aldrich, St. Louis (MS, USA)
Phenylmethylsulfonyl fluoride	Roth-Chemie, Karlsruhe
Potassium chloride	Merck, Darmstadt
Potassium dihydrogen phosphate	Merck, Darmstadt
Sodium chloride	neoFroxx, Einhausen
Sodium dodecyl sulfate (SDS)	Merck, Darmstadt Serva Electrophoresis
Sodium hydroxide	Fisher Scientific, Loughborough (UK)
Sulfuric acid	Fisher Scientific, Loughborough (UK)

Reagent	Supplier
T4 ligase	New England Biolabs, Ipswich (MS, USA)
T4 ligase buffer (10x)	New England Biolabs, Ipswich (MS, USA)
N,N,N',N'-Tetramethylethylenediamine (TEMED)	Roth-Chemie, Karlsruhe
N[3(Trimethoxysilyl)propyl]ethyldiamine	Sigma-Aldrich, St. Louis (MA, USA)
Tris(hydroxymethyl)aminomethane (Tris)	Sigma-Aldrich, St. Louis (MA, USA)
Tryptone	Difco, Lawrence (KS, USA)
Urea	Sigma-Aldrich, St. Louis (MS, USA)
Zinc sulfate heptahydrate	Honeywell Specialty Chemicals, Seeltze

5.2 Buffers

Table 2: Composition of buffers. Buffers are listed in alphabetical order. Values in parenthesis denote the concentration factor of the stock solution. All buffers were prepared with Millipore water in 90% of the final volume. All reagents were mixed at room temperature if not stated otherwise. The pH value of all buffers was adjusted after adding all reagents. Afterwards, solvent was added to the final volume. Buffers without BSA or SDS were filtered through a 0.45 µM syringe filter. If not stated otherwise, buffers were stored at room temperature (RT, approximately 21 °C).

Buffer	Component	Amount	Unit
Annealing buffer (10x)	Tris/HCl, pH 7.5	100	mM
	NaCl	500	mM
	EDTA	10	mM
APS stock solution (10x)	APS	10	% (w/v)
	Storage at -20 °C		
Blocking buffer	Tris/HCl, pH 7.8	10	mM
	BSA	2	mg/mL
	Storage at -20 °C.		
Denaturing DNA loading buffer	Formamide	95	%
	SDS	0.02	%
	Bromphenol blue	0.02	%
	Xylen Cyanol	0.01	%
	EDTA	1	mM
Folding buffer (10x)	Tris/HCl, pH 7.6	100	mM
	NaCl	50	mM
	$MgCl_2$	200	mM
	EDTA	10	mM
Glucose oxidase-catalase stock solution (10x)	Tris/HCl, pH 7.5	50	mM
	Glucose oxidase	75	U/mL
	Catalase	10	kU/mL
	The reagents were gently mixed at 4 °C, portioned at 50 µL aliquots in PCR tubes and frozen in liquid nitrogen. Storage at -80 °C.		
Glucose stock solution (10x)	α-D-glucose	100	mg/mL
	Storage at -20 °C.		
Hs1 buffer	HEPES/NaOH, pH 7.8	50	mM
	Ammonium acetate	500	mM
	TCEP	1	mM
	Glycerol	10	% (v/v)
Hs2 buffer	Tris/HCl, pH 8.0	20	mM
	NaCl	150	mM
	DTT	1	mM
	EDTA	0.5	mM

Buffer	Component	Amount	Unit
Mj1 buffer	200 mM Tris/acetate, pH 7.9	200	mM
	Magnesium acetate	100	mM
	$ZnSO_4$	0.1	mM
	Potassium acetate	300	mM
	Glycerol	10	% (v/v)
	2-Mercaptoethanol	0.05	% (v/v)
Mj2 buffer	Na_2HPO_4/ NaH_2PO_4, pH 7.0	25	mM
	NaCl	1	M
	Potassium acetate	1.5	M
NeutrAvidin solution	Tris/HCl pH 7.6	50	mM
	NaCl	50	mM
	NeutrAvidin	0.1	mg/mL
PEG passivation solution	$NaHCO_3$	1	mM
	Methoxy-PEG succinimidyl valerate 5000	200	mg/mL
	Biotin-PEG	5	mg/mL
Peroxomonosulfuric acid	Sulfuric acid	70	% (v/v)
	Hydrogen peroxide solution	30	% (v/v)
Pf1 buffer	Tris/HCl, pH 8.0	50	mM
	NaCl	50	mM
	$MgCl_2$	10	mM
	Glycerol	20	% (v/v)
Pf2 buffer	HEPES/NaOH, pH 7.8	20	mM
	NaCl	250	mM
	EDTA	2	mM
	Glycerol	10	% (v/v)
	2-Mercaptoethanol	5	mM
	Phenylmethylsulfonyl fluoride	0.5	mM
	Storage at -80 °C		
Pf3 buffer	HEPES/NaOH, pH 7.5	25	mM
	NaOH	300	mM
	Glycerol	15	% (w/v)
Photo-stabilization buffer	any sample buffer plus:		
	Trolox/trolox quinone stock solution	2	mM
	α-D-Glucose	10	g/mL
	Tris/HCl pH 7.5	5	mM
	Glucose oxidase	7.5	U/mL
	Catalase	1	kU/mL
	The reagents were gently mixed in the sample buffer used (e.g. T78) at RT immediately before use.		
Precipitation buffer	Tris/HCl, pH 7.6	100	mM
	NaCl	500	mM
	EDTA	1	mM
	PEG-8000	15	% (w/v)
Sa1 buffer	Tris / HCl, pH 7.5	25	mM
	NaCl	300	mM

Buffer	Component	Amount	Unit
Sa2 buffer	Tris/HCl, pH 8.0	25	mM
	$MgCl_2$	10	mM
	$ZnSO_4$	0.1	mM
	NaCl	300	mM
	TCEP	1	mM
	Glycerol	5	% (v/v)
Sa3 buffer	Tris/HCl pH 7.5	20	mM
	NaCl	50	mM
	$MgCl_2$	1	mM
	EDTA	0.4	mM
	DTT	0.1	mM
	Glycerol	12.5	% (v/v)
Silane coupling solution	N[3(Trimethoxisilyl)propyl]ethyldiamineAcetic acids	2	
	The reagents were mixed in methanol immediately	4	% (v/v)
	before use.		% (v/v)
T78 Buffer (2x)	Tris/HCl, pH 7.8	200	mM
	KCl	120	mM
	$MgCl_2$	6	mM
	Glycerol	2	% (v/v)
	BSA	2	mg/mL
	Storage at -20 °C		
T78M Buffer (2x)	Tris/HCl, pH 7.8	200	mM
	KCl	120	mM
	$MgCl_2$	30	mM
	DTT	4	mM
	Glycerol	2	% (v/v)
	BSA	2	mg/mL
	Storage at -20 °C		
Tris-Acetate-EDTA (TAE) buffer (50x)	Tris/acetate, pH 8.2	500	mM
	Acetic acid	1000	mM
	EDTA	50	mM
Tris-Acetate-EDTA-magnesium buffer (TAEM)	Tris/acetate, pH 8.2	10	mM
	Acetic acid	20	mM
	EDTA	1	mM
	$MgCl_2$	12.5	mM
Tris-Borate-EDTA (TBE) buffer (10x)	Tris /borate, pH 8.0	893	mM
	Boric acid	890	mM
	EDTA	27	mM
Tris buffered saline (TBS)	Tris/HCl, pH 7.6	10	mM
	NaCl	50	mM
Tris-EDTA (TE) buffer	Tris/HCl, pH 8.0	10	mM
	EDTA	1	mM
Trolox/trolox quinone stock solution (50x)	Trolox	100	mM
	Trolox was dissolved in water-free DMSO and partially photo-oxidized to trolox quinone under UV light (BioDoc-It, 302 nm) for 20 min. Storage at -20 °C.		

5.3 Proteins

All proteins used in experiments were kindly supplied by members of the Department of Microbiology (University Regensburg) or external collaborators (Table 3) and were expressed and purified as described in the listed references. Upon arrival, proteins were partitioned into low volume aliquots (2–20 µL), frozen in liquid nitrogen and stored at -80 °C. Before use, the samples were thawed and stored on ice for a maximum of 24 h.

Table 3: List of used proteins. The protein variant, tag, storage buffer, supplier and literature reference (Ref.) are listed. Affinity tag refers to the fully purified protein. The complete amino acid sequences of all proteins are listed in Table 14. *The used TFIIA single chain variant is a fusion protein incorporating the listed segments of the αβ and γ subunits of TFIIA.

Protein Organism (Abbreviation)	**Residues**	**Affinity tag**	**Storage buffer**	**Supplier**	**Ref.**
TBP *Homo sapiens* (HsTBP)	159–339	none	Hs1 buffer	Dr. Jerome Gouge, laboratory of Prof. Dr. Alessandro Vannini, Institute of Cancer Research, London, UK	[277]
Brf2 *Homo sapiens* (HsBrf2)	62–419	none	Hs1 buffer	Dr. Jerome Gouge, laboratory of Prof. Dr. Alessandro Vannini, Institute of Cancer Research, London, UK	[277]
Bdp1 *Homo sapiens* ($HsBdp1_{ES}$)	130–484	none	Hs1 buffer	Dr. Jerome Gouge, laboratory of Prof. Dr. Alessandro Vannini, Institute of Cancer Research, London, UK	[277]
Bdp1 *Homo sapiens* ($HsBdp1_{S}$)	241–396	none	Hs1 buffer	Dr. Jerome Gouge, laboratory of Prof. Dr. Alessandro Vannini, Institute of Cancer Research, London, UK	[277]
TFIIB *Homo sapiens* (HsTFIIB)	1–316	none	Hs1 buffer	Dr. Jerome Gouge, laboratory of Prof. Dr. Alessandro Vannini, Institute of Cancer Research, London, UK	-
TFIIA (single-chain)* *Homo sapiens* (HsTFIIA)	γ (2–103) αβ (2–58) αβ (327–376)	C-terminal 6x histidine	Hs2 buffer	Dr. Kapil Gupta, laboratory of Prof. Dr. Imre Berger, University of Bristol, UK	[375]
TBP *Pyrococcus furiosus* (PfTBP)	1–191	none	Pf1 buffer	Dr. habil. Winfried Hausner, University Regensburg	[127]
TFB1 *Pyrococcus furiosus* (PfTFB1)	1–300	N-terminal 6x histidine	Pf2 buffer	Dr. habil. Winfried Hausner, University Regensburg	[127]
TFB-RF1 *Pyrococcus furiosus* (PfTFB-RF1)	1–100	N-terminal 6x histidine	Pf3 buffer	Dr. habil. Winfried Hausner, University Regensburg	[285]
TBP *Methanocaldococcus jannaschii* (MjTBP)	1–183	none	Mj1 buffer	Prof. Dr. Dina Grohmann, University Regensburg	[250]

TBP *Sulfolobus acidocaldarius* (SaTBP)	1–197	N-terminal 6x histidine	Sa1 buffer	Frank Schult, laboratory of Prof. Dr. Bettina Siebers, University Duisburg Essen	[376]
TFB1 *Sulfolobus acidocaldarius* (SaTFB1)	1–307	C-terminal 6x histidine	Sa2 buffer	Frank Schult, laboratory of Prof. Dr. Bettina Siebers, University Duisburg Essen	[376]
TFB2 *Sulfolobus acidocaldarius* (SaTFB2)	1–291	N-terminal 6x histidine	Sa2 buffer	Frank Schult, laboratory of Prof. Dr. Bettina Siebers, University Duisburg Essen	[376]

5.4 DNA oligonucleotides

Synthetic DNA oligonucleotides were ordered at production scales ranging from 5-20 µmol with salt-free purification for non-modified DNA and HPLC purification for modified DNAs. The concentration was checked via absorption spectroscopy upon arrival and oligonucleotides were stored at -20 °C. The annealed double stranded DNA constructs are listed in the relevant method section.

Table 4: Sequences and modifications of oligonucleotides. Internal nucleotide modifications are color coded. 5'-end and 3'-end modifications are given in square brackets at the appropriate positions. Suppliers are coded according to the following numbers: (1) IBA Lifesciences, Göttingen, (2) Sigma-Aldrich, St. Louis (MS, USA), (3) Eurofins Genomics, Luxemburg, LUX, (4) Metabion, Planegg, (5) Biomers, Ulm.

Name	Description and sequence (5'-3')	Supplier
H1	CCTCCCTAGCAAGCCGCTGCTACGG	(3)
H2	[Cy3]CCGTAGCAGCGCGAGCGGTGGG	(3)
H3	[Biotin]CCCACCGCTCGGCTCAACTGGG	(3)
H4	CCCAGTTGAGCGCTTGCTAGGG[Cy5]	(3)
S1	[ATTO 647N]CAGTATTTAAACTTTACTCCAATCTCCGGCGATGGTCGCGCTTTCGGTCCG	(1)
S2	[Biotin]CGGACCGAAAGCGCGACCATCGCCGGAGATTGGAGTAAAGTTTAAATACTG Cy3B	(1)
U1	TCAAGGGTTACTCTCACACCTATTTTAAGCCCTTCAATCAAATCATCTTGGTCCG ATTO 647N	(1)
U2	[Biotin]CGGACCAAGATGATTTGATTGAAGGGCTTAAAATAGGTGTGAGAGTAACCCTTGA ATTO 532	(1)
F1	AAGCTTTAGGGCGCCTATAAAAG ATTO 532	(1)
F2	[Phosphate]GGGGTTCGGGCG ATTO 647N	(1)
F3	TTCGCGCCCGAACCCCCTTTTATAGGCGC	(2)
F4	CGCCCGAACCCCCTTTTATAGGCGCCCTAAAGCTT	(3)
F5	CGGACCAAGATGATTTGATTGAAGGGCTTAAAATA ATTO 532	(1)
F6	[Phosphate]GGTGTTAGAGTAACCCTTGA ATTO 647N	(1)
F7	GGTTACTCTAACACCTATTTTAAGCCCTTC	(2)
F8	TCAAGGGTTACTCTAACACCTATTTTAAGCCCTTCAATCAAATCATCTTGGTCCG	(3)
F9	TCATAGGATCCCCGGGTA	(4)
F10	TTTTGCTTTCATCAACATTAAATCCGTAATCGTAACCTTGGGTACAGG	(3)

Name	Description and sequence (5'-3')	Supplier
F11	TTTTAAGTTTCATTCCTCTGGAGAGGCTATACGCCAGGGTTTTCCCAGT	(3)
F12	TTTTCGCTCATGGACGAGCCG	(3)
F13	TTTTACTTGCCTGAGTAGAAGTAATTCCACGATT	(3)
F14	AGCCTTCACCGCCTGGCGTTATCCGCTCACATAAC	(3)
F15	GCTACAACATAAATACCATTGCAACAGGAAAAATTTT	(3)
F16	ATGCAATGGTGAGAAAGGCATGATTAAGGTGCATCAGATTGTAATT	(3)
F17	GTCAATAGCAAGGCACAGGCACCTCAGAGCTTTAA	(3)
F18	TTTCCTGTGTGAAATTCCTGAGAGGGGTCG	(3)
F19	GGGGATGTGCTACCTGTTTAGCTTTTT	(3)
T1	[Biotin]AGTACAAACCTAAGCTCTGAACTACAGAGTTTGACCTGAGTATAAATACCT[ATTO 647N]	(3)
T2	AGGTATTTATACTCAGGTCAAACTCTGTAGTTCAGAGCTTAGGTTTGTACT ATTO 532	(3)
T3	[Biotin]AGTACAAACCTAAGCTCTGAACTACAGAGTTTGACAAAAGTATAAATACCT[ATTO 647N]	(3)
T4	AGGTATTTATACTTTTGTCAAACTCTGTAGTTCAGAGCTTAGGTTTGTACT ATTO 532	(3)

5.5 Expendable items

Table 5: List of expendable items. Items are listed in alphabetical order. *Quartz microscope slides were custom-fitted with four or six 1 mm-drill holes to attach the tubing for flow chamber used in wide-field single-molecule experiments by the glassblowing workshop of the Faculty of Chemistry and Pharmacy, University Regensburg.

Item	Manufacturer
1.5ml TubeOne Microcentrifuge Tube	STARLAB Group, Hamburg
Acrodisc 25 mm Syringe Filters 0.45 µm	Pall Corporation, Port Washington (NY, USA)
CELLview slides	Greiner Bio-One, Frickenhausen
Disposable Pasteur pipettes, graduated	Roth-Chemie, Karlsruhe
Disposable needles Sterican, 0.60 mm x 30 mm	B. Braun Melsungen AG, Melsungen
HSW NORM-JECT 2-part disposable syringes 1 ml	Henke-Sass Wolf, Tuttlingen
LoBind microcentrifuge tubes 1.5 ml	Eppendorf, Hamburg
Microscope cover glasses (high precision) 24 x 60 x 0.17 mm	Roth-Chemie, Karlsruhe
neoProtect-Nitrile gloves, powder-free	neoLab Migge, Heidelberg
Parafilm „M" Laboratory Film	Bemis NA, Neenah (WI, USA)
PCR Tubes with Attached Flat Caps	VWR International, Radnor (PA, USA)
Pipette tips TipOne 1000 µl blue graduated	STARLAB Group, Hamburg
Pipette tips TipOne 200 µl graduated	STARLAB Group, Hamburg
Pipette tips TipOne 200 µl yellow	STARLAB Group, Hamburg
Quartz microscope slides 76 x 25.4 x 1 mm *	Plano, Wetzlar Polysciences Inc., Warrington (PA, USA)
Reagent & centrifuge tube 15ml	Sarstedt, Nümbrecht
Reagent & centrifuge tube 50ml	Sarstedt, Nümbrecht
Rotilabo-FEP tube, transparent, 0.8 mm	Roth-Chemie, Karlsruhe
Rotilabo-syringe filters, PES, sterile	Roth-Chemie, Karlsruhe
Safe-Lock microcentrifuge tubes 2.0 mL	Eppendorf, Hamburg
Tube VERSILON 2001, 1.6 mm	Roth-Chemie, Karlsruhe
Two-component epoxy resin adhesive	Faserverbundwerkstoff, Waldenbuch
Vacuum foil	CASO Design, Arnsberg
Whatman ME 25 Membrane Filters	GE Healthcare, Chicago (IL, USA)

5.6 Devices

Table 6: List of electronic devices. Items are listed in alphabetical order. Microscopy related instrumentation is listed in Table 7 and Table 8.

Type	Model	Manufacturer
Analytical balance	Sartorius CP2202S	Sartorius, Göttingen
Autoclave	Sanoclav LaM-MCS	Maschinenbau Wolf, Bad Überkingen-Hausen
Centrifuge	Avanti J-25	Beckman Coulter, Brea (CA, USA)
Electrophoresis system	Mini-PROTEAN® 3 Cell	Bio-Rad Laboratories, Hercules (CA, USA)
Electrophoresis system	Mini-Sub Cell GT system	Bio-Rad Laboratories, Hercules (CA, USA)
Freezer	Liebherr Comfort	Liebherr, Bulle (CH)
Freezer	Liebherr Premium	Liebherr, Bulle (CH)
Freezer	New Brunswick Innova U725-G	Eppendorf, Hamburg
Fridge	Liebherr UK1720	Liebherr, Bulle (CH)
Fridge	Sanyo Labcool MPR-720	Ewald Innovationstechnik, Bad Nenndorf
Gel documentation system	ChemiDoc MP	Bio-Rad Laboratories, Hercules (CA, USA)
Gel documentation system	BioDoc-It	UVC LLC, Upland (CA, USA)
Heating/drying cabinet	T 5090 E	Heraeus, Hanau
Heating/drying cabinet	UT 6120	Heraeus, Hanau
Ice flaker	Scotsman MF26	Scotsman Ice Systems, Vernon Hills (IL, USA)
Incubation shaker	Infors WIE Multitron Pro	Infors AG, Bottmingen (CH)
Magnetic stirrer	Heidolph MR 3002	Heidolph Instruments, Schwabach
Magnetic stirrer	IKAMAG RET-G	IKA-Werke, Staufen im Breisgau
Mini-Centrifuge	Galaxy MiniStar	VWR International, Radnor (PA, USA)
Mini-Centrifuge	PerfectSpin Mini	PEQLAB Biotechnologie, Erlangen
Mini-Centrifuge	Sprout Minizentrifuge	Biozym Scientific, Hessisch Oldendorf
pH meter	PHM82 Standard	Radiometer A/S, Kopenhagen (DK)
Photometer	NanoDrop ND 1000	ThermoFisher Scientific, Waltham (MS, USA)
Pipette filler	pipetus	Hirschmann Laborgeräte, Eberstadt
Power supply	PowerPac Basic	Bio-Rad Laboratories, Hercules (CA, USA)
Power supply	PowerPac HV	Bio-Rad Laboratories, Hercules (CA, USA)
Precision balance	Acculab Atilon ATL-224-I	Sartorius, Göttingen
Rotation shaker	Roto-Shake Genie	Scientific Industries Inc., Bohemia (NY, USA)
Tabletop Centrifuge	Biofuge 13	Heraeus, Hanau
Tabletop Centrifuge	Centrifuge 5424	Eppendorf, Hamburg
Tabletop Centrifuge	Centrifuge 5810 R	Eppendorf, Hamburg
Tabletop Centrifuge	MC-13	Amicon Bioseparations, Beverly (MA, USA)
Thermocycler	Mastercycler Personal	Eppendorf, Hamburg
Thermocycler	MJ Mini	Bio-Rad Laboratories, Hercules (CA, USA)
Thermocycler	MyCycler	Bio-Rad Laboratories, Hercules (CA, USA)
Thermocycler	Primus 25 advanced	PEQLAB Biotechnologie, Erlangen
Thermomixer	ThermoMixer C	Eppendorf, Hamburg
Ultrasonic bath	Elmasonic S 30 H	Elma Schmidbauer, Singen
Vacuum sealer	VC100	CASO Design, Arnsberg
Vortex mixer	Reax top	Heidolph Instruments, Schwabach
Vortex mixer	Vortex-Genie 2	Scientific Industries, Bohemie (NY, USA)

5.7 Microscope components

Confocal fluorescence microscopy was performed with a commercial MicroTime 200 system (PicoQuant, Berlin) equipped to perform various fluorescence-based measurements. Thus, only critical components are listed in Table 7.

Table 7: List of optical components and devices integrated in the MicroTime 200 confocal fluorescence microscope. Items are sorted based on function.

Component	Model number	Manufacturer
Optical table		
Optical workstation	Vision IsoStation	Newport Corporation, Irvine (CA, USA)
Excitation		
Pulsed laser diode head	LDH-P-FA-530B	PicoQuant, Berlin
Pulsed laser diode head	LDH-D-C-640	PicoQuant, Berlin
Microscope		
Microscope body	Olympus IX72	
Objective	UplanSApo ×60/1.20 W	Olympus, Tokio (JP)
Detection		
Single photon detector	SPCM-AQRH-14-TR	Excelitas Technologies, Dumbery (CAN)
TCSPC module	HydraHarp 400	PicoQuant, Berlin
Filter/dichroic mirrors		
Bandpass filter emission	582/64 nm BrightLine	Semrock, Rochester (NY, USA)
Bandpass filter emission	H690/70	Chroma Technology, Bellow Falls (VT, USA)
Dichroic mirror excitation	ZT 532/640RPC	AHF Analysentechnik, Tübingen
Dichroic mirror emission	T 635LPX	Chroma Technology, Bellow Falls (VT, USA)
Narrow band cleanup filter	ZET 635/10	AHF Analysentechnik, Tübingen

Table 8: List of optical components and devices used in the construction of the home-built prism TIRF microscope setup. Items are sorted based on function.

Component	Model number	Manufacturer
Optical table		
Optical table board	HDT 200/25	Opta, Bensheim
Optical table base	RMT 3 FAB	Opta, Bensheim
Enclosure		
Black hardboard plates	TB4	Thorlabs, Newton (NJ, USA)
Excitation		
DPSS Laser	OBIS 488LS	Coherent, Santa Clara (CA, USA)
DPSS Laser	OBIS 532LS	Coherent, Santa Clara (CA, USA)
DPSS Laser	OBIS 561LS	Coherent, Santa Clara (CA, USA)
Diode Laser	OBIS 637LX	Coherent, Santa Clara (CA, USA)
Laser control	OBIS LX/LS Scientific Remote	Coherent, Santa Clara (CA, USA)
Camera/laser signal synchronization	Multistream	Cairn Research, Faversham (UK)
Post-mounted optics		
Pedestal base adapter	BE1/M	Thorlabs, Newton (NJ, USA)
Post holder	PH50/M-P5	Thorlabs, Newton (NJ, USA)
Clamping fork 175 mm	CF175C/M	Thorlabs, Newton (NJ, USA)
Clamping fork 125 mm	CF125C/M	Thorlabs, Newton (NJ, USA)
Optical post 75 mm	TR75/M	Thorlabs, Newton (NJ, USA)
Dielectric mirror	BB1-E02	Thorlabs, Newton (NJ, USA)
Kinematic mount	KM100	Thorlabs, Newton (NJ, USA)

Component	Model number	Manufacturer
Optical post 50 mm	TR50/M	Thorlabs, Newton (NJ, USA)
Kinematic base magnetic	KB25/M	Thorlabs, Newton (NJ, USA)
Kinematic mount	KM100SL	Thorlabs, Newton (NJ, USA)
M4 x 0.7 Threaded Counterbore Adapter	CBA4M	Thorlabs, Newton (NJ, USA)
Variable neutral density filter	NDC-100C-4M	Thorlabs, Newton (NJ, USA)
Beam blocker	LB1/M	Thorlabs, Newton (NJ, USA)
Pedestal pillar	RS4P/M	Thorlabs, Newton (NJ, USA)
Pillar post	RS300/M	Thorlabs, Newton (NJ, USA)
Rotating beam steering assembly	RS99B/M	Thorlabs, Newton (NJ, USA)
Post clamp	RM1D/M	Thorlabs, Newton (NJ, USA)
Illumination		
XYZ-translation stage	VT 45-25-XYZ-SK	Owis, Staufen im Breisgau
Right angle clamp	RA90/M	Thorlabs, Newton (NJ, USA)
Optical post 30 mm	TR30/M	Thorlabs, Newton (NJ, USA)
Optical post 200 mm	TR200/M	Thorlabs, Newton (NJ, USA)
Lense mount	LMR1/M	Thorlabs, Newton (NJ, USA)
Focusing lense	AC254-150-A-ML	Thorlabs, Newton (NJ, USA)
Angle bracket	DTSA03/M	Thorlabs, Newton (NJ, USA)
X-translation stage	DTS50/M	Thorlabs, Newton (NJ, USA)
UV fused silica right-angle prism	PS610	Thorlabs, Newton (NJ, USA)
Detection		
Optosplit III emission beamsplitter	P280/310/0LS	Cairn Research, Faversham (UK)
Optosplit filter cube	P290/000/200	Cairn Research, Faversham (UK)
EMCCD camera	iXon Ultra 897	Andor Technology, Belfast (UK)
Microscope		
DMi8 microscope body	11889110	Leica microsystems, Wetzlar
DMi8 optics	11889039	Leica microsystems, Wetzlar
DMi8 ocular	11507802	Leica microsystems, Wetzlar
DMi8 object stage	11522076	Leica microsystems, Wetzlar
C-mount adapter	11541510	Leica microsystems, Wetzlar
Objective	HC PL APO 63x/1.20 W CORR CS2	Leica microsystems, Wetzlar
Slide mounting frame	K100	Leica microsystems, Wetzlar
Filter/dichroic mirrors		
Narrow band cleanup filter	ZET 635/10	Chroma Technology, Bellow Falls (VT, USA)
Dichroic mirror excitation	ZT 488RDC	Chroma Technology, Bellow Falls (VT, USA)
Dichroic mirror excitation	ZT 532RDC	Chroma Technology, Bellow Falls (VT, USA)
Dichroic mirror excitation	H 568LPXR superflat	AHF Analysentechnik, Tübingen
Dichroic mirror emission	HC BS 560 imaging	Semrock, Rochester (NY, USA)
Longpass filter emission	488 LP Edge Basic	Semrock, Rochester (NY, USA)
Bandpass filter emission	525/40 BrightLine HC	Semrock, Rochester (NY, USA)
Dichroic mirror emission	HC BS 640 imaging	Semrock, Rochester (NY, USA)
Longpass filter emission	635 LP Edge Basic	Semrock, Rochester (NY, USA)
Bandpass filter emission	595/50 H Bandpass	Semrock, Rochester (NY, USA)
Bandpass filter emission	582/75 BrightLine HC	Semrock, Rochester (NY, USA)
Longpass filter emission	568 LP Edge Basic	Semrock, Rochester (NY, USA)

5.8 Software

Table 9: List of software. Items are listed in alphabetical order**.** Only the most recent version is listed.

Software	Version	Producer
Andor Solis I	4.31	Andor Technology, Belfast (UK)
Coherent Connection	3.0.0.8	Coherent, Santa Clara (CA, USA)
FPS	1.1	Laboratory of Prof. Dr. Claus Seidel, University Düsseldorf
ImageLab	6.0	Bio-Rad Laboratories, Hercules (CA, USA)
iSMS	1.06	Laboratory of Prof. Dr. Victoria Birkedal, Aarhus University, Aarhus (DK) [377]
MATLAB, version	R2019b	The MathWorks, Natick (MA, USA)
Mendeley Desktop	1803	Mendeley, London (UK)
MS Office 365		Microsoft Corporation, Redmond (WA, USA)
NanoDrop 1000	3.8.0	ThermoFisher Scientific, Waltham (MS, USA)
Origin 2019		OriginLab Corporation, Northampton (MA, USA)
PIE Analysis in MATLAB (PAM)	1.20 development version	Laboratory of Prof. Dr. Don C. Lamb, LMU Munich [378]
SymPhoTime 64	2.5	PicoQuant, Berlin
UCSF Chimera	1.13.1	Resource for Biocomputing, Visualization, and Informatics, UCSF, San Francisco (CA, USA)

6 Methods

6.1 Annealing of DNA oligonucleotides

For the preparation of dsDNA constructs, 10 µM of the appropriate oligonucleotides (Table 4) were mixed in 20 µL annealing buffer, heated to 90 °C for 3 min and cooled down to 20 °C for 80 min using a linear thermal ramp. Annealed DNA was stored at -20 °C and freshly diluted prior to experiments.

6.2 Absorption spectroscopy

The concentration of proteins and nucleic acids was determined via absorption spectroscopy. To this end, absorption spectra at the appropriate wavelength were recorded with a NanoDrop absorption spectrometer. The concentration was calculated using Lambert-Beer's law:

$$c = A_\lambda \cdot \varepsilon_\lambda \cdot d \qquad \textbf{Equation 17}$$

Where c is the concentration, A_λ is the absorbance at wavelength λ (λ = 260 nm for nucleic acids, λ = 280 nm for proteins), ε_λ is the extinction coefficient at λ and d is the layer thickness of the sample. The concentration of commercial oligonucleotides and supplied proteins was verified prior to storage. Extinction coefficients for proteins were calculated using the webservice ProtParam [379].

6.3 Preparation of DNA origami force clamps

Scaffold DNAs for the Adenovirus major late promoter (MLP) and U6 snRNA promoter (U6P) variant of the DNA origami FC (Table 15) were kindly provided by Dr. Andrés Manuel Vera (laboratory of Prof. Dr. Philip Tinnefeld, LMU Munich). The purified SSV T6 promoter (T6P) variant of the FC was kindly provided by Tim Schröder (laboratory of Prof. Dr. Philip Tinnefeld, LMU Munich)

6.3.1 Preparation of doubly labelled promoter DNA

In order to detect TBP-induced promoter DNA bending via smFRET, two fluorescent dyes flanking the TATA-box are required. Typically, one of the fluorophores is attached to the template strand and the other to the non-template strand of the promoter, because chemical synthesis of a DNA carrying two modifications is less efficient and hence more expensive. Since modifying the scaffold DNA for DNA origami FCs with fluorescent dyes is not feasible, both fluorophores had to be placed in the strand that complements the promoter regions in the origami scaffold to form a double-stranded and doubly labelled promoter region. These were prepared from individual DNA strands that carry either the donor or the acceptor fluorophore, which are ligated via a partially complementary strand [94] (Figure 14). To this end, 10 µM of the appropriate donor strand (MLP: F1, U6P: F5, Table 4), a 5'-phosphorylated acceptor strand (MLP: F2, U6P: F6, Table 4) and a complementary ligation strand (MLP: F3, U6P: F7, Table 4) were annealed in 100 µL annealing buffer, heated to 90 °C for 3 min and cooled down to 20 °C over the course of 2 h. For ligation, 20 µL 10x T4 ligase buffer, 70 µL Millipore water and 10 µL T4 DNA ligase were added to the

annealed DNAs and incubated for 60 min at 20 °C to facilitate ligation of the donor- and acceptor-coupled oligonucleotides. For purification of the doubly labeled single-stranded promoter DNA strand, the ligated DNA was separated on a preparative denaturing 15% TBE gel (Table 10). To this end, denaturing DNA loading buffer was added to the ligation reaction and the sample was heated to 80 °C and cooled on ice.

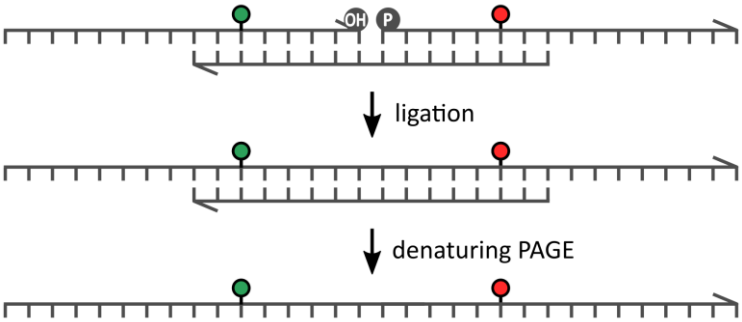

Figure 14: Preparation of doubly labelled promoter DNA for DNA origami force clamps. Two synthetic oligonucleotides carrying a donor (green) or acceptor (red) fluorophore were annealed to a shorter complementary strand, ligated and purified via denaturing PAGE. The 5' end of the DNA is indicated as an arrow. P: 5' phosphate group, OH: 3' hydroxyl group.

The DNA was separated via electrophoresis at 200 V over 40 min. The gel was visualized under UV light and the band corresponding to the doubly labelled DNA strand was excised and pulverized with mortar and pestle. DNA was extracted by adding 1 mL TBE buffer and light shaking at 4 °C for 2 h. The gel debris was pelleted via centrifugation (30 min, RT, 15000 rcf) and the supernatant was extracted (repeated once). Afterwards, the DNA was precipitated by addition of 0.1 volumes of 5 M ammonium acetate solution (pH 5) and 2.5 volumes of 100% ethanol. The sample was incubated at -80 °C for 1 h followed by centrifugation (1 h, 4 °C, 15000 rcf). The supernatant was carefully decanted, and the DNA was washed by addition of 5 mL of ice cold 70% ethanol and centrifugation (30 min, 4 °C, 15000 rcf). The supernatant was completely removed, the pellet dried for 10 min at 21 °C and resuspended in annealing buffer.

Table 10: Composition of a 15% denaturing TBE-PAGE gel. The volumes of each component are given for one gel in a 1 mm gel cassette assembly for the Mini-PROTEAN® 3 Cell. The third column shows the final concentrations of the components.

Component	**Volume (5 mL)**		**Final concentration**	
	Amount	**Unit**	**Amount**	**Unit**
Millipore water	Add to 5.00	mL		
40% (v/v) bis-acrylamide/acrylamide (19:1)	1.88	mL	15.0	% (v/v)
TBE (10x)	0.50	mL	10.0	% (v/v)
Urea	1.8	g	6.0	M
APS stock solution (10x)	50	µL	0.1	% (w/v)
TEMED	5	µL	0.1	% (v/v)

6.3.2 Restriction digestion of origami scaffolds

In order to generate FCs with 0 pN force, the spring DNA was cleaved with BamHI restriction endonuclease (Figure 15a). To this end, 200 µM of the single-stranded scaffold DNA and 3x molar excess of the oligonucleotide complementary to the BamHI restriction site (F9, Table 4) were annealed in FastDigest Green buffer by heating the sample to 90 °C followed by gradual cooling to 20 °C for 2 h. Afterwards, 1 U of FastDigest BamHI was added, incubated at 37 °C for 4 h. Subsequently, BamHI was heat inactivated at 80 °C for 10 min. To evaluate the complete digestion of the DNA, 1 µL of the digested scaffold mixed with 0.5 µL Midori Green Direct and 3.5 µL Millipore water was loaded on a 1% TAE agarose gel (Table 11) and separated via electrophoresis at 80 V for 40 min. The intact circular scaffold (Figure 15b -BamHI) migrates slower than the linearized scaffold (Figure 15b +BamHI) indicating a successful digestion reaction.

Table 11: Composition of a 1% TAEM agarose gel. The given volumes of each component are needed for one gel in a Mini-Sub Cell GT system. The third column shows the final concentrations of the components.

Component	Volume (50 mL)		Final concentration	
	Amount	Unit	Amount	Unit
TAEM	50	mL		
Agarose	0.5	g	1	% (w/v)

Figure 15: Enzymatic digestion of force clamp scaffold DNA. a) The single-stranded force clamp scaffold was annealed with a complementary DNA strand generating a double stranded BamHI restriction site (red). This enables the enzymatic digestion (dashed line) of the spring region of the force clamp, resulting in a 0 pN force on the promoter. **b)** Agarose gel analysis of the FC7267_MLP DNA origami with scaffold with (+) and without (-) BamHI was visualized on a 1% TAEM agarose gel stained with Midori Green Direct. M: GeneRuler 1 kb Plus.

6.3.3 Thermal annealing and purification

DNA origamis were assembled as described previously [94]. For the folding reaction, the scaffold DNA (25 nM), core staple strands (200 nM), force staple strands (400 nM), biotin adapter staple strands (200 nM) and the complementary fluorescently doubly labelled promoter DNA strand (200 nM, Chapter 6.3.1**)** were mixed in folding buffer (total volume 30 µL) and subjected to a multistep thermocycler protocol (Table 12). Afterwards, the origami was purified by addition of 30 µL volume of precipitation puffer and centrifugation (30 min, 4 °C, 20000 rcf). The supernatant was decanted and the pellet resuspended in 30 µL folding buffer for 30 min at 30 °C under constant shaking (300 rpm, ThermoMixer C). All purification steps were repeated once. The concentration of purified DNA origami force clamps was checked via absorption spectroscopy prior to storage at -20 °C.

Table 12: Temperature ramp for the annealing of DNA origami force clamps. The DNA origami mix including all staple strands was heated for 2 min (lid temperature 95 °C) and subsequently annealed using a non-linear temperature ramp.

Temperature (°C)	Time per °C (min)	Temperature (°C)	Time per °C (min)	Temperature (°C)	Time per °C (min)
65	2	55	75	38–37	15
64–61	3	54–45	90	36–30	8
60–59	15	44	75	29–25	2
58	30	43	60	8	storage
57	45	42	45		
56	60	41–39	30		

6.4 Calculation of forces for DNA origami force clamps

The single-stranded DNA in the spring of the force clamp can be modeled as a freely jointed chain (FJC) formed by *N* monomers (nucleotides) with a defined length L_N (L_N = 0.63 ± 0.08 nm [94]). For semi-flexible polymers like ssDNA, the actual length of an individual stiff chain segment is called the Kuhn length L_K given as twice the persistence length (for ssDNA L_K = 1.5 nm [94]). Thus, the fully stretched contour length L_C of the polymer chain is calculated as (Figure 16a):

$$L_C = N \cdot L_N = N_K \cdot L_K \qquad \text{Equation 18}$$

where N_K is the number of Kuhn segments of the chain ($L_K > L_N$, $N_K < N$).

In the FJC, the three-dimensional orientation of each segment is random and independent of the previous segment and every combination of orientations is equally likely to occur. Additionally, self-avoidance is neglected. The polymer chain can adopt several conformations for each possible end-to-end distance *d*. The number of possible conformations increases when *d* is reduced ($d << L_C$, Figure 16b) and decreases, when *d* is extended (*d* approaches L_C, Figure 16c). This reduction in the number of conformations that can be adopted, however, is accompanied by a reduction in the chain's entropy. Thus, in order to maximize the entropy of the ssDNA chain, a force is exerted between the two free ends that reduces *d* and collapses the chain into a more coil-like conformation.

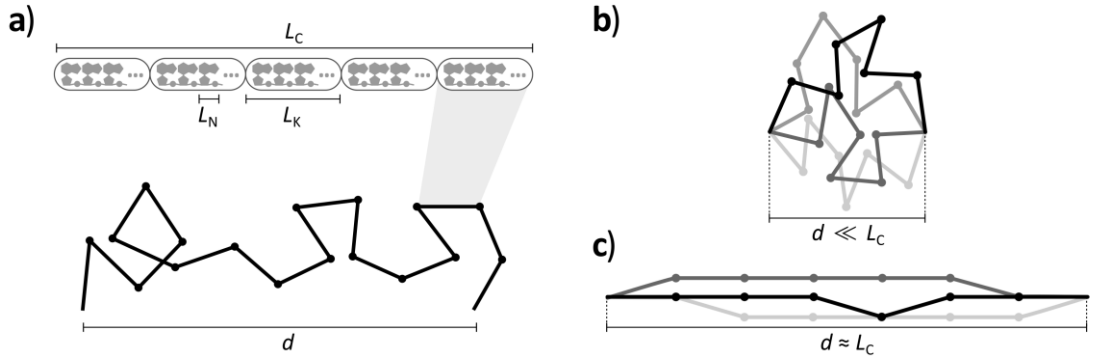

Figure 16: Freely jointed chain model of single-stranded DNA. a) Single-stranded DNA can be described as a polymer chain of a contour length L_C (fully stretched polymer) and an end-to-end distance *d* consisting of multiple nucleotides of length L_N. In the context of the freely jointed chain model, several nucleotides are grouped as stiff Kuhn segments with a length L_K. **b)** For short end-to-end distances ($d << L_C$) the chain can adopt a high number of different conformations (depicted in shades of gray), **c)** with the amount of possible structures decreasing as d approaches L_C.

For low forces (long chain, short end-to-end distance $d << L_C >> L_K$), the average force over multiple conformations $\langle F \rangle$ exerted on each end of an FJC with a fixed end-to-end distance d can be expressed as:

$$\langle F \rangle = \left(\frac{-3 \cdot k_B T}{N_K \cdot L_K^2} \right) \cdot d \qquad \textbf{Equation 19}$$

where k_B is the Boltzmann constant and T is the absolute temperature. The term in parentheses effectively is the spring constant of the FCJ following the linear force-extension of Hooke's law. However, at higher forces the F/d relation is no longer linear and for the FJC can be described as follows:

$$d(F) = L_C \cdot \left[\coth\left(\frac{F \cdot L_K}{k_B T} \right) \cdot \frac{k_B T}{F \cdot L_K} \right] \qquad \textbf{Equation 20}$$

The force-extension behavior of the single-stranded spring DNA is well described by a modified FJC model which includes a stretchable Kuhn segment [380], termed extensible freely FJC (exFJC) model:

$$d(F) = L_C \cdot \left[\coth\left(\frac{F \cdot L_K}{k_B T} \right) \cdot \frac{k_B T}{\mathrm{F} \cdot L_K} \right] \cdot \left(1 + \frac{F}{S} \right) \qquad \textbf{Equation 21}$$

where S is the polymer stretch modulus (for ssDNA S = 800 pN [380]).

For the force clamp, d = 42.84 nm is fixed by the origami geometry (Figure 17a). However, the double-stranded promoter region inserted into the spring is relatively rigid compared to ssDNA (persistence length of dsDNA = 50 nm [381]) and thus effectively reduces the flexible end-to-end distance d. This was accounted for by subtracting the width of the double-stranded promoter w_{ds} from d (Figure 17a). Note that each promoter construct has a different width and thus the negative contribution to d and the resulting force varies (Figure 17b).

Additionally, w_{ds} changes during the experiment, when the DNA is bent by TBP (Figure 17c). For simplicity, forces are calculated with w_{mean}, the mean width of the unbent promoter w_{unbent} and bent promoter w_{bent}, given as:

$$w_{\mathrm{unbent}} = w_U + w_D \qquad \textbf{Equation 22}$$

$$w_{\mathrm{bent}} = \sqrt{w_U^2 + w_D^2 - 2 \cdot w_U \cdot w_D \cdot \cos\alpha} \qquad \textbf{Equation 23}$$

where α is the bending angle of the DNA and w_U and w_D are the widths of the promoter segments upstream and downstream of the center of the TATA-box, calculated as:

$$w_U = N_U \cdot L_B \qquad \textbf{Equation 24}$$

$$w_U = N_U \cdot L_B \qquad \textbf{Equation 25}$$

where N_U and N_D are the number of base-pairs upstream and downstream of the center of the TATA-box, respectively, L_B is the length of a single base-pair (L_B = 0.34 nm) (Figure 17a). L_C is determined by the length of the single stranded DNA in the. The force applied to the ends of the spring can be adjusted by exchanging the set of ten staple strands that fix the position of the spring

inside the rigid origami body and control the amount of DNA from the reservoir region transferred to the spring, and thus L_C (F10–19, Table 4, Chapter 6.3.3). The parameters of all force clamps incorporating the three different promoter constructs are listed in Table 13.

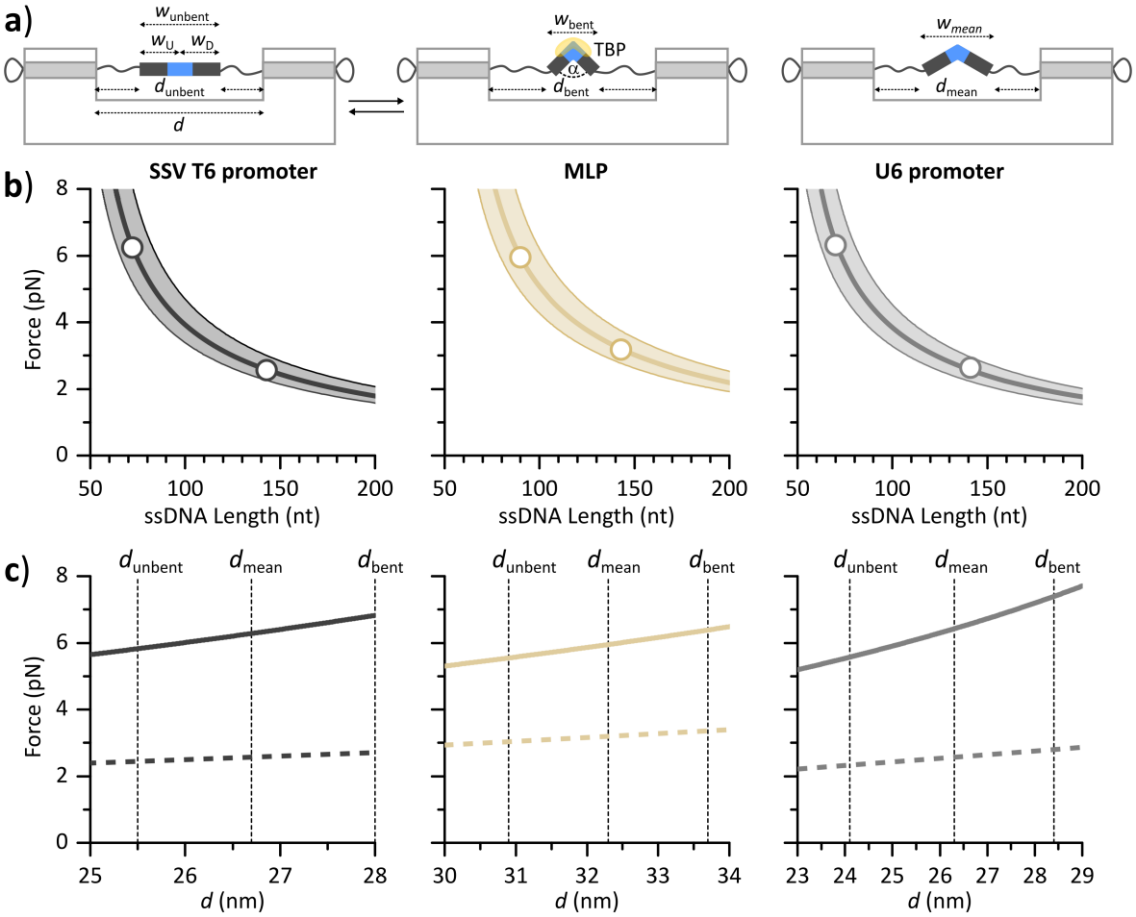

Figure 17: Force-extension calculation for DNA origami force clamps. a) Geometric model of the DNA origami highlighting the double-stranded promoter within the single-stranded DNA spring in the unbent, bent and mean state used for the calculation of forces. The upstream (w_U) and downstream (w_D) segments are modeled as rigid rods with the bending angle α. TATA-box (blue), spring anchor region (grey). **b)** Entropic force as a function of ssDNA length for all promoter constructs used in this work. The forces resulting from the used staple sets are indicated as circles. The shaded area represents the error y-axis error derived from the error of L_N. **c)** Fluctuation of the entropic force resulting from the length differences between the unbent and fully bent state of the DNA. 2.5 pN staple set (dashed line), 6.2 pN staple set (solid line, black, grey), 5.9 pN staple set (solid line, tan).

Table 13: Parameters of DNA origami force clamps. Parameters were determined for the archaeal SSV T6 promoter (T6P) and eukaryotic Adenovirus major late promoter (MLP) and U6 snRNA promoter (U6P) variant of the FC. N_U and N_D are the number of base-pairs upstream and downstream of the center of the TATA-box, respectively, α is the bending angle of the DNA. *d* is the end-to-end distance of the ssDNA and *w* is the width of the dsDNA promoter for the unbent, bent and mean conformation, respectively. The 2.5 pN and 6.2 pN staple sets are identical to reference [94]. The 5.9 pN staple set was newly designed for the MLP (F10–F19, Table 4).

Parameter	T6P	MLP	U6P
scaffold length [nt]	7283	7267	7285
dsDNA [nt]	51	35	55
N_U	8	16	24
N_D	43	19	31
α	90°	100°	100°
w_{unbent} [nm]	17.34	11.90	18.70
d_{unbent} [nm]	25.50	30.94	24.14
w_{bent} [nm]	14.87	9.14	14.41
d_{bent} [nm]	27.97	33.70	28.44
w_{mean} [nm]	16.11	10.52	16.55
d_{mean} [nm]	26.73	32.32	26.29
Δw ($w_{unbent} - w_{bent}$) [nm]	2.47	2.76	4.29
spring ssDNA [nt] (2.5 pN staple set)	143	143	141
F [pN], (2.5 pN staple set)	2.5	3.2	2.6
spring ssDNA [nt] (6.2 pN staple set)	72	-	70
F [pN] (6.2 pN staple set)	6.2	-	6.3
spring ssDNA [nt] (5.9 pN staple set)	-	90	
F [pN] (5.9 pN staple set)	-	5.9	

6.5 Transmission electron microscopy

Transmission electron microscopy (TEM) measurements were kindly performed by Prof. Dr. Christoph Engel (University Regensburg) using the listed reagents for sample preparation and equipment and software tools for data acquisition and analysis.

Electron microscopy grids (copper, 400 mesh; PlanoEM, Germany) were pre-coated with an around 8 nm-thick carbon support film generated with a “Turbo Carbon Coater” (Cressington Scientific Instruments, UK). 4 µL of force clamp solution (10 nM) was applied to glow-discharged grids for 30 s, blotted off and the grids washed for 30 s (bi-distilled water). Grids were dried and imaged without staining using a JEM2100F transmission electron microscope (Jeol, Japan) equipped with TemCamF416 detector (TVIPS, Germany). A total of 94 micrographs were semi-automatically collected at 40000 magnification (2.7 Å/pix) and a defocus range of −2.5 to −4.5 µm using the Serial-EM software package [382]. Contrast transfer function (CTF) estimation and manual particle picking were carried out in Relion 3 [383]. A total of 2133 particles (2× binned; box size 180 pixels/ 100 nm) were extracted, contrast-inverted and 2-D classified into three classes with CTF-amplitude correction from the first peak onward.

6.6 Confocal single-molecule fluorescence microscopy experiments

Single-molecule fluorescence experiments on freely diffusing complexes in solution were conducted using a commercial MicroTime 200 confocal fluorescence microscope. A general overview of the layout and function of the microscope setup is given in the following paragraph (bold numbers refer to Figure 18):

The microscope is equipped with pulsed laser diodes for excitation at 532 nm (LDH-P-FA-530B, **1**) and 636 nm (LDH-D-C-640, **2,** cleanup filter ZET 635/10, **3**) that are combined and directed through a single-mode fiber. The excitation beams are reflected at a multiband dichroic mirror (ZT 532/640RPC, **4**) and focused through a water-immersion microscope objective (UplanSApo ×60/1.20W, **5**) into the sample chamber. Molecules diffusing through the resulting confocal volume are excited and emit fluorescence which is collected using the same objective and then focused on a 50 µm confocal pinhole (**6**). A dichroic mirror (T 635LPX, **7**) separates donor and acceptor fluorescence. Additional bandpass filters (donor: FF01-582/64, **8**, acceptor: H690/70, **9**) complete spectral separation of the fluorescence signals. Each filtered photon stream is detected by an avalanche photodiode detector (SPCM-AQRH-14-TR, **10**) and processed by a time-correlated single-photon counting (TCSPC) module (HydraHarp 400, **11**) which allows time-stamping of individual photon detection events. Operation of the microscope and data acquisition was controlled and performed using the SymPhoTime 64 software package.

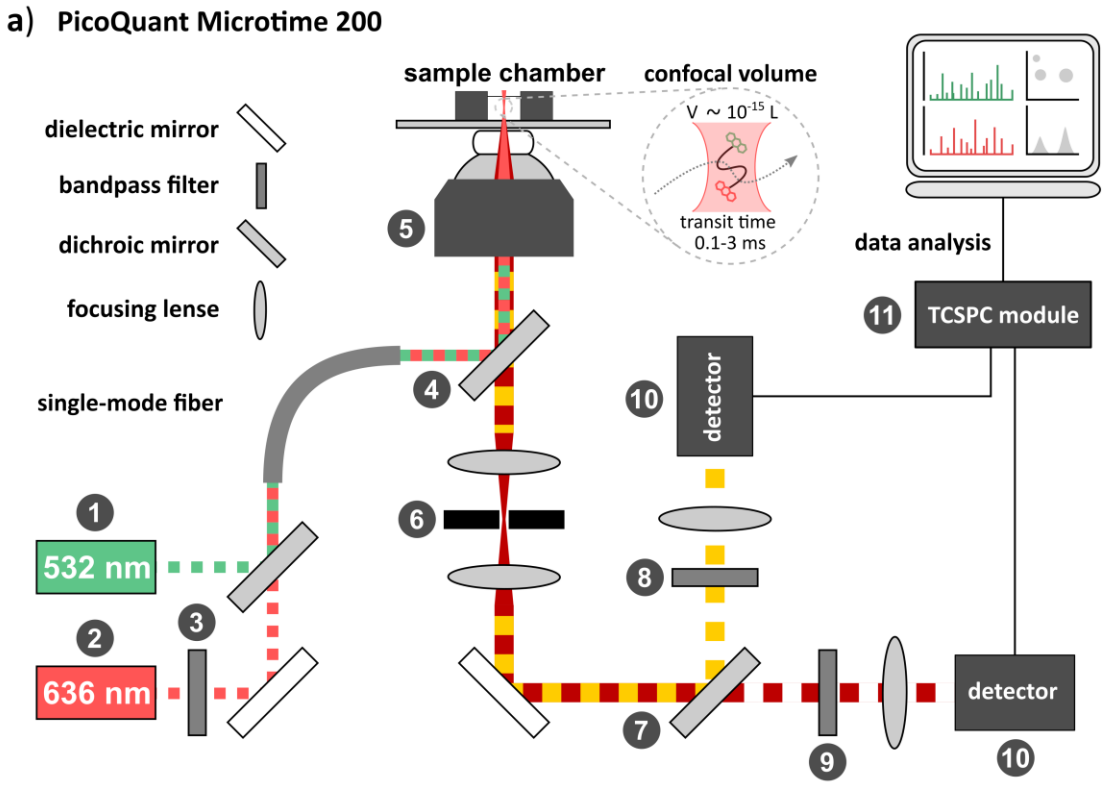

Figure 18: Confocal single-molecule fluorescence microscopy. A schematic overview of the PicoQuant MicroTime 200 confocal fluorescence microscope. All components are labeled according to Table 7: (1) 532 nm pulsed laser diode LDH-P-FA-530B, (2) 636 nm pulsed laser diode LDH-D-C-640, (3) clean-up filter ZET 635/10, (4) excitation dichroic mirror ZT 532/640RPC, (5) water-immersion objective UplanSApo ×60/1.20W, (6) 50 µM confocal pinhole, (7) emission beam splitter T 635LPX, (8) emission filter FF01-582/64, (9) emission filter H690/70, (10) avalanche photodiode SPCM-AQRH-14-TR, (11) HydraHarp 400.

6.6.1 Pulsed Interleaved Excitation

For FRET experiments, donor and acceptor fluorophores were excited using an excitation scheme called Pulsed Interleaved Excitation (PIE, Figure 19). Here, two lasers that are synchronized by a clock signal are alternated on a nanosecond timescale such that every synchronization period contains both laser pulses. Thus, molecules passing through the confocal volume are sequentially excited at 532 nm and 636 nm. The direct excitation of the acceptor enables probing of the emission of the acceptor independently of FRET to confirm if the detected particle is coupled to both, a donor and acceptor fluorophore (spectral sorting). This is especially valuable for samples with incomplete labeling of the biomolecules and samples with a low FRET efficiency that is indistinguishable from crosstalk effects when donor-only excitation is employed. Consequently, the information from separate detection channels and excitation events can be used to spectrally sort the molecules according to their labelling status and to calculate correction factors to account for crosstalk effects (see Chapter 6.7.1). A crucial step in utilizing PIE is adjusting the synchronization period so that the emission after one laser pulse completely decays before the next pulse. The utilized fluorophores ATTO 532 and ATTO 647N have a fluorescence lifetime of 3.8 ns and 3.5 ns, respectively, allowing the fluorescence to decay completely within the chosen 25 ns separation time between pulses.

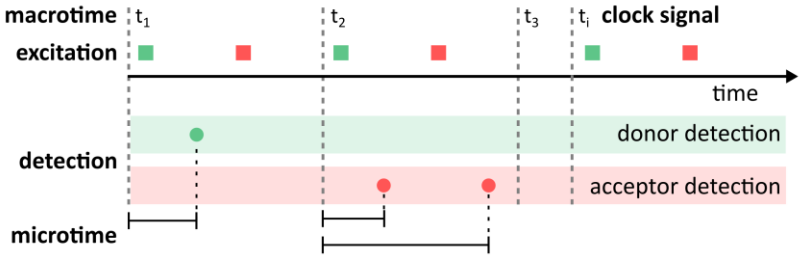

Figure 19: Pulsed interleaved excitation. In pulsed interleaved excitation (PIE), the sample is excited separately at 532 nm and 636 nm using pulsed lasers (squares) synchronized by a clock signal. Emitted photons (circles) detected after spectral separation are time-stamped with a macrotime, the time since the start of the experiment, and a microtime, the time interval since last clock signal. (adapted from [378])

6.6.2 Diffusion-based single-molecule FRET measurements

Prior to sample loading, the sample chambers (Cellview slide, Greiner Bio-One) were passivated with 200 µL blocking buffer for 10 min to saturate surfaces with adhering BSA and washed once with the appropriate sample buffer. Fluorophores were excited using PIE with a pulse frequency of 40 MHz at 532 nm and 636 nm with a set power of 20 µW each. All subsequent experimental conditions were tailored to fit each specific sample and are listed separately below:

i. **Measurements with DNA origami FCs and human transcription factors (Chapter 7.3)**
For steady state measurements, complexes were formed with 20 pM DNA origami force clamp (MLP or U6P) and a combination of 20 nM HsTBP, 20 nM HsBrf2, 20 nM HsBdp1, 2 µM TFIIA and 200 nM TFIIB and incubated for 30 min at room temperature in T78M buffer. Control reactions contained the corresponding linear promoter constructs (MLP: F1F2+F4, U6P: F5F6+F8, Table 4). The sample was transferred to the prepared sample chamber and signals of diffusing molecules were collected for 30 min.

For time course experiments, 20 pM DNA origami in 1x T78M buffer were loaded into the sample chamber and data acquisition was started to measure the unbound DNA state. After 2 min, 20 nM HsTBP was added to initiate complex formation. Data acquisition was continued for 30 min.

ii. Measurements with *S. acidocaldarius* transcription factors (Chapter 7.4.1)

To facilitate complex formation, 0.5 nM SSV T6 promoter (S1+S2, Table 4) and a combination of 1.8 µM SaTBP, 0.35 µM SaTFB and 1.05 µM or 2.1 µM SaTFB2 were incubated for 20 min at 65 °C in 20 µL Sa3 buffer. Afterwards, 30 µL Sa3 buffer (preheated to 65 °C) was added and the sample was transferred to the prepared sample chamber. Data were collected for 30 min.

i. Measurements with *P. furiosus* transcription factors (Chapter 7.4.2)

To facilitate complex formation, 50 pM of either a SSV T6 promoter (S1+S2, Table 4), a native *pf1089* promoter (P_{nat}, T1+T2, Table 4) or a TFBRF1 promoter with a consensus TATA-box and BRE (P_{con}, T3+T4, Table 4) and a combination of 0.3 µM PfTBP, 0.3 µM PfTFB and 0.3 µM PfTFB-RF1 were incubated for 5 min at 65 °C in Pf2 buffer. Afterwards, the sample was transferred to the prepared sample chamber. Data were collected for 30 min. For time course experiments, 50 pM P_{nat} or P_{con} promoter and a combination of 0.3 µM PfTFB and 0.3 µM PfTFB-RF1 in PF2 buffer were loaded into the sample chamber and data acquisition was started to measure the unbound DNA state. After 2 min, 0.3 µM PfTBP was added to initiate complex formation. Data were collected for 30 min at room temperature.

ii. Measurements with DNA origami FCs and archaeal transcription factors (Chapter 7.4.3)

For complex formation, 20 pM SSV T6 promoter force clamp and 50 µM MjTBP or 100 µM PfTBP and 20 µM PfTFB were incubated for 30 min at RT in Mj2 buffer or Pf2 buffer, respectively. Afterwards, samples were transferred to the sample chamber and data were collected for 30 min.

6.7 Data analysis for confocal fluorescence microscopy experiments

Analysis of data collected during confocal FRET measurements was performed with the software package PAM [378]. The data file generated by a PIE FRET experiment contains the continuous photon streams detected by both detectors. Each photon was designated two time-stamps: i) a macrotime, the run time of the experiment at the detection event (Figure 18b) and ii) a microtime, the time interval between the last clock signal and the detection event (Figure 18b). The latter is used to determine whether a photon resulted from a 532 nm (donor excitation) or 636 nm (acceptor excitation) laser pulse. This is accomplished using defined time gates on the microtime information. Donor and acceptor excitation laser pulses were separated by a 25 ns time gap, resulting in a total 50 ns synchronization period. All photons detected during the first 25 ns of this time window were defined to originate from donor excitation and consequently, photons detected in the latter 25 ns resulted from acceptor excitation. In PAM, these information in combination with the respective detector signals (donor/acceptor) are used to sort photons into three so-called PIE channels: i) , donor detection upon donor excitation (DD, donor signal), ii) acceptor detection upon donor excitation, (DA, FRET and crosstalk) and iii) acceptor detection

upon acceptor excitation, (AA, acceptor signal) (Figure 20a).Burst search and determination of FRET efficiency

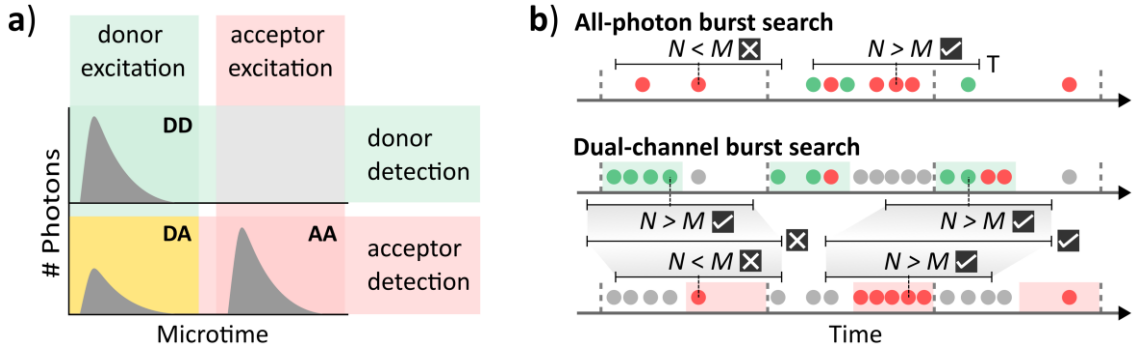

Figure 20: PIE channel definition and burst search in PAM. a) Data from single-molecule FRET experiments employing pulsed interleaved excitation (PIE) were processes with the PAM software package. Photons are sorted based on the excitation laser pulse and the detection channel. The excitation laser assigned to a photon is determined by its microtime: **b)** The photon bursts emitted by diffusing single molecules were extracted from the photon stream using one of two available burst search algorithms: all-photon burst search slides a time window of duration T over the trace of all detected photons and detects a burst, if the number of photons (circles) within the time window N is greater than the threshold *M* (here: *M* = 3). A dual-channel burst search operates in a similar way but separately on all photons originating from donor and acceptor excitation, respectively (indicated by background color). Only bursts in which photons in both channels are detected are selected for further processing. The synchronization clock signal is indicated by grey dashed lines. Grayed out photons are ignored for the respective search.

Bursts of photons emitted by single molecules were extracted from the PIE channel-sorted photon count-time traces using a burst search algorithm. The variant used in this work employs a sliding time window of duration *T* centered around individual photons that is moved along the time axis of the photon stream and identifies a burst if at least *M* photons lie within the window. As a final filtering step, all bursts with a total photon count < *L* were excluded from the search.

PAM implements two variants of the algorithm: a search on all photons together (all-photon burst search, APBS) or independently on photons resulting from donor (DD+DA) and acceptor excitation (AA), keeping only bursts detected in both searches (dual-channel burst search, DCBS) (Figure 20b). The APBS includes signals from molecules that are labelled only with a donor or acceptor fluorophore. These signals are required for the calculation of correction factors (Chapter 6.7.1). The DCBS excludes these molecules, yielding only signals from doubly labeled molecules. The burst search parameters were adjusted according to the sample under investigation. For an APBS, the FRET efficiency of each burst as proximity ratio E_{PR} and the raw stoichiometry factor S_{raw} were calculated as:

$$E_{\mathrm{PR}} = \frac{N_{\mathrm{DA}}}{N_{\mathrm{DD}} + N_{\mathrm{DA}}} \qquad \textbf{Equation 26}$$

$$S_{\mathrm{raw}} = \frac{N_{\mathrm{DD}} + N_{\mathrm{DA}}}{N_{\mathrm{DD}} + N_{\mathrm{DA}} + N_{\mathrm{AA}}} \qquad \textbf{Equation 27}$$

where N_{DD}, N_{DA} and N_{AA} are the number of photons detected in the respective PIE channels. These were used to calculate the donor leakage and direct excitation correction factors. For DCBS, the FRET efficiency *E* and the stoichiometry factor *S* of each burst were calculated as:

$$E = \frac{N_{\mathrm{DA}} - (c_{\mathrm{leak}} \cdot N_{\mathrm{DD}} + c_{\mathrm{dir}} \cdot N_{\mathrm{AA}})}{\gamma \cdot N_{\mathrm{DD}} + N_{\mathrm{DA}} - (c_{\mathrm{leak}} \cdot N_{\mathrm{DD}} + c_{\mathrm{dir}} \cdot N_{\mathrm{AA}})} \quad \textbf{Equation 28}$$

$$S = \frac{\gamma \cdot N_{\mathrm{DD}} + N_{\mathrm{DA}} - (c_{\mathrm{leak}} \cdot N_{\mathrm{DD}} + c_{\mathrm{dir}} \cdot N_{\mathrm{AA}})}{\gamma \cdot N_{\mathrm{DD}} + N_{\mathrm{DA}} + \beta \cdot N_{\mathrm{AA}} - (c_{\mathrm{leak}} \cdot N_{\mathrm{DD}} + c_{\mathrm{dir}} \cdot N_{\mathrm{AA}})} \quad \textbf{Equation 29}$$

where c_{leak} is the correction factor for donor leakage, c_{dir} is the correction factor for direct excitation of the acceptor, γ and β are the detection and excitation correction factors (Chapter 6.7.1).

6.7.1 Calculation of correction factors

In order to determine accurate FRET efficiencies, the burst data were corrected for the contribution of crosstalk effects (donor leakage and direct excitation of the acceptor), different detection efficiencies and quantum yields of donor and acceptor fluorophore (γ-factor) and different excitation efficiencies of donor and acceptor (β-factor). Donor leakage occurs when the donor emission is detected in the acceptor channel, due to incomplete spectral separation. The correction factor c_{leak} was determined from the proximity ratio of the donor only population $E_{\mathrm{PR,GG}}$ ($0.8 < S_{\mathrm{raw}} < 1.1$) in APBS burst histograms as:

$$c_{\mathrm{leak}} = \frac{E_{\mathrm{PR,DD}}}{1 - E_{\mathrm{PR,DD}}} \quad \textbf{Equation 30}$$

Analogously, the correction factor c_{dir} was calculated from the raw stoichiometry factor of the acceptor only population $S_{\mathrm{raw,AA}}$ ($E > 0.1$, $-0.2 < S_{\mathrm{raw}} < 0.2$):

$$c_{\mathrm{dir}} = \frac{S_{\mathrm{raw,AA}}}{1 - S_{\mathrm{raw,AA}}} \quad \textbf{Equation 31}$$

The correction tool utility of the PAM Burst Browser was used for this purpose. The APBS histograms of all measurements (with identical fluorophores) recorded in one session were pooled and $E_{\mathrm{PR,DD}}$ and $S_{\mathrm{raw,AA}}$ where determined by fitting the respective population with a Gaussian distribution (Figure 21a).

Subsequently, these correction factors were applied to the respective DCBS histograms of all pooled measurements to calculate the γ- and β- factor using a global fit on multiple *E/S*-separated FRET populations. First, all populations were fitted using one or multiple two-dimensional Gaussians to determine the mean *E* and *S* positions, which were plotted as 1/*S* versus *E*. A linear fit was performed to obtain the slope *m* and y-axis intercept *n* to calculate the γ and β factor as (Figure 21b):

$$\gamma = \frac{n - 1}{n + m - 1} \quad \textbf{Equation 32}$$

$$\beta = n + m - 1 \quad \textbf{Equation 33}$$

Correction factors were calculated for datasets acquired at the same day. Fully corrected dataset (Figure 21c) were used for further analysis.

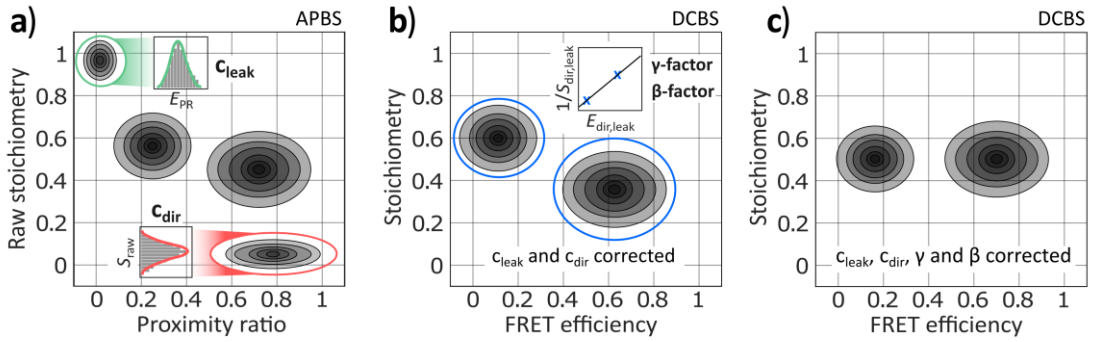

Figure 21: Determination of correction factors for confocal smFRET data. a) The correction factors for donor leakage c_{leak} and direct excitation of the acceptor c_{dir} are determined from E_{PR}/S_{raw} histograms based on an all-photon burst search (APBS). For c_{leak}, the mean FRET efficiency of the donor-only population (green circle) and for c_{dir}, the mean stoichiometry of the acceptor only population (red circle) are determined by Gaussian fits (insets). **b)** The excitation and detection correction factor β- and γ- are calculated from c_{leak} and c_{dir} corrected E/S histograms based on a dual channel burst search (DCBS). The mean E and S value for at least two E/S separated population are determined via Gaussian fits (blue circles) and a linear fit of 1/S vs E (inset) determines the y-axis intercept and slope. **c)** The c_{leak}-, c_{dir}-, γ- and β- corrected histogram has a mean stoichiometry of S = 0.5. The cumulative E and S histograms of the current (black) and previous (blue) step are shown for comparison.

6.7.2 Calculation of FRET efficiency histograms

The final analysis of corrected DCBS burst data was performed with Origin 2019b. FRET efficiency histograms were calculated from all bursts using a binning range of 0–1 with a bin size of 0.025 (40 bins). Histograms were normalized to the total number of counts and the mean of each bin was calculated for three technical replicates to generate the final histogram. To determine the mean FRET efficiency of each population, the data were fitted with a Gaussian distribution using one or multiple peaks with a fixed y-offset of 0. Additionally, experiments with DNA origami force clamps which showed a medium FRET density were fitted with a triple Gaussian fit due to a medium FRET density (E = 0.4–0.5) that was observed in all origami experiments involving proteins, but not in control measurements with linear promoter constructs. Therefore, this effect seems to have no connection to the biological system. To account for this density during data analysis, the additional Gaussian with a fixed area was added to improve the overall fit quality but was not included in the analysis.

6.7.3 TBP-induced bending probability

The TBP-DNA system can be modeled as fluctuating between two discrete energetic states: the low-energy unbent state and the high-energy bent conformation. In equilibrium, the probability P of encountering the system in the respective state is directly proportional to the relative distribution of bent and unbent molecules. Thus, the bending probability of TBP P_{bent} can be calculated from the ratio of the low (unbent) and high FRET (bent) populations measured in equilibrium smFRET experiments as:

$$P_{\mathrm{bent}} = \frac{a_{\mathrm{HF}}}{a_{\mathrm{HF}} + a_{\mathrm{LF}}} \qquad \textbf{Equation 34}$$

where a_{LF} and a_{HF} are the areas of the fitted Gaussians for the low FRET efficiency and high FRET efficiency population. The probability is dependent on the difference in free energy Δ*G* between the two states given by the Boltzmann factor:

$$\frac{P_{\text{bent}}}{P_{\text{unbent}}} = e^{\frac{-\Delta G}{k_B T}} \qquad \textbf{Equation 35}$$

where, k_B is the Boltzmann constant and *T* the absolute temperature. Thus, Δ*G* can be calculated as:

$$\Delta G = -\ln\left(\frac{P_{\text{bent}}}{P_{\text{unbent}}}\right) \cdot k_B T \qquad \textbf{Equation 36}$$

When force is applied to the promoter, the resulting change in the probability distribution can be described by the Boltzmann distribution:

$$P_i = \frac{e^{\frac{-\varepsilon_i}{k_B T}}}{\sum_{j=1}^{M} e^{\frac{-\varepsilon_j}{k_B T}}} \qquad \textbf{Equation 37}$$

where p_i is the probability of state *i*, ε_i is the energy of state *i*, and *M* is the total number of states available to the system. Thus, for the two state DNA/TBP system, the force dependent bending probability can be calculated as:

$$P_{\text{bent}} = \frac{\mathrm{e}^{\frac{-\Delta G_{0pN} - F\cdot\Delta w}{k_B T}}}{\mathrm{e}^{\frac{-F\cdot\Delta w}{k_B T}} + \mathrm{e}^{\frac{-\Delta G_{0pN} - F\cdot\Delta w}{k_B T}}} \qquad \textbf{Equation 38}$$

where ΔG_{0pN} is the difference in free energy between the unbent and bent state at 0 pN, *F* is the force applied to the promoter DNA and Δ*w* is the end-to-end distance change of the dsDNA promoter segment (Δ*w* = 0 for the unbent state).

6.7.4 Dwell time calculation for diffusion-based experiments

Data were processed as described above. All bursts were sorted according to their FRET efficiency population and binned by macrotime using a range appropriate for the respective complex with a bin size of 2 min. Low FRET and high FRET bins were normalized to the combined sum to determine relative ratios of both populations over time.

For complex association experiments, where TBP was added after the start of the experiment, fitting the decaying unbent population to a mono-exponential model yields the complex assembly rate superimposed with the simultaneous complex disassembly $k = \tau^{-1}$ and the low FRET ratio in the new equilibrium $[u]_{new}$. A perturbation-relaxation kinetics model was used to extract both rates from the data [384]. The model DNA-TBP-system is in an equilibrium of two states: the unbent state and the bent state.

$$\text{unbent} \underset{k_{\text{bent}}=\tau_{\text{unbent}}^{-1}}{\overset{k_{\text{bent}}=\tau_{\text{unbent}}^{-1}}{\rightleftharpoons}} \text{bent} \qquad \textbf{Equation 39}$$

Where k_{bent} is the bending rate and k_{unbent} is the unbending rate. Conversely, τ_{unbent} and τ_{bent} are the mean lifetimes of a molecule in the unbent or bent state. The equilibrium constant K is given by the ratio of bent and unbent fractions $[b]$ and $[u]$:

$$K = \frac{[b]}{[u]} = \frac{1-[u]}{[u]} = \frac{k_{\mathrm{unbent}}}{k_{\mathrm{bent}}} \qquad \textbf{Equation 40}$$

The system is perturbed by a change in the TBP concentration (spike-in of TBP after the start of the experiment) and will relax in a first order process to its new equilibrium. Since k_{bent} is concentration dependent, the unbent fraction $[u]$ will vary according to:

$$[u](t) = [u]_{\mathrm{new}} + A \cdot \mathrm{e}^{-\frac{t}{\tau}} \qquad \textbf{Equation 41}$$

The amplitude A is the change of the unbent fraction and the new equilibrium unbent fraction is $[u]_{new}$. The relaxation time τ is given by both rate constants:

$$\tau = \frac{1}{k_{bent} + k_{unbent}} \qquad \textbf{Equation 42}$$

With the new equilibrium constant K_{new}:

$$K_{new} = \frac{1-[u]_{new}}{[u]_{new}} \qquad \textbf{Equation 43}$$

and the relaxation time τ, both rate constants can be calculated for the new equilibrium as:

$$k_{\mathrm{bent}} = \frac{K_{\mathrm{new}}}{\tau(K_{\mathrm{new}}+1)} = \frac{1}{\tau_{\mathrm{unbent}}} \qquad \textbf{Equation 44}$$

$$k_{\mathrm{unbent}} = \frac{1}{\tau(K_{\mathrm{new}}+1)} = \frac{1}{\tau_{\mathrm{bent}}} \qquad \textbf{Equation 45}$$

6.7.5 FRET-2CDE filter

In order to assess whether molecular complexes showed conformational dynamics on the microsecond timescale, that is, during the transition through the confocal volume and at the level of individual photon bursts, the data were analyzed with the FRET-2CDE (two-channel kernel based density distribution estimator) filter implemented in PAM [385]. In essence, the filter grades individual bursts based on the stability of the donor/acceptor photon ratio over the duration of the burst. This is achieved by calculating the local FRET efficiency (± 5 τ_{Fl}) around each donor photon $E_{local,D}$ in analogy to Equation 26 as:

$$E_{\mathrm{local,D}} = \frac{1}{N_{\mathrm{XD}}} \cdot \sum_{\mathrm{i}=1}^{N_{\mathrm{XD}}} \frac{KDE^{\mathrm{A}}_{\mathrm{D,i}}}{KDE^{\mathrm{D}}_{\mathrm{D,i}} + KDE^{\mathrm{A}}_{\mathrm{D,i}}} \qquad \textbf{Equation 46}$$

where N_{XD} is the number of photons in the donor detection channel, $KDE^{\mathrm{D}}_{\mathrm{D,i}}$ (kernel density estimator) is the density of donor photons around the ith donor photon and $KDE^{\mathrm{A}}_{\mathrm{D,i}}$ is the density

of acceptor photons around the i[th] donor photon. For a static distribution of donor and acceptor photons, $E_{\mathrm{local,D}}$ converges to the average E_{PR} (Figure 22a). However, for non-static distributions, time intervals with low FRET efficiency are considered more often, due to the inherently higher number of donor photons and in turn gain a higher weight in the calculation $E_{\mathrm{local,D}}$. In such a case, $E_{\mathrm{local,D}}$ converges to values lower than the average E_{PR} (Figure 22b). Similarly, the local "inverse-FRET efficiency" around each red photon $(1 - E)_{\mathrm{local,A}}$ calculates as:

$$(1-E)_{\mathrm{local,A}} = \frac{1}{N_{\mathrm{XA}}} \cdot \sum_{\mathrm{j}=1}^{N_{\mathrm{XA}}} \frac{KDE^{\mathrm{D}}_{\mathrm{A,j}}}{KDE^{\mathrm{A}}_{\mathrm{A,j}} + KDE^{\mathrm{D}}_{\mathrm{A,j}}} \qquad \textbf{Equation 47}$$

where N_{XA} is the number of photons in the acceptor detections channel, $KDE^{\mathrm{A}}_{\mathrm{A,j}}$ is the density of acceptor photons around the j[th] acceptor photon and $KDE^{\mathrm{D}}_{\mathrm{A,j}}$ is the density of donor photons around the j[th] acceptor photon. Accordingly, $(1 - E)_{\mathrm{local,A}}$ converges to the average $1 - E_{\mathrm{PR}}$ value for static photon distributions (Figure 22a) and values smaller than the average $1 - E_{\mathrm{PR}}$ for non-static distributions (Figure 22b). Combining Equation 46 and Equation 47 yields the final form of the FRET-2CDE filter:

$$\text{FRET-2CDE} = 110 - 100 \cdot \left[E_{\mathrm{local,D}} + (1-E)_{\mathrm{local,A}}\right] \qquad \textbf{Equation 48}$$

For a static in-burst photon distribution the FRET-2CDE value is 10. For bursts showing fluctuations in FRET efficiency, the term in parenthesis becomes < 1, and thus FRET-2CDE values become > 10.

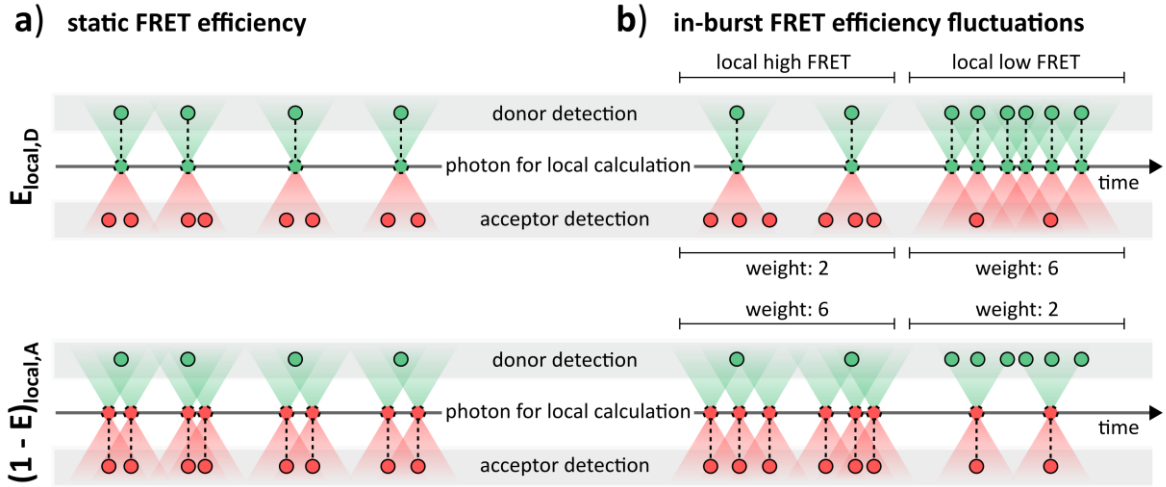

Figure 22: Working principle of the FRET-2CDE filter. The filter calculates the average local FRET efficiency around donor photons $E_{\mathrm{local,D}}$ by estimating the local donor/acceptor photon density (green/red cones) and its counterpart $(1 - E)_{\mathrm{local,A}}$ by estimating the photon density around acceptor photons. **a)** For static FRET efficiency across the burst, the local photon density is evenly distributed. **b)** For fluctuations in the local FRET efficiency, $E_{\mathrm{local,D}}$ gives more weight to stretches of local low FRET efficiency and $(1 - E)_{\mathrm{local,A}}$ gives more weight to stretches of local high FRET efficiency.

6.7.6 Fluorescence correlation spectroscopy

In fluorescence correlation spectroscopy (FCS), time dependent change in a fluorescence signal's self-similarity is used to infer information on diffusion behavior. This is accomplished by calculating the autocorrelation function $G(t_{corr})$ as:

$$G(t_{\mathrm{corr}}) = \frac{\langle I(t)\, I(t + t_{\mathrm{corr}})\rangle}{\langle I(t)\rangle^2} - 1 \qquad \textbf{Equation 49}$$

where t_{corr} is the correlation time, I is the signal intensity and t is the experiment time. Triangular brackets denote the time-averaged value. Generally, slowly diffusing species display a higher auto-correlation at high t_{corr}, as the molecule stays inside the confocal volume for extended periods of time. The inverse holds true for fast diffusing species.

FCS analysis of DNA origamis and short linear DNA constructs was performed with the PicoQuant software package SymPhoTime 64. The autocorrelation of the acceptor signal for an arbitrary 10 min interval of each data set was calculated and the resulting curve was fitted to an exponential decay model that also accounts for photoblinking of the observed fluorophores with one (linear dsDNA) or two (origami) diffusion components (n_{Diff}):

$$G(t_{\mathrm{corr}}) = \left[1 + T\left[\mathrm{e}^{\frac{t_{\mathrm{corr}}}{\tau_{\mathrm{Trip}}}} - 1\right]\right] \sum_{i=0}^{n_{Diff}-1} \frac{\rho[\mathrm{i}]}{\left[1 + \frac{t_{\mathrm{corr}}}{\tau_{\mathrm{Diff}}[i]}\right]\sqrt{1 + \frac{t_{\mathrm{corr}}}{\tau_{\mathrm{Diff}}[i]\kappa^2}}} \qquad \textbf{Equation 50}$$

where T is the fraction of triplet state molecules, τ_{Trip} is the lifetime of the triplet state, ρ_i is contribution of the i^{th} diffusing species and κ is the length to diameter ratio of the confocal volume. Note, that the diffusion times given were calculated with a non-calibrated confocal volume and are only comparable within the respective dataset.

6.8 TIRF microscopy experiments

For the experimental part of this work, a TIRF microscope with single-molecule sensitivity was constructed to conduct measurements on immobilized molecules. A detailed overview of the construction is given in Chapter 6.10. The general layout and function of the system will be given in this section (bold numbers refer to Figure 23):

The TIRF microscope is equipped with four continuous wave lasers for excitation at 488 nm, 532 nm, 561 nm (OBIS LS, **1–3**) and 637 nm (OBIS 640LX, **4**, cleanup filter ZET 635/10, **5**). For experiments in this work, only a maximum of two lasers were used simultaneously. The excitation beams are combined with dielectric and dichroic mirrors (**6–8**) and focused onto the sample. The biomolecules in the sample are immobilized in a custom-built sample chamber consisting of a quartz microscope slide and coverslip with the sample volume sandwiched in between (Chapter 6.8.3). The excitation beams are guided through a quartz prism (**9**) that is connected to the sample chamber with a thin layer of glycerol to create a uniform light guide. The incident angle of the excitation beam at the quartz/buffer interface is 72°, which is greater than the critical angle $\Theta_{critical}$ = 65°, and thus the light is totally internally reflected at the quartz/buffer interface. The sample immobilized on the quartz slide is excited by the resulting evanescent field that

reaches 110–130 nm into the sample (Equation 13). Assuming a height of 100 µm for the sample chamber this reduces the background signal by a factor of 830 (0.12 µm/100 µm). The fluorescence is collected by a water immersion objective (HC PL APO 63x/1.20 W CORR CS2, **10**) and directed to an Optosplit III emission beamsplitter that incorporates all optical components for spectral separation of up to three channels. An aperture adjusts the entering emission. A dichroic mirror (HC BS 640 imaging, **11**) splits the emission into donor and acceptor fluorescence, which are passed through additional bandpass filters (donor: 582/75 BrightLine HC, **12**, acceptor: 635 LP Edge Basic, **13**) to complete spectral separation. Each filtered signal is detected and spatially separated on the same EMCCD camera (iXon Ultra 897, **14**).

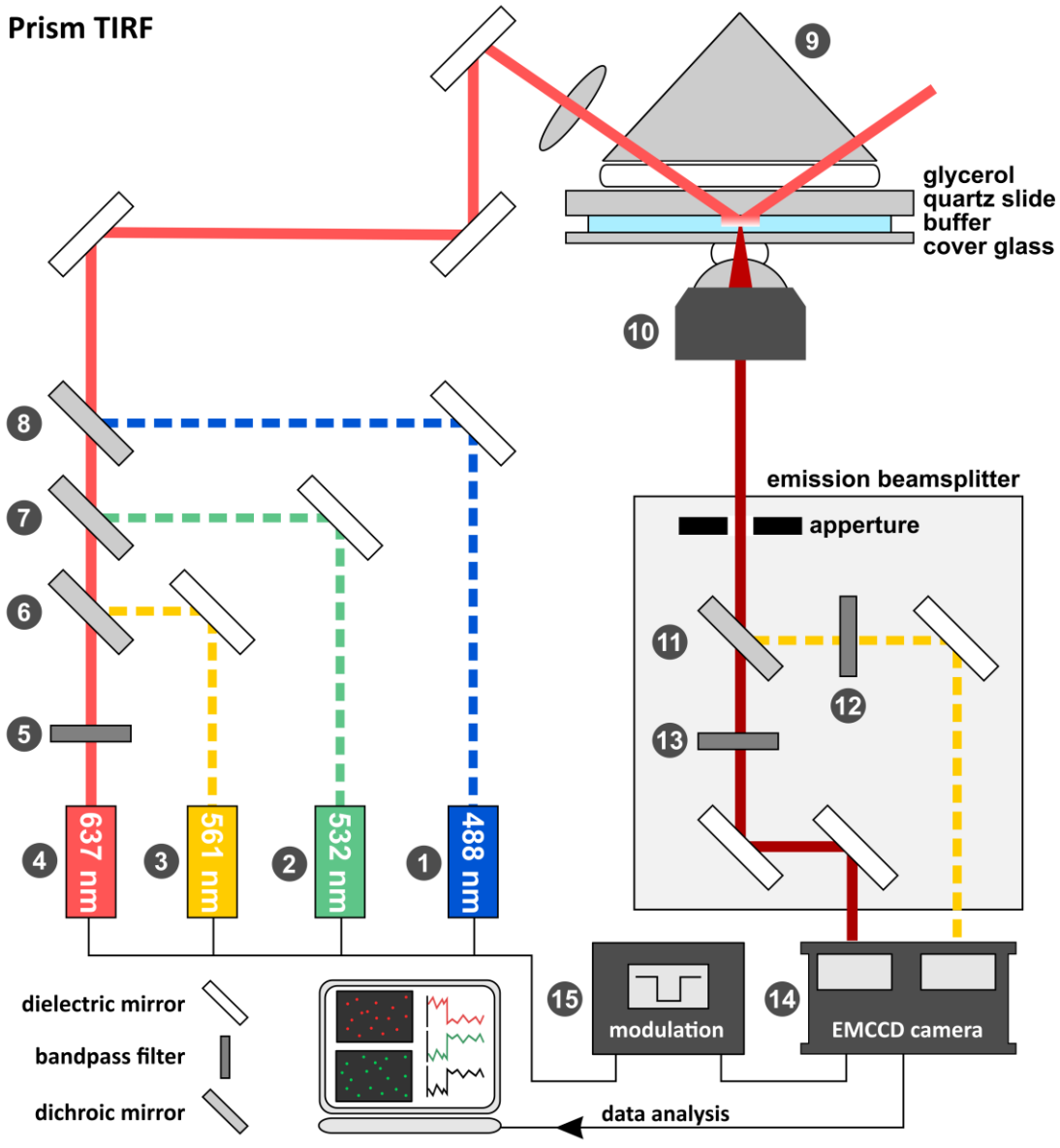

Figure 23: Total internal reflection fluorescence (TIRF) microscopy. A schematic overview of the home-built prism TIRF microscope. All components are labeled according to Table 8: (1) 488 nm laser OBIS 488LS, (2) 532 nm laser OBIS 532LS, (3) 561 nm laser OBIS 561LS, (4) 561 nm laser OBIS 561LS, (5) clean-up filter ZET 635/10, (6) dichroic mirror ZT 568LPXR superflat, (7) dichroic mirror ZT 532RDC, (8) dichroic mirror ZT 488RDC, (9) quartz prism PS610, (10) water immersion objective HC PL APO 63x/1.20 W CORR CS2 (11) emission beam splitter HC BS 640 imaging, (12) emission filter 582/75 BrightLine HC, (13) emission filter 635 LP Edge Basic, (14) EMCCD camera iXon Ultra 897, (15) camera/laser synchronization device Multistream.

6.8.1 Alternating laser excitation

For FRET experiments, a special illumination scheme called alternating laser excitation (ALEX) was used, which functions analogous to PIE (Chapter 6.6.1), but on the millisecond to microsecond timescale [386]. With ALEX, the donor and acceptor are individually and sequentially excited. Combined with the separate detection of donor and fluorophore emission, the ALEX excitations scheme allows to verify the existence of both, a donor and acceptor fluorophore on each measured particle. The fluorescence intensity of each individual fluorophore can then be further used to calculate correction factors to account for crosstalk effects caused by imperfect spectral separation (Chapter 6.9.1). ALEX is integrated in the TIRF setup via the commercial Multistream device (Figure 23 **15**) that synchronizes the camera's frame-trigger signal with the lasers and modulates their intensity in a manner such that only one of the two used lasers is active per given frame.

6.8.2 Passivation of microscope slides

To facilitate surface immobilization of biotin-modified nucleic acids, the quartz microscope slides used for wide-field single-molecule experiments were functionalized with biotin-doted PEG. This modification also limits the unspecific adherence of proteins and nucleic acids to the charged quartz surface [387], thus reducing the background signal and allowing finer control of protein concentration in solution (reviewed in [15]).

Prior to functionalization, quartz microscope slides were cleaned in freshly prepared peroxomonosulfuric acid for 30 min and washed three times with Millipore water followed by incubation in 2% Hellmanex washing solution for 10 min and a further washing step with Millipore water under sonication for 10 min. From this point on, all preparation steps where additionally performed with microscope cover glasses.

Microscope slides and cover glasses were incubated in methanol for 20 min and sonicated for 5 min. For silane modification, the slides and cover glasses were incubated in a freshly prepared silane coupling solution for 10 min, sonicated for 1 min and incubated again for 10 min. Afterwards, the slides and cover glasses were rinsed with methanol five times, an additional 20 times with Millipore water and dried for 1 h at 37 °C. For PEG-modification, 100 µL of freshly prepared PEG passivation solution was sandwiched between a slide and a cover glass. The slides were placed on elevated racks in closed boxes above a water film and incubated for 2 h in under humid atmosphere. Afterwards, slides and cover glasses were separated, rinsed with Millipore water 20 times and dried at 37 °C (2- 3 h). The fully dried slides and cover glasses were transferred to 50 mL centrifuge tubes (one slide and one cover glass per tube), vacuum-sealed in those tubes and stored at -20 °C.

6.8.3 Flow chamber preparation

For the construction of flow chambers, the passivated quartz microscope slides and cover glasses were equilibrated to room temperature before breaking the vacuum seal. The assembly scheme is depicted in Figure 24:

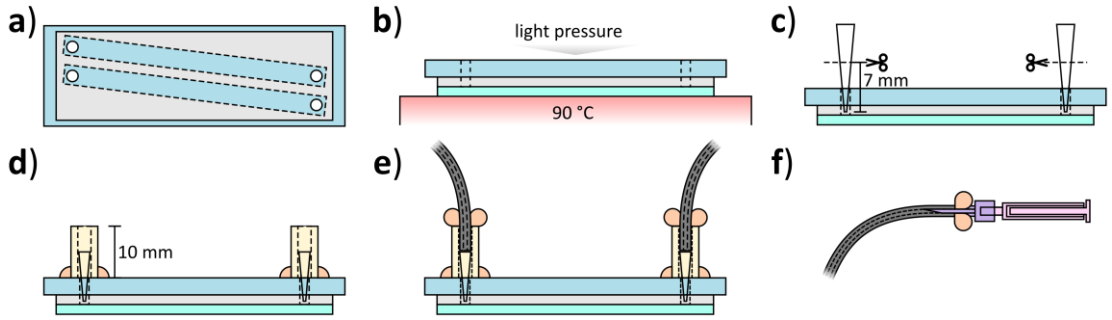

Figure 24: Flow chamber assembly. Schematic workflow for the assembly of a flow chamber for wide-field single-molecule experiments. **a)** A Parafilm sheet (gray) with cut channels connects the drill holes of the microscope slide (blue). **b)** The stacked slide, parafilm and cover glass (cyan) are fused by heat and pressure. **c)** Cut pipette tips (white) are inserted as tube adapters. **d)** 0.4 mm tube pieces (yellow) as adapters are fixed with epoxy resin (orange). **e)** 0.1 mm tube (black) for sample-loading sealed with epoxy resin. **f)** Syringe-needle (purple) and 1 mL syringe (pink) for sample-loading sealed to one tube per channel.

a) A sheet of Parafilm with incisions connecting the drill holes is sandwiched between a microscope slide and a cover glass and **b)** heated to 90 °C on a flat surface under light pressure (e.g. a heated magnetic stirrer) until the Parafilm becomes transparent (30–120 s). **c)** After cooling, the lower 7 mm of a 10 µL pipette tip are cut and inserted into the drill holes. **d)** A 10 mm piece of a 0.4 mm tube (tube VERSILON) is placed over the pipette tips and sealed to the quartz slide with 5 min-epoxy resin. **e)** After hardening of the resin, 15–20 cm pieces of 0.1 mm FEP tubes are inserted into the 0.4 mm tubes and sealed with 5 min-epoxy resin and hardened again. **f)** For each flow chamber channel, one tube is equipped with a syringe-needle for the attachment of a 1.5 mL syringe for sample loading, sealed with epoxy resin and hardened.

6.8.4 Photo-stabilization

For quantitative FRET measurement on immobilized complexes a stable fluorescence emission of the dyes is required over the time course of the experiment (seconds to minutes). The two main factors that can impair fluorophore stability are: i) photobleaching, the irreversible conversion of the fluorophore to a non-fluorescent species, and ii) blinking, a transient conversion of the fluorophore to a non-emitting species.

Reactive oxygen species are primary contributors to photobleaching as they can rapidly react with exposed chemical groups of the fluorophore, thereby disrupting the delocalized π-electron system resulting in non-fluorescent dyes. This can severely limit the observation time or the number of usable traces in an experiment. In order to decrease the impact of reactive oxygen species, the sample buffer is supplemented with an enzymatic oxygen scavenging system that depletes molecular oxygen (O_2). The most commonly used system is based on a combination of glucose oxidase/catalase [388] or protocatechuate-dioxygenase [389]. The first variant is employed for experiments in this work (Figure 25a). In the first reaction step, β-D-glucose is oxidized to D-glucono-1,5-lactone by glucose oxidase under the consumption of O_2 and the release of hydrogen peroxide (H_2O_2). The resulting D-glucono-1,5-lactone can hydrolyze in the aqueous buffer to D-gluconic acid. Catalase converts H_2O_2 to water and O_2. The accumulation of gluconic acids can reduce the pH value of the buffer over prolonged experiments. This is mitigated by using a high buffer capacity (typically 100 mM).

Photoblinking is a recurring transition of the fluorophore to a dark state, usually on the microsecond to millisecond timescale [390]. Blinking is mainly induced by triplet states [391], radical ions[390] and isomerization of the fluorophore[392]. Triplet oxygen efficiently quenches dye triplet states and therefore plays a key role in modulating dye stability. Thus, the depletion of O_2 incurs an increase of blinking [393]. Blinking is especially detrimental for quantitative studies of DNA/protein dynamics as no information is gained on conformational transition occurring during the fluorophore's off state. To remedy this, the buffer is additionally supplemented with a reducing and oxidizing system (ROXS) that depopulates triplet states via electron transfer and quickly recovers the formed radical ions through the complementary redox reaction [394] (Figure 25b). The variant employed in this work uses the ROXS pair trolox and its oxidized form trolox quinone [394–396] (Figure 25c).

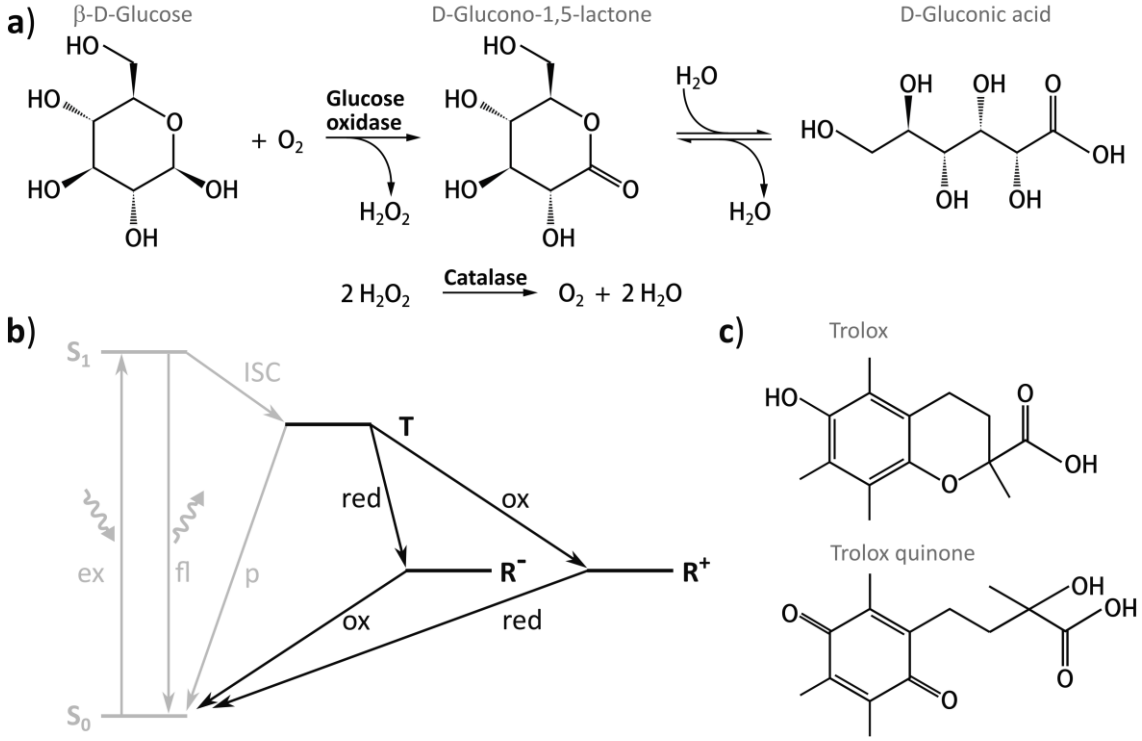

Figure 25: Mechanisms of photo-stabilization. a) The combination of two-enzyme-catalyzed reaction is used to deplete molecular oxygen in the sample buffer for single-molecule FRET experiments. β-D-glucose is oxidized to D-glucono-1,5-lactone by glucose oxidase under release of hydrogen peroxide. In the aqueous buffer, D-Glucono-1,5-lactone hydrolyses to D-gluconic acid. The resulting hydrogen peroxide is converted to water and molecular oxygen by the enzyme catalase. **b)** The fluorophore is excited (ex) to the S_1 excited state and relaxes under emission of fluorescence (fl). Inter system crossing (ISC) competes with fluorescence and leads to the formation of the triplet state (T) that can slowly relax via emission of phosphorescence (p). The ROXS system (black lines) rapidly depopulates the triplet state via reduction (red) or oxidation (ox) of the dye leading to the formation of a radical anion (R^-) or radical cation (R^+). The radical ions are subsequently recovered to the ground state (S_0) via the complementary redox reaction (adapted from [396]). **c)** Molecular structure of the ROXS pair trolox (reducing agent) and trolox quinone (oxidizing agent).

6.8.5 Surface-based single-molecule FRET measurements

Single-molecule FRET measurements on immobilized DNA/protein complexes were carried out in custom-built flow chambers (Chapter 6.8.3). For all experiments, the flow chamber was first incubated with 0.1 mg/mL NeutrAvidin solution for 5 min and washed with 500 µL TBS. This step is crucial to enable surface immobilization of biotinylated oligonucleotides. All subsequent experimental conditions were tailored to fit each specific sample and are listed separately below:

i. **Conformational dynamics of a DNA Holliday junction (Chapter 7.1)**
The chamber was flushed with the annealed Holliday junction (Table 4, annealed with H1+H2+H3+H4, afterwards diluted to 10 pM in TBS), incubated until a density of 200–300 molecules per field of view was reached and washed with 500 µL Tris/HCl (pH 7.5). Afterwards, the chamber was flushed with 250 µL Tris/HCl (pH 8.0)-photo-stabilization buffer supplemented with 0- 200 mM $MgCl_2$. The sample was incubated for 5 min before video acquisition was started in order to allow for the oxygen-scavenging reaction to proceed. The fluorophore Cy3 was excited at 532 nm (donor excitation, no ALEX) with a set power of 50 mW. Videos of 400 frames were recorded at a rate of 20 Hz with an EM gain of 200. Depending on sample density, 3–10 videos were collected per experimental condition.

ii. **Measurements with linear DNA constructs and human TFIIIB (Chapter 7.2)**
The flow chamber was flushed with the annealed U6P DNA (Table 4, annealed with U1+U2, afterwards diluted to 10 pM in TBS), incubated until a density of 200–300 molecules per field of view was reached and washed with 500 µL TBS. Afterwards, the chamber was flushed with 250 µL T78-photo-stabilization buffer supplemented with a combination of 10 nM HsTBP, 1 nM HsBrf2 and/or 1 nM HsBdp1. The sample was incubated for 5 min before video acquisition was started to facilitate complex formation oxygen depletion. The fluorophores ATTO 532 and ATTO 647N were excited using ALEX at 532 nm and 637 nm with a set power of 30 mW and 50 mW, respectively. Videos of 400 frames were recorded at a rate of 40 Hz. Depending on sample density, 5- 15 videos were collected per experimental condition. In order to assess the complex stability, the sample chamber was then flushed with 500 µL T78 buffer to wash off any non-bound proteins. Afterwards, the chamber was flushed with T78-photo-stabilization buffer and incubated again for 5 min before another set of videos was taken.

iii. **Measurements with DNA origami FCs and human transcription factors (Chapter 7.3.3)**
The chamber was flushed with the biotinylated U6P force clamp (diluted to 10 pM in folding buffer), incubated until a density of 200–300 molecules per field of view was reached (5-20 s) and washed with 500 µL folding buffer. Afterwards, the chamber was flushed with 250 µL T78m-photo-stabilization buffer supplemented with 10 nM HsTBP. The sample was then incubated for 5 min before video acquisition was started in order to facilitate complex formation and oxygen depletion. The fluorophores ATTO 532 and ATTO 647N were excited using ALEX at 532 nm and 637 nm with a set power of 30 and 50 mW, respectively. Videos of 600 frames were recorded at a rate of 40 Hz. Depending on sample density, 10–15 videos were collected per experimental condition.

6.9 Data analysis for TIRF microscopy experiments

The videos were analyzed employing the iSMS software package [377]. For the detection of doubly labeled molecule spots, the donor and acceptor channel regions within the video were defined and overlaid. Molecule spots were detected using a signal to noise threshold of 50/30 for Cy3 and Cy5 and 100/150 for ATTO 532 and ATTO 647N. Donor and acceptor molecule spots within a 3 pixels distance (254 nm per pixel) were considered as co-localized and subsequently analyzed. Fluorescence intensity-time traces were calculated from a 21 pixel group that averages the intensity point spread function (PSF) of each molecule spot. The average intensity of all dark pixels on a 2 pixel radius around the center was subtracted as a background correction (Figure 26a). These traces were corrected for donor leakage, acceptor direct excitation and γ using the tools implemented in iSMS (Chapter 6.9.1). Afterwards, the FRET efficiencies *E* and stoichiometry values *S* were calculated as:

$$E = \frac{I_{\mathrm{DA}} - (c_{\mathrm{leak}} \cdot I_{\mathrm{DD}} + c_{\mathrm{dir}} \cdot I_{\mathrm{AA}})}{\gamma \cdot I_{\mathrm{DD}} + I_{\mathrm{DA}} - (c_{\mathrm{leak}} \cdot I_{\mathrm{DD}} + c_{\mathrm{dir}} \cdot I_{\mathrm{AA}})} \qquad \textbf{Equation 51}$$

$$S = \frac{\gamma \cdot I_{\mathrm{DD}} + I_{\mathrm{DA}} - (c_{\mathrm{leak}} \cdot I_{\mathrm{DD}} + c_{\mathrm{dir}} \cdot I_{\mathrm{AA}})}{\gamma \cdot I_{\mathrm{DD}} + I_{\mathrm{DA}} + I_{\mathrm{AA}} - (c_{\mathrm{leak}} \cdot I_{\mathrm{DD}} + c_{\mathrm{dir}} \cdot I_{\mathrm{AA}})} \qquad \textbf{Equation 52}$$

where *I* is the average fluorescence intensity before the first bleaching event. The indices DD and DA denote donor and acceptor detection after donor excitation, respectively. The index AA denotes acceptor detection after acceptor excitation, c_{leak} is the correction factor for donor leakage, c_{dir} is the correction factor for direct excitation and γ is the detection correction factor. Note, that no β-correction was applied as the software does not support this function.

6.9.1 Calculation of correction factors

The iSMS correction tool calculates correction factors from individual time traces. Donor leakage occurs when the donor emission is detected in the acceptor channel as a result of incomplete spectral separation. The correction factor c_{leak} is calculated from fluorescence intensity-time traces showing acceptor photobleaching as (Figure 26b):

$$c_{\mathrm{leak}} = \frac{I_{\mathrm{DA,t2}}}{I_{\mathrm{DD,t2}}} \qquad \textbf{Equation 53}$$

Where $I_{\mathrm{DA,t2}}$ denotes the average fluorescence intensity of the acceptor upon donor excitation and $I_{\mathrm{DD,t2}}$ is the average fluorescence intensity of the donor upon donor excitation, each after the acceptor has bleached. Direct excitation of the acceptor occurs when the emission spectrum of the laser used for donor excitation overlaps with the acceptor absorption spectrum.

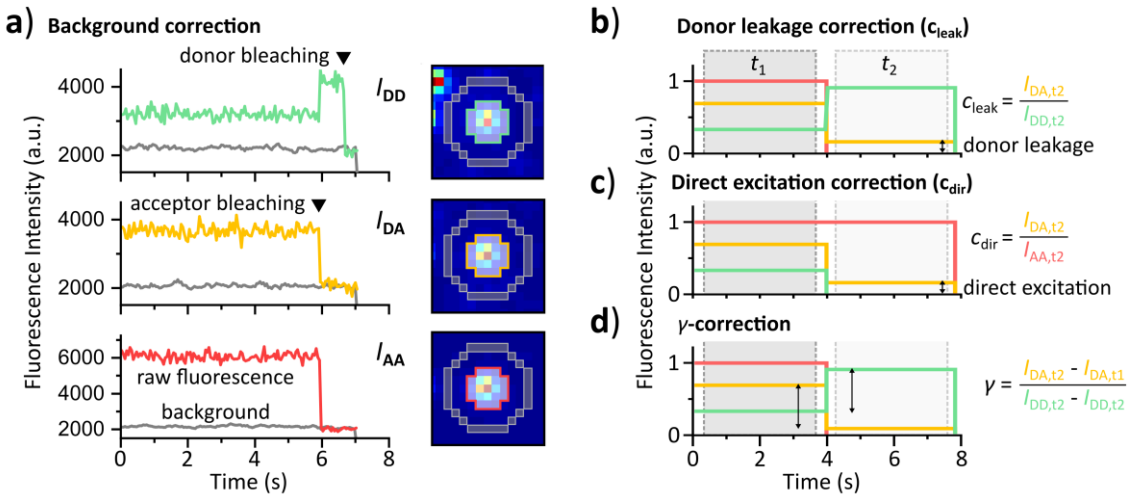

Figure 26: Determination of correction factors for wide-field smFRET experiments. a) Video images of detected single molecule spots showing donor and acceptor fluorescence and the resulting fluorescence intensity-time trace. Raw fluorescence intensity was calculated as the average of a 21 pixel set (colored border) that approximates the point spread function of the emission. Background signal was calculated from blank pixels with a 2 pixel distance to the molecule spot (grey border). **b)** Donor leakage correction, **c)** Direct excitation correction, **d)** γ correction. I_{DA}, I_{DD} and I_{AA} denote the average fluorescence intensity of the acceptor upon donor excitation, donor upon donor excitation and acceptor upon acceptor excitation, respectively. The average intensity before (t_1) and after (t_2) after photobleaching is indicated by subscripts. Arrows indicate the intensity profiles used for calculation.

The correction factor c_{dir} is calculated from individual fluorescence intensity-time traces showing donor photobleaching as (Figure 26c):

$$c_{\mathrm{dir}} = \frac{I_{\mathrm{DA,t2}}}{I_{\mathrm{AA,t2}}} \qquad \textbf{Equation 54}$$

where $I_{AA,t2}$ is the average fluorescence intensity of the donor upon donor excitation after the donor has bleached. Additionally, the γ factor corrects for differences in detection of the donor and acceptor fluorophores and is given by:

$$\gamma = \frac{\Phi_{\mathrm{A}} \cdot \eta_{\mathrm{A}}}{\Phi_{\mathrm{D}} \cdot \eta_{\mathrm{D}}} \qquad \textbf{Equation 55}$$

where Φ and η are the quantum yields and detection efficiencies of the donor (D) and acceptor (A) fluorophores, respectively. Experimentally, the factor can be determined from fluorescence intensity-time traces showing acceptor photobleaching (Figure 26d) as:

$$\gamma = \frac{I_{\mathrm{DA,t2}} - I_{\mathrm{DA,t1}}}{I_{\mathrm{DD,t2}} - I_{\mathrm{DD,t1}}} \qquad \textbf{Equation 56}$$

Since all excitation events that resulted in FRET should contribute to donor fluorescence after the acceptor has bleached, the ratio of I_{DA} and I_{DD} before (t_1) and after (t_2) bleaching of the acceptor can be used to infer whether detection is biased towards donor ($\gamma < 1$) or acceptor ($\gamma > 1$).

6.9.2 Calculation of FRET efficiency histograms

Traces were manually selected based on quality, i.e. stable signal of the acceptor-only trace (acceptor emission after acceptor excitation), no molecule spots overlapping with the 21 pixel PSF, bleaching of donor or acceptor. Additionally, non-bleaching traces showing FRET efficiency profiles comparable to bleaching traces were considered for analysis. Traces were categorized as either static (if no conformational changes occurred during the video), or dynamic (if at least one transition between different FRET efficiencies was observed). FRET efficiency histograms were calculated in Origin 2019b from all frames of traces with either static FRET efficiency or dynamic switching between states with a stoichiometry value of 0.4–0.6 using a binning range of 0–1 with a bin size of 0.025 (40 bins). Histograms were normalized to the total number of frames and the mean of each bin was calculated for three technical replicates to generate the final histogram. To determine the mean FRET efficiency of each histogram peak, the data were fitted with a Gaussian distribution with a fixed y-offset (y_0) of 0.

6.9.3 Dwell time calculation from FRET efficiency-time traces

FRET efficiency-time traces displaying dynamic switching between different FRET efficiencies were further analyzed to calculate the average dwell time in the respective FRET state. To this end, the traces were fitted with the vbFRET algorithm [397] (integrated in iSMS). The algorithm fits the FRET efficiency time traces using a Hidden Markov Model (HMM), a probabilistic model in which an observed signal, the FRET efficiency, is dependent on an unobserved parameter: the conformation of the DNA. The algorithm fits stretches of similar FRET efficiency to a discrete state of dwell time *t*, effectively removing shot noise (Figure 27a). Generally, traces within the boundaries of the respective FRET efficiency histogram population with at least five transitions were chosen. All dwell times adhering the above criterion were used to calculate the dwell time histogram with Origin 2019b. For the analysis of DNA Holliday junctions, a binning range of 0–3 s with a bin size of 0.1 s was chosen, and for the analysis of TBP dynamics a binning range of 0–5 s and a bin size of 0.2 s was used. Histograms were normalized to a range of 0- 1 and the mean dwell time τ in each fitted state was determined from the fit with a mono-exponential decay function (Equation 57, Figure 27b):

$$N(t) = \mathrm{y0} + \mathrm{A} \cdot \mathrm{e}^{-\frac{t}{\tau}} \qquad \textbf{Equation 57}$$

where $N(t)$ is the occurrence of dwell time t and A is the amplitude of the decay. Information on occurring transitions were visualized in a density plot displaying possible transitions of individual traces or entire data sets (Figure 27c).

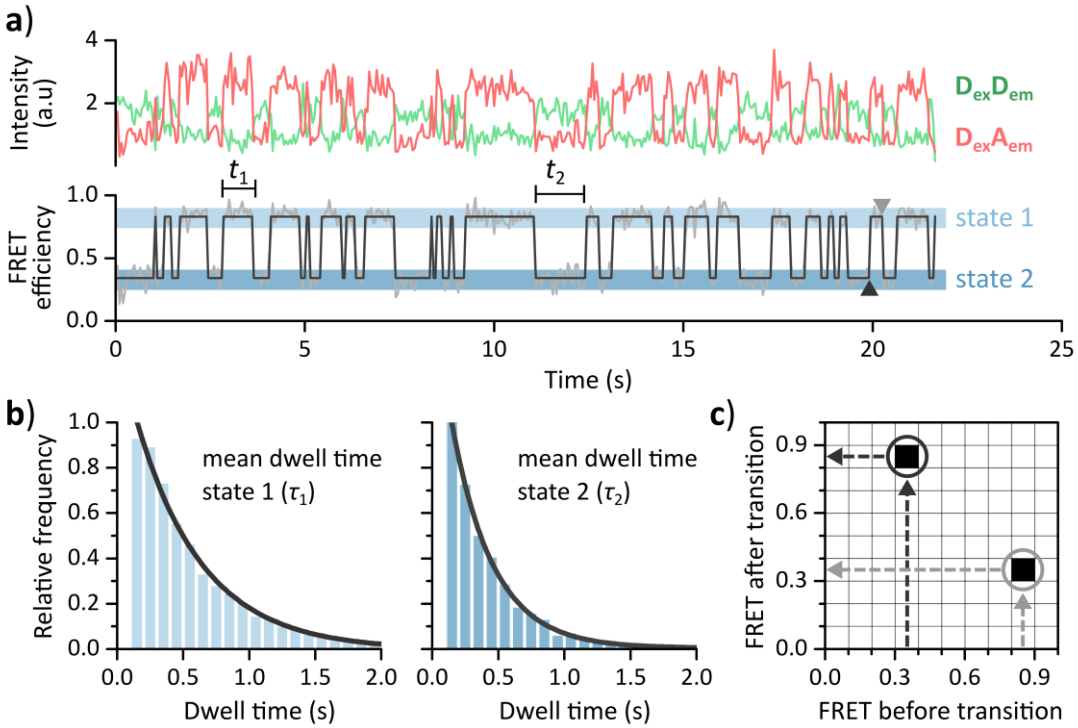

Figure 27: Dwell time analysis of dynamic FRET traces using a hidden Markov model. a) Exemplary fluorescence intensity-time traces showing donor excitation followed by donor emission ($D_{ex}D_{em}$, green) and acceptor emission ($D_{ex}A_{em}$, red) and the resulting FRET efficiency (gray) fitted with a two-state hidden Markov model (black). The two fitted states are highlighted in light/dark blue. **b)** Individual dwell times (*t*) in one state were then counted in a histogram and fitted with a mono-exponential decay (black line) to determine the mean dwell time τ in that state. **c)** Transitions between states were visualized in a density plot showing the relative occurrence of state 1-state 2 (gray arrows) and state 2-state 1 transitions (black arrows); relative occurrence indicated by gray scale from low occurrence (white) to high occurrence (black).

6.10 Construction of a prism-type TIRF microscope

This section covers the key modules of the TIRF microscope setup and provides insight into underlying design-decisions. From an experimental point of view, the construction is focused on smFRET measurements on immobilized proteins and/or nucleic acids. Hence, the microscope is set on an optical table resting on a base with rubber shock absorbers. This confers passive isolation to ambient shocks and vibrations which is serviceable for smFRET experiments. The table breadboard is fitted with a 25 x 25 mm grid of M5 screw threads, which simplifies spacing and installation of components. The setup is divided into three functional units: i) laser-combining, ii) illumination and iii) detection, which will be covered in detail in the following sections (Figure 28, Figure 29).

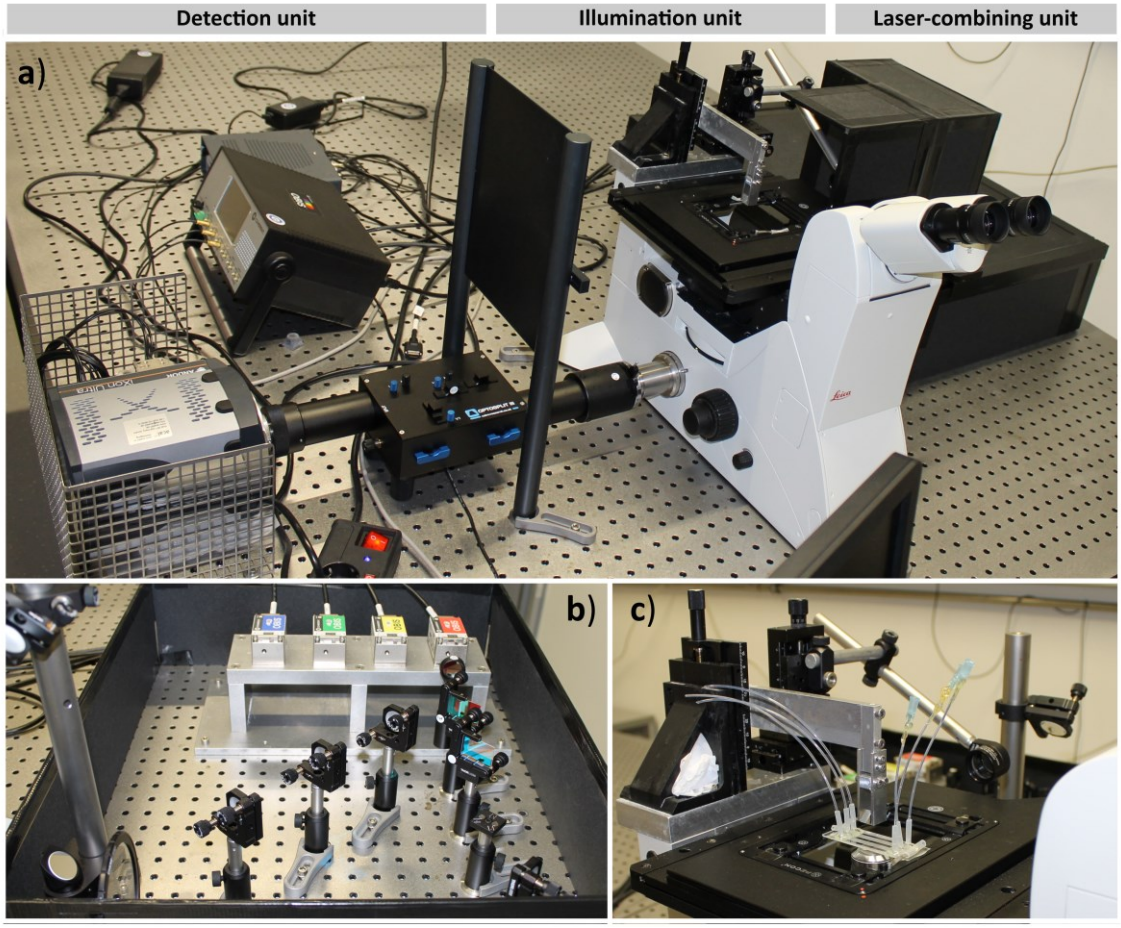

Figure 28: Photographs of the home-build TIRF microscope setup. a) Overview of the entire microscope setup, showing the (right to left): laser-combining unit with the protective enclosure, the illumination unit based on the Leica DMi8 microscope and the detection unit with the beamsplitter and EMCCD camera. **b)** Close-up of the laser-combining unit with the four lasers and beam paths (Chapter 6.10.1). **c)** Close-up of the illumination unit with prism-mount and lense mount (Chapter 6.10.2). A flow chamber is set on the object stage. Photographs were kindly provided by Katharina Lippl, Department of Microbiology, University Regensburg.

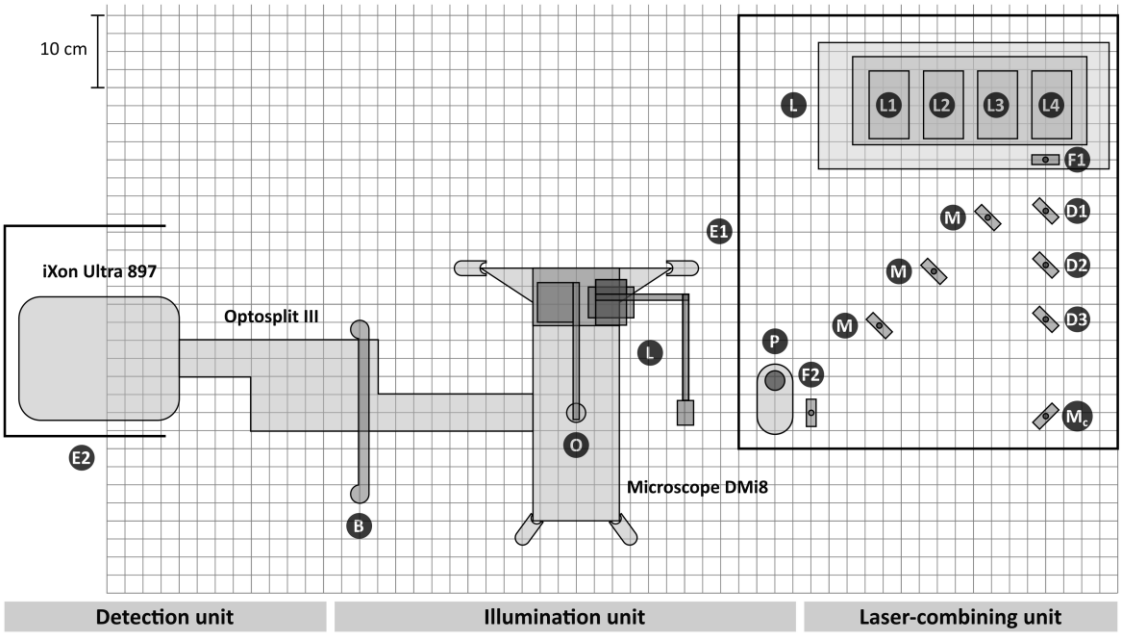

Figure 29: Layout of the home-built TIRF microscope setup. A true to scale top view of all components that were installed on an optical table fitted with a 25 x 25 mm grid of M5 screw threads. (E1) Custom-built enclosure for laser-combining unit. (L) Custom-built laser-mount (Figure 30). Excitation lasers (L1) OBIS 488LS, (L2) OBIS 532LS, (L3) OBIS 561LS, and (L4) OBIS 637LX. (M) Post-mounted dielectric mirrors (Figure 31a). (F1) Post-mounted clean-up filter (Figure 31b). Post-mounted dichroic mirrors (D1) H 568LPXR superflat, (D2) ZT 532RDC, and (D3) ZT 488RDC (Figure 31c). (F2) Post-mounted variable neutral density filter (Figure 31d). (P) Periscope assembly (Figure 31e). (L) Custom-built prism- and lens-mount. (O) water immersion objective HC PL APO 63x/1.20 W CORR CS2, (B) Custom-build beam blocker. (E2) Custom-built enclosure for the EMCCD camera. The DMi8 microscope is fixed on the table using four CF125C/M clamping forks. All components were fixed to the table using M5 screws. The Optosplit III emission beamsplitter is attached to the C-mount of the DMi8. The iXon Ultra 897 EMCCD camera is attached to the C-mount output port of the Optosplit III and rests on a sheet of insulating foam placed directly on the optical table.

6.10.1 Laser-combining unit

This unit houses four lasers that are set on a custom-built aluminum pedestal (Figure 29 L, Figure 30) that elevates them to the height of other optical components (approximately 100 mm) and provides heat conductance through the 175 x 375 mm baseplate. Three diode-pumped solid state lasers allow excitation at 488 nm (Figure 29 L1), 532 nm (Figure 29 L2) and 561 nm (Figure 29 L3) and a diode laser excitation at 637 nm (Figure 29 L4). The 637 nm laser is further cleaned up through a 635/10 narrow band filter (Figure 29 F1, Figure 31b) because of its broad emission spectrum (637 ± 5 nm [398]).

The laser beams are directed via dielectric mirrors (Figure 29 M, Figure 31a) and longpass dichroic mirrors (Figure 29 D1–3, Figure 31c) to converge at mirror M_c. The dichroic mirrors are set up in a sequential manner from 568 nm longpass to 488 nm longpass so that in principal, all four lasers can be combined simultaneously. The dichroic mirrors are installed on magnetic bases to exchange without compromising the overall alignment of the beam path. The beam positions of the lasers L1-L3 can each be controlled with one mirror and one dichroic mirror to provide four degrees of freedom for positioning. L4 functions as a reference laser and can only be controlled with mirror M_c from which all combined beams are directed to the periscope (Figure 29 P, Figure 31e) of the illumination unit. Although the laser power can be controlled via the software,

a variable neutral density filter (Figure 29 F2, Figure 31d) was installed in the beam path for immediate control of the laser intensity. For safety, the entire laser-combining unit and the periscope are housed within an enclosure constructed of laser absorbing hardboard plates (Figure 29 E1).

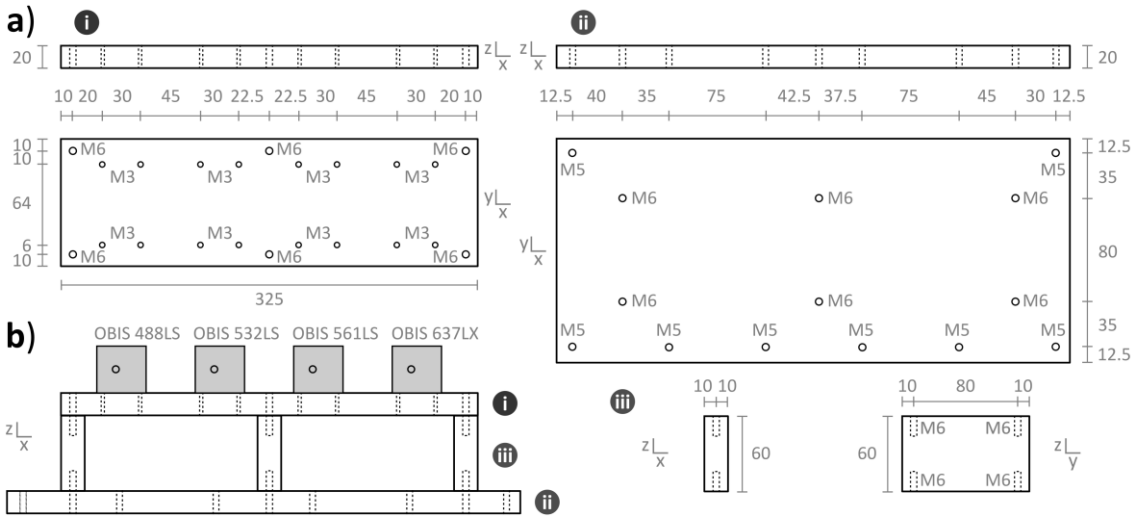

Figure 30: Construction plan of the laser-mount. a) (i) Top plate, (ii) connector bars, and base plate. **b)** Front view (xz) of the finalized assembly. Custom-built components are depicted in white and labeled according to **a)**. Commercial components are depicted in gray and labeled according to Table 8. All lengths are indicated in millimeters. All components were assembled using the designated screws. Custom-made aluminum components were produced by the workshop of the Faculty of Biology and Preclinical Medicine, University Regensburg.

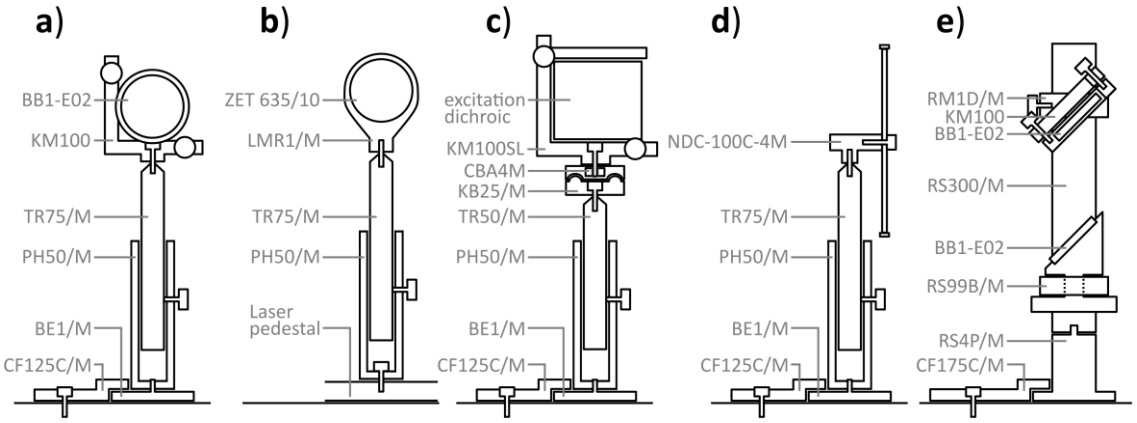

Figure 31: Assembly of post-mounted optical components. Schematics of **a)** post mounted dielectric mirrors, **b)** post-mounted excitation filters, **c)** post-mounted variable neutral density filters, **d)** post-mounted dichroic mirrors and **e)** periscope assemblies. All components are labeled according to Table 8.

6.10.2 Illumination unit

The periscope is used to direct the excitation beam upwards at a 90° angle to reach the height of the microscope object stage. The upper mirror is used to direct the light towards the prism at the angle required for total internal reflection. The core of the illumination unit consists of a commercial Leica DMi8 inverse microscope body fitted with a left-side C-mount as the emission output. The illumination turret is replaced with a prism- and lens-mount (Figure 29 L, Figure 32) to enable total internal reflection at the sample chamber.

The mounts are set on a custom-built aluminum base (Figure 32a i) that attaches to the default illumination turret holder of the DMi8 on which the other components are installed.

The lense-mount (Figure 32d) consists of a xyz-translation stage to adjust the lense position during use and the attachment rods that are used to position the lense in the beam path so that the beam is focused directly above the microscope objective (O). Varying the x-axis position of the lense to be out-of-focus (focal length: 150 mm) is utilized to adjust the size of the illumination area. Varying the xy-axis position of the lense provides control over the positioning of the illumination area within the field of view.

The prism-mount (Figure 32c) features a clamp construction with two side-plates (Figure 32a iv, v, vi), which stabilize the prism between two Parafilm sheets. The clamp is connected to the main-arm (Figure 32a iii) which is attached to a precision x-translation stage to facilitate up- and down movement of the prism. At installation, the wide drillings for M2.5-screws in the side plates and for M5-screws in the main-arm are used to position the central axis of prism above the objective.

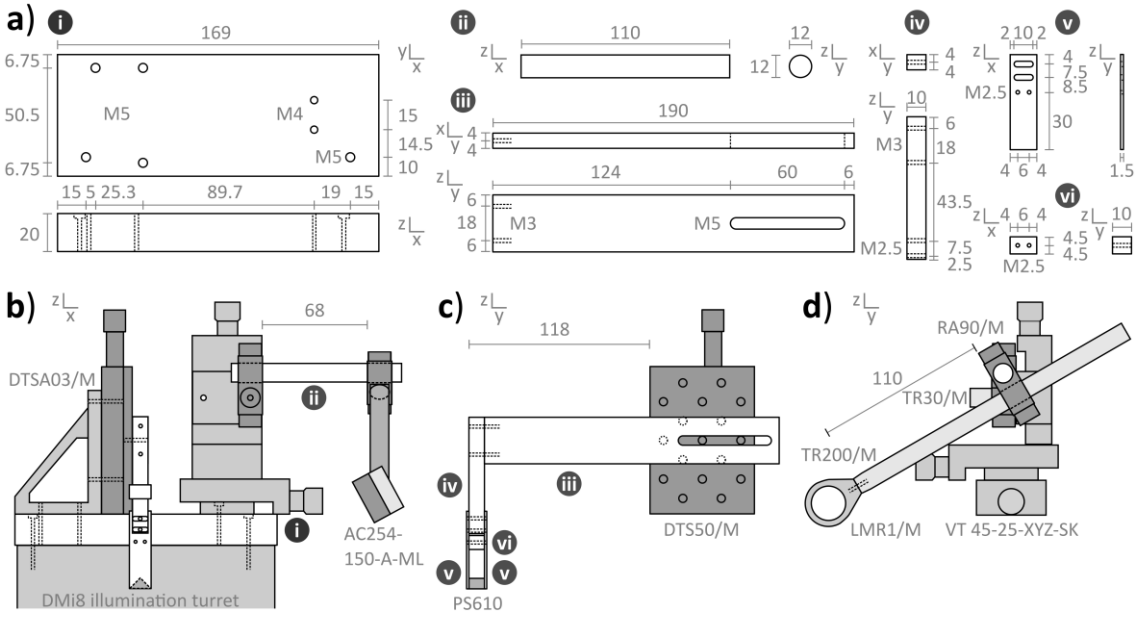

Figure 32: Construction plan of the prims- and lense-mounts. a) (i) base plate for the attachment to the DMi8 illumination turret. (ii) connection rod for the lense-mount. (iii) Main-arm, (iv) attachment-arm, (v) side-plates, and (vi) connector of the prism-mount. The prism is fixed between the side-plates with para-film. **b)** Front (xz) view of the complete assembly. Side view (yz) of **c)** the prism mount and **d)** the lense-mount. Custom-built components are depicted in white and labeled according to a). Commercial components are depicted in gray and labeled according to Table 8. All lengths are indicated in millimeters. All components were assembled using the designated screws. Custom-made components were produced by the workshop of the Faculty of Biology and Preclinical Medicine, University Regensburg.

In order to achieve total internal reflection at the sample chamber, the upper mirror of the periscope directs the excitation beam to hit the prism front side at a height of approximately 1 mm with a 37° angle of incidence with respect to the prism plane normal (Figure 33). This can be achieved with a 265 mm distance between the prism and the periscope and a 35 mm height difference. The beam is thus refracted at a 25° angle at the air/quartz interface.

A thin layer of glycerol is used to connect the prism to the quartz slide of the sample chamber to create a uniform light guide (refractive index n_{quartz} = 1.46, $n_{glycerol}$ = 1.47 [399,400]). The excitation beam reaches the quartz/buffer interface at a 72° angle of incidence, which is greater than the critical angle $\Theta_{critical}$ = 65° and is thus the beam is totally internally reflected. This configuration allows for sample buffers with a refractive index of up to 1.38 which is equivalent to a glycerol content of up to 35% [401]. Sodium chloride increases the refractive index of a water/NaCl solution by approximately 0.02 per 1 M of NaCl [402]. For most experiments, the NaCl concentration was in the range of 50–100 mM and can be neglected. The resulting evanescent field reaches approximately 110–130 nm into the sample chamber (Chapter 2.1.3) and primarily excites molecules immobilized on the surface of the quartz slide. The resulting fluorescence is transmitted through the sample chamber and collected by a water immersion objective HC PL APO 63x/1.20 W CORR CS2 and guided to the C-mount output port via the integrated optics of the DMi8. The objective is corrected for chromatic aberrations, which result from the different refractive behavior of light of different wavelengths. In essence, this shifts the xy-position of donor and acceptor channel images which interferes with exact alignment of the channels.

For safety, a beam blocker (Figure 29 B, Figure 34) is installed opposite of the periscope to capture the excitation beam exiting the prism. A commercial multi-layered stack of black aluminum sheets absorbs the main beam and an additional back wall of black anodized aluminum blocks diffuse reflections that may be caused by impurities in the glycerol.

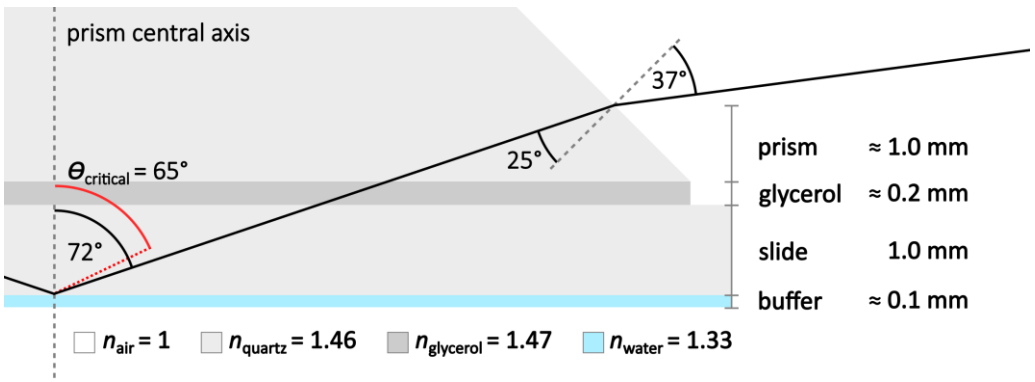

Figure 33: Total internal reflection at the prism/sample interface. The beam path of the laser (solid line) and the angle of refraction in relation to the plane normal (dashed line) are shown. The laser hits the air/prism interface at a height of approximately 1 mm above the microscope slide at an incident angle of 37° and is refracted towards the planed normal. The angle of incidence at the slide/buffer interface is 72° > $\Theta_{critical}$ = 65° (red) resulting in the total internal reflection of the beam. The refractive indices *n* and the layer thickness of the propagation materials are indicated by color. No refraction was calculated for the

quartz/glycerol interface due to the negligible difference of the refractive indices.

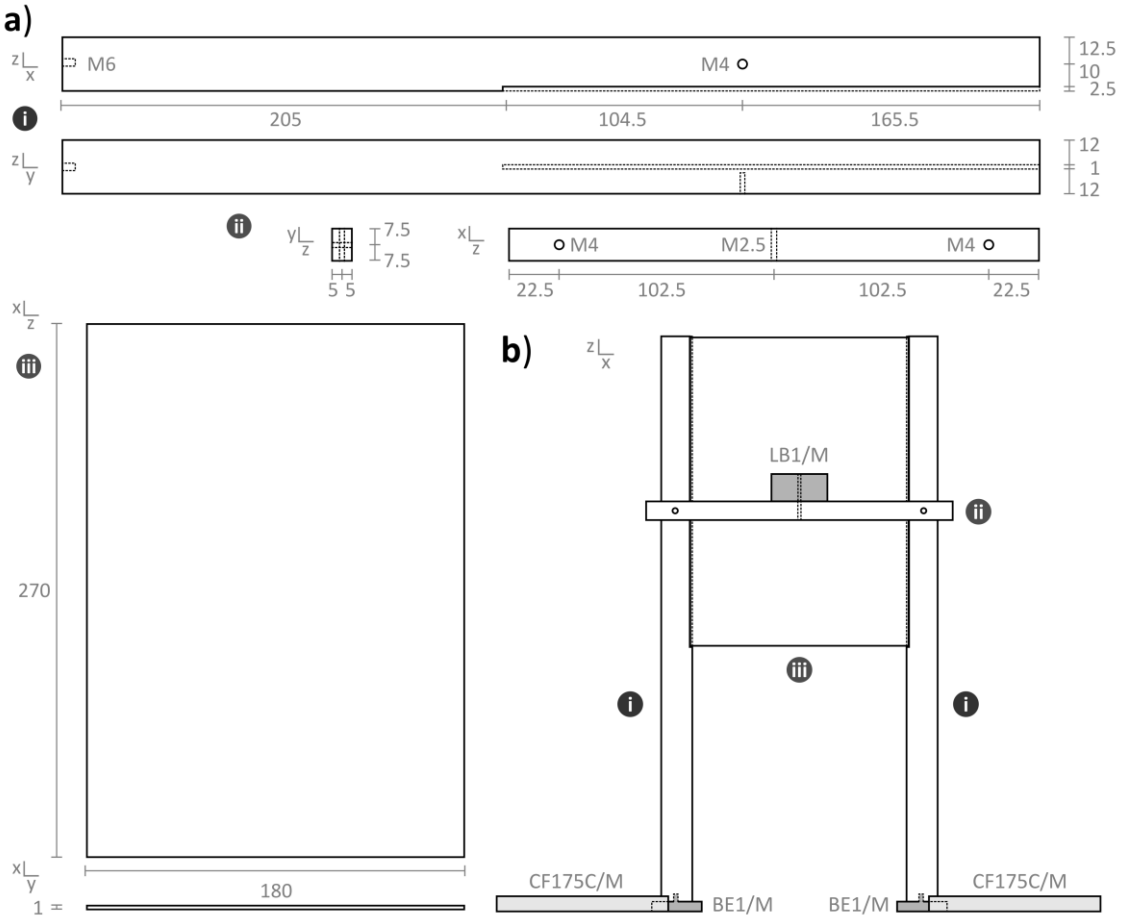

Figure 34: Construction plan of the beam blocker assembly. a) (i) Post, (ii) mounting-bar for beam blocker, (iii) back wall. **b)** Front (xz) view of the finalized assembly. Custom components are depicted in white and are labeled according to (a). Commercial components are depicted in gray and labeled according to Table 8. All lengths are indicated in millimeters. All components were assembled using the designated screws. Custom-made aluminum components were produced by the workshop of the Faculty of Biology and Preclinical Medicine, University Regensburg. All components are anodized in matte-black to minimize reflectivity.

6.10.3 Detection unit

The emission light is collected by the Optosplit III emission beamsplitter that is attached to the C-mount output port of the DMi8 and integrates all components for cropping of the emission and for spectral separation of donor and acceptor fluorescence. Light entering the Optosplit III is focused on a set of apertures to adjust the section of the recorded image. This is critical when multiple spectrally separated images are projected onto the same camera chip for detection. The Optosplit III supports the separation of up to three emission channels. However, for experiments conducted in this work only two channels were used simultaneously. The two-channel configuration of the Optosplit III will be explained for the ATTO 532/ATTO 647N fluorophore pair that was used for most FRET measurements (Figure 35).

A 640 nm longpass dichroic mirror reflects both, the donor excitation laser (532 ± 2 nm) and the ATTO 532 fluorescence (emission maximum: 552 nm). Additionally, the acceptor excitation laser (637 ± 5 nm) is partially reflected. For the donor detection channel, a 582/75 bandpass filter limits

the detection window to only include the ATTO 532 fluorescence (Figure 35 top). Congruently, the wavelengths transmitted by the dichroic mirror include the acceptor excitation laser and the ATTO 647N fluorescence (emission maximum: 664 nm). A 645 nm longpass filter (note: the filter is labeled as 635 LP by the supplier) is used to exclude the excitation light from the acceptor detection channel. Additionally, a minor part of the ATTO 532 emission is also transmitted by the chosen filter (Figure 35 bottom). This is acceptable as the spectral crosstalk can be corrected during data analysis (Chapter 6.9.1) and excluding this section of the spectrum would omit the emission peak of ATTO 647N. The final mirrors in each beam path of the Optosplit III can be rotated to adjust the position of each image on the detector, a back illuminated EMCCD camera iXon Ultra 897. The camera features a 512 x 512 pixel detector (pixel size 16 µm) and allows for detection at up to 56 frames per second when the full detector is used. This is equivalent to an 18 ms time resolution, suitable for many biological processes. To reduce background noise generated from internal electronics (darkcurrent), the camera is cooled to -80 °C during use via an integrated thermoelectric cooling system. A main feature of the camera, the electron multiplier (EM) gain, enables high detection sensitivity at high readout speed. Owing to the high brightness of the used fluorophores, only a moderate EM gain of 30 was set for all experiments. However, for experiments involving fluorescent proteins (also performed with this microscope setup), which are considerably dimmer than organic fluorophores, a higher EM gain (200–300) should be used. Due to space constrains, the camera is placed directly on the optical table on a thin Styrofoam sheet in a sideways manner. To protect the camera, a custom-built enclosure from perforated steel plate (Figure 29 E2) was installed.

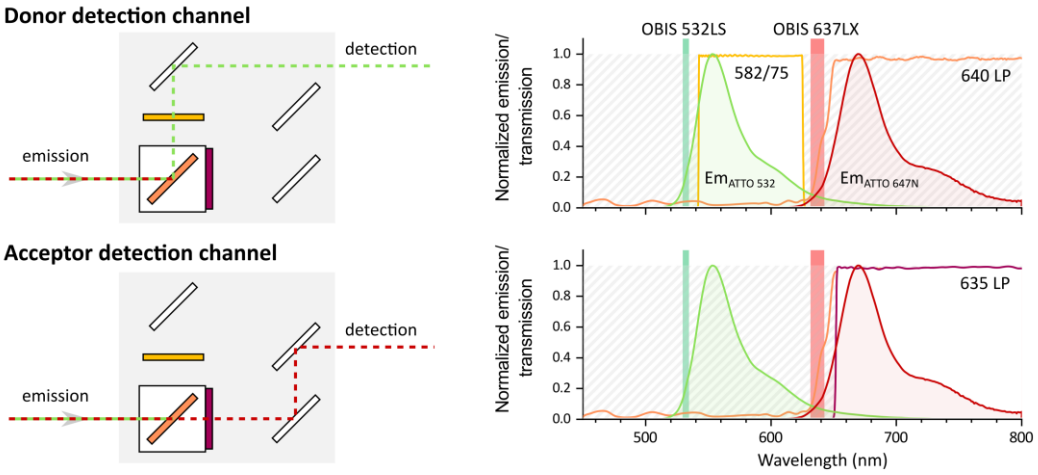

Figure 35: Emission detection channels for ALEX experiments. The filter configuration for the Optosplit III emission beam splitter enables the separate detection of the emissions of the FRET donor/acceptor fluorophores ATTO 532 ($Em_{ATTO\ 532}$) and ATTO 647N ($Em_{ATTO\ 647N}$) after alternating excitation at 532 nm and 637 nm. The normalized transmission of the applied filters and normalized emission of the fluorophores and lasers, as well as the transmitted (white) and non-transmitted (grey strikes) spectra are plotted against the wavelength. Dichroic mirrors and bandpass/longpass filters are color coded: HC BS 640 imaging (orange), 582/75 BrightLine HC (yellow), 635 LP Edge Basic (purple) [398,403].

6.10.4 Control of electronic devices

Electronic devices were set up to be controllable from the desktop workstation via the appropriate software:

All lasers used in an experiment were coupled to the OBIS LX/LS Scientific Remote which is connected to the workstation via USB 2.0. This allows remote control of e.g. laser power and operation mode (continuous wave/digital modulation) via the Coherent Connection software. The OBIS LX/LS Scientific Remote is additionally connected to the Multistream, which interfaces the camera trigger signal with the laser control and allows the execution of ALEX (Chapter 6.8.1). The Multistream does not support connection to a workstation and has to be controlled manually. The EMCCD camera is connected to the workstation via a USB 2.0 port and all functions are controlled by the Andor Solis software e.g. cooling, live view of the sample and video acquisition.

7 Results

7.1 Conformational dynamics of DNA Holliday junctions

In this chapter, measurements on immobilized DNA Holliday junctions (HJ) were performed as a proof of concept to assess the performance of the home-built TIRF microscope in time resolved smFRET experiments. The HJ is a four-stranded DNA intermediate formed during genetic recombination, e.g. in a crossing-over event during meiosis or double-strand break repair [404–406]. The structure is formed by two homologous dsDNA molecules that are joined by a single-strand crossover resulting in a four-way dsDNA junction (Figure 36a). Upon formation, two types of structural dynamics determine the outcome of the recombination event: i) branch migration, whereby the heteroduplex region shifts or extends along the strands, which determines the length of the genetic overlap [407–409] and ii) conformer exchange between structural isoforms through base-stacking interactions [410,411]. Junction resolving enzymes can recognize and resolve these intermediates [412–414]. Which conformational isoform is bound by junction resolving enzymes (e.g. by RuvC) dictates whether enzyme-mediated cleavage of the junction includes or excludes the flanking parental DNA sequences [415]. The conformer dynamics are also influenced by metal ions [410,416]. In the absence of metal ions, repulsion between phosphate groups of the DNA enforces a four-fold symmetric structure with an open center, hence termed open conformation [417]. Upon addition of metal ions (e.g. Mg^{2+}), the structure folds into an "X"-shape by coaxial pairwise stacking of the arms [418–420]. Depending on sequence, a junction can adopt two possible stacked structures.

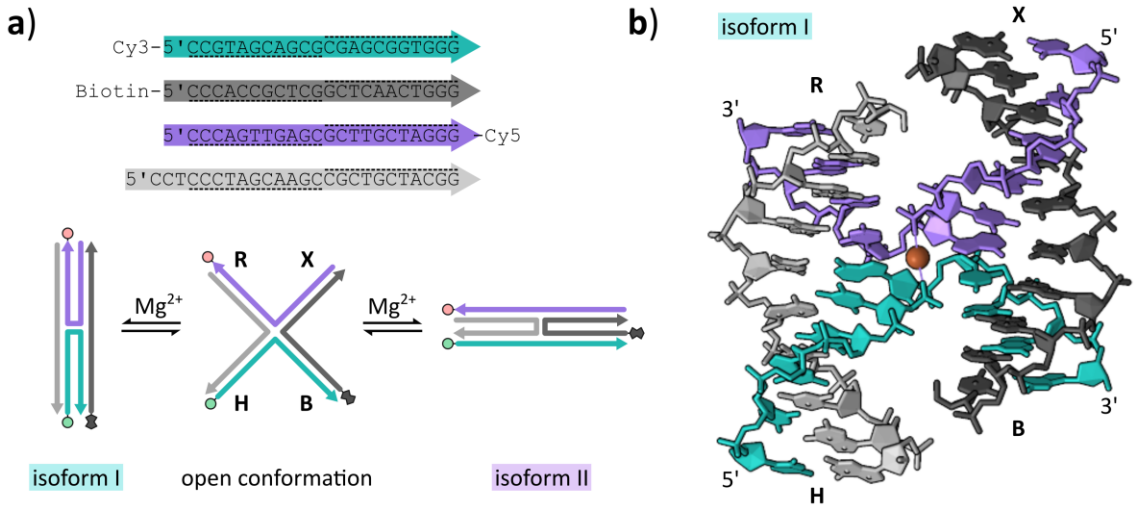

Figure 36: Sequence and structure of a synthetic DNA Holliday junction. a) Nucleotide sequences of the four synthetic oligonucleotides. DNA modifications of the oligonucleotides engineered to enable TIRF-based single-molecule FRET measurements are shown. Underlying colored arrows represent 5'–3' directionality. Dashed sequences base-pair with each other. Schematic representation of conformational isoforms of the Holliday junction. In the absence of metal ions (e.g. Mg^{2+}), the junction is in the open conformation. Addition of metal ions stabilizes the stacked conformations isoform I and II. DNA modification depicted as: Cy3 (green circle), Cy5 (red circle), biotin (gray octagon). **b)** X-ray crystal structure of a stacked Holliday junction isoform (PDB: 1DCW) adopting isoform I. A coordinated Na^{+} ion is colored in brown. Note that the 3 nt 5'-overhang of strand 4 (light gray) is irrelevant for the experiments shown.

In isoform I, arm B is stacked with arm H, whereas in isoform II, arm B is stacked with arm X (Figure 36a, b) [410]. The conformational dynamics of this structure and its impact on genetic recombination have been subject to extensive studies, and smFRET measurements played a pivotal role in this endeavor owing to their unparalleled ability to dissect non-synchronizable dynamics [407,409–411,416,421]. In turn, the HJ presents an ideal model system for smFRET experiments due to highly recognizable differences between structural isoforms and conveniently tunable dynamics, and is frequently used as such[6,94,407,422–424]. Since the following experiments do not present new data they are only briefly discussed in parallel to the results and will not be revisited in the discussion section.

7.1.1 Magnesium-dependent conformational dynamics of DNA Holliday junctions

A synthetic HJ was assembled from four strands of 22–25 nt length resulting in a junction with four 11 nt double-stranded helical arms. Sequences were chosen to prevent conformational bias and branch migration[410]. The donor fluorophore Cy3 and the acceptor Cy5 where coupled to the 5'-end of the H arm and 3'-end of the R arm, respectively to monitor the conformational state of the junction via FRET. The pre-annealed DNAs were immobilized on the surface of a biotin-PEG coated TIRF flow chamber via the biotin coupled to the 5'-end of the B arm (Figure 37a). Fluorescence intensity-time traces were recorded for a Mg^{2+}-concentration range from 0- 200 mM. In the absence of Mg^{2+} ions, recorded traces show exclusively static FRET efficiency (Figure 38a) and the resulting FRET efficiency histogram has a single peak centered at E = 0.47 with a relatively broad distribution (FWHM = 0.24), indicating that the HJ adopts an open conformation (Figure 38b). Upon addition of 10 mM Mg^{2+} ions (Figure 38b), traces show noticeable switching between two FRET efficiency states (Figure 38a). Accordingly, the resulting histograms show two mostly overlapping populations centered at E_I = 0.33 and E_{II} = 0.67 with approximately equal width as the open conformation showing a FWHM of 0.25 and 0.23, respectively. This confirms that the Mg^{2+} ions stabilize the two stacked conformations, isoform I and II by masking the positive charges of the phosphate backbone at the center and thus enable greater proximity between strands [410].

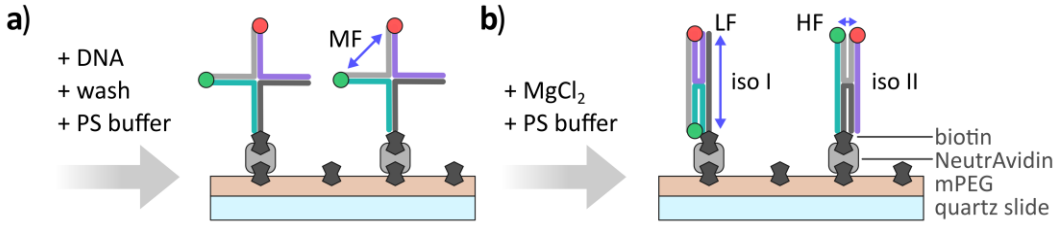

Figure 37: Experimental setup for smFRET analysis of DNA Holliday junction dynamics. a) Synthetic DNA Holliday junctions modified with a donor (Cy3, green) and acceptor (Cy5, red) fluorophore and biotin (gray octagon) were flushed into the sample chamber and immobilized on the mPEG-passivated quartz microscope slide via biotin-NeutrAvidin coupling. Excess DNA was washed off and dyes were stabilized by addition of photo-stabilization (PS) buffer. In the absence of metal ions, medium FRET (MF) can be measured between the conjugated fluorophores. **b)** $MgCl_2$ addition to the sample chamber induces formation of stacked conformations, identifiable by a change in FRET efficiency to either low (LF) or high FRET efficiency (HF).

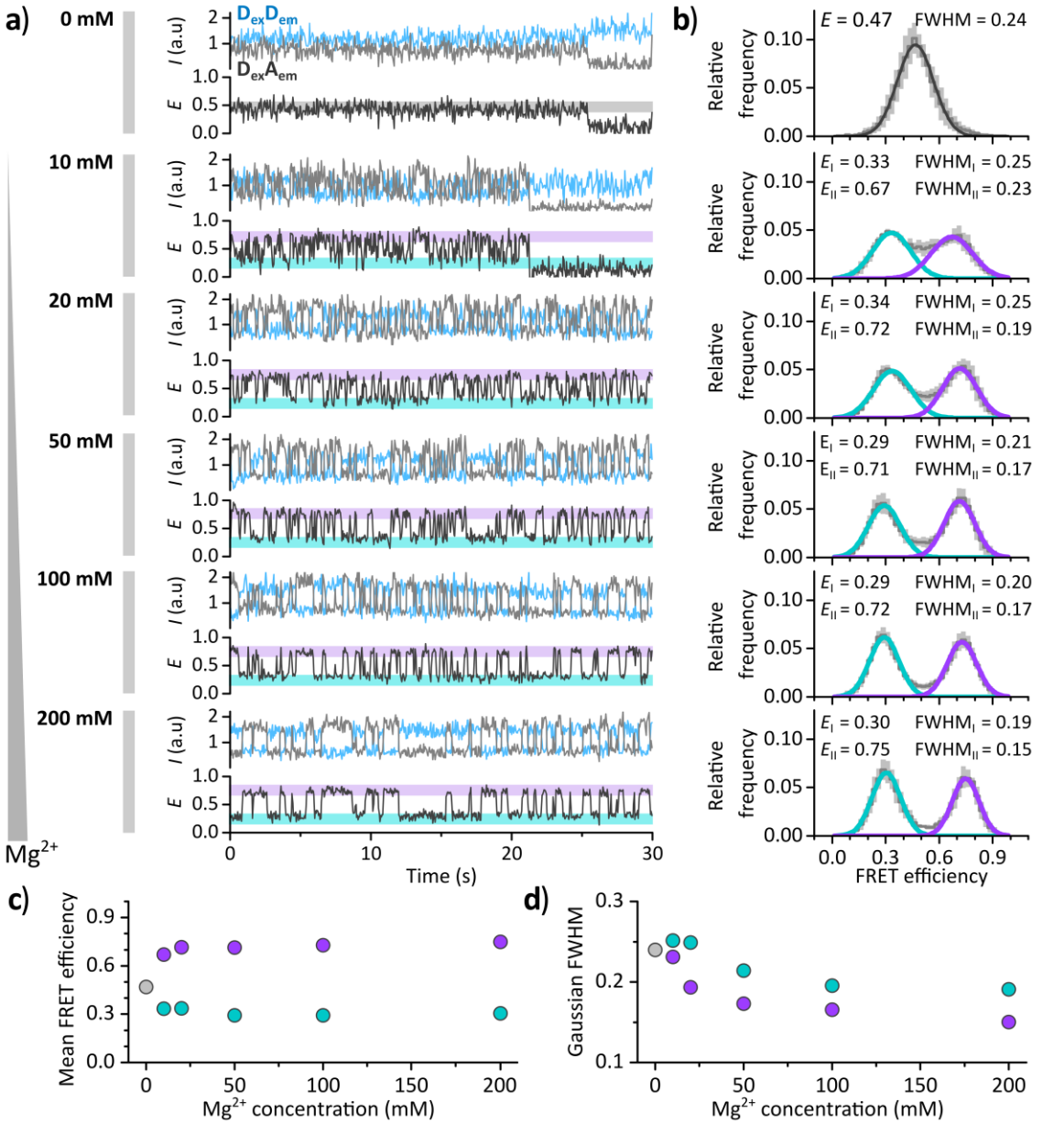

Figure 38: Magnesium dependent conformational dynamics of DNA Holliday junctions. The fluorescence signal of single immobilized HJs at varying $MgCl_2$ concentrations from 0- 200 mM was analyzed using single-molecule sensitive TIRF microscopy. The FRET efficiency reports on the conformational state of the HJ; low FRET efficiency: isoform I (teal), medium FRET efficiency: open conformation (dark gray), high FRET efficiency: isoform II (purple). **a)** Representative fluorescence intensity (*I*)-time traces show donor emission upon donor excitation ($D_{ex}D_{em}$, blue) or acceptor emission after donor excitation ($D_{ex}A_{em}$, gray) and the resulting FRET efficiency (*E*, black). **b)** FRET efficiency histograms of all static (0 mM) or dynamic traces. The mean FRET efficiency (dark gray) and standard deviation (gray) of five independent experiments are shown. Histograms were fitted with a Gaussian distribution to determine the mean FRET efficiency of the individual populations. **c)** Overview of peak mean FRET efficiencies and **d)** full-width half maxima (FWHM) as a function of Mg^{2+} concentration. See Appendix C.1. for molecule counts and fit parameters.

Further Increase of the Mg^{2+} concentration to 20 mM reduced the interconversion rate of states observed in fluorescence time traces. The isoform II population becomes more defined ($FWHM_{II}$ = 0.19) and the peak center diverges from the position of the open conformation (E_{II} = 0.71) while the isoform I population remains relatively unchanged (E_I = 0.34, $FWHM_I$ = 0.19, Figure 38b).

This trend continues and is further enhanced by Mg^{2+} addition up to 200 mM with FRET efficiencies of isoform II population diverging from the FRET efficiency of the open state and becoming increasingly defined and stabilizes at E_{II} = 0.73 with a $FWHM_{II}$ = 0.15 (Figure 38c, d). Concurrently, the peak center of isoform I also diverges from the open state position and becomes more defined with a final mean FRET efficiency of E_I = 0.29 and a $FWHM_I$ = 0.18. Stabilization of the isoform, however, requires higher Mg^{2+} concentrations than observed for isoform II (Figure 38c, d). An increase in the FRET efficiency of isoform II has be observed in previous smFRET studies of HJs [423] and likely results from improved screening of backbone charges at the center resulting in closer distance between the FRET pair. Additionally, similar dynamics occur in DNA hairpin structures that switch between zipped and unzipped conformations on the sub-millisecond timescale and stabilize in the zipped conformation at higher salt concentrations. Potentially, the 3 nt overhang of the R-arm interacts with the H-arm in isoform II through base stacking and thus slightly stabilizes this conformation[425].

7.1.2 Kinetics of isoform I–isoform II conformational dynamics

In order to extract further quantitative information on the conformational dynamics, recorded traces were fitted with a HMM that assigns FRET efficiencies to discrete states. Based on the obvious isoform I-II dynamics, this fit was initially performed for exactly two states to determine the dwell times in both stacked conformations. To this end, the frequency of each dwell time in isoform I and II were separately counted in a histogram and fitted with a mono exponential decay to calculate the mean dwell time τ in the respective state (Figure 39a). This analysis reveals that the respective mean dwell times for both isoforms are nearly identical at all Mg^{2+} concentrations, differing at most by 8%. Furthermore, τ increases with addition of Mg^{2+} ions to the sample buffer from τ = 0.18 s at 10 mM to $\tau \approx$ 0.75 s at a concentration of 200 mM.

In addition, density plots of all recorded transitions were calculated for the full Mg^{2+} concentration range providing an overview of possible directions for state transitions. Here, all transitions occurred between two states, as pre-defined by the two-state HMM. The plots also visualize the decreasing width of the density distribution with increasing Mg^{2+} concentration, a trend already observed in the FRET efficiency histograms. At 200 mM Mg^{2+}, transitions occur exclusively between two well defined states with $E \approx 0.35$ and $E \approx 0.75$ (Figure 39b). Consequently, on a macroscopic level, there is no conformational bias between both isoforms, which relates to the choice in HJ sequence. A preference for one isoform depends primarily on the central three nucleotides of each arm [426]. It has been demonstrated before that the sequence used in this work is not biased to either isoform I or II [410,423,426], which was faithfully reproduced in the above experiments. In direct comparison to previous smFRET experiments that quantified the dwell times of stacked conformations (Figure 40), the above data display slightly longer dell times in both isoforms but follow the general trend of increasing dwell time with increasing Mg^{2+} concentration as well as the equal distribution of conformers. McKinney *et al*. included 2-mercaptoethanol in their measurement buffers, which could potentially cause acceptor blinking and thus reduce apparent dwell times [389].

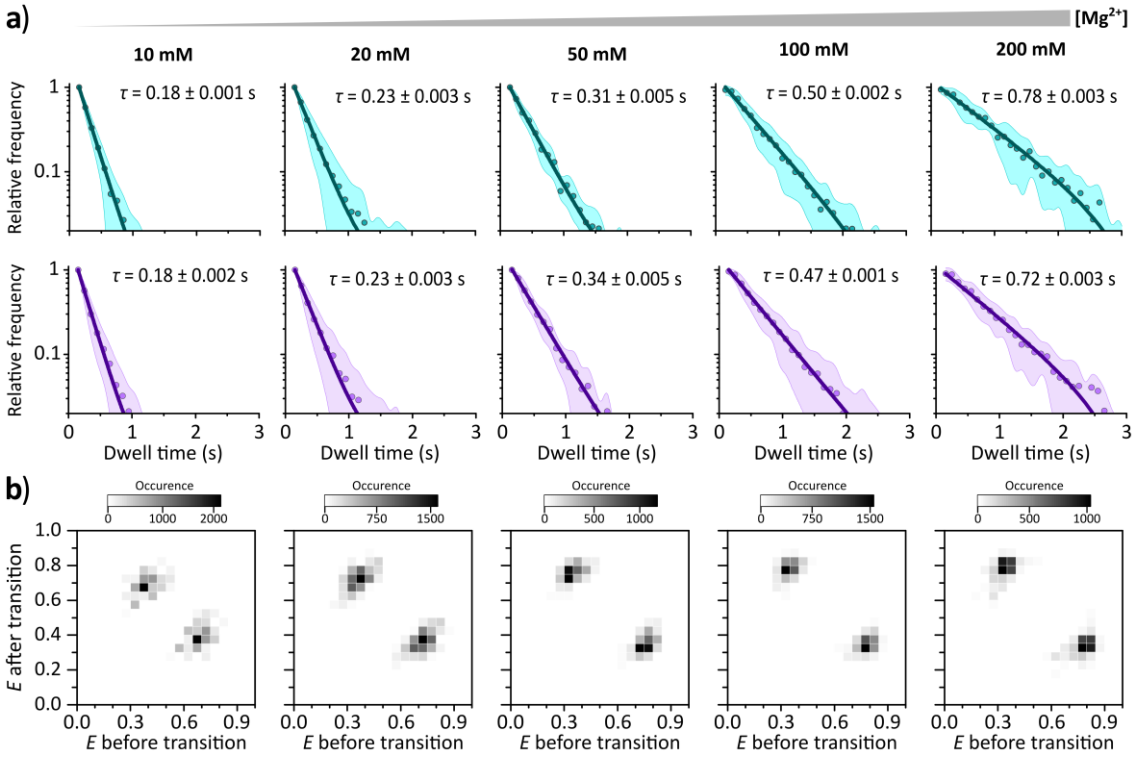

Figure 39: Kinetics of isoform I–isoform II conformational dynamics. Fluorescence intensity-time traces of DNA HJs at different Mg^{2+} concentrations were fitted using a Hidden Markov Model (HMM) limited to two states. The FRET efficiency states determined by the HMM were assigned either to isoform I (teal) or II (purple). **a)** The mean dwell time τ in either state was determined by fitting the relative occurrence of each dwell time with a mono-exponential fit. Mean ± standard deviation (dots, colored area) of five independent experiments are shown. **b)** transition density plots visualize the occurrence of transitions between states of different FRET efficiency *E* color-coded from no occurrence (white) to high occurrence (black). See Appendix C.1. for molecule counts and fit parameters.

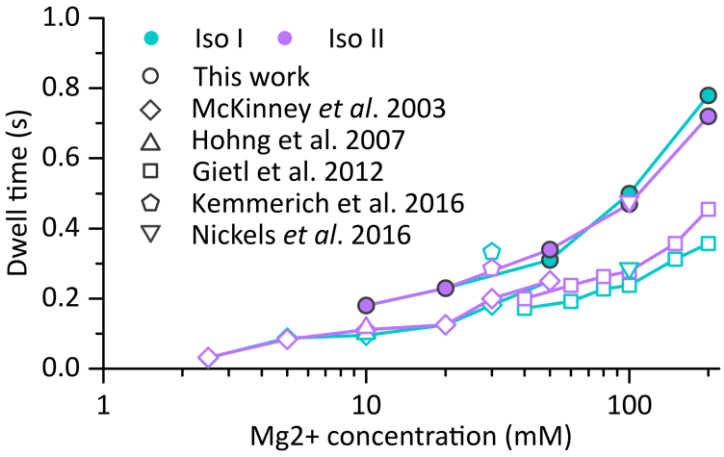

Figure 40: Comparison of Holliday junction conformer kinetics between independent studies. Dwell time data for isoform I (Iso I) and isoform II (Iso II) as a function of Mg^{2+} concentration retrieved from different smFRET studies [6,94,410,427,428] and comparison to data generated in this work. Please note, Nickels *et al*. utilized a HJ integrated into a DNA origami force clamp that is biased towards one conformation.

Single-molecule techniques, however, offer further insight into the behavior of individual molecules. A separate analysis of the relative high FRET state occupancy for each trace reveals a considerable degree of heterogeneity between traces (Figure 41a). On the one hand, the median HF occupancy of approximately 0.50 is quite stable and half of all traces fitted with an HMM exhibit a HF occupancy between 0.42 and 0.58. Samples at medium Mg^{2+} concentrations (20–50 mM) seem to display a slightly broader distribution.

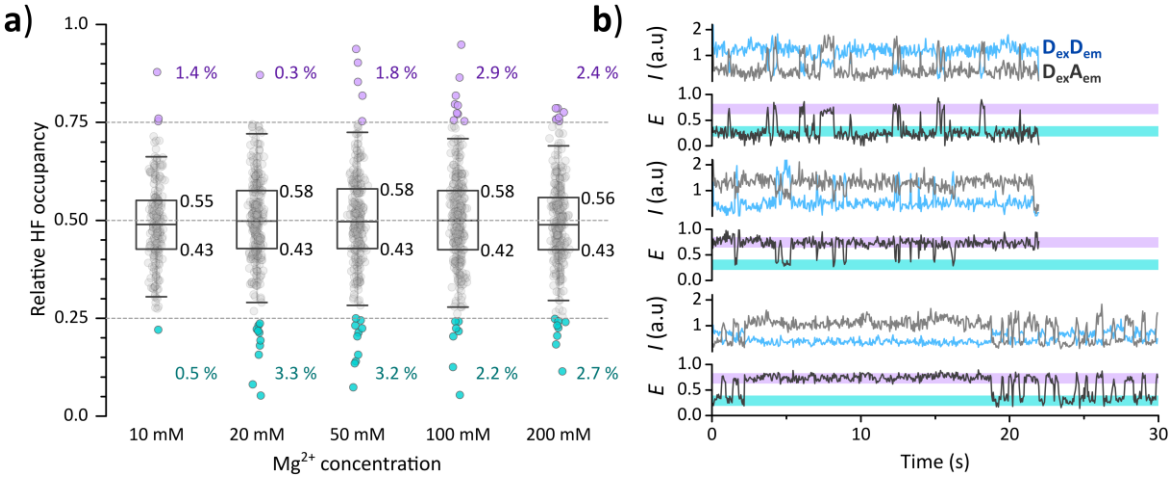

Figure 41: Variability in conformational dynamics of DNA Holliday junctions. a) The relative occupancy of the high FRET state of individual dynamic traces fitted with a Hidden Markov Model as a function of Mg^{2+} concentration. The boxes encase the 2nd to 3rd quartile with the median as center line. Whiskers indicate 1 inter quartal range. Data points of traces displaying a HF (> 0.75 HF occupancy, purple) or LF bias (< 0.25 HF occupancy, teal) are highlighted by color and their total ratio of all traces is shown. **b)** Exemplary fluorescence intensity (*I*) time traces showing donor excitation followed by donor emission ($D_{ex}D_{em}$) or acceptor emission ($D_{ex}A_{em}$) and the resulting FRET efficiency (*E*). See Appendix C.1. for molecule counts and fit parameters.

On the other hand, around 0.3 to 3.3% of all traces show a severe bias (< 25% or > 75% HF) towards either isoform I or II. These traces either predominantly remain in one state and only transiently switch between conformations (Figure 41b, top, middle) or they display regular dynamic behavior and then get trapped in one state for extended periods of time (Figure 41b, bottom). This analysis highlights the presence of kinetic heterogeneity in a conformationally homogenous system. Traces showing bias to either conformation may present unspecific interaction of HJs with the surface-coating mPEG, as artificially entangling of two arms of the HJ has been show to significantly alter the conformational distribution [423].

7.1.3 Role of the open conformation in Holliday junction dynamics

Based on the observed variance in conformer occupancy, it was tested whether a two-state HMM, introduced a bias in the dynamic analysis. To this end, a new fit allowing for up to four states was performed on all traces. Interestingly, the relative fraction of traces fitted with two states decreases from 73% at 10 mM Mg^{2+} to 33% at 200 mM while the fraction of traces fitted with three states increases with the Mg^{2+} concentration from 27% to 52%. Additionally, between 0–24% of traces were fitted with four states (Figure 42a).

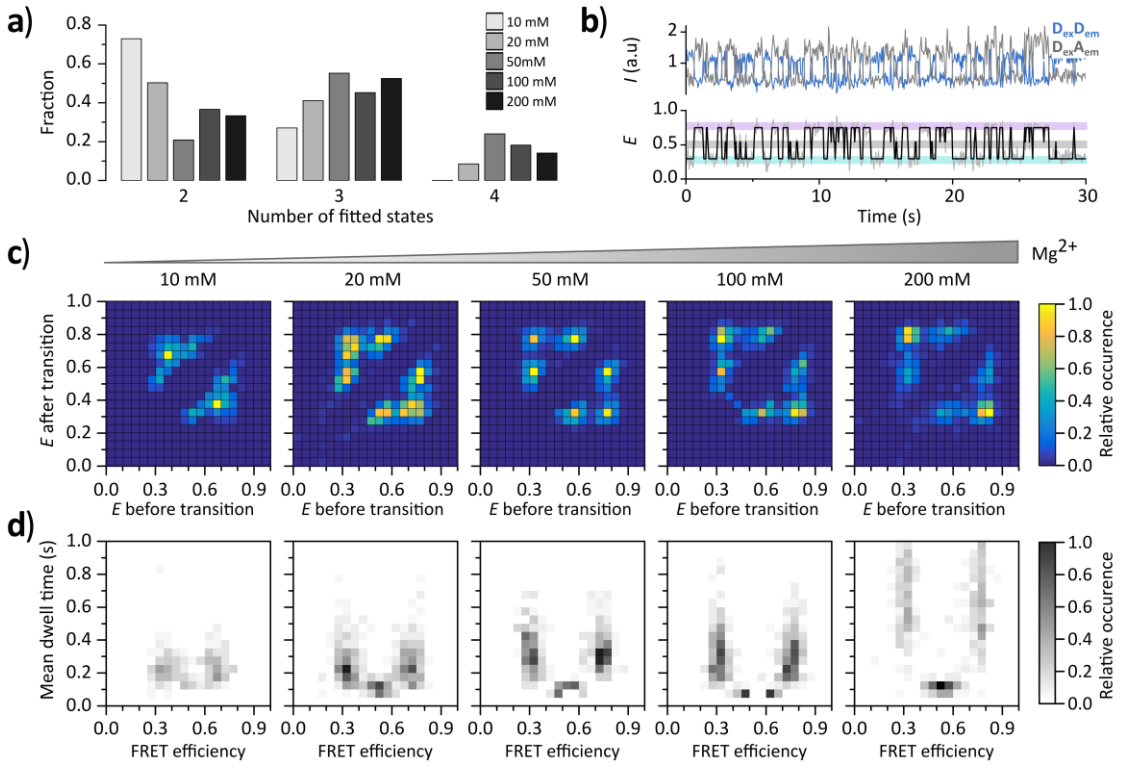

Figure 42: Transition state dynamics of DNA Holliday junctions. a) Relative fractions of traces fitted with 2, 3 and 4 states using a four-state HMM. **b)** Exemplary fluorescence intensity (*I*)-time trace showing donor excitation followed by donor emission ($D_{ex}D_{em}$) or acceptor emission ($D_{ex}A_{em}$) and the FRET efficiency (*E*) fitted with a two-state HMM (fit: black, trace: gray). The trace displays three-state dynamics between the open conformation (gray), isoform I (teal) and isoform II (purple). **c)** Transition density plots of occurring transition in a four-state HMM. **d)** Mean dwell times of fitted FRET efficiency states.

Generally, traces displaying three state dynamics are marked by transient switches to the medium FRET state observed for the open conformation of the HJ at 0 mM Mg^{2+} (Figure 42b). This indicates that even at higher Mg^{2+} concentrations, the open conformation still plays a role in the conformational cycle of the HJ. To further quantify the contribution of the open conformation to the dynamics cycle, the transition density plots for the new set of fits were calculated, now showing six populations at all Mg^{2+} concentrations (Figure 42c). In addition to the isoform I-II and II-I transitions (Figure 42b), isoform I to open conformation ($E \approx 0.55$), isoform II to open and the respective reverse transitions are visible. The open conformation is therefore accessible from either of the stacked conformations. The relative contribution of the open conformation to the conformational dynamics peaks at 20 mM Mg^{2+} and decreases with further Mg^{2+} addition (Figure 42c). Furthermore, at 10 mM Mg^{2+} the boundaries between stacked and open conformation are less defined.

Further insight on the three state dynamics could be derived by determining the mean dwell time of all FRET efficiency states (Figure 42d). The mean dwell times of states with FRET efficiencies corresponding to the stacked conformation increase along with Mg^{2+} concentration from 0.2 s at 10 mM Mg^{2+} to approximately 0.7 s at 200 mM confirming the result of the two-state model (Figure 39a). However, the mean dwell times of states with a FRET efficiency of 0.4–0.6 remain constant at 0.1 s at all Mg^{2+} concentrations. This marks the open conformation as a purely

transitional state that is accessed for only 1–2 frames (50–100 ms). This is in agreement with data obtained from smFRET experiments that identified the open conformation as an intermediate that is required in conformer exchange and branch migration [410,411,424]. Coarse-grained simulations of HJs further suggest that practically all transitions between isoform I and II use the open conformation as an intermediate [429]. These simulations also predict on average 6% of junctions in an ensemble to reside in the open conformation, even at high salt concentrations, which explains why the open conformation is detectable for all sampled Mg^{2+} concentrations.
Taken together, the experiments on immobilized HJs could faithfully reproduce results of previous smFRET studies and revealed mechanistic details such as variability in conformational bias and rare transition states, suggesting that the home-build microscope setup well-suited for advanced smFRET studies.

7.2 Assembly of human TFIIIB at the U6 snRNA promoter

The dynamic assembly of TFIIIB, the central initiation factor of the human RNAP III system, was investigated using smFRET experiments. The proteins used here are identical to the ones used to determine the crystal structure of the TFIIIB complex (HsTBP, HsBrf2, HsBdp1$_S$) [277]. Furthermore, an extended variant of Bdp1, Bdp1$_{ES}$ (residues 357–363), was included in smFRET experiments to potentially observe additional interaction or conformational changes within the complex (Figure 43). The crystal structure provides information on the positions of key structural features within the complex that can form the basis for informed smFRET measurements [277] (Figure 44). The TFIIIB complex shows a compact assembly centered around the bent U6 snRNA promoter (U6P) fragment (Figure 44a). The conformational change in the DNA induced by the assembly of TFIIIB can be detected via FRET between a donor-acceptor dye pair flanking the TATA-box without the need to fluorescently label the protein (Figure 44) [232]. Structural information is also instrumental to place fluorophores in positions that do not interfere with complex assembly. The crystal structure highlights the “molecular pin” structure in the C-terminal extension of HsBrf2 (Figure 44b). The α-helix formed by residues 357–363 of HsBrf2 buries into a hydrophobic pocket at the DNA/HsTBP interface, with the highly conserved cysteine residue C361 facing the DNA Figure 44b). In its oxidized state, C361 strongly impairs DNA/HsTBP/HsBrf2 complex formation (up to 80% reduction [186]). This cysteine-based structural switch can potentially interfere with smFRET experiments due to the required ROX buffer system for fluorophore stabilization (Chapter 6.8.4).

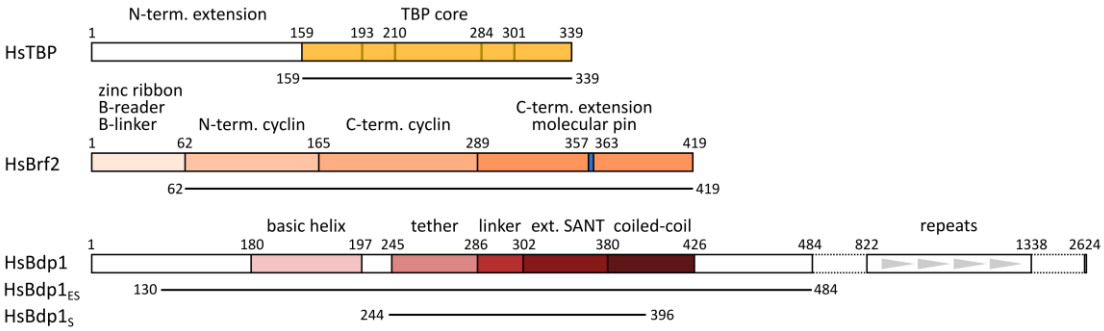

Figure 43: Domain organization of human TFIIIB subunits. Schematic overview of structural features and domains in HsTBP, HsBrf2 and HsBdp1. The truncated variants used in this work are indicated as black lines. The four conserved phenylalanine residues in TBP are indicated as dark yellow lines. Ext. SANT: extended SANT domain.

All Bdp1-proteins contain an N-terminal core of approximately 500 amino acids featuring a conserved extended SANT domain (residues 302–380) and an N-terminal linker, which are both necessary for efficient transcription [264–266]. The human genome additionally encodes isoforms of HsBdp1, which contain a repetitive C-terminal extension of variable length [183]. The C-terminal extension is not strictly required for transcription as a truncated HsBdp1 analogous to the *S. cerevisiae* Bdp1 is capable to faithfully initiate transcription *in vitro* [264]. HsBdp1$_S$ only includes the extended SANT domain and N-terminal linker (residues 357–363) and is transcriptionally inactive [277] whereas HsBdp1$_{ES}$, (residues 130–484) is transcriptionally active [264]. The SANT-domain constitutes the primary interaction site with the DNA/HsTBP/HsBrf1(2) complex

[183,264,265]. The SANT-domain recognition helix interacts with the major groove of the DNA as and TBP through charged residues (Figure 44c), whereas the linker is anchored to the DNA backbone via conserved aromatic residues (Y299, F294) opposite of TBP (Figure 44d).

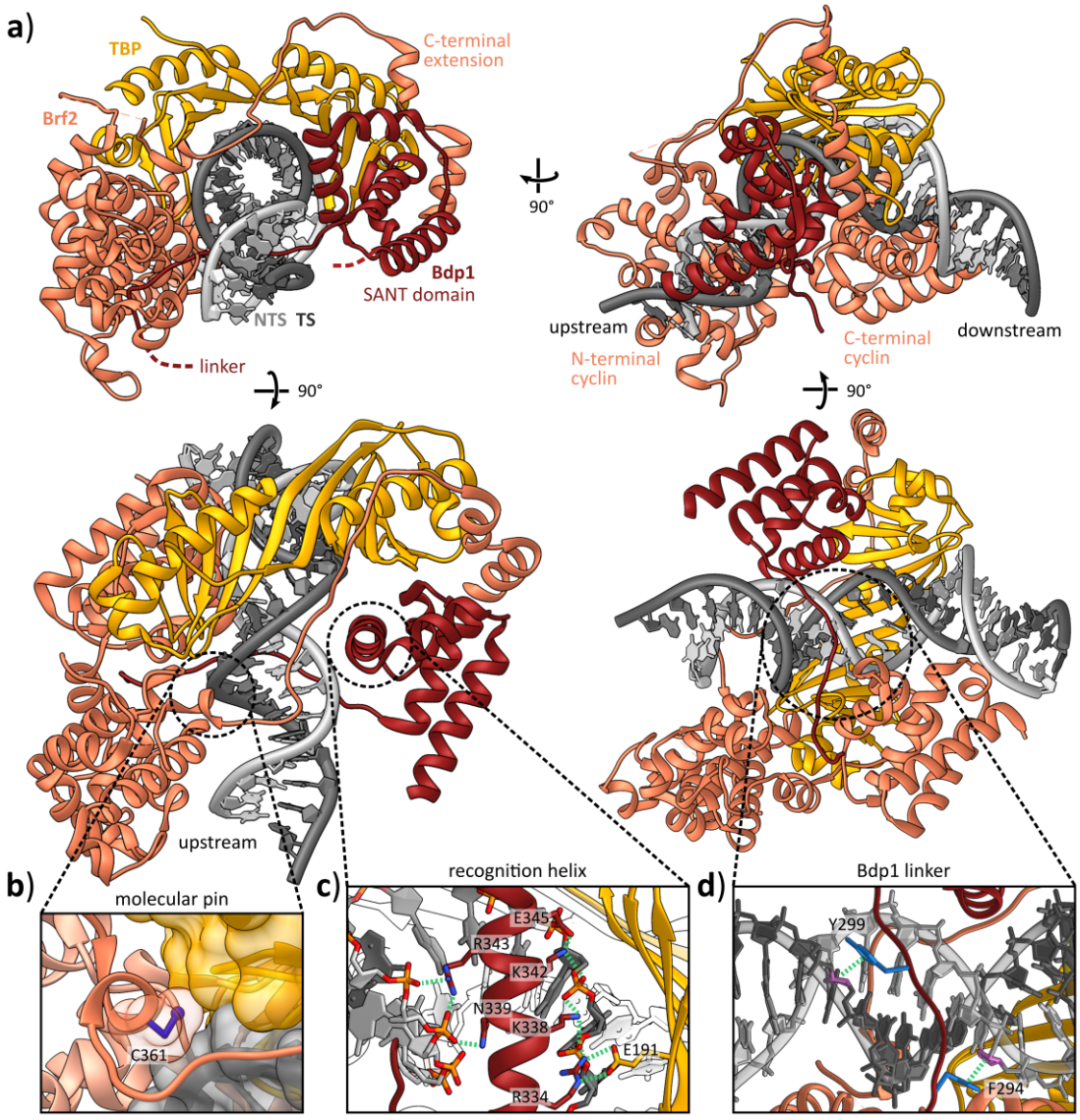

Figure 44: Structural features of the human TFIIIB complex. a) Crystal structure of the human U6P/TFIIIB complex (PDB: 5N9G) including the SANT and linker domain of Bdp1. The C- and N-terminal Bdp1 extensions of the Bdp1 variant (HsBdp1$_{ES}$; residues 130–484) are indicated as dashed lines. Molecules are color coded as follows: TBP (yellow), Brf2 (orange), Bdp1 (red), non-template strand (NTS, light gray), template strand (TS, dark gray). **b)** Close-up of the molecular pin structure in the C-terminal extension of Brf2 (residues 357–363). The cysteine residue C361 (blue) is buried in the interface between TBP (yellow space filling) and the TS (gray space filling) and prevents Brf2 binding when oxidized. **c)** Close-up of the Bdp1 recognition helix contacting the TS and NTS backbone phosphates and TBP via charged residues (green dashed lines). **d)** Close-up of the Bdp1 linker interacting with the minor groove by aromatic residue (blue)-sugar (purple) interactions (green dashed lines) (adapted from [277]).

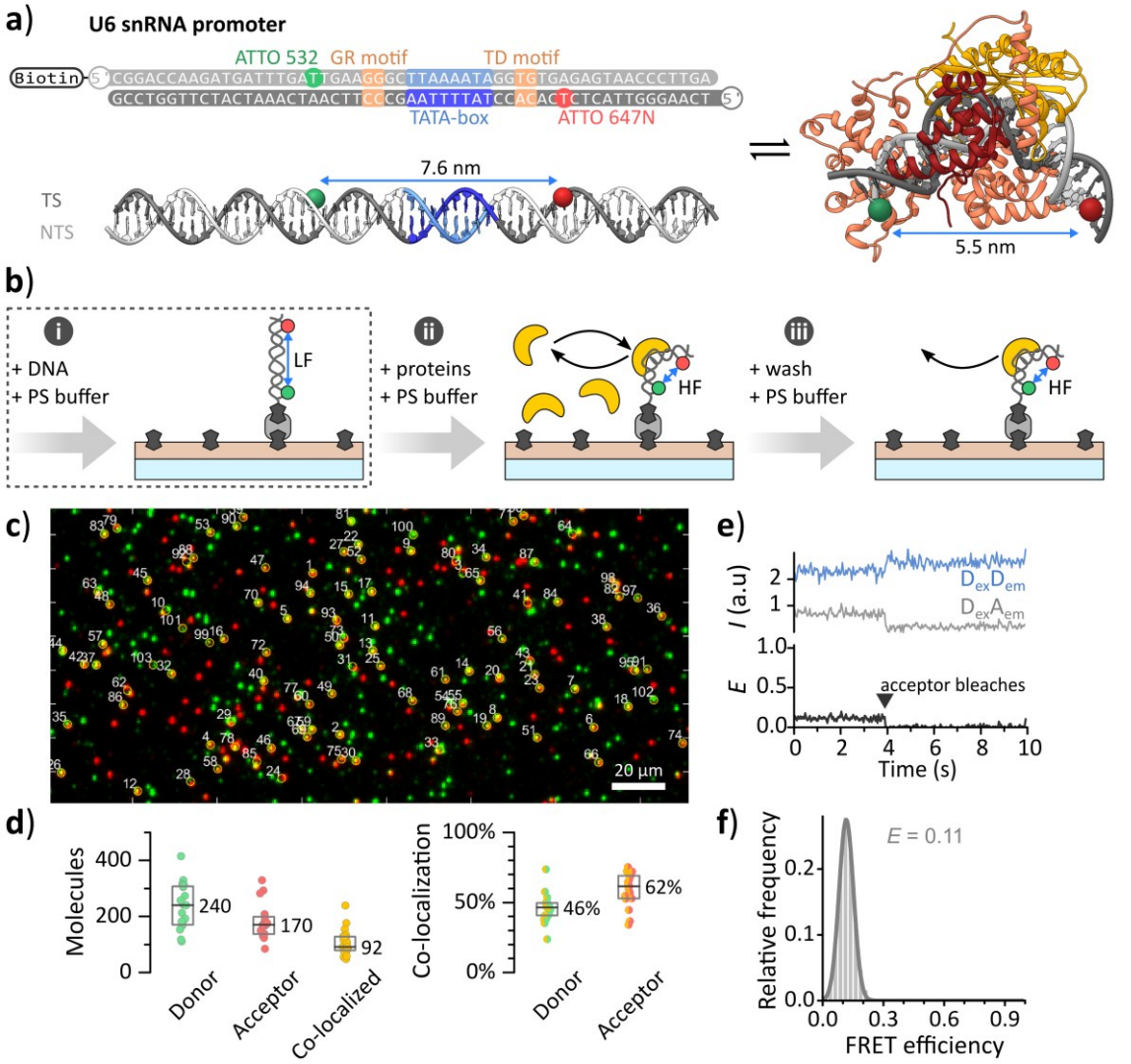

Figure 45: Experimental setup and smFRET TFIIIB promoter bending assays using TIRF microscopy. **a)** Nucleotide sequence and structural model of the U6 snRNA promoter. The position of the donor (ATTO 532, green sphere) and acceptor (ATTO 647N, red sphere) fluorophore, as well as promoter elements are color coded. The structural model illustrates the inter-dye distance change upon TBP binding. **b)** Schematic overview of the experimental workflow i) fluorescently labeled promoter DNA is immobilized on a quartz microscope slide (blue) passivated with biotin doted (black octagon) mPEG (tan) via NeutrAvidin (gray sphere). In this unperturbed state, the dye-pair exhibits a low FRET efficiency (LF). ii) Addition of proteins and photo-stabilization (PS) buffer allows DNA/protein complex formation and dissociation under equilibrium conditions. TBP-induced DNA bending (TBP in yellow) reduces the inter-dye distance, which is detectable by the high FRET efficiency (HF) in these complexes. iii) A washing step and reapplication of PS buffer removes unbound and transiently bound proteins. **c)** Overlay of the average images of donor (green) and acceptor channel (red) reflecting immobilized labelled U6P molecules. Co-localized molecule spots are circled in yellow and labelled according to relative intensity. **d)** Average number of detected donor and acceptor molecule spots. The total and relative number of co-localized spots is given. Boxes enclose the 25-75% percentile of data points. The center line indicates the median (N = 17 videos). **e)** Exemplary traces of donor fluorescence (blue) and acceptor fluorescence (gray) after donor excitation and the resulting FRET efficiency (black). **f)** FRET efficiency histogram of all analyzed traces fitted with a Gaussian distribution. The mean FRET efficiency *E* is given. See Appendix C.2 for molecule counts, fit parameters and standard deviations.

HsTBP-induced bending of the U6P DNA was interrogated using a FRET-based DNA bending assay (Figure 45a) [430]. The donor (ATTO 532) and acceptor (ATTO 647N) fluorophores were placed 13 nt upstream and 11 nt downstream of the center of the TATA-box, respectively.
In the absence of additional factors, the large distance between both dyes (7.6 nm) results in a low energy transfer efficiency from donor to acceptor. Upon TBP binding, the DNA is bent and the resulting decrease in inter-fluorophore distance is detectable as an increase in FRET efficiency (Figure 45a). Thus, a low FRET efficiency (LF) corresponds to the unbent promoter, whereas a high FRET efficiency (HF) reports on DNA bending and in extension, on the presence of HsTBP. TIRF microscopy was used to detect signals of individual promoter complexes. For this, the synthetic U6P was immobilized on a biotin-PEG coated quartz flow chamber via biotin-NeutrAvidin coupling (Figure 45b.i). Fluorescence of donor and acceptor molecules was recorded and double-labeled complexes were identified by superimposing the individual channels (Figure 45c). On average, 240 donor and 170 acceptor molecules were detected per field of view, 92 of these co-localized (46% of donor, 62% of acceptor spots) (Figure 45d). The FRET efficiency of stable fluorescence traces (Figure 38e) yielded a single population with E = 0.11 (Figure 38f). This confirms that the U6P DNA in the absence of additional factors shows a uniformly relaxed conformation.

7.2.1 Assembly of TFIIIB subcomplexes under equilibrium conditions

In the next step, 10 nM HsTBP was added to the flow chamber and measurements were carried out with proteins in the sample buffer allowing for repeated association and dissociation of TBP with and from the DNA (equilibrium conditions, Figure 46a.ii). Fluorescence traces (10 s) were sorted into groups of traces showing dynamic switching between LF and HF (49%), static LF (43%) and static HF (8%). The E histogram calculated from dynamic traces features two FRET efficiency populations, one at E = 0.12 corresponding to the unbent promoter, and one at E = 0.40 corresponding to the bent DNA state with an unbent/bent ratio of 32%/68%. The E histogram calculated from static traces also shows two populations at E = 0.11 and E = 0.37 but the unbent/bent ratio is skewed towards the unbent state at 84%/16% (Figure 46b). These results demonstrate that binding and subsequent promoter DNA bending by TBP is highly dynamic, and only few DNA/TBP complexes persist for longer than 10 s.
Addition of both, 10 nM HsTBP and 1 nM HsBrf2, to the sample chamber shifts the distribution of traces to 8% dynamic, 27% stable LF and 64% HF efficiency indicating a stabilization of the bent DNA state by Brf2. The E histogram calculated from dynamic traces shows two populations with E = 0.11 and E = 0.36, with an unbent/bent ratio of 33%/67%, akin to the conditions with TBP only. The E histogram for static traces shows two FRET efficiency populations, with most molecules (68%) in the bent state with E = 0.41 (Figure 46c) indicating that HsBrf2 does not induce further conformational changes, which has been reported for yeast TFIIB [232].
The simultaneous addition of all three proteins, 10 nM HsTBP, 1 nM HsBrf2 and 1 nM HsBdp1$_{ES}$, allows for the formation of a complete TFIIIB complex. As a result, the ratio of dynamic/static traces shifts further towards stable complexes with only 6% of traces showing dynamic switching, 21% static LF and 73% a stable HF signal. The E histogram derived from dynamic traces is similar to the histogram determined for the U6P/HsTBP/HsBrf2 complexes, featuring two populations

with *E* = 0.13 and *E* = 0.39 with an unbent/bent ratio of 42%/58%. The *E* histogram calculated from static traces demonstrates a further stabilization of the bent state with only 23% of molecules in the unbent state with *E* = 0.12 and 77% in the bent state at *E* = 0.45 (Figure 46d).

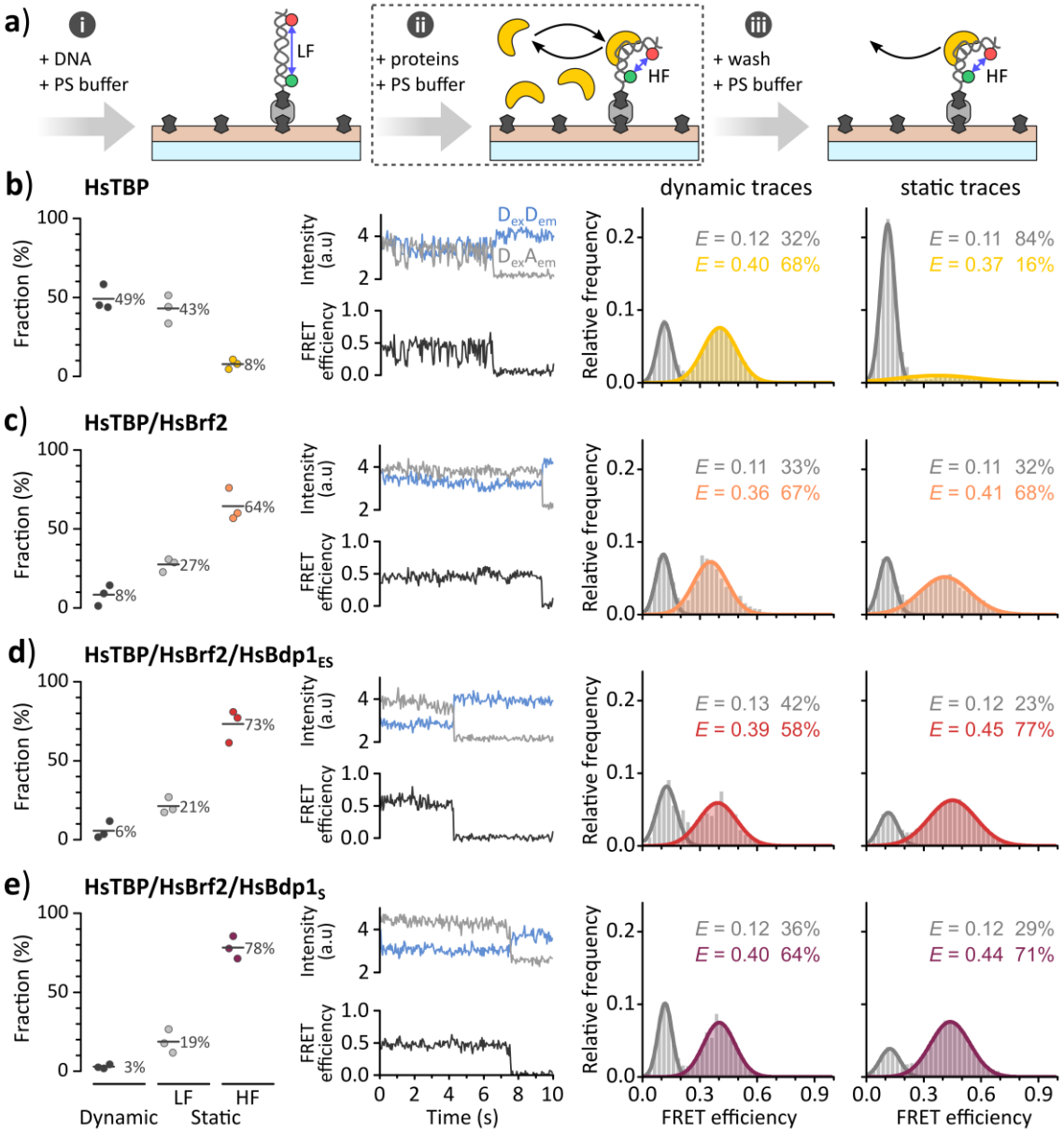

Figure 46: Analysis of immobilized U6 promoter/HsTFIIIB subcomplexes under equilibrium conditions. **a)** Signals of single immobilized complexes were measured using a TIRF microscope. The FRET efficiency reports on the unbent (LF) or bent state (HF) of the U6P (see Figure 45b for details). Measurements were performed with **b)** HsTBP (10 nM), **c)** HsTBP/HsBrf2 (10 nM/1 nM), **d)** HsTBP/HsBrf2/HsBdp1$_{ES}$ (10 nM/1 nM/1 nM), or **e)** HsTBP/HsBrf2/HsBdp1$_{S}$ (10 nM/1 nM/1 nM) in the sample buffer. Recorded fluorescence-time traces were sorted based on dynamic switching between unbent/bent state (black dots) or static LF (gray dots) and static HF (colored dots) signal. Lines indicate the mean of three independent experiments. Exemplary traces of donor fluorescence ($D_{ex}D_{em}$, blue) and acceptor fluorescence ($D_{ex}A_{em}$, gray) after donor excitation and the resulting FRET efficiency (black) are depicted for the most prominent fraction. FRET efficiency histograms were calculated from dynamic or static traces. The mean FRET efficiency *E* and relative peak area derived from the Gaussian fit are indicated by color: LF (gray), HF (color coded): U6P/HsTBP (yellow), U6P/HsTBP/HsBrf2 (orange), U6P/HsTBP/HsBrf2/HsBdp1$_{ES}$ (red) and U6P/HsTBP/HsBrf2/HsBdp1$_{S}$ (purple). See Appendix C.2 for molecule counts, fit parameters and standard deviations.

Additionally, measurements were performed with a TFIIIB complex that incorporates HsBdp1$_S$, a further truncated variant that includes only the SANT domain and linker domain of HsBdp1. This was done for comparison with the corresponding X-ray crystal structure that contains this variant of TFIIIB. Here, the distribution of traces indicates that HsBdp1$_S$ stabilizes the complex to a similar degree as HsBdp1$_{ES}$ with only 3% of traces showing dynamics, 19% static LF and 78% static HF. The *E* histogram calculated from dynamic traces resembles the sample with only TBP, as all previous experiments, showing two populations with $E = 0.12$ and $E = 0.40$ and unbent/bent ratio of 36%/64%. The histogram calculated from static traces is similar to the sample with HsBdp1ES, featuring two populations with $E = 0.12$ and $E = 0.44$ with an unbent/bent ratio of 29%/71% (Figure 46e). Notably, FRET efficiencies calculated for the bent state for both Bdp1 variants were nearly identical to the U6P/HsTBP and U6P/HsTBP/HsBrf2 complexes providing evidence that no conformational changes to the promoter DNA are introduced after addition of HsTBP. This is also supported by the two corresponding crystal structures that display nearly identical DNA conformations for the U6P/HsTBP/HsBrf2 and U6P/HsTBP/HsBrf2/HsBdp1$_S$ complexes[186,277] (for control experiments see Figure 48).

The result obtained from equilibrium smFRET experiments overall suggests that HsBrf2 plays a major role in the primary stabilization of HsTBP on the U6P and abrogates most dynamic binding events (from 49% dynamic traces to 8%). Additionally, HsBrf2 seems to increase the DNA-binding affinity of the HsTBP/HsBrf2 complex since the number of stable LF traces decreases. This is consistent with results obtained for yeast Brf1, were an up to 17-fold increase of binding affinity was observed[431][431]. Both HsBdp1 variants tested further stabilize the TFIIIB/DNA complex. However, the difference to the HsTBP/HsBrf2 complex is minor, judging from the 4–13% increased HF population for static traces. Notably, all histograms calculated from dynamic FRET traces bear a striking resemblance to the measurement with HsTBP only and the corresponding traces display distinct TBP-like dynamics. This suggests that dynamic traces stem from HsTBP that is not bound by HsBrf2 most likely as a result of the 10-fold molar excess of HsTBP.

7.2.2 Stability of TFIIIB subcomplexes after depletion of unbound proteins

DNA/TFIIIB complexes have been reported to be highly stable and resistant to high salt concentrations and heparin competition [189,191,269,270]. To test whether this also holds true at single-molecule concentrations and to quantify the stabilization, a second set of measurements for each subcomplex was performed. To this end, the flow chamber was flushed with 500 µL sample buffer to remove any unbound or transiently bound proteins (Figure 47a.ii).

Experiments including HsTBP only showed that washing removed almost all complexes, leaving 90% of promoters vacant (static LF). 4% of the traces exhibited dynamics. The fraction of traces showing static HF is relatively unchanged at 6%. The FRET efficiency histogram calculated from the remaining dynamic traces is nearly identical to the FRET distribution before washing showing two populations with $E = 0.13$ and $E = 0.42$ with unbent/bent ratio of 36%/64% (Figure 47b). The histogram from static traces is unchanged. This demonstrates that practically all HsTBP-DNA interactions are transient and susceptible to washing, whereas a small fraction remains stably bound.

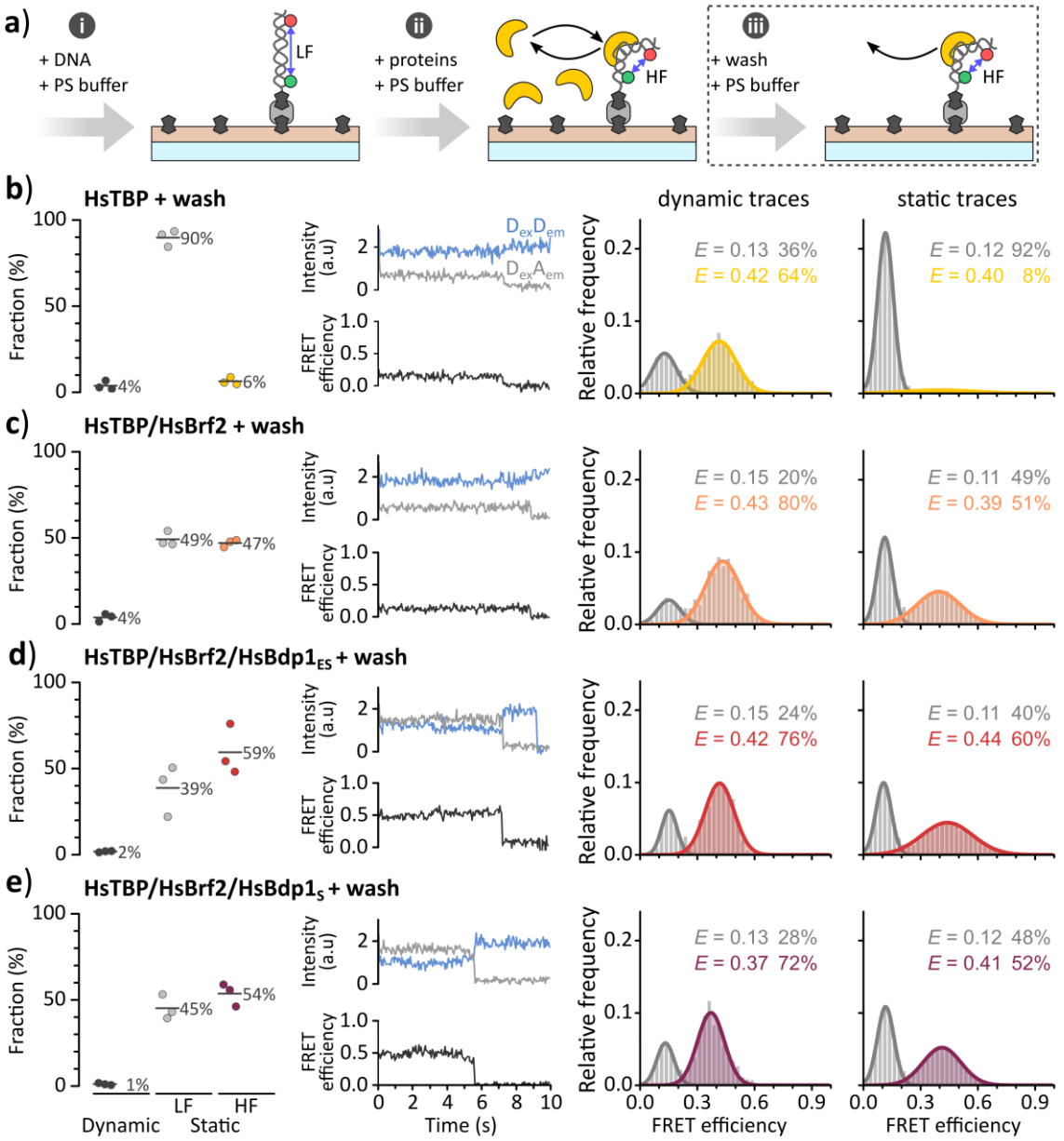

Figure 47: Analysis of immobilized U6 promoter/HsTFIIIB subcomplexes after washing. a) Signals of single immobilized complexes were measured via TIRF microscopy. The FRET efficiency reports on the unbent (LF) or bent state (HF) of the U6 snRNA promoter. Measurement were performed after washing off unbound proteins (see Figure 45b for details). Panels **b)**–**e)** correspond to the respective panels in Figure 46. Recorded fluorescence-time traces were sorted based on dynamic switching between unbent/bent state (black dots) or static LF (gray dots) and static HF (colored dots) signal. Lines indicate the mean of three independent experiments. Exemplary traces of donor fluorescence ($D_{ex}D_{em}$, blue) and acceptor fluorescence ($D_{ex}A_{em}$, gray) after donor excitation and the resulting FRET efficiency (black) are depicted for the most prominent fraction. FRET efficiency histograms calculated from dynamic and static traces. The mean FRET efficiency *E* and relative peak area derived from the Gaussian fit are indicated by color. LF (gray), HF (color coded): U6P/HsTBP (yellow), U6P/HsTBP/HsBrf2 (orange), U6P/HsTBP/HsBrf2/HsBdp1$_{ES}$ (red) and U6P/HsTBP/HsBrf2/HsBdp1$_{S}$ (purple). See Appendix C.2 for molecule counts, fit parameters and standard deviations.

The U6P/HsTBP/HsBrf2 complex displays considerably higher resistance to washing, retaining 47% of promoters in the bent state while 49% are found in the unbent state. The relative number of dynamic molecules is further reduced to 4%. Notably, the unbent/bent ratio of the histogram calculated from dynamic traces is shifted to 20%/80%. The reduction in stable HF traces is also reflected in the corresponding FRET efficiency histogram, which shows an unbent/bent ratio of 49%/51% compared to 32%/68% before the washing step (Figure 47c). This represents a stabilization by a factor of 6.4 compared to the U6P/HsTBP complex.

The two variants of HsTBP/HsBrf2/HsBdp1 complexes were accounted for the highest percentage of static HF traces before washing. After the removal of weakly bound molecules, the $Bdp1_{ES}$ variant still shows the highest relative occupancy of the bent state at 59%, while 39% of traces show static LF. Only 2% of traces were dynamic. Similar to the HsTBP/HsBrf2 complex, the FRET efficiency histogram is shifted to a higher unbent/bent ratio of 24%/76% with similar FRET efficiencies as before. The histogram calculated from static traces only shows a shift in the unbent/bent ratio to 40%/60% with no change in FRET efficiency (Figure 47d).

For the $HsBdp1_S$ variant, the relative fraction of static HF traces decreased to 54%, while 45% of promoters are vacant and 1% of traces show dynamic switching. The histogram derived from dynamic traces is skewed towards the bent state with a 28%/72% unbent/bent ratio, while the histogram calculated from static traces shows an equal ratio of LF and HF molecules with 48%/52% (Figure 47e). Both histograms show no change in FRET efficiency. Overall, the results obtained from analyzing only stably bound molecules show the same trends as observed for equilibrium conditions. HsBrf2 seems to be the primary contributor to complex stability (6.4-fold stabilization), whereas in the presence of either HsBdp1 variant nearly identical retention of bent state complexes was observed.

In order to confirm that HsTBP is the TFIIIB component necessary and sufficient for promoter bending, HsBrf2 and both HsBdp1 variants were tested in isolation. FRET efficiency histograms under these conditions yield exclusively static LF traces with FRET efficiencies between E = 0.11–0.13 (Figure 48a), demonstrating that HsTBP is necessary and sufficient to bend the U6P DNA. Since dynamic traces after washing showed an increased ratio of the bent population for the HsTBP/HsBrf2/$HsBdp1_{ES}$ and HsTBP/HsBrf2/$HsBdp1_S$ complexes, these were probed in the absence of HsBrf2 to check, whether HsBdp1 has an effect on the dynamic promoter bending activity of HsTBP. For the HsTBP/$HsBdp1_{ES}$ complex, 50% of traces showed dynamics, 39% static LF and 11% HF under equilibrium conditions. Dynamic traces exhibit an unbent/bent ratio of 24%/76%. After a washing step, 92% of promoters are vacant, with 6% showing stable HF and 2% dynamic switching between LF and HF (Figure 48b).

Probing the HsTBP/HsBdp1S complex resulted in similar distributions of traces, with 46% showing dynamics, 48% stable LF and 6% stable HF in equilibrium. A washing step again removes most proteins, leaving 92% of promoters empty, 6% with stably bound complex and 2% with dynamics (Figure 48c). Based on these results, HsBdp1 appears to have no stabilizing effect on the bent U6P/HsTBP complex in the absence of HsBrf2. This result is in accordance with previous reports of weak HsTBP/HsBdp1 interaction [262].

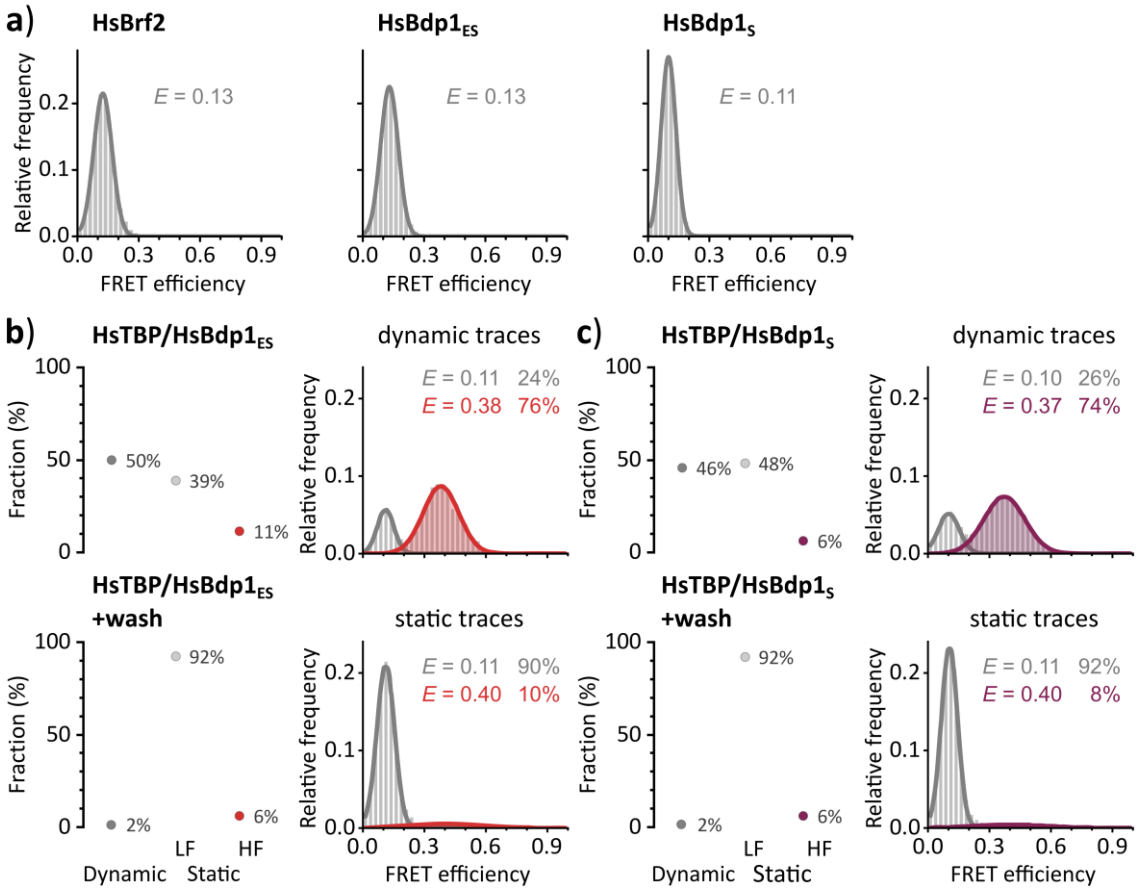

Figure 48: Control experiments for smFRET analysis of human TFIIIB components. Signals of single fluorescent molecules were measured employing TIRF microscopy. The FRET efficiency reports on the unbent (LF) or bent state (HF) of the U6 snRNA promoter. **a)** Analysis of the bending capability of HsBrf2, HsBdp1$_{ES}$ and HsBdp1$_{S}$ in the absence of other proteins. No dynamic traces were recorded. **b)** DNA binding of a TBP/Bdp1$_{ES}$ complex and **c)** a TBP/Bdp1$_{S}$ complex under equilibrium conditions and after a washing step. FRET efficiency histograms calculated from dynamic and static traces. The mean FRET efficiency E and relative peak area derived from the Gaussian fit are indicated by color. LF (gray), HF (color coded): U6P/HsTBP/HsBdp1$_{ES}$ (red) and U6P/HsTBP/HsBdp1$_{S}$ (purple). Data from single experiments are shown. See Appendix C.2 for molecule counts and fit parameters.

7.2.3 Dynamics of HsTBP-induced promoter DNA bending

Dynamic traces recorded for experimental conditions without HsBrf2 showed fast dynamic switching on the millisecond timescale (Figure 46b). In order to extract further quantitative information on the conformational dynamics of the complex, these traces were fitted with a Hidden Markov Model (Figure 49a), to reduce the complex FRET efficiency traces to discrete states. Since the FRET efficiency histograms calculated from dynamic traces showed only two populations for all analyzed complexes, this fit was limited to only account for two states. The possible transitions for each complex were evaluated with a transition density plot (Figure 49b). For HsTBP as well as the two HsTBP/HsBdp1 complexes, exclusively transitions from E = 0.15 to E = 0.40 and vice-versa were observed, which is in line with the corresponding FRET efficiency histograms.

The dwell time histograms for all LF and HF states (Figure 49c) were fitted with a mono-exponential decay to determine the mean dwell time τ in the unbent and bent state. The fits yield

an unbent state dwell time of $\tau_{unbent} \approx 0.14$ s for all analyzed complexes. The dwell time in the bent state was calculated as $\tau_{bent} \approx 0.56$ s for U6P/HsTBP and the U6P/HsTBP/HsBdp1$_S$ complex. A slightly higher mean dwell time of $\tau_{bent} \approx 0.67$ s was calculated for the U6P/HsTBP/HsBdp1$_{ES}$ complex. These values translate to a $\tau_{unbent}/\tau_{bent}$ ratio of approximately 0.25/0.75, which again corresponds well to unbent/bent ratio observed for the FRET efficiency histograms. The above data support a model in which HsTBP binds to the U6P in a transient manner and rapidly dissociates. Under equilibrium conditions, this allows for continuous exchange of bound HsTBP, whereas a washing step removed these proteins. The measurements with added HsBdp1 further confirm, that in the absence of HsBrf2, this factor has no additional stabilizing effect on the U6P/HsTBP interaction.

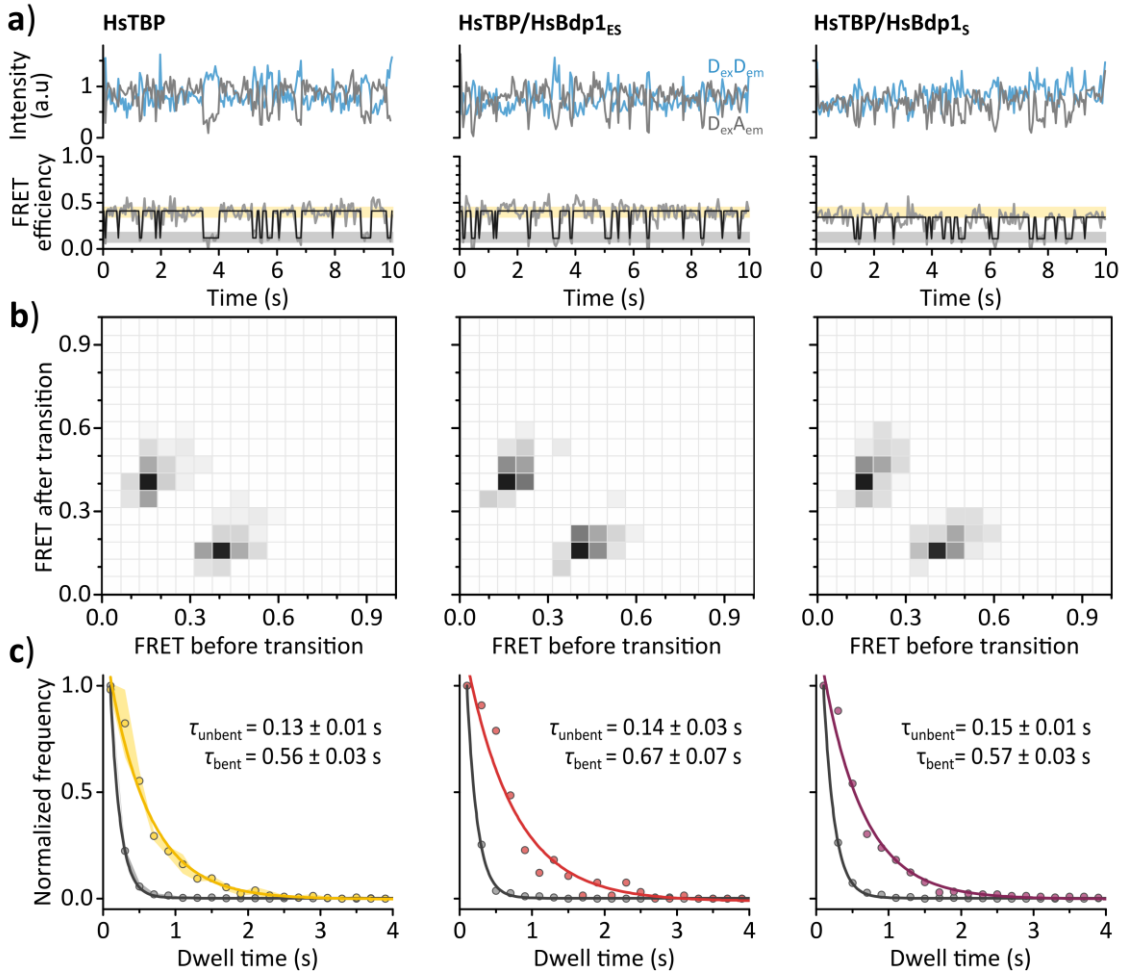

Figure 49: Analysis of dynamics in smFRET time traces of human TFIIIB subcomplexes. Signals of single molecules were measured employing TIRF microscopy. The FRET efficiency reports on the unbent (LF) or bent state (HF) of the U6 snRNA promoter. **a)** Representative dynamic traces of donor fluorescence (blue) and acceptor fluorescence (gray) after donor excitation and the resulting FRET efficiency (gray) fitted with a two-state Hidden Markov Model (black) are shown. **b)** Transition density plots calculated from fitted traces showing all measured combinations of FRET before and after a transition. The relative occurrence is depicted in gray scale from white (lowest) to black (highest). **c)** Dwell time histograms were fitted with a mono-exponential decay to calculate the mean dwell time τ in the unbent (gray) and bent (colored) state. The standard deviation of three technical replicate for the U6P/HsTBP complex is shown as light gray/yellow area. U6P/TBP (yellow), U6P/HsTBP/HsBdp1$_{ES}$ (red), U6P/HsTBP/HsBdp1$_S$ (purple). Data from three (HsTBP) or one experiment (HsTBP/HsBdp1) are shown. See Appendix C.2 for molecule counts and fit parameters.

Taken together, the analysis of the HsTFIIIB complex provides a picture of a high dynamic range of interaction timescales starting at fast millisecond dynamics for the initial HsTBP binding step that results in a bent promoter complex. The TFIIB-like factor HsBrf2 proved to be the primary stabilizer of the complexes, fixing HsTBP on the promoter and allowing subsequent assembly of HsBdp1. The crystal structures of U6P/HsTBP/HsBrf2/HsBdp1$_S$ complex shows extended interactions o HsTBP and HsBrf2 (Figure 44), which link the experimental results of this work with structural data [186,277]. Both tested HsBdp1 variants conferred minor additional stabilization under equilibrium conditions, but no major contribution to complex retention after washing was observed. This may in part be due to use of sub-stoichiometric amounts of both additional factors, although HsBrf2 functioned well under these conditions. Taken together, these finding suggest a hierarchical assembly of TFIIIB wherein transient DNA-TBP-interactions are stabilized by HsBrf2, drastically increasing the bent state dwell time which allows for subsequent entry of HsBdp1 into the complex, which provides minor additional stabilization.

7.3 Force-dependency of DNA binding by RNAP II and III transcription factors

The above experiments established the HsBrf2 subunit of human TFIIIB as the critical factor in formation of stable initiation complex in the RNAP III system, whereas the stabilizing effect observed for HsBdp1 was minor. However, several studies emphasize the importance of HsBdp1 in conveying complex stability [189,191,269,270]. RNAP III transcription relies heavily on reinitiation by recycling the same TFIIIB complex. Hence, TFIIIB must endure repeated promoter escape events [341,345,432]. Furthermore, reports of DNA/TFIIIB complexes acting as genomic roadblock [346], coupled with complex lifetime of 95 min [271], imply an overall high mechanical resilience. Within the chromatin structure in living cells, DNA is subjected to strain from cellular processes, in particular transcription [76–78] and DNA compaction [82–84] that can be transmitted over several kilobases [322,325,326,433]. At the U6P promoter as well as other SNAPc-controlled promoters, TFIIIB is positioned close to a nucleosome essential for cooperative SNAPc-Oct-1 binding [258]. Hence, these binding sites could be subjected to increased amounts of strain. To gain further insight into the mechanical properties of the U6P/TFIIIB complex, experiments on strained promoter DNA constructs were conducted by using a DNA origami-based FC system that can exert forces in the low piconewton range on a short promoter construct [94] (Figure 50a) (Chapter 6.3).

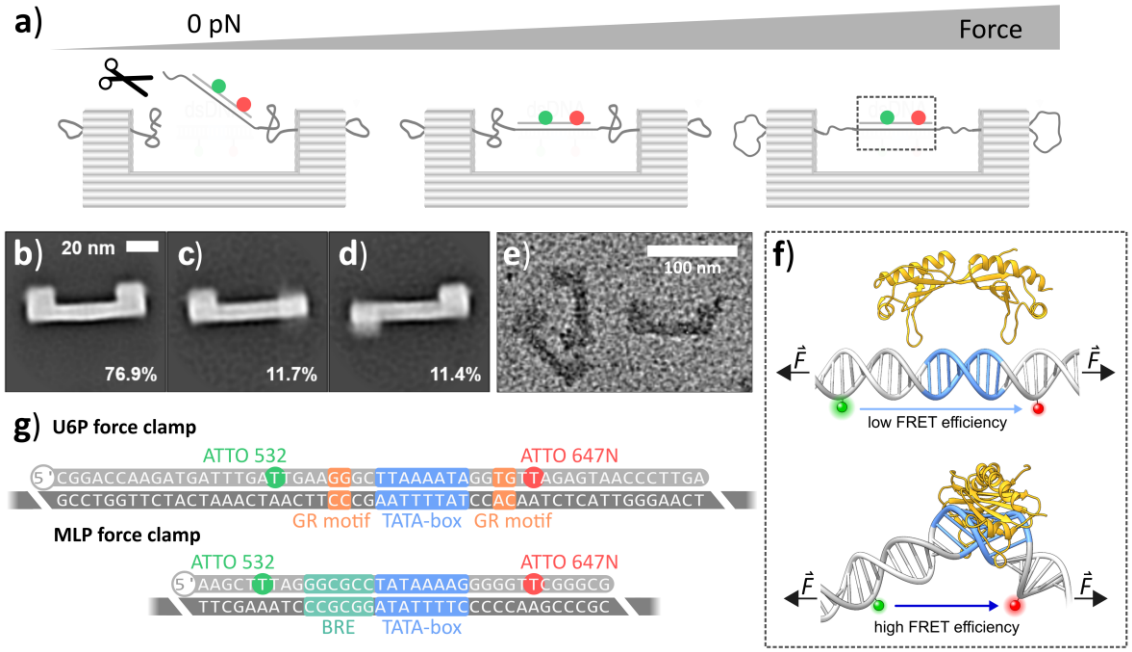

Figure 50: Experimental setup for DNA origami based single-molecule force measurements. a) Schematic model of the DNA origami force clamp (FC). Entropic force is generated by a constraint ssDNA spring. The applied force is tuned by reducing the length of the ssDNA spring, thereby decreasing the entropy of the system and increasing the force. Enzymatic restriction of the spring generates a 0 pN FC. **b-d)** 2D-class averages DNA Origami particles imaged with TEM and their relative occurrence. **e)** Representative electron micrograph of a 3 pN U6P FC sample. **f)** Force *F* is applied to the central dsDNA promoter segment. Binding of TBP to the TATA-box bends the DNA and leads to an increase in FRET efficiency between the donor and acceptor fluorophore flanking the TATA-box. **g)** Sequence of the dsDNA U6P and MLP annealed to the spring of the FC. The template strand (dark gray) is part of the DNA origami scaffold (indicated as white dash). Sequence elements and fluorophore modifications of the non-template strand (light gray) are color coded. Adapted from [434].

This setting is meant to simulate the *in vivo* situation, where transcription initiation occurs on DNA under force by surrounding cellular processes. Therefore, the necessary step of DNA bending by TBP must be achieved in opposition to local strain on the DNA matrix. Folded DNA origami samples were analyzed using TEM (Figure 50b–d). The 2D class averages show a high yield (76.9%) of correctly folded origami structures (Figure 50b), whereas 23.1% of particles are potentially immobilized in a different orientation or are structurally deformed (Figure 50c, d).
For further comparison, the RNAP II-specific initiation factors HsTFIIA and HsTFIIB were chosen. Initiation factor complexes recruiting RNAP II are generally less stable, which allows for finely tuned regulation [435,436]. In addition, RNAP II PIC assembly occurs predominantly in nucleosome depleted regions, suggests an overall higher susceptibility of RNAP II initiation complexes to mechanical force [349,437]. As a promoter, the strong Adenovirus major late promoter (MLP) was chosen as a model system for the RNAP II transcription system. The MLP contains a TATA-box and BRE sequence, which are recognized by HsTBP and HsTFIIB (Figure 50g), respectively, whereas HsTFIIA mainly interacts with the phosphate backbone upstream of the TATA-box [141,142], occupying a position similar to HsBdp1 [277] (Figure 51a, b).

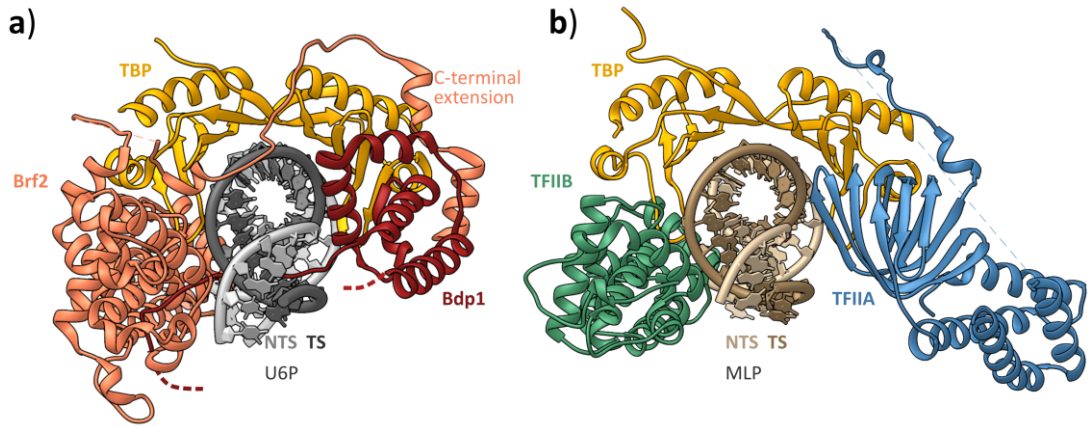

Figure 51: Structure comparison of RNAP II and III initiation factor complexes. a) Crystal structures of the human U6P/TBP/Brf2/Bdp1 complex (PDB: 5N9G) and **b)** the human MLP/TBP/TFIIA/TFIIB complex (PDB: 5IYB). The Bdp1 variant used in experiments comprises residues 130–484 as compared to residues 286-384 in the structure (indicated as red dashed lines). The structures are color-coded: MLP-DNA (tan), TBP (yellow), TFIIA (blue), TFIIB (green), U6P-DNA (gray), Brf2 (orange), Bdp1 (SANT domain and linker domain, red). Adapted from [434]

The interaction of TFIIIB subcomplexes with the DNA origami were examined with confocal fluorescence microscopy on diffusing complexes. As a readout for promoter binding, the already established FRET assay was used (Figure 50b). The donor (ATTO 532) and acceptor fluorophores (ATTO 647N) were incorporated into the NTS of the promoter that was hybridized to the complementary sequence nested within the spring region of the FC. The successful hybridization of the fluorescently labelled DNA strand is demonstrated by fluorescence correlation spectroscopy measurements, yielding relative diffusion times of 0.48 ms and 3.40 ms for the linear and DNA origami U6P, respectively (Figure 52). For the MLP, relative diffusion times of 0.36 ms and 2.56 ms were determined for the respective constructs (Figure 52a). Overall, the short dsDNA promoter diffuses approximately seven times faster than the respective DNA origami where the labelled DNA is part of the high molecular weight DNA origami structure (Figure 52a).

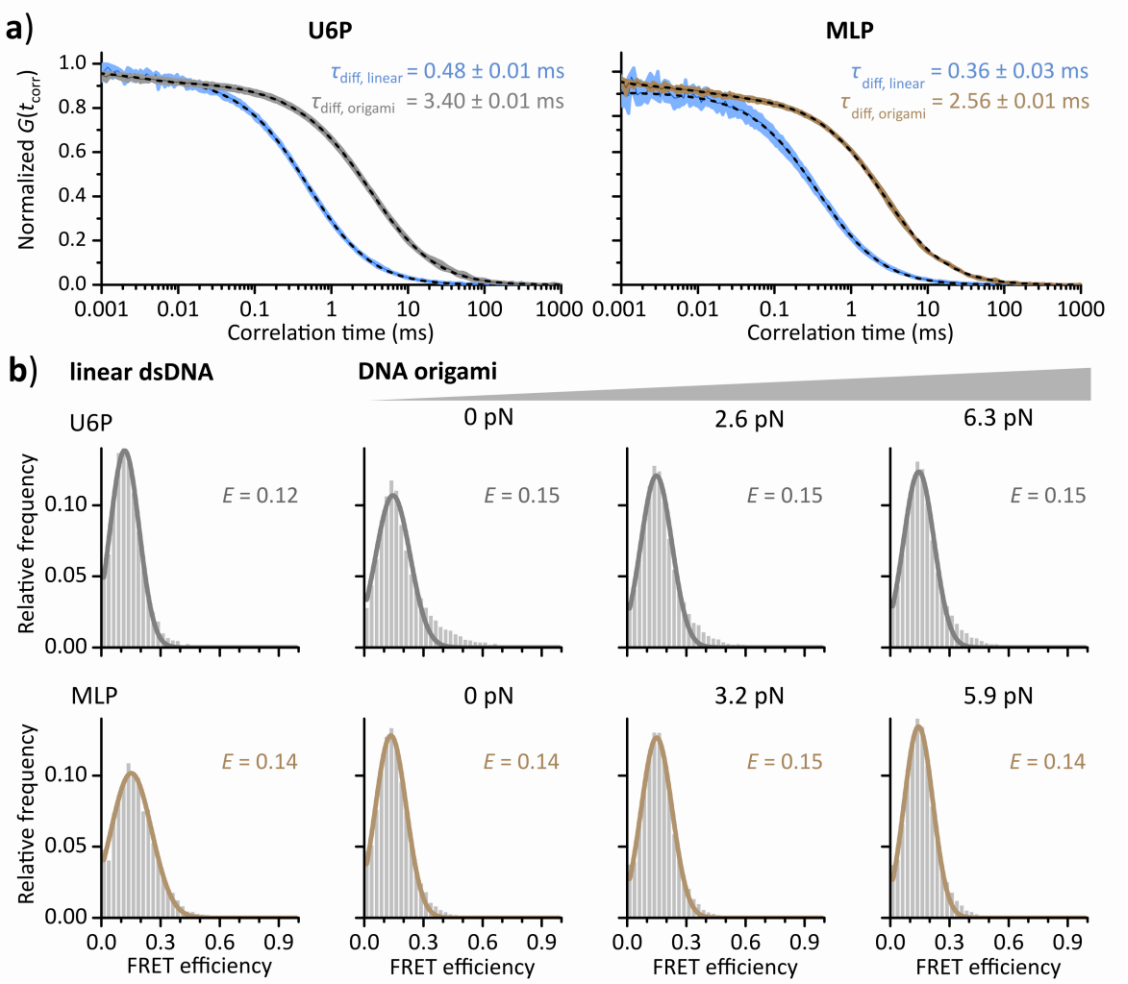

Figure 52: Comparison of U6 promoter and MLP DNA origami force clamps to linear double-stranded promoters. DNA constructs were analyzed using confocal fluorescence microscopy. **a)** The relative diffusion time τ_{diff} of a 55 bp linear dsDNA U6P and 35 bp MLP (blue) were compared to the same promoters annealed to the spring region of a DNA origami FC (gray/tan) via fluorescence correlation spectroscopy. Values are given as mean ± s.e. of the exponential fit model (dashed line). $G(t_{corr})$ is the autocorrelation function of the acceptor fluorescence intensity, t_{corr} is the correlation time. **b)** FRET between the donor (ATTO 532) and acceptor (ATTO 647N) reports on the unbent (gray/tan) or bent state of the promoter DNA. The mean FRET efficiency E of the fitted Gaussian is indicated by color. Data from three technical replicates are shown. Adapted from [434]. See Appendix C.3 for molecule counts, fit parameters and standard deviations.

Initially, smFRET measurements on freely diffusing DNA origamis were performed revealing a single uniform low FRET population with an average FRET efficiency of $E \approx 0.15$ for all forces for the U6P and MLP FCs. For the MLP, the measured FRET efficiencies are in good agreement with FRET efficiencies obtained from linear double-stranded promoter DNAs ($E = 0.14$). However, for the U6P, the FRET efficiency measured for the linear construct is slightly lower at $E = 0.12$ (Figure 52b). Additionally, U6P FCs show light tailing towards higher FRET efficiencies. Overall, this demonstrates that the conformation of the promoter DNA is not significantly changed when it is incorporated into the DNA origami FC and forces are applied.

Next, TBP-induced DNA bending was monitored for the above linear promoter constructs and the corresponding 0 pN FCs using 20 nM HsTBP (Figure 53). These FCs were generated by enzymatic cleavage of the ssDNA spring on one side, leaving the dsDNA promoter segment connected to the FC body.

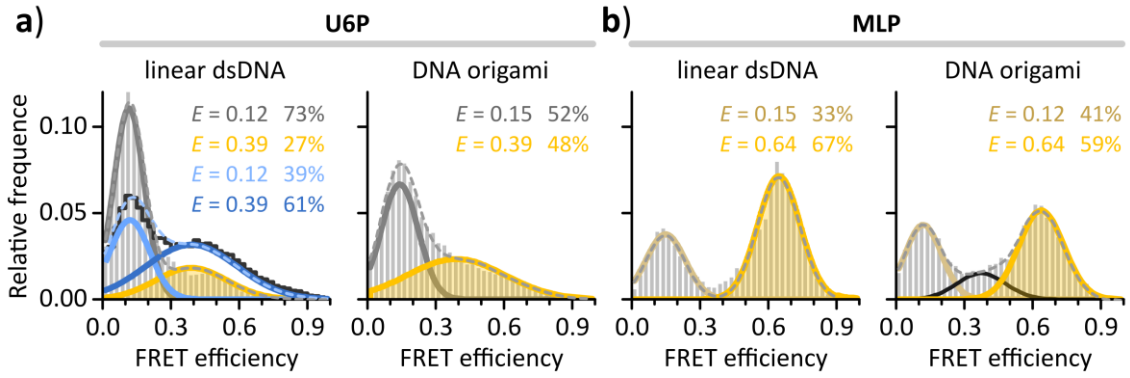

Figure 53: Comparison of TBP-induced DNA bending for linear double-stranded DNA promoters and DNA origami force clamps. a) The U6P or **b)** the MLP as linear dsDNA or annealed to the spring region of a 0 pN DNA origami FC with 20 nM HsTBP were analyzed using confocal fluorescence microscopy. FRET between the donor (ATTO 532) and acceptor (ATTO 647N) reports on the unbent (gray/tan/light blue) or bent state (yellow/dark blue) of the promoter DNA. For the linear U6P, a measurement using 100 nM HsTBP (black steps in a), blue Gaussians) was performed to allow for more accurate fitting of the HF population. A third Gaussian (black line) was included to fit the central density observed in FC samples but was excluded from the calculation of relative areas. The mean FRET efficiency *E* and relative peak area of the fitted Gaussian are indicated by color. Data from one (linear DNA) and three (FC) technical replicates are shown. Adapted from [434]. See Appendix C.3 for molecule counts, fit parameters and standard deviations.

For the linear U6P, relatively inefficient bent state formation was observed with a relative bent fraction of 27% (Figure 53a). In contrast, a broad distribution with a bent-state fraction of 48% was observed for the 0 pN U6P FC, indicating more efficient HsTBP binding. Due to the broad FRET efficiency distribution, the measurements with the linear U6P were additionally performed using 100 nM HsTBP (Figure 53a). This resulted in a relative bent state fraction of 61% and allowed for more accurate fitting of the HF population to determine the mean FRET efficiency of the bent state as E =0.39 for both, linear DNA and the FC.

In contrast, experiments with a linear MLP and 20 nM HsTBP yielded two well defined FRET efficiency populations with a HF fraction of 67% (Figure 53b). The FRET efficiency of the bent state (E = 0.64) is considerably higher than the one determined for the U6P. For the 0 pN MLP FC, the FRET efficiencies of the main LF and HF population are highly similar to the linear promoter with E = 0.12 and E = 0.64 (Figure 53b). In addition, molecules with a broadly distributed medium FRET efficiency connecting both populations were noticed and included in the fit as a third Gaussian with a mean FRET efficiency of E = 0.37 (Figure 53b, dashed curve). This population was later observed in all FC experiments (Figure 54, Figure 55, Figure 65) as a FRET efficiency density between 0.3–0.5 with varying amplitude and did not occur in experiments using linear dsDNA. Additionally, the relative area was not correlated to the applied force. Based on these observations, the population seems not relevant for the biology of the system. It was included as an additional Gaussian to improve overall fit quality but was excluded from further analysis and will be revisited in the discussion. Since FCs and their corresponding short linear DNA constructs showed identical bent state FRET efficiencies for the U6P and MLP, respectively, it can be assumed that the mode of DNA bending is not changed between both constructs and the biological function of HsTBP is not altered when added to the DNA origami FC.

7.3.1 Force dependency of human TBP-induced promoter DNA bending

Similar to the characterization of the human TFIIIB complex with short linear DNA in TIRF experiments, the canonical HsTBP, HsTBP/HsBrf2 and HsTBP/HsBrf2/HsBdp1$_{ES}$ subcomplexes were analyzed using the DNA origami FC in confocal solution experiments to evaluate the effects of promoter strain on the DNA bending induced by HsTBP (Figure 54). For comparison, the analogous complexes of the RNAP II system were tested in parallel (Figure 55).

HsTBP is the shared initiation factor among all three eukaryotic transcription systems. Without additional factors, HsTBP binding should mainly be affected by the TATA-box promoter sequence[207]. Following up on the above measurements using a 0 pN U6P FC that represents efficient complex formation, an intact FC that applies 2.6 pN was used to probe the DNA bending induced by 20 nM HsTBP (Figure 54a). This resulted in a decrease of the bent-state fraction to 21%. A further increase of the force to 6.3 pN had no effect. These data show that DNA bending of the U6P is force-dependent (Figure 54a).

Next, the application of DNA strain was probed for the MLP. In the above comparison, a similar bent state occupancy was observed for the U6P and MLP variants of the 0 pN FC (Figure 53a, b). However, increasing the force applied to the MLP to 3.2 pN only decreased the bent state fraction to 43% and a further increase to 6.2 pN was required to decrease the fraction to 18%, similar to the 21% observed for the U6P (Figure 55a). This demonstrates that HsTBP binding to a strong viral promoter is force-dependent as well, but overall binding is more stable as compared to U6P/HsTBP complexes at identical HsTBP concentrations and similar forces (Figure 55a).

These results correlated well to the TATA-box sequence present in the respective promoters. The MLP (TATAAAAG) features a perfect eukaryotic consensus TATA-box sequence (TATAWAWR), whereas the U6P (TTAAAATA) deviates in position two and three. These data also fit the highly dynamic DNA bending measured for HsTBP at the linear U6P. Whereas for the well-studied MLP, a dwell time of approximately 5 s was reported for HsTBP[235]. Surprisingly, the FRET efficiency of the bent state differs considerably between the two promoters. This can only in part be explained by the 1 bp difference in dye position (Figure 50a, b). No crystal structure of just TBP bound to the U6P is available for comparison. Though it has been reported that TBP-induced bending angles in solution can vary significantly between different promoters and their respective crystal structures [438,439]. Notably, the FRET efficiency of the bent state remains constant at all forces for the respective promoters suggesting an independence of the DNA-bending angle from the applied force.

7.3.2 Influence of RNAP II and III transcription factors on TBP-induced DNA bending

In TIRF experiments, complementing the U6P/HsTBP complex with HsBrf2 resulted in a 6.4-fold stabilization of the complex. Following up on this finding, the effect of this factor under mechanical strain was tested. Addition of HsBrf2 to the U6P/HsTBP complex at 0 pN force gave rise to a population with E = 0.74, corresponding to the bent U6P/HsTBP/HsBrf2 complex occupied by 78% of the molecules (Figure 54b). As observed for the U6P/HsTBP complex, an increase in force lead to the decline of the HF fraction to 56% at 2.6 pN and 36% at 6.3 pN. This demonstrates that HsBrf2

conveys stability against mechanical stress. Nevertheless, the U6P/HsTBP/HsBrf2 complex remains sensitive to higher forces.

For HsTFIIB, a stabilization of HsTBP binding to the MLP could be observed. At 0 pN, 69% of complexes were found in the bent state. With force application, this fraction decreased to 58% at 3.2 pN and 31% at 5.9 pN, respectively, indicating comparable stabilization as observed for HsBrf2. However, HsTFIIB was added at 10-fold higher concentrations than HsBrf2 (200 nM). Notably, HsTFIIB shifts the FRET efficiency of the bent population from $E \approx 0.63$ to $E \approx 0.72$, which is in agreement with previous smFRET studies that showed that *S. cerevisiae* TFIIB not only prolongs the DNA/TBP complex lifetimes but also shifts the equilibrium towards the fully bent state [232].

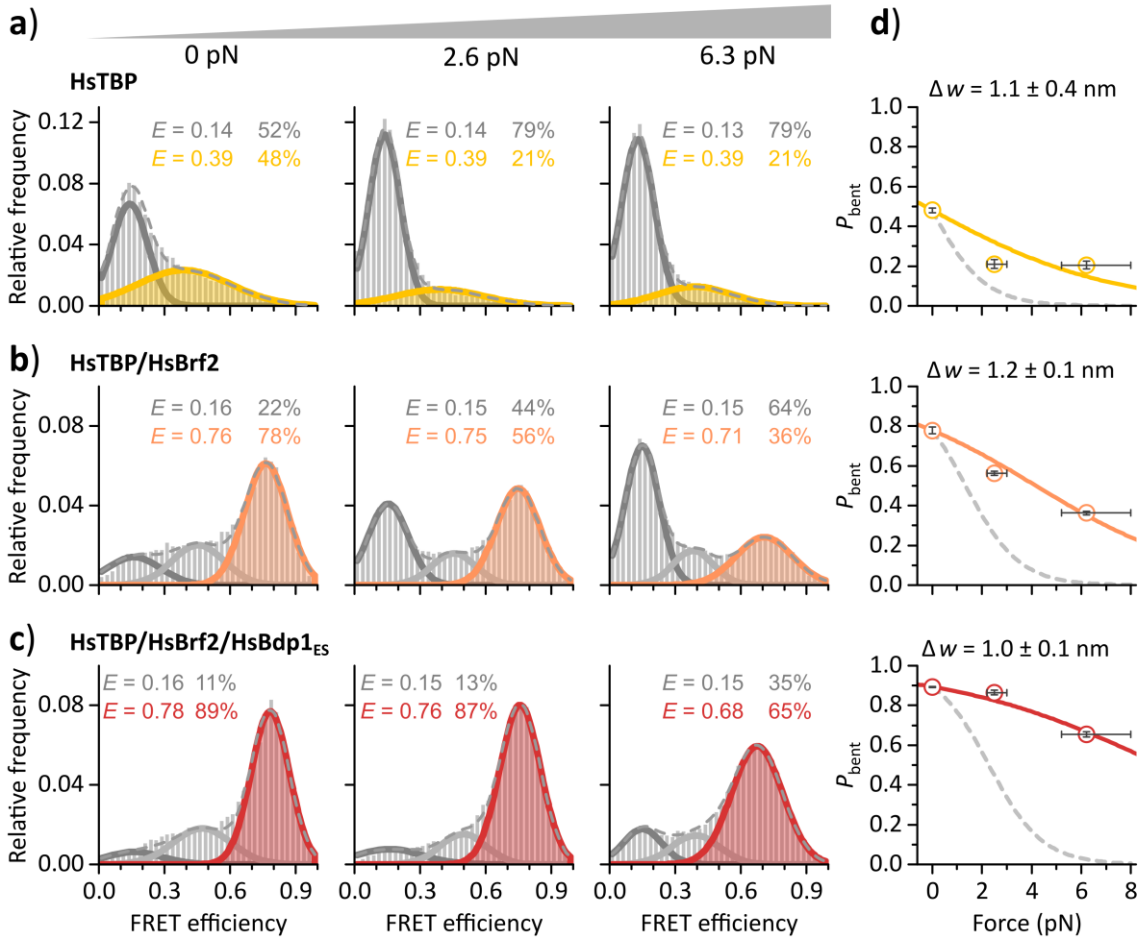

Figure 54: Force-dependency of TFIIIB subcomplex assembly at the U6 promoter. Confocal single-molecule FRET measurements on diffusing molecules monitor HsTBP-induced DNA bending after addition of **a)** HsTBP (20 nM), **b)** HsTBP/HsBrf2 (20 nM/20 nM) and **c)** HsTBP/HsBrf2/HsBdp1$_{ES}$ (20 nM/20 nM/20 nM) to U6P FCs at increasing forces (0, 2.6, 6.3 pN). FRET efficiency histograms show the relative distribution between the unbent DNA state (LF, gray) and TBP-induced bent states in the absence and presence of additional initiation factors (HF, colored). Mean FRET efficiency *E* and the relative area of the fitted Gaussians are indicated by color. The cumulative fit is shown as a dashed line. Data from three technical replicates is shown. **d)** The bent state probability P_{bent} (HF peak area) was fitted with a Boltzmann distribution (solid line) to calculate the end-to-end distance change Δw of the promoter, given as mean ± s.e. of the fit. For comparison, the curve for the geometric model with $\Delta w = 4.29$ nm is shown (dashed line). The x-axis error results from the variance of the single-nucleotide length and the y-axis error is derived via error propagation from the Gaussian fit. Adapted from [434]. See Appendix C.3 for molecule counts, fit parameters and standard deviations.

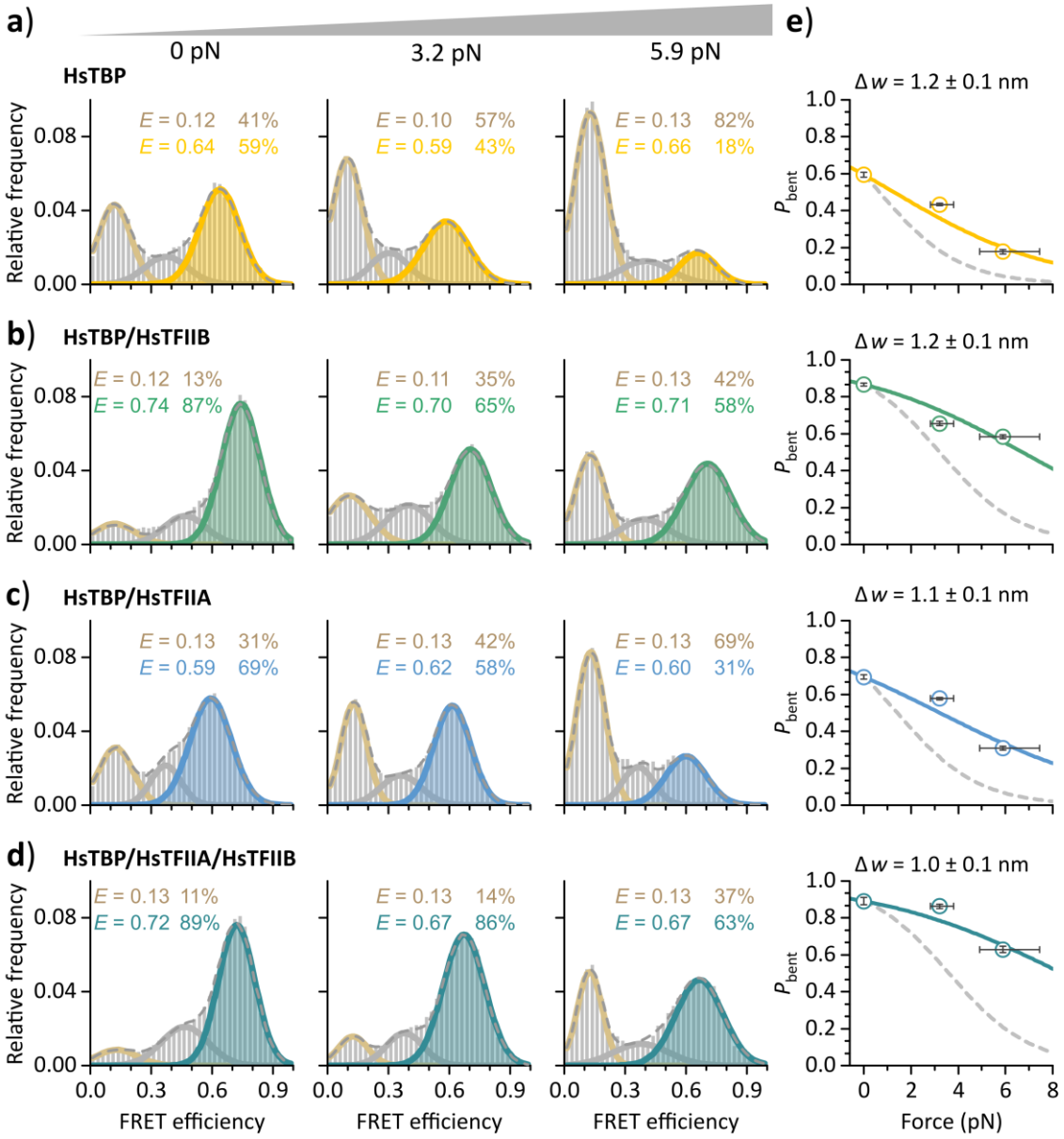

Figure 55: Force-dependency of RNAP II initiation factor assembly at the MLP. Confocal smFRET measurements on diffusing molecules monitor HsTBP-induced DNA bending in the presence of **a)** HsTBP (20 nM), **b)** HsTBP/HsTFIIB (20 nM/200 nM) and **c)** HsTBP/HsTFIIA (20 nM/2 µM) and **d)** HsTBP/HsTFIIA/HsTFIIB (20 nM/2 µM/200 nM) to the MLP FCs at increasing forces (0, 3.2, 5.9 pN). FRET efficiency histograms show the relative distribution between the unbent DNA state (LF, tan) and TBP-induced bent state in the absence and presence of additional initiation factors (HF, colored). Mean FRET efficiency *E* and the relative area of the fitted Gaussians are indicated by color. Data from three technical replicates are shown. **e)** The bent state probability P_{bent} (HF peak area) was fitted with a Boltzmann distribution (solid line) to calculate the end-to-end distance change Δ*w* of the promoter given as mean ± s.e. of the fit. For comparison, the curve for the geometric model with Δ*w* = 2.40 nm is shown (dashed line). The x-axis error results from the variance of the single-nucleotide length (0.63 ± 0.08 nm) and the y-axis error is derived via error propagation from the Gaussian fit. Adapted from [434]. See Appendix C.3 for molecule counts, fit parameters and standard deviations.

Overall, the similarities in complex stabilization for HsBrf2 and HsTFIIB are unsurprising, given the conserved core structure and binding interfaces of both factors. However, HsBrf2 features the additional C-terminal extension that extensively interacts with HsTBP[186,277] (Figure 51a).
In a final step, the U6P/HsTBP/HsBrf2 complex was complemented by $HsBdp1_{ES}$ to allow formation of the full human TFIIIB complex. Earlier experiments showed that $Bdp1_{ES}$ enhances the stability of the complex only by approximately 13–25%. HsBdp1 has also been reported to be the key factor in conveying heparin resistance to the TFIIIB complex [189,191,269,270]. Based on this, it is interesting to test how the force sensitivity of TFIIIB is affected. At 0 pN, 89% of molecules were observed in the bent state after addition of $HsBdp1_{ES}$ with FRET efficiencies comparable to the complex without this factor (E = 0.78). Strikingly, applying 2.6 pN force did not notably decrease the bent fraction (down to 87%) and at 6.3 pN, 65% of complexes are still in the bent state. Concluding from that, $HsBdp1_{ES}$ is the crucial initiation factor that renders the initiation complex fully stable against mechanical strain (Figure 54c).
No homolog of Bdp1 exists in the RNAP II transcription system. However, TFIIA was shown to stabilize TBP on the promoter and to bind the DNA/TBP complex in a similar position to Bdp1 [141,142] (Figure 51 e, f). Thus, it was included in this analysis to explore whether factors that use similar binding positions confer the same degree of stabilization to the DNA/TBP complex. In contrast to Bdp1, TFIIA alone should have a stabilizing effect on the DNA/TBP complex [141,440]. This was tested in experiments using an MLP FC. Across all forces tested, addition of HsTFIIA slightly increased the fraction of bent complexes to 69% at 0 pN (compared to 59% for MLP/HsTBP) and 31% at 5.9 pN (compared to 18% for MLP/HsTBP) (Figure 55b). However, for this stabilization, a relatively high molar concentration was required (2 µM as compared to 20 nM for HsTBP). In contrast to HsTFIIB, no conformational change in the DNA was observed ($E \approx 0.60$).
Addition of both, HsTFIIA and HsTFIIB to the MLP/TBP complex, mimicking TFIIIB, shows practically no effect at 0 pN with 89% of complexes in the bent state as compared to 87% with only HsTFIIB. However, HsTFIIA-induced stabilization becomes noticeable at 3.2 pN with 86% of complexes remaining in the bent state compared to 65% when only HsTFIIB was added. At 5.9 pN, only a minor stabilization was observed (63% HF complexes with HsTFIIA/HsTFIIB versus 58% with HsTFIIB only). This suggests that HsTFIIB represents the crucial factor in the RNAP II system that stabilizes the TBP-DNA interaction at higher forces.
Concluding from these data, the MLP/HsTBP/HsTFIIA/HsTFIIB complex shows comparable force resistance to the U6P/TBP/Brf2/$Bdp1_{ES}$ complex. However, for RNAP II factors, higher concentrations were required to achieve comparable levels of bent state stabilization as RNAP III initiation factors suggesting overall weaker binding of RNAP II initiation factors for the DNA. Additionally, from a perspective of minimal factor requirement for RNAP II versus RNAP III recruitment, HsTBP/HsTFIIB shows less stabilization compared to TFIIIB, suggesting an evolutionary inclination towards higher mechanical resilience for RNAP III initiation factors.
As a final comparison, the probability to encounter the DNA/protein complex in the bent state P_{bent}, which for the above equilibrium measurements is equivalent to the relative HF peak area, was plotted against the applied force (Figure 54d, Figure 55e). P_{bent} is related to the force-dependent change in free energy of the complexes through the Boltzmann distribution (Equation

34). Hence, data points were fitted to a two-state unbent/bent promoter model to retrieve information on the end-to-end distance change Δ*w* of the DNA upon bending, which in turn relates to the amount of work performed by the protein complex. As a reference, the calculated distance change derived from the geometric bending model of the promoter (Chapter 6.4) is plotted as a dashed line. This model assumes the TATA-box center to act as a two-dimensional hinge around which the two stiff, rod-like halves of the promoter DNA rotate upon bending. Data from both transcription systems consistently shows a distance change of 1.1 ± 0.1 nm independent of the promoter sequence or the factors used. Strikingly, this distance change deviates considerably from the predicted value of 2.76 nm for the MLP and 4.29 nm for the U6P. This disparity indicates that either calculated forces are overestimated by a factor of two, or the geometric model does not adequately describe the conformational changes to the promoter DNA.

7.3.3 Influence of mechanical strain on DNA bending kinetics

Experiments performed in this work as well as other smFRET data [217,232,235,236,441] demonstrated that human and *S. cerevisiae* transcription initiation factors display DNA bending dynamics on the microsecond to minutes timescale. The DNA origami FC offers the possibility to study how mechanical forces affect the conformational dynamics of the DNA/TBP system as well as the impact of additional initiation factors. In this context, it is especially interesting whether the increase in strain reduces the lifetime of the TBP-bound bent state (enhanced TBP dissociation with increase in force) or prolongs the lifetime of the unbent DNA state (inhibited TBP association with increase in force).

Based on the data generated in Chapter 7.2.3, the U6P/HsTBP interaction under force was analyzed in a time-resolved manner using TIRF microscopy. DNA origami FCs were immobilized to biotin-PEG coated flow chambers by exploiting several biotin-coupled staple strands incorporated into the underside of the DNA origami FC ensuring correct positioning of the FC structure on the microscope slide [427] (Figure 56a).

While the corresponding confocal experiments where performed with 20 nM HsTBP, this concentration severely reduced trace quality in TIRF experiments and consequently, the HsTBP concentration was reduced to 10 nM, equal to the experiments performed on linear U6P. Examination of fluorescence-time traces from time-resolved measurements of immobilized U6P FCs reveal dynamic switching between LF and HF on the microsecond timescale at forces of 0 pN and 6.3 pN (Figure 56a).

To further quantify the kinetics of the conformational dynamics, the dwell times derived from individual traces via fitting with a HMM were counted in a histogram and fitted with a mono-exponential decay function to determine the mean dwell time τ in the unbent and bent state. At 0 pN, τ_{unbent} is 0.21 s and τ_{bent} is 0.54 s for the HsTBP-U6P interaction (Figure 56b).

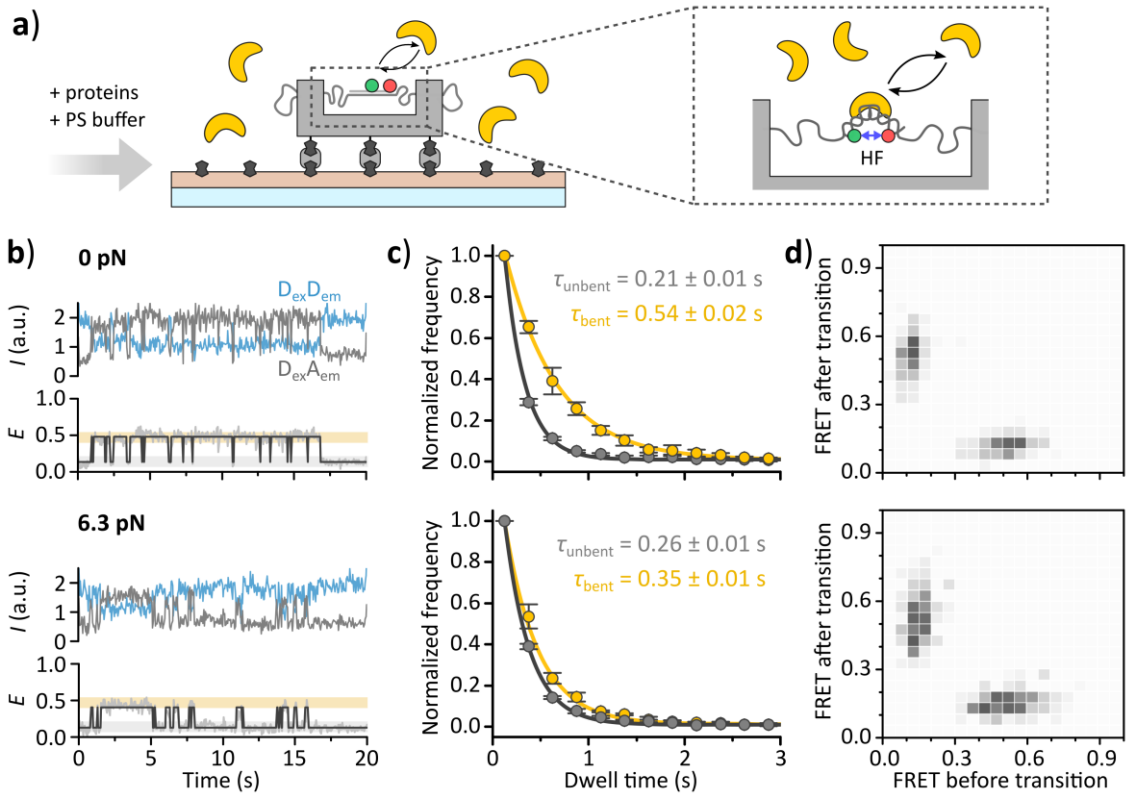

Figure 56: Force-dependency of HsTBP-induce DNA bending dynamics at the U6 promoter. a) DNA origami FCs (0 or 6.3 pN) were immobilized on mPEG coated quartz microscope slides via biotin-NeutrAvidin coupling (see Figure 45 for details). Time resolved smFRET experiments employing TIRF microscopy were performed with 10 nM HsTBP in the sample buffer (equilibrium conditions). The FRET efficiency reports on the unbent (LF) or bent state (HF) of the promoter. **b)** Exemplary fluorescence-time traces showing donor emission ($D_{ex}D_{em}$) or acceptor emission ($D_{ex}A_{em}$) upon donor excitation and the resulting FRET efficiency trace (gray) fitted with a two-step HMM (black). **c)** Dwell time histograms were fitted with a mono-exponential decay function to calculate the mean dwell time τ in the unbent and bent state. Dots and error bars indicate the mean and standard deviation of three technical replicates. **d)** Transition density plots calculated from fitted FRET efficiency traces showing all measured combinations of FRET before and after a transition. The relative occurrence is depicted in gray scale from white (lowest) to black (highest). See Appendix C.3 for molecule counts and fit parameters.

This compares well with the data generated using a short linear promoter, which displayed τ_{unbent} and τ_{unbent} values of 0.14 s and 0.56 s, respectively. Upon applying a force of 6.3 pN, the unbent state dwell time is increased to τ_{unbent} = 0.26 s whereas τ_{bent} decreases to 0.35 s. This amounts to a total increase of τ_{unbent} by 24% and a 38% decrease of τ_{bent} compared to the condition without strain. Previous experiments suggest that the U6P/HsTBP bending dynamics are well described by a two state HMM. To test whether this holds true on a strained system, the transition density plots of samples at all forces were generated (Figure 56d). At both forces, transitions occur exclusively between two well separated states with $E \approx 0.15$ and $E \approx 0.50$.

To probe the dynamics of the MLP/TBP interaction, measurements on immobilized MLP FCs were conducted using TIRF microscopy. To account for the expected higher stability of the HsTBP-MLP complex, the acquisition time was increased to 60 s. In an experiment using 10 nM HsTBP and 0 pN FC, 56% of measured fluorescence-time traces show dynamic switching between different FRET efficiencies, 20% static LF and 24% static HF (Figure 57a).

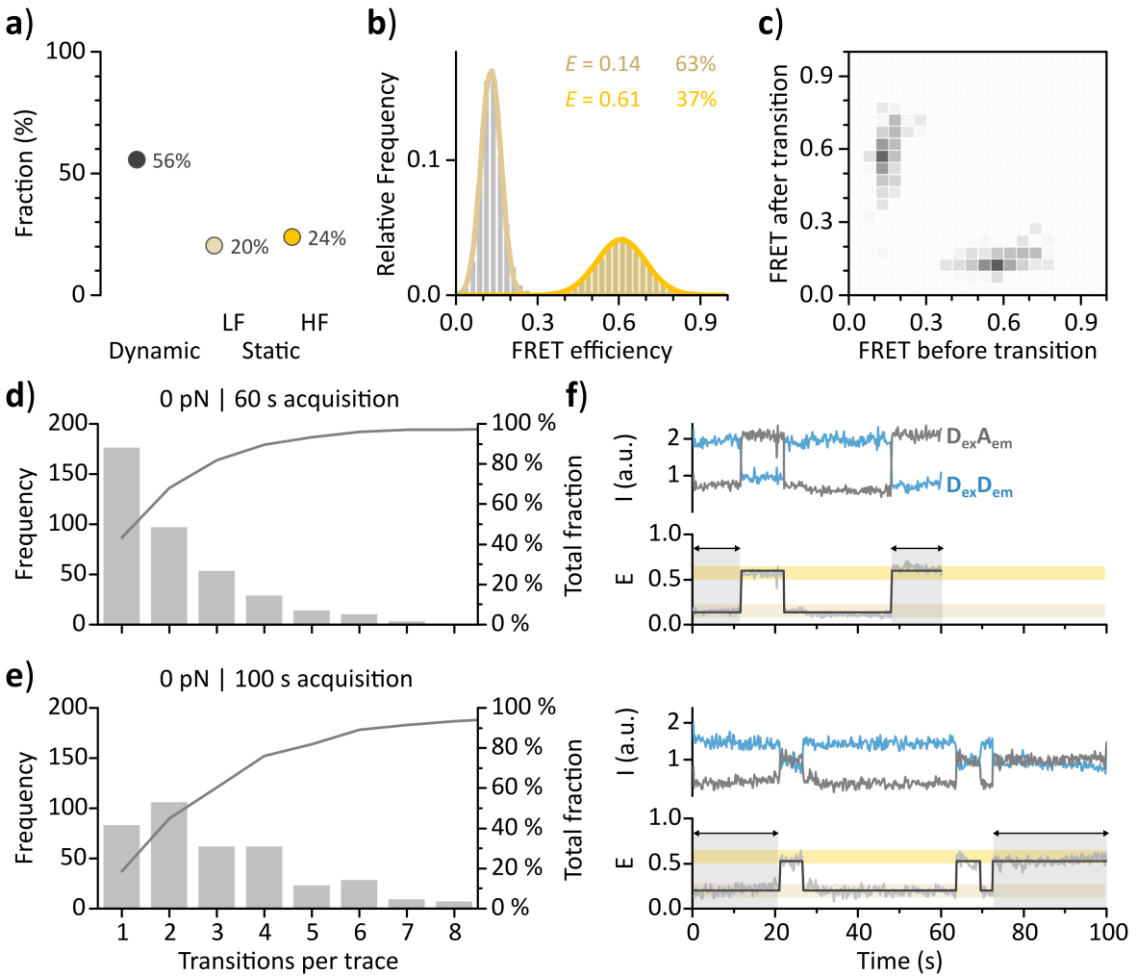

Figure 57: Force-dependency of MLP/HsTBP DNA-bending dynamics analyzed with TIRF microscopy. Immobilized complexes of HsTBP (10 nM in sample buffer) and 0 pN MLP FCs were analyzed with TIRF microscopy. The FRET efficiency reports on the unbent (LF) or bent state (HF) of the promoter. **a)** Fluorescence-time traces were classified based on dynamic switching between unbent/bent or static signal. **b)** FRET efficiency histograms calculated from dynamic traces. The mean FRET efficiency calculated by fitting the data with a Gaussian distribution and the relative fit area are color-coded. **c)** Transition density plot calculated from fitted fluorescence traces showing all measured combinations of FRET before and after a transition. The relative occurrence is depicted in gray scale from white (lowest) to black (highest). **d)** Per-trace transition frequency (bars, left axis) and cumulative fraction (line, right axis) of fluorescence time traces recorded for 60 s and e) 100 s. f) Exemplary fluorescence time traces showing donor excitation followed by donor emission ($D_{ex}D_{em}$) or acceptor emission ($D_{ex}A_{em}$) and the resulting FRET efficiency trace (gray) fitted with a two-step HMM (black). Grayed-out time periods are ignored for dwell time calculation. Data from one experiment are shown. See Appendix C.3 for molecule counts.

The FRET efficiency histogram calculated from dynamic traces shows two fully separated populations with $E = 0.14$ and $E = 0.63$ with a unbent/bent ratio of 37%/63% (Figure 57b). To extract quantitative information on state dwell times, FRET efficiency traces were fitted with a two state HMM. The resulting transition density plot reveals transitions exclusively occurring between $E \approx 0.15$ and $E \approx 0.55$, in line with the FRET efficiency histograms. However, despite 56% of traces showing at least one transition, the overall occurrence of transitions is low. For 60 s acquisition time, 91% of traces contain < 5 state transitions, which is insufficient for accurate dwell time analysis (Figure 57d). Increasing the acquisition time to 100 s did not achieve a substantial improvement. Indeed, more traces contain two instead of one state transition, but still 78% of

traces display < 5 transitions (Figure 57e). Since the initial and final state (Figure 57f, shaded area) of any trace are discarded for dwell time analysis due to unknown start/end time, at least two transitions are required to determine a single dwell time per trace (Figure 57f). Moreover, the relatively high number of static HF traces indicates that the stable bent complex may persist for > 100 s. Thus, TIRF microscopy ultimately seems unsuited for the analysis of HsTBP-MLP interactions.

As an alternative approach to calculate the complex dwell time, confocal microscopy measurements were chosen. The DNA origami FCs and all proteins except HsTBP were added to the sample chamber and 2 min after the start of the experiment, HsTBP was added to initiate complex formation. The relative occupancy of the LF and HF state were used to monitor complex assembly in solution. As formed complexes also disassemble during this time, a perturbation-relaxation kinetics model (Chapter 6.7.4) was used to extract both, assembly and decay constants of the complexes (or the reciprocal dwell times). The model exploits the fact that all complexes analyzed in previous experiments settle in a dynamic equilibrium that is never fully shifted to one side. Following complex assembly into equilibrium allows deconvolution of the combined association/dissociation rate based on the final ratios between unbent and bent state (Figure 58a).

Results from these measurements and analyses show that at 0 pN, the MLP/HsTBP complex is an order of magnitude (τ_{bent}=310 s) more stable than the U6P/HsTBP complex (τ_{bent} = 0.54 s). Increasing force to 5.9 pN has no effect on the bent state lifetime of MLP/HsTBP complexes (remains at 310 s) but the unbent state dwell time increases from 350 s to 800 s (Figure 58b).

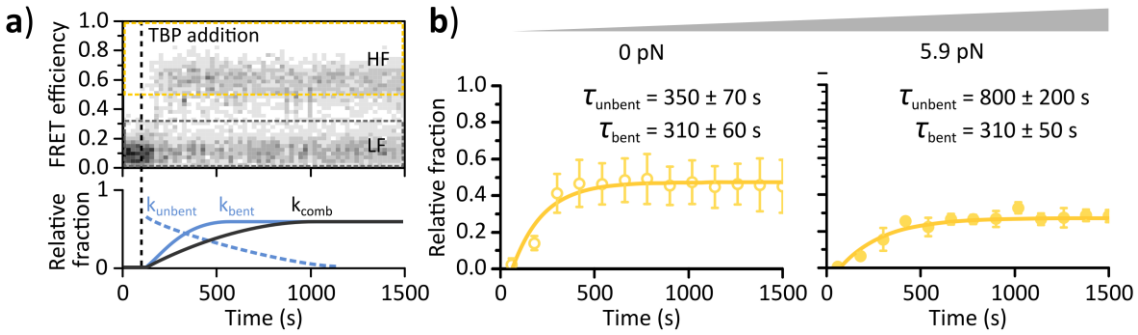

Figure 58: Force-dependency of HsTBP/MLP association and dissociation kinetics analyzed via confocal microscopy. a) Schematic overview of a perturbation-relaxation kinetics experiment. (top) After perturbing the system by TBP addition, HsTBP/MLP complex assembly can be followed over time based on the relative ratio of LF (gray dashed box) to HF signal (yellow dashed box) indicated in grayscale from no occurrence (white) to high occurrence (black). (bottom) As the system relaxes, complexes assemble with the combined association/dissociation rate k_{comb} until an equilibrium is reached from which the individual association rate k_{bent} and dissociation rate k_{unbent} are determined. **b)** Relative fraction of MLP/HsTBP complexes in the bent state as a function of time at 0 pN and 6.3 pN. Data were fitted with a mono-exponential decay function and rate constants were extracted using a perturbation-relaxation kinetics model. Data from three technical replicates is shown. See Appendix C.3 for molecule counts and fit parameters.

Aside from the fact that dwell times differ by an order of magnitude between both promoters, some general trends can be observed for TBP-induced bending of the DNA for each promoter. Data for the U6P/HsTBP complex mainly show a decrease in bent state lifetime, while the reverse is true for the MLP/HsTBP complex, where the unbent state dwell time increases by a factor of

2.3. These data suggest that two factors contribute to the reduction of the bent DNA states at higher forces: i) destabilization of the DNA/TBP complex with increased probability of TBP dissociation from the DNA at higher forces due to the elastic response of the bent DNA in case of the U6P [442] and ii) a decreased probability of TBP to form a stable complex with DNA (TBP entry denial) at the MLP, potentially due to the reduced occurrence of favorable DNA conformations for TBP binding.

7.4 Mechanisms of transcriptional regulation in archaea

In this section the interaction of the transcriptional machinery with regulatory proteins will be explored for three archaeal organisms. Furthermore, the effect of DNA strain will be explored in an analogous fashion as shown for the eukaryotic transcription initiation complexes. *S. acidocaldarius* is a thermophilic crenarchaeon with an optimal growth temperature of approximately 78 °C [443]. *P. furiosus* and *M. jannaschii* are both hyperthermophilic euryarchaea with an optimal growth temperature of around 100 °C and 85 °C, respectively [444,445]. These organisms all live in environments not only characterized by high temperature but additional factors such as high pressure and acidic pH levels and thus demand optimal adaptation and finely tuned genetic regulation. Thus far, the molecular mechanism underlying the function of transcriptional regulators in these organisms have mostly been studied using classical biochemical approaches that only probe general molecular interaction or the influence of these factors on transcription but give no information on conformational changes induced by these interactions. Here, smFRET assays are employed to gain novel insights on the molecular mechanism of a prototypical archaeal transcriptional regulator and a TFB paralog. Additionally, the sensitivity of extremophilic proteins to mechanical strain was probed employing the DNA origami FC technique.

7.4.1 The role of *Sulfolobus acidocaldarius* TFB2 in transcription initiation

The role of the TFB paralog SaTFB2 in transcription initiation in *S. acidocaldarius* is still unexplored. SaTFB2 has 34% amino acid sequence identity to SaTFB1, the housekeeping TFB, and features an identical domain structure, which raises the question, whether SaTFB2 can replace SaTFB1 as a transcription initiation factor. A notable difference is found in the N-terminal cyclin domain, which shows overall low sequence identity in DNA contacting residues (Figure 59a, b). In particular the R/K-G residue pair that contacts the DNA downstream of the TATA-box, which is highly conserved among TFIIB-like factors [121], is only partially present in SaTFB2 (Figure 59b). Bending of the promoter DNA presents a critical step in archaeal PIC formation and in *S. acidocaldarius* was shown to strictly require both, SaTBP and SaTFB1 [232]. In order to investigate the SaTBP/SaTFB1-induced bending of the promoter DNA and to test the capability of SaTFB2 to substitute SaTFB1, smFRET measurements on single diffusing DNA/protein complexes were performed using confocal fluorescence microscopy. The SSV T6 promoter (T6P) derived from the Sulfolobus virus-like particle SSV1, was chosen as a strong native promoter[446] (Figure 59c). In analogy to the above smFRET assay to probe TBP-induced promoter DNA bending of the U6P and MLP, a donor (Cy3B) and acceptor fluorophore (ATTO 647N) were placed in the TS and NTS, yielding a LF signal in the unbent and HF signal in the bent state [232] (Figure 59c). Since *S. acidocaldarius* is a hyperthermophilic organism, the promoter DNA and initiation factors were incubated at 65 °C for 5 min to facilitate complex formation and were diluted by a factor of 50 upon transfer to the buffer-filled sample chamber for smFRET measurements.

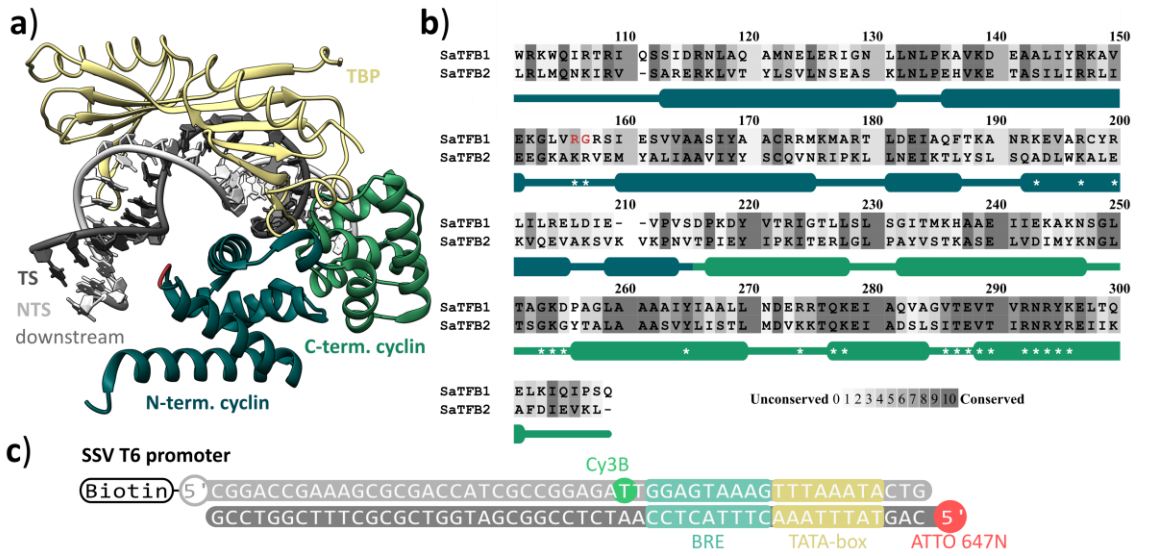

Figure 59: Sequence conservation of *Sulfolobus acidocaldarius* TFB1 and TFB2. a) Crystal structure of the *Pyrococcus woesei* DNA/TBP/TFB complex (PDB: 1D3U) as model for the SSV T6 promoter/SaTBP/SaTFB1 complex. Molecules are color coded: TBP (yellow), TFB C-terminal cyclin (medium green), TFB N-terminal cyclin (dark green), conserved R/K-G motif (red), non-template strand (NTS, light gray), template strand (TS, dark cyan). **b)** Sequence alignment (PRALINE webservice) of SaTFB1 and SaTFB2 cyclin domains. Amino acid conservation is based on chemical properties of the residues and displayed in grayscale. Domains are color coded as in a); α-helices are displayed as rounded boxes. The red R/K-G residues are highly conserved in TFIIB-like factors [121]. Asterisks indicate residues involved in BRE and downstream DNA contacts, based on [121]. **c)** Nucleotide sequence of the SSV T6 promoter. Sequence elements and modifications are indicated by color.

As an initial control, binding of SaTBP only to the T6P was tested. The resulting FRET efficiency histogram shows a single population with $E = 0.19$ confirming that SaTBP alone is incapable of bending even a strong viral promoter (Figure 60a). Further addition of SaTFB2 to the T6P/SaTBP complex yields an identical population, demonstrating, that SaTFB2 does not stabilize SaTBP on the promoter (Figure 60b). In contrast, addition of SaTFB1 to the T6P/SaTBP complex gives rise to a second population with a FRET efficiency of $E = 0.51$ corresponding to the bent DNA conformation. The unbent/bent ratio observed under these conditions was 44%/56% (Figure 60c). Next, SaTFB2 was added to the T6P/SaTBP/SaTFB1 complex to test whether this influences complex formation. Interestingly, addition of a three-fold molar excess of SaTFB2 (compared to SaTFB1) to the T6P/SaTBP/SaTFB1 complex lead to a decrease in the relative HF population to 46%, while the FRET efficiency is not affected. This suggests that SaTFB2 destabilizes the canonical T6P/SaTBP/SaTFB1 pre-initiation complex. To confirm that this effect is dependent on the SaTFB2 concentration, a six-fold molar excess of TFB2 was added, further decreasing the relative HF peak area to 27% (Figure 60d).

Monitoring the change in the relative area of the HF population over time allows to compare the overall stability of individual complexes over the course of the experiments (Figure 60e). All complexes decay at approximately equal rate, losing 0.22–0.27 relative peak area during the 20 min acquisition time. This translates to a 35% reduction for the T6P/SaTBP/SaTFB1.

For the T6P/SaTBP/SaTFB1/SaTFB2 samples, this represents a reduction by 47% and 66% for 3-fold and 6-fold molar excess of SaTFB2, respectively. A comparison of the FRET-2CDE filter values of these complexes shows all populations centered on a FRET-2CDE value of 10, thus providing no evidence for sub-millisecond dynamics. Hence, bent T6P/SaTBP/SaTFB1 complexes are relatively stable at room temperature, even after a factor 50 dilution step but decay noticeably faster in the presence of SaTFB2. Overall, the experiments demonstrate that SaTFB2, while having similar domain organization to SaTFB1, does not function as a canonical transcription initiation factor. Instead, it is possible that the observed destabilization of the canonical T6P/SaTBP/SaTFB1 complex by SaTFB2 represent a regulatory function.

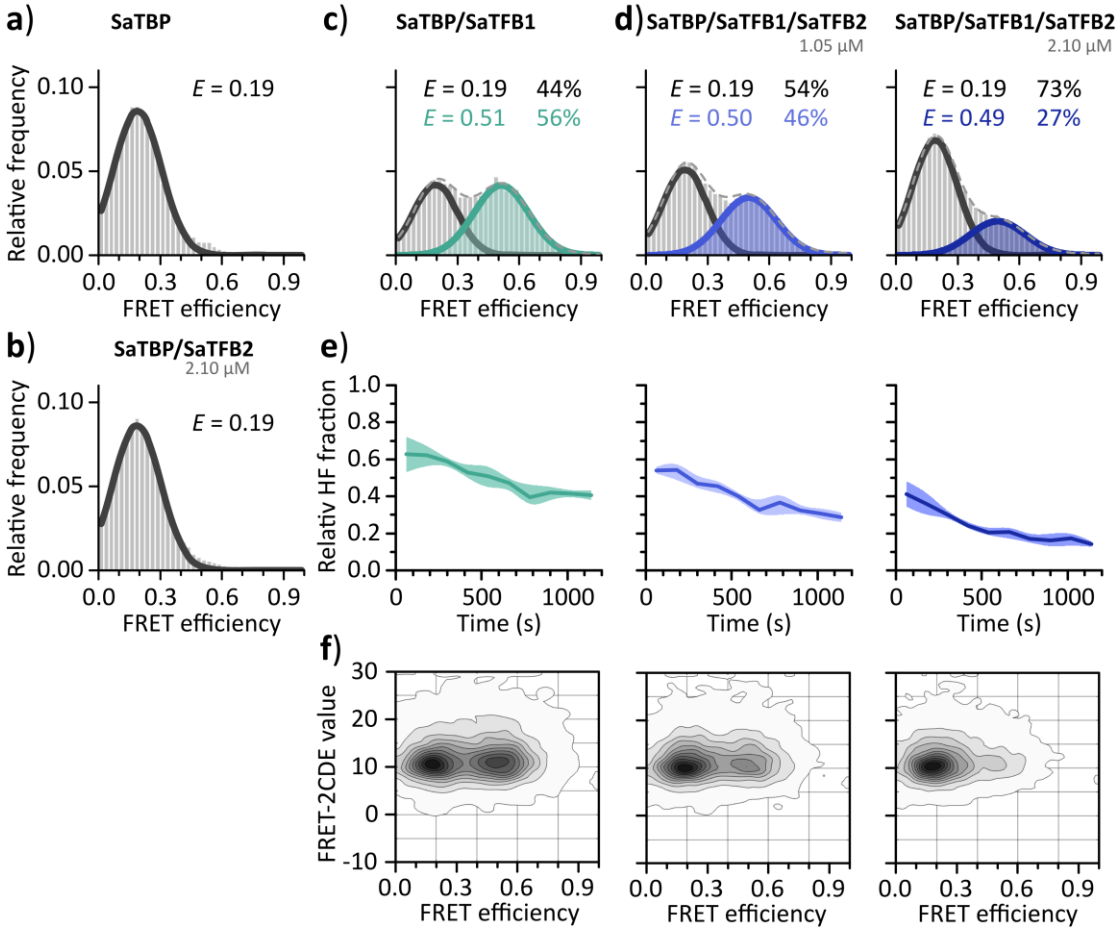

Figure 60: Effects of SaTFB1 and SaTFB2 on promoter DNA bending. The conformational state of the SSV T6 promoter bound by of SaTBP (1.8 µM), SaTFB1 (0.35 µM) and SaTFB2 (1.05–2.10 µM) was probed in confocal smFRET experiments. The FRET efficiency reports on the unbent (LF, black) or bent state (HF, colored) of the promoter DNA. Diffusing complexes of **a)** DNA/SaTBP, **b)** DNA/SaTBP/SaTFB2, **c)** DNA/SaTBP/SaTFB1 and **d)** DNA/SaTBP/SaTFB1/SaTFB2 were measured after 5 min incubation at 65 °C followed by a 50-fold dilution in sample buffer. The mean FRET efficiency *E* and relative area of the Gaussian fit are indicated by color. **e)** The relative HF fraction as a function of time (shaded areas indicate the standard deviation of three technical replicates). **f)** Calculated FRET-2CDE filter values as a function of FRET efficiency. A FRET-2CDE value of 10 indicates stable FRET efficiency. The relative occurrence is depicted in gray scale from white (lowest) to black (highest). See Appendix C.4 for molecule counts, fit parameters and standard deviations.

7.4.2 Analysis of *Pyrococcus furiosus* TFB RF1-assisted transcription initiation

The *P. furiosus* transcriptional regulator PfTFB-RF1 is an ArsR-type stimulates recruitment of PfTFB1 to promoters with weak BREs like the *pf1089* locus [285,288]. PfTFB-RF1 is a single domain factor with a predicted winged HTH DNA binding motif, which is supported by a crystal structure of the homologous protein (amino acid identity 77%) from *Pyrococcus horikoshii* [289] (Figure 61a). ArsR-type transcription factors recognize DNA in a dimer configuration enabling both recognition helices to interact with the major groove of the binding site [289]. PfTFB-RF1 binds to a sequence element directly upstream of the BRE [285] (Figure 61b), which deviates from the *P. furiosus* consensus sequence at all PfTFB-RF1-controlled promoters [288,447]. In order to examine how PfTFB-RF1 affects initiation factor binding, smFRET experiments on freely diffusing DNA/protein complexes were performed. Promoter DNA bending serves as a sensitive readout for the combined presence of PfTBP and PfTFB1 since this step requires both factors in *P. furiosus* [233]. The efficiency of DNA bending was compared for three promoter sequences: i) a native *pf1089* promoter featuring the upstream PfTFB-RF1 binding site and weak BRE (P_{nat}) [285]. ii) An analogous sequence in which the *pf1089* BRE is substituted by a *P. furiosus* consensus BRE (P_{con}). iii) The SSV T6 promoter (Chapter 7.4.1) that does not contain the upstream PfTFB-RF1 binding site. To sense promoter DNA bending via FRET, the donor fluorophore ATTO 532 was positioned at the upstream edge of the BRE and the acceptor ATTO 647N downstream of the TATA-box (Figure 61c).

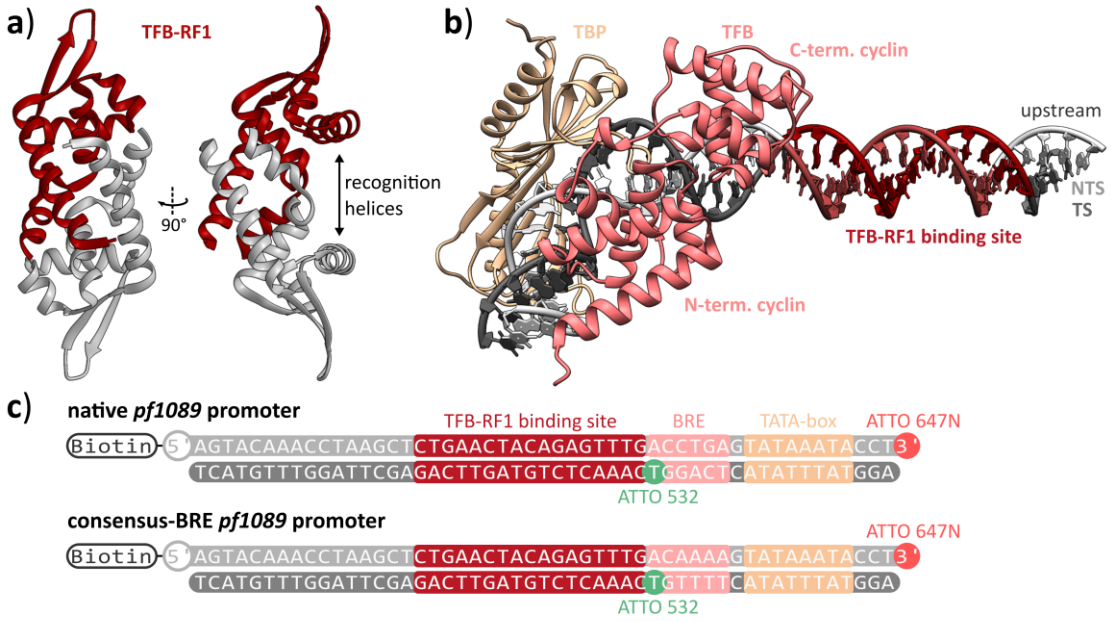

Figure 61: Structural features of the *Pyrococcus furiosus* DNA/TBP/TFB1 complex and TFB-RF1. a) Crystal structure of a *Pyrococcus horikoshii* ArsR-type transcription factor (PDB: 1UB9) that is homologous to PfTFB-RF1. The protein forms a homodimer (red/gray) in solution. **b)** Crystal structure of the *Pyrococcus woesei* DNA/TBP/TFB complex as a model of the P. *furiosus* DNA/TBP/TFB1 complex (PDB: 1D3U), modified with extended upstream DNA to visualize the PfTFB-RF1 binding site (red). Molecules are color-coded: TBP (peach), TFB cyclin core (pink), non-template strand (NTS, light gray), template strand (TS, dark gray). **c)** Schematic overview of the synthetic promoter constructs of the native *pf1089* promoter (P_{nat}) and the analogous variant with a consensus BRE (P_{con}). NTS (light gray), TS (gray).

As a first experiment, the PfTBP/PfTFB1 dependency for DNA bending was tested for the P_{con}. Prior to sample loading, promoter DNA and initiation factors were incubated at 65 °C for 5 min to facilitate complex formation. For the empty promoter, the FRET efficiency histogram shows a single population with a FRET efficiency of 0.33. Addition of PfTBP to the promoter gave the same result with a single population at $E = 0.35$. This confirms that PfTBP alone is insufficient for promoter bending. Adding PfTFB1 to the DNA/TBP complex gives rise to a second population with a FRET efficiency of 0.66. The unbent/bent ratio is nearly even with 46%/54%, demonstrating that the P_{con} is only efficiently bound and bent in the presence of both factors (Figure 62a).

Performing the same set of experiment with the P_{nat} yielded analogous results for the naked promoter and experiments with PfTBP only. Here, only single FRET populations with a FRET efficiency of 0.35 and $E = 0.37$, respectively, were observed. For the P_{nat}, however, addition of PfTFB1 does not lead to the formation of a bent promoter complex, yielding only a single population with a FRET efficiency of 0.37 (Figure 62b). These results are in line with *in vitro* transcription experiments that recorded very low transcriptional output from the *pf1089* promoter in the absence of PfTFB-RF1[285].

Subsequently, PfTFB-RF1 was added to DNA/PfTBP/PfTFB1 complexes of both promoters. For the P_{con}, the two populations observed for the complex without PfTFB-RF1 are still present, however the unbent/bent ratio of 16%/84% now strongly favors the bent state. No change in FRET efficiency was observed indicating that PfTFB-RF1 does not induce conformational changes in the vicinity of the TATA-box (Figure 62a). For the P_{nat}, addition of PfTFB-RF1 induced the formation of a bent promoter complex with two populations at $E = 0.37$ and $E = 0.67$. No reference values for the P_{nat}/PfTBP/PfTFB1 complex are available, but the high similarity to the P_{con} suggests that no conformational change is induced in this case either. Notably, the unbent/bent ratio of 18%/82% is nearly identical to the P_{con}. This demonstrates that in the presence of PfTFB-RF1 both promoters are bound and bent with the same efficiency despite no observable binding at the P_{nat} without PfTFB-RF1 (Figure 62b). These results partially agree with the observations of Ochs *et al*., where *in vitro* transcription experiments quantified PfTFB-RF1 induced enhancement of transcription at the native *pf1089* promoter at 7-fold, whereas no increase was observed for a promoter with a strong BRE, corresponding to the P_{con}. Here, PfTFB-RF1 enhanced DNA bending of the P_{con} by 50 %. No fold-change can be calculated for the P_{nat}, as no bent state formation was observed in the absence of PfTFB-RF1. Moreover, the presence of a LF population in both experiments involving PfTFB-RF1 suggests that promoter DNAs were not saturated with protein.

Additional experiments performed with reduced factor combination demonstrate that PfTFB1 alone is unable to induce promoter bending, as is PfTFB-RF1. Measurements with only PfTBP and PfTFB-RF1 confirm that PfTFB-RF1 is unable to stabilize PfTBP on the promoter DNA as no bent state formation was observed (Figure 62c).

The requirement for the PfTFB-RF1 binding site was probed using the SSV T6 promoter (Figure 62c), that features a similar BRE to the P_{con} but does not contain the downstream PfTFB-RF1 binding motif. These experiments demonstrate that the PfTBP/PfTFB1 complex assembles even more efficiently on the SSV T6, as the FRET efficiency histogram shows two population with $E = 0.19$ and $E = 0.45$ with an unbent/bent ratio of 54%/46% with one third of the protein

concentrations applied for the P_{con}. However, addition of PfTFB-RF1 to the bent SSV T6 promoter complex does not increase the HF fraction as observed for the P_{con}, confirming that PfTFB-RF1 activity is dependent on the upstream binding site.

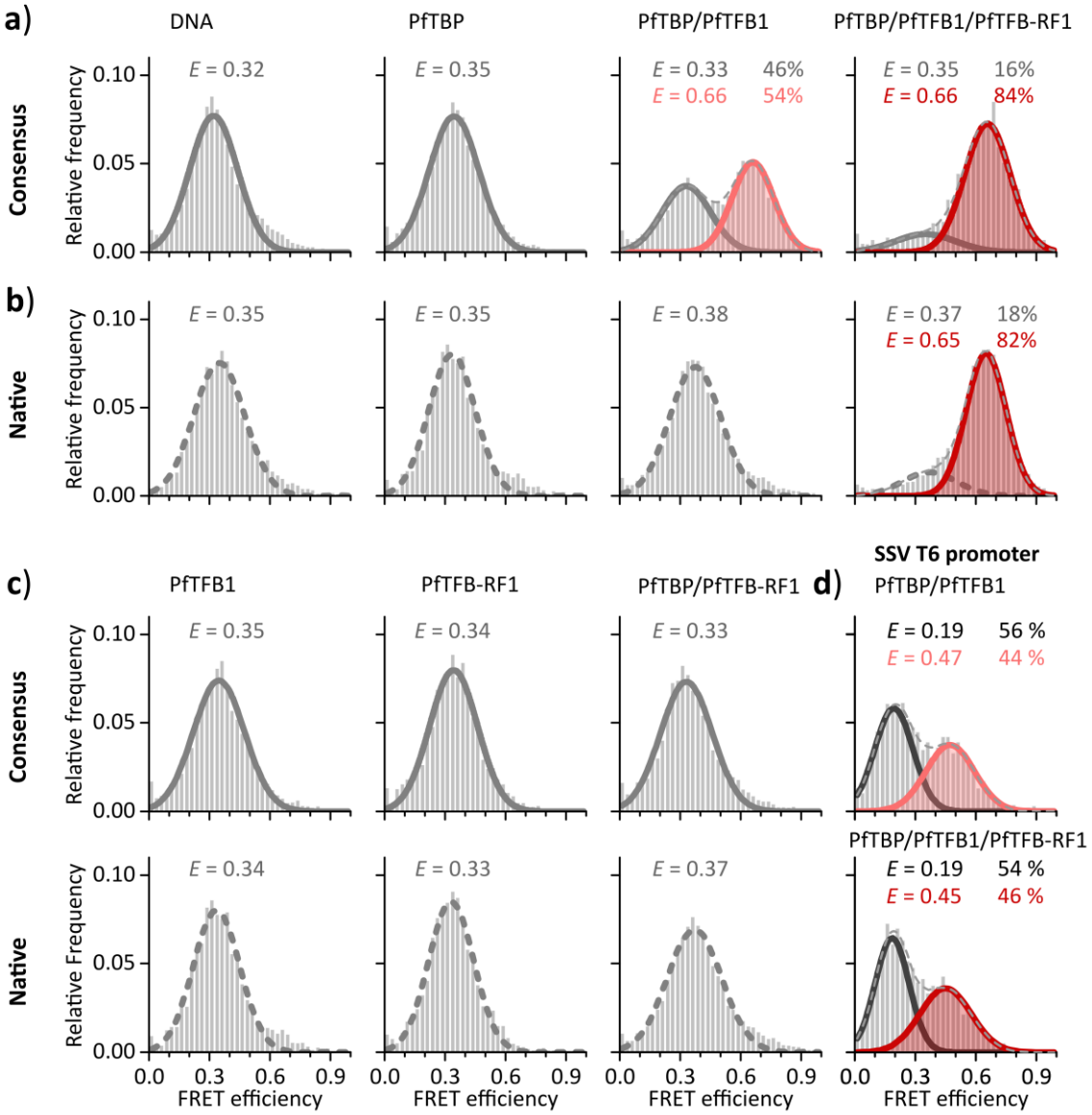

Figure 62: Initiation factor and regulator assembly in the *Pyrococcus furiosus* transcription system. The initiation factor and PfTFB-RF1 regulator assembly on **a)** a *pf1089* promoter with a *P. furiosus* consensus BRE (solid lines) and **b)** a native *pf1089* promoter (dashed lines) was monitored using confocal smFRET measurements on diffusing complexes. Samples of PfTBP (300 nM), PfTFB1 (300 nM), PfTFB-RF1 (300 nM) and promoter DNA were assembled at 65 °C for 5 min. The FRET efficiency reports on the unbent (LF, gray) or bent state (HF, colored) of the promoter DNA. **c)** Control measurements using non-canonical factor combination. **d)** Control measurement using an SSV T6 promoter (black lines) lacking the PfTFB-RF1 binding site. Samples of PfTBP (100 nM), PfTFB1 (100 nM), PfTFB-RF1 (300 nM) and promoter DNA were assembled at 65 °C for 5 min. Data from three (a, b), one (c) and two (d) technical replicates are shown. See Appendix C.5 for molecule counts, fit parameters and standard deviations.

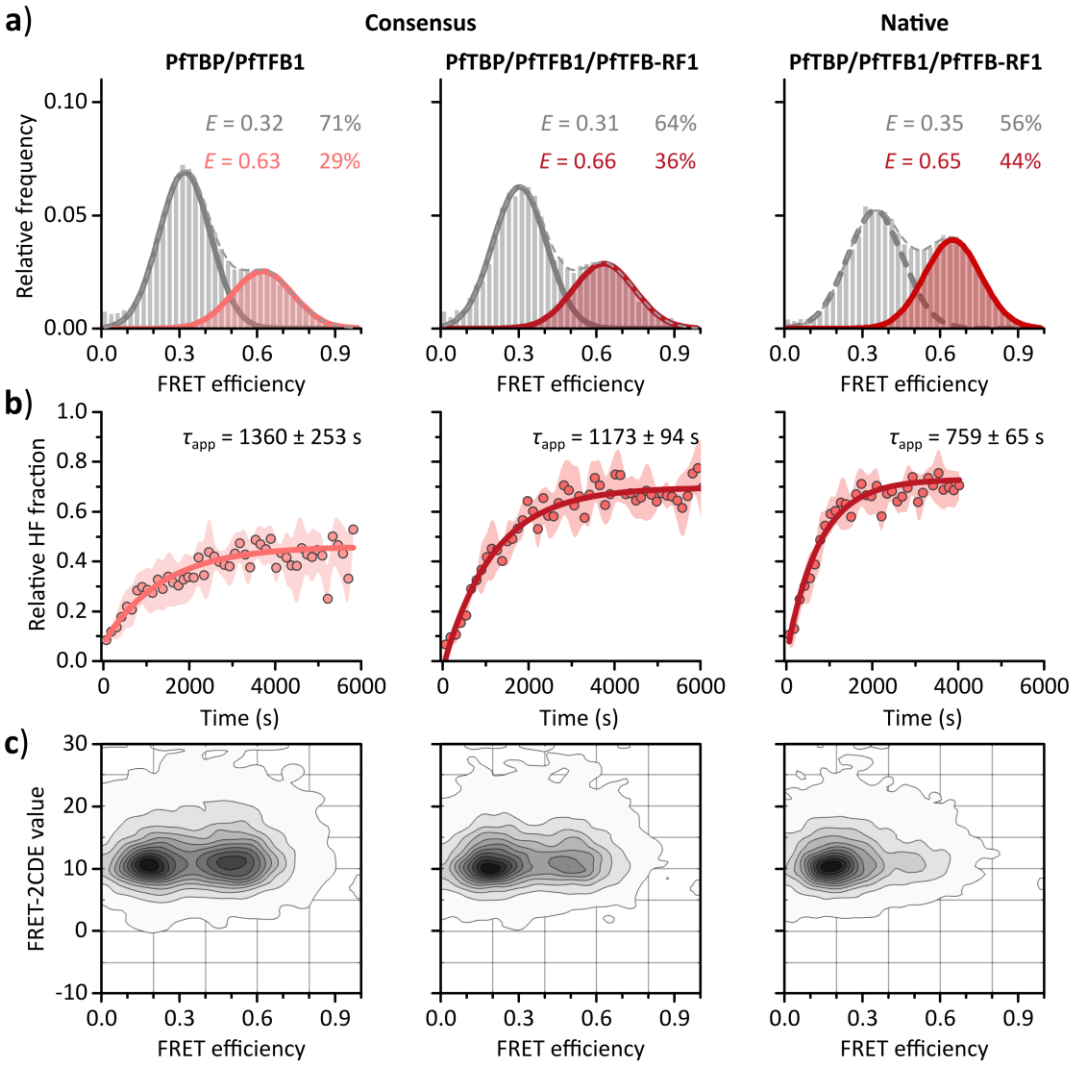

Figure 63: Kinetics of PfTFB-RF1 facilitated TFB recruitment. The initiation factor assembly on a native PfTFB-RF1-controlled promoter and an equivalent promoter with consensus BRE and TATA box was monitored over time using confocal smFRET measurements on diffusing complexes at room temperature. The FRET efficiency reports on the unbent (LF, gray) or bent state (HF, colored) of the promoter DNA. **a)** FRET efficiency histograms calculated for the first 35 min of time course experiments. The mean FRET efficiencies and relative areas of the Gaussian fit are indicated by color. **b)** The relative fraction of HF signals was monitored over time. The apparent mean dwell time in the unbent state was derived from a mono-exponential fit (solid line). The mean and standard deviation (dots and shaded area) of three experiments are shown. **c)** FRET-2CDE filter values calculated as a function of FRET efficiency. A FRET-2CDE value of 10 indicates stable FRET efficiency over the duration of a burst. The relative occurrence is depicted in gray scale from white (lowest) to black (highest). See Appendix C.5 for molecule counts, fit parameters.

To further analyze the different behavior of both *pf1089* derived promoters, the formation rate for all bent promoter complexes was monitored over time. These experiments were performed at room temperature as the samples cannot be heated during the measurement. At the concentrations used, *P. furiosus* initiation factors assemble on the promoter DNA even at room temperature, albeit with lower efficiency as compared to 65 °C (Figure 63a). FRET efficiency histograms calculated for the first 35 min of room temperature time course experiments display similar FRET efficiencies compared to the respective 65 °C pre-incubation datasets. However, for the P_{con}, the unbent/bent ratio is almost identical for both, the P_{con}/PfTBP/PfTFB1 and

P_{con}/PfTBP/PfTFB1/PfTFB-RF1 complexes with 71%/29% and 64%/36% respectively. In comparison, the histograms calculated for the P_{nat}/PfTBP/PfTFB1/PfTFB-RF1 complex shows a considerably higher unbent/bent ratio of 56%/46% (Figure 63a).

These results correlate well with apparent mean dwell times calculated from the entire time course series (Figure 63b). Here, similar mean unbent state dwell times were observed for the P_{con}/PfTBP/PfTFB1 (τ_{app} = 1350 s) and P_{con}/PfTBP/PfTFB1/PfTFB-RF1 complexes (τ_{app} = 1173 s). Assembly of the P_{nat}/PfTBP/PfTFB1/PfTFB-RF1 complex proceeds approximately 40% faster with a mean apparent unbent state dwell time of 759 s. Notably, both PfTFB-RF1 containing complexes reach the same equilibrium unbent/bent ratio of approximately 28%/72% (Figure 63b).

A comparison of the FRET-2CDE filter values for all analyzed complexes does not reveal dynamics on the microsecond timescale, as all populations are centered around FRET-2CDE values of 10, suggesting that all complexes are relatively stable a room temperature (Figure 63c).

These results demonstrate that PfTFB-RF1 is active at room temperature. Moreover, they indicate that, at these conditions, PfTFB-RF1 only has a minor effect of the rate of PfTFB1 recruitment at the P_{con} while still affecting the equilibrium state. This may imply competition between canonical binding of PfTFB1 to the BRE with PfTFB-RF1-facilitated PfTFB1 recruitment at the consensus promoter that does not occur at the native promoter due to the weak BRE.

7.4.3 Force-dependency of DNA bending induced by archaeal transcription factors

The above data as well a previous studies demonstrated the strict dependence of *P. furiosus* and *S. acidocaldarius* on the presence of TBP as well as TFB in the critical promoter bending step [232,233]. In this context, it is interesting to study how force affects a system that is strictly dependent on the binding of two factors. Here, the TBP/TFB-induced promoter bending was investigated using the DNA origami FC (Figure 64a). The *P. furiosus* transcription system is well suited for this investigation as the above measurements verified that PfTBP and PfTFB1 efficiently assemble at room temperature (Figure 64a). This is a crucial factor, as the DNA origami unfolds at higher temperatures.

For comparison, an archaeal transcription system that can achieve a bent promoter conformation with only TBP was chosen. The *M. jannaschii* transcription machinery fulfills this criterion [232] and was also the first protein to be probed using the DNA origami FC technique, providing a solid reference point[94]. In the proof of concept study, Nickels *et al.* investigated the force-dependency of MjTBP binding to an SSV T6 promoter. Their findings suggest that MjTBP is relatively force resistant at 35 °C, as binding could still be observed at forces up to 11.4 pN. Consequently, the SSV T6 promoter was used here as a promoter sequence.

First, the SSV T6 promoter FC was tested in isolation. FCS experiments confirmed the correct hybridization of the doubly labeled promoter strand, as the measured relative diffusion time for the FC is approximately six times higher than for a 55 nt linear SSV T6 promoter (Figure 64b). FRET efficiency histograms show a single uniform population for all forces with a mean FRET efficiency of E = 0.19–0.21 indicating that force does not affect the conformational state of the DNA (Figure 65c).

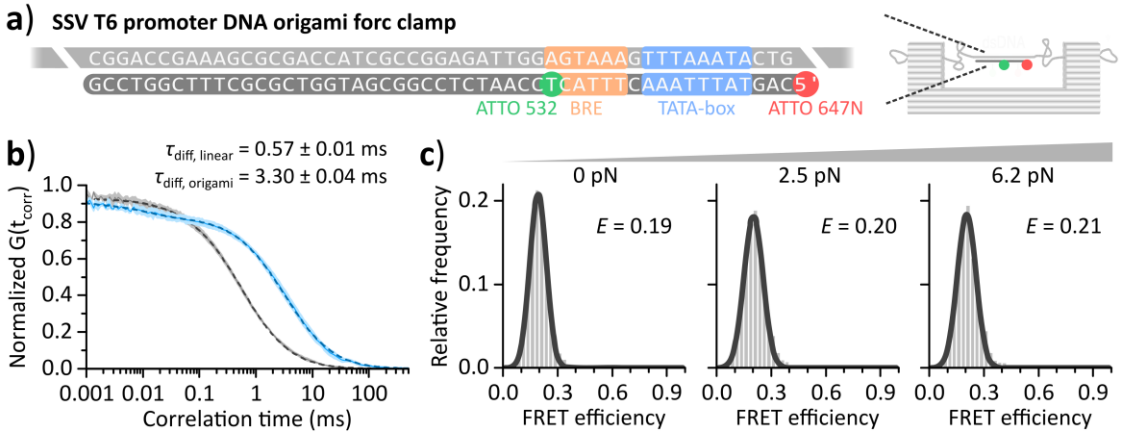

Figure 64: Comparison of a linear double stranded SSV T6 promoter to a DNA origami force clamp. DNA constructs were analyzed using confocal fluorescence microscopy on diffusing molecules. **a)** Schematic model of the DNA origami FC and nucleotide sequence of the dsDNA promoter positioned inside the spring. The non-template strand (light gray) is part of the origami scaffold (indicated white dash). Sequence elements and fluorophore modifications of the template strand (dark gray) are color-coded. FRET between the donor (ATTO 532) and acceptor dye (ATTO 647N) reports on the unbent/bent state of the SSV T6 promoter. **b)** The relative diffusion speed τ_{diff} of a 55 nt linear dsDNA SSV T6 promoter and an SSV T6 promoter annealed to the spring region of a DNA origami FC were compared based on FCS measurements. Values are given as mean ± s.e. of the exponential fit model. **c)** The conformational state of the promoter DNA in the absence of proteins was probed using smFRET measurements. Data from three experiments are shown. See Appendix C.6 for molecule counts, fit parameters and standard deviations.

Addition of 50 µM MjTBP to a 0 pN FC gave rise to an additional population with E = 0.62 corresponding to the bent promoter state as well as additional density at E = 0.44, that was also observed for the MLP and U6 FCs (Figure 65a). Since this population does not show any force dependency and seems unconnected to the functionality of the initiation factors, it was accounted for by fitting a third Gaussian with a fixed area and will be disregarded for the remainder of this section. Without force, the unbent/bent ratio observed for the bent DNA/TBP complex is 44%/56% suggesting efficient complex formation. When force is applied, a stepwise reduction of the HF population was observed, decreasing to 38% at 2.6 pN and 21% at 6.2 pN. FRET efficiencies seem overall unaffected by the increase in force with E = 0.19 and E = 0.59 at 6.2 pN. Notwithstanding the central FRET density, these results are in line with the reference data from Nickels *et al*. and the unbent/bent ratios observed here are similar, demonstrating reliable force calibration of the DNA origami.

Next, PfTBP and PfTFB1 were analyzed using the same FC. Since previous experiments established that TBP is insufficient for promoter bending, tests using the isolated factors were omitted. In experiments using a 0 pN FC, two populations arise with FRET efficiencies of E =0.21 and E = 0.52. Complex formation is efficient with an unbent/bent ratio of 34%/66% as previous experiments demonstrated (Figure 65d). Notably, compared to the *M. jannaschii* system, the overall lower FRET efficiencies of the HF state suggest a slightly different conformation for the bent promoter complex. Upon force exertion the relative area of the HF population decreases to 55% at 2.6 pN and 37% at 6.2 pN, demonstrating that the two-factor *P. furiosus* system is equally effective at bending the promoter DNA against external force. Consistent with the previous FC experiments, the FRET efficiency of the bent state is unaffected by an increase in force with E = 0.51 at 0 pN and E = 0.49 ant 6.2 pN.

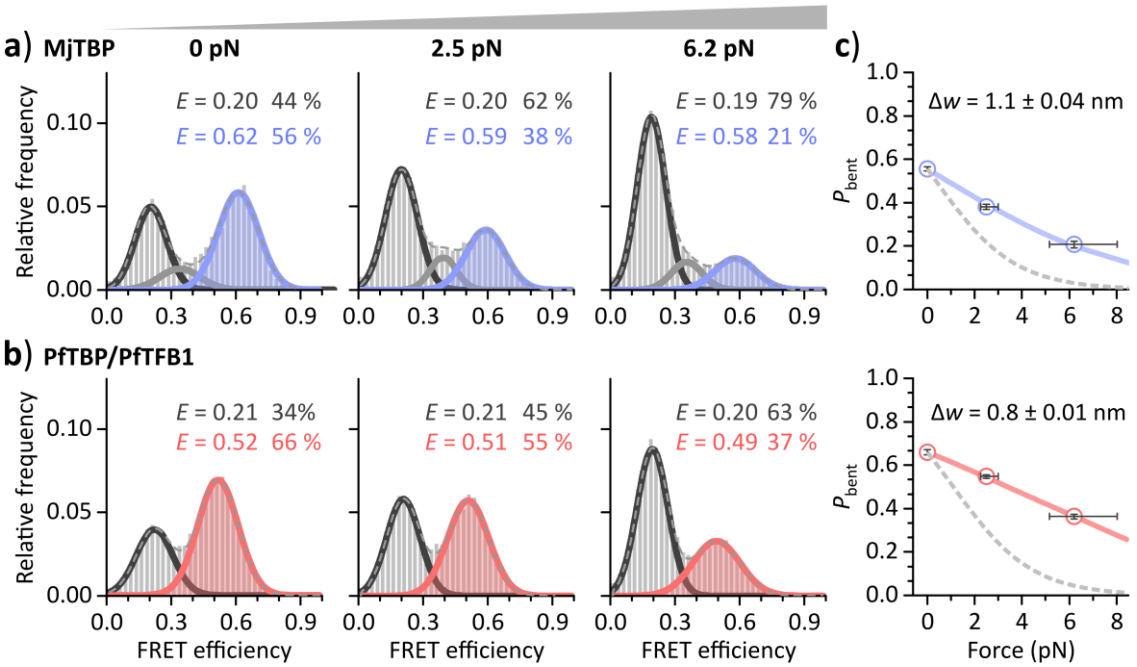

Figure 65: Force-dependency of promoter DNA bending by archaeal transcription initiation factors. Complex formation of **a)** MjTBP (50 µM), **b)** PfTBP (100 nM) and PfTFB1 (100 nM) at the SSV T6 promoter was probed at different forces using a DNA origami FC. Confocal smFRET measurements were performed on diffusing complexes. The FRET efficiency reports on the unbent (LF, black) or bent (HF, colored) state of the promoter. The mean FRET efficiency and relative area of the Gaussian fit are indicated by color. The center population (gray) in a) was included to improve fitting accuracy but excluded from further analysis. **c)** The bent state probability P_{bent} (HF peak area) was fitted with a Boltzmann distribution (solid line) to calculate the end-to-end distance change Δw of the promoter, given as mean ± s.e. of the fit. For comparison, the curve for the geometric model with Δw = 2.53 nm is shown (dashed line). The x-axis error results from the variance of the single-nucleotide length and the y-axis error is derived via error propagation from the Gaussian fit. Mean values were obtained from three technical replicates. See Appendix C.6 for molecule counts, fit parameters and standard deviations.

The relative fit areas of the HF population directly translate the probability of encountering the complex in the bent state P_{bent}. Fitting these experimental data to a Boltzmann distribution for the two-state promoter system provides information on the resulting end-to-end distance change Δw of the promoter DNA. For the *M. jannaschii* system, Δw = 1.1 nm and for the *P. furiosus* system, Δw = 0.8 nm. These values deviate considerably from the expected 2.5 nm derived from the geometric model. However, the higher distance change for the *M. jannaschii* system is consistent with the observed higher FRET efficiency of the bent state.

In conclusion, probing the force dependency of DNA bending by archaeal initiation factors demonstrated that the FC presents a reliable way to compare forces, yielding a similar bent state probability decay in relation to force as observed in previous experiments [94]. The bent state probabilities derived from these results in combination with the above data for the U6P and MLP do, however, point out that the model used to describe the force-DNA extension relation requires further refinement. From the newly tested *P. furiosus* transcription factors it becomes evident that mandatory three-factor interactions such as PfTBP/PfTFB1-induced DNA bending can occur under strained conditions.

8 Discussion

8.1 Influence of individual subunits on TFIIIB assembly

The stepwise assembly of human TFIIIB from its individual subunits was analyzed using TIRF microscopy on immobilized U6P DNA fragments. Complex formation was detected by the change in FRET efficiency upon HsTBP binding. Individual fluorescence intensity-time traces revealed dynamic bending of the promoter DNA in addition to traces with stable FRET efficiency. The relative fractions of dynamic, static LF and static HF traces were compared for two different conditions: i) with proteins in the measurement chamber and ii) after a washing step to evaluate the effect of HsBrf2 and two truncated HsBdp1 variants on bent state stabilization and DNA conformation. In addition to the characterization of the hierarchical assembly of HsTFIIIB with TIRF microscopy, the individual subcomplexes were probed for their mechanical resistance using the DNA origami FC technique. These experiments were compared side-by-side with homologous subcomplexes of the human RNAP II transcription system using a strong viral MLP to determine differences in complex stabilization at the early stages of PIC assembly. In this section, results obtained for the individual TFIIIB subcomplexes will be discusses with respect to both experimental approaches as they are complementary in nature. The effect of force observed in confocal microscopy experiments will be addressed in Chapter 8.2.

8.1.1 Influence of DNA sequence on HsTBP-induced DNA bending dynamics

TIRF microscopy experiments with immobilized short linear U6P constructs as well as DNA origami FCs demonstrated that HsTBP binds to the promoter in a highly transient manner with a mean bent state lifetime of 0.54–0.56 s and only a minor fraction of fluorescence traces showed static HF (8 %). In line with this, practically no dynamic traces were observed after a washing step but a minor fraction of static HF traces (6%) remained intact. This suggests the presence of two kinetically distinct U6P/HsTBP complex variants, one displaying short and the other long binding times. This has been reported by others measurements employing similar smFRET measurements on immobilized MLP/HsTBP complexes [235]. In their study, the authors observed a majority of transient binding events with a bent state lifetime of 5 s and a minor fraction with complex lifetimes of 50 s

Comparable results using a consensus TATA-box promoter similar to the MLP (TATA-box sequence: TATAAAAG) were obtained by another study that applied an ensemble approach to determine a slow and a fast rate for HsTBP dissociating from the promoter after competitor addition, translating to a bent state dwell time of 50 s for the fast and >10 min for the slow dissociating species [236]. Thus, the fraction of stable HF traces observed in this work likely presents a long-lived subpopulation with a bent state lifetime longer than the 10–20 s acquisition time used here. Congruent with the references, FRET efficiencies are identical for dynamic and static species [235,236]. Overall, bent state dwell times for the U6P/HsTBP complex are markedly shorter than those obtained for the MLP, which suggests a lower affinity of HsTBP for the U6P. The TATA-box of the U6P (TTAAAATA) deviates from the human consensus TATA sequence (TATAWAWR [201]), specifically in the first highly conserved TATA tetranucleotide which has long

been known to be essential for efficient binding and bending by TBP [204,448]. *In silico* studies provide a DNA-mechanical explanation for this phenomenon [205]. In their computational analysis, the authors compared the influence of different nucleotides at each base pair step of the TATA box on TBP-selectivity. They particularly highlighted the importance of an adenine at position two of the TATA-box that minimized the cost of bending. Furthermore, molecular dynamics simulations of DNA/TBP complexes determined one of the main dissociation mechanisms for TBP to be a pincer-motion of the stirrups that withdraws the phenylalanine residues inserted between the first base pairs of the TATA-box [449]. The first TT base pair step in the U6P represents a major difference between the U6P and MLP and might be a deciding factor for the faster unbent/bent state transitions observed for the U6P.

The kinetics analysis of individual FRET efficiency-time traces showed uniform transitions between two states and no intermediate step with a distinct bending angle. This result is congruent with other smFRET data collected for HsTBP, where only two states where observed for the MLP/HsTBP complex [235,236]. In contrast, smFRET studies [232] or tethered particle motion experiments [450] reported three (or more [441]) binding steps for *S. cerevisiae* TBP (hereafter denoted as Sc in protein names). In their model, ScTBP fluctuates between an unbent, partially and fully bent state that all differ in bending angle. In smFRET studies using the *S. cerevisiae* H2B promoter [232] or the MLP [441], these distinct bending angles are detectable as different FRET efficiency states. Additionally, these investigations detected orientational isoforms of each state corresponding to TBP bound to the DNA in inverse orientation [217] that were described by previous ensemble studies [209,234,451].

None of the above phenomena were detectable in TIRF experiments with the U6P as well as the initial TIRF microscopy analysis of HsTBP binding to MLP FCs and both are in agreement with reference smFRET studies using HsTBP [235,236]. Intriguingly, this mode of operation is reminiscent of archaeal transcription systems, where TBP or TBP/TFB bind and bend the promoters DNA in a single step [232]. Whether single-step bending is specific to the promoter sequence or constitutes a general feature of HsTBP will require further investigation.

The effect of promoter flanking sequences on HsTBP binding has been investigated by Hieb *et al.* using smFRET constructs with identical TATA-box sequences and different length of TATA-flanking DNA (total length 14–27 bp) and detected a considerable broadening of the bent state population for longer DNA constructs [236]. Based on kinetics data, the authors reason that HsTBP first binds the DNA in an unspecific manner until reaching thermodynamic equilibrium at the TATA-box [236]. It is likely that a similar effect is causal for the different width of bent state populations observed in confocal experiments for the U6P (55 bp) compared to the MLP (35 bp). A broadened HF population was, however, not observed in TIRF experiments with the U6P. Possibly, such unspecific binding events resulted in fluorescence traces with low quality that were not included in the analysis. In addition to broadening of the bent state population, the authors observed reduced binding affinities for longer DNA constructs [236]. This further supports the difference in DNA binding affinity observed for the long U6P and shorter MLP construct.

Extending the scope of the analysis beyond the TATA-box, additional factors become significant for TBP-binding. In this work, only the isolated TATA-box and flanking regions of the U6-2 snRNA

promoter were probed for TFIIIB assembly, however, *in vivo* the situation is more complex. Of several identified U6 snRNA gene copies, only five (U6-1, U6-2, U6-7, U6-8, U6-9) are actively transcribed [452]. A study that compared the *in vivo* and *in vitro* transcription efficiency of the individual gene copies reported low *in vitro* transcription output from the U6-2 promoter, which correlates well with the transient HsTBP binding observed here (Figure 66). In contrast, *in vivo* transcription from plasmids transfected into human HEK293 cells was most efficient for the U6-2 [452]. Interestingly, the non-canonical TATA-box of the U6P is overall conserved for all active gene copies. Still, all other copies showed higher *in vitro* transcription rates than U6-2 (Figure 66). The authors linked the high variation to differences in the PSE sequence around -15 relative to the TATA-box. The findings of Domitrovich and coworkers demonstrate that, while functional as an isolated system *in vitro*, HsTFIIIB directed transcription by RNAP III is heavily modified by additional factors *in vivo*. The TATA-box is not the final determinant for transcription efficiency of the U6P, however, its presence is a crucial factor to distinguish RNAP II and RNAP III transcribed snRNA genes by means of the selectivity factor SNAPc [260,261].

Figure 66: Sequence alignment of the promoter regions of human U6 snRNA genes. The immediate upstream promoter region of the five actively transcribed human U6 snRNA loci was aligned using the T-COFFEE webservice [453] and a consensus logo including the TATA-box (yellow) as well as upstream GR and downstream TD motif (orange) were generated using the MEME suite motif discovery [454]. Transcription efficiency values relative to U6-1 are taken from reference [452].

8.1.2 Different DNA bending angles for U6 promoter and MLP complexes

Even though the same HsTBP was used in DNA-bending experiments with the U6P and MLP, the FRET efficiency measured for the bent state differed considerably between the U6P/HsTBP (E = 0.39) and MLP/HsTBP complex (E = 0.63). This indicates a difference in donor-acceptor fluorophore distance and in extension, a different bending angle of the DNA. A study which compared differences in DNA bending angle induced by ScTBP for several mutated TATA-box sequences using ensemble FRET measurements determined that even single nucleotide changes in the sequence can drastically change the bending angle [438].

A possible explanation for this observed difference in apparent bending angles may lie in the inherent mechanical properties of both promoter sequences. A study employing gel mobility assays examined the influence of dinucleotide steps within the TATA-box on TBP-induced DNA bending [455]. The authors determined that an AG dinucleotide at position 7/8, as present in the MLP sequence, leads to the largest bending angles (65–76°). Interestingly, the second largest angles (63–65°) were measured for the TA dinucleotide found in the human U6P sequence [455]. Moreover, both sequences contain a central tetra-adenine sequence (A-tract) which is known for

its inherent rigidity [456] and has been shown to significantly contribute to DNA/TBP complex stability and lead to larger bending angles [455]. Thus, from a DNA mechanical perspective, large bending angles should be expected from both promoter constructs.

The FRET efficiencies obtained from smFRET experiments can be used to calculate donor-acceptor distances r_{DA} [29]. For the U6P/HsTBP complex, r_{DA}(FRET) equals a distance of 6.36 nm. No crystal structure for the U6P/HsTBP complex is available and a comparison with the HsTFIIIB complex yields an r_{DA}(PDB) of 5.50 nm for the fluorophore positions in the linear U6P construct and 4.90 nm for the fluorophore positions in the DNA origami FC. Thus, the DNA without Brf2 and Bdp1 potentially displays a considerably smaller bending angle.

For the MLP/HsTBP complex, a r_{DA}(FRET) value of 5.40 nm was determined in experiments. The corresponding crystal structure (PDB: 1CDW) [457] does not include the bases corresponding to the fluorophore positions used in this study. Still, a comparison to a structure using a longer DNA fragment (PDB: 5IYB) shows a highly similar DNA trajectory. Mapping the fluorophore positions to this structure shows an r_{DA}(PDB) of 4.64 nm, which implicates a shorter distance as determined by FRET (5.40 nm). This may in part be attributed to the fact that the structure of the complete human RNAP II PIC that also includes transcription factors TFIIA, TFIIB, TFIIE, TFIIF, TFIIH and RNAP II was used [52]. Taking into consideration that addition of HsTFIIB to the MLP/HsTBP complex changed the FRET efficiency of the bent state to 0.72, which translates to an r_{DA}(FRET) of 5.04 nm, the distance calculated for the TBP-promoter DNA complexes seem feasible and the value calculated for the MLP/HsTBP complex may represent a relevant conformation. Moreover, it has been shown that DNA bending angles in crystal structures can differ significantly from those in solution [439]. In addition, fluorophores are attached to the DNA using approximately 1.5 nm linkers, which has been shown to lead to greater effective r_{DA} values that the distance between the attachment points [30,458,459]. Models have been proposed that determine the spatial volume accessible to each fluorophore, resulting in more accurate distance calculations [30,459].

Another caveat concerning the smFRET experiments performed in this work is that the anisotropy of the donor and acceptor fluorescence was not tested. Therefore, it is possible that one of the fluorophores is spatially constraint. If that is the case, the generalization of a κ^2-value, the orientation factor between donor and acceptor fluorophore (Chapter 2.1.2), of 2/3 is not applicable. Still, κ^2-values only differ significantly from 2/3 if both fluorophores are static, which is highly unlike for the complexes studied here [69]. Other effects may affect the measured fluorescence intensity, such as contact quenching and protein induced fluorescence enhancement (PIFE), although the latter has so far not been observed for the fluorescent dyes used in this study [63,460]. Nevertheless, the relative distribution of FRET efficiencies is not influenced by these factors. Thus, all experiments that rely on the comparison of LF and HF peak areas remain unaffected.

8.1.3 Stabilization of the U6 promoter-TBP complex by Brf2

Addition of HsBrf2 drastically stabilized the bent U6P/HsTBP complex, as almost no dynamic binding was observed in equilibrium TIRF experiments and the majority of complexes remained stable after a washing step. In confocal solution experiments, HsBrf2 addition similarly reduced the unbent DNA fraction but also shifted the FRET efficiency of the bent state from E = 0.39 to 0.72. The observed complex stabilization is in agreement with various biochemical studies [185,186,262,271,431,461], and can mostly be attributed to the C-terminal extension present in all Brf-proteins, as truncation of this domain severely reduces the binding affinity to HsTBP [186,262]. Indeed, the C-terminal extension allows direct interaction between HsTBP and HsBrf2 in solution [262]. This agrees well with the observed decrease in static LF trances in TIRF experiment of U6P/HsTBP/HsBrf2 complexes as compared to the conditions with U6P/HsTBP indicating an increased affinity of the HsTBP/HsBrf2 complex for the U6P DNA. Studies using ScTBP/ScBrf1 reported a 12–17-fold increase in promoter DNA affinity upon addition of ScBrf1 to ScTBP [431,461]. In TIRF experiments in this study, addition of HsBrf2 resulted in an increase in static HF traces to 64% (8-fold increase). In confocal solution experiments, however, HsBrf2-addition resulted in a 78% HF ratio (1.6-fold increase). The more modest increase in affinity likely resulted from the sub-stoichiometric amounts of HsBrf2 (1 nM compared to 10 nM HsTBP) used in TIRF experiments. Alternatively, the different TATA-box sequences of the *S. cerevisiae* U6P (TATAAATA [431]) and human U6P (TTAAAATA) may also affect complex binding, as already discussed for the promoter binding efficiency of HsTBP. An *in vivo* study in mice showed that the loss of TBP-binding affinity induced by mutations in the C-terminal extension of Brf2 could be compensated by SNAPc bound to the PSE, as formation of the DNA/TBP/Brf2 complex was abolished, while the DNA/SNAPc/TBP/Brf2 complex could still form [260]. This underlines the importance of the local as well as distal environment of the promoter in gene regulation, in particular for human snRNA transcription [261].

8.1.4 Stabilization of the U6 promoter-TBP-Brf2 complex by Bdp1

In TIRF experiments, two different HsBdp1 variants were probed for the ability to further stabilize the ternary DNA-bound HsTBP/HsBrf2 complex. HsBdp1$_S$ (residues 241–396) was used to determine the crystal structure of the human U6P/TFIIIB complex [277]. HsBdp1$_{ES}$ is an N- and C-terminally extended variant (residues 130–484) (Figure 67a). In equilibrium experiments and after washing off unbound/dynamic proteins, addition of equimolar concentrations (compared to HsBrf2) of either HsBdp1 variant resulted in a 14–25% increase of static HF traces compared to the ternary U6P/HsTBP/HsBrf2 complex. Furthermore, the FRET efficiency of the bent state was similar (0.41–0.45) among all histograms calculated from static traces, for both Bdp1 variants. The bent state FRET efficiency is also remarkably similar to that of the ternary complex suggesting that no conformational change in the DNA was induced by HsBdp1 binding. Similarly, confocal solution experiments did not show a change in FRET efficiency between the U6P/HsTBP/HsBrf2 and U6P/HsTBP/HsBrf2/HsBdp1$_{ES}$ complexes. This is in overall agreement with the respective crystal structures (PDB: 4ROC, 5N9G) where no drastic changes in DNA conformation are visible [186,277].

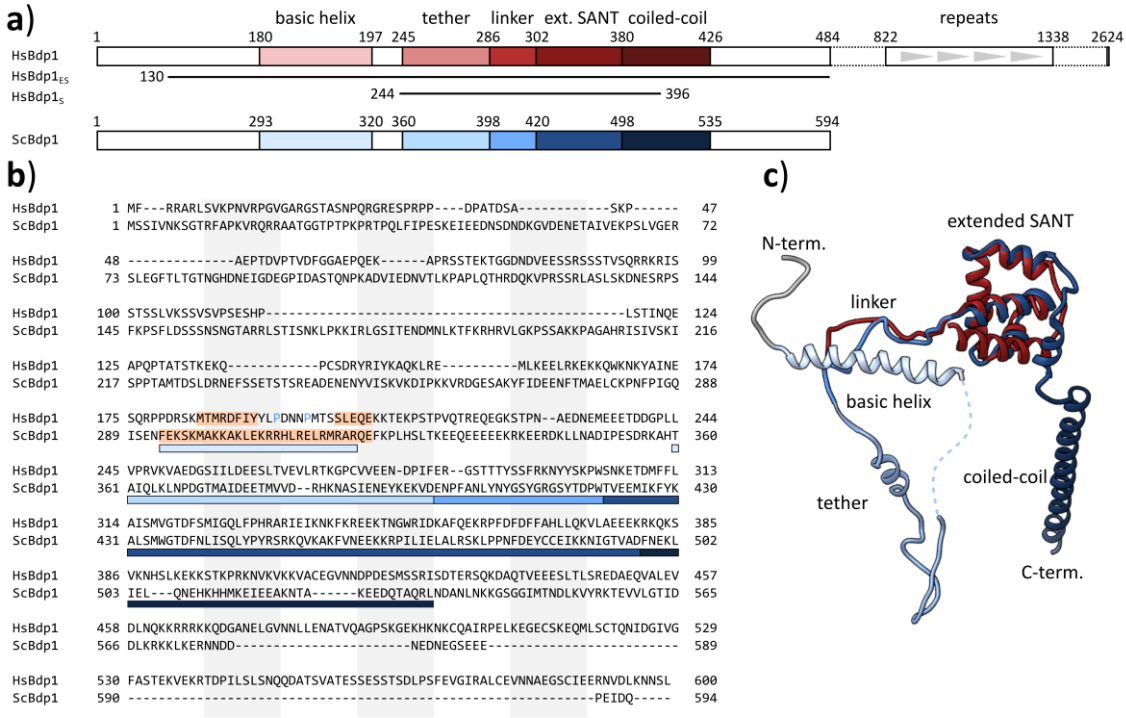

Figure 67: Domain organization of human and *S. cerevisiae* Bdp1. a) Comparison of homologous domains in human and *S. cerevisiae* Bdp1 (adapted from [194,277]). The parts of the sequence corresponding to the truncated variants used in this work are highlighted as solid lines. **b)** Amino acid sequence alignment of the first 600 residues of HsBdp1 and the complete sequence of ScBdp1. Domains as in a) are highlighted. Secondary structure prediction of α-helical elements (PRALINE webservice) in the basic helix domain for ScBdp1 and HsBdp1 are highlighted in orange. **c)** Structure comparison of HsBdp1 (red, PDB: 5N9G) and ScBdp1 (blue, PDB: 6F40).

A minor displacement of the NTS in the U6P/HsTBP/HsBrf2/HsBdp1$_{ES}$ structure compared to the ternary complex was noted at the downstream TATA-flanking region [277], but the observed shift by one nucleobase was undetectable for the methodology used here.

The complete TFIIIB complex has been described to form extraordinarily stable complexes with DNA in various studies. These stable complexes are resistant to heparin competition and high salt concentration (150-300 nM NaCl) [189,191,269,270] and act as a genomic roadblock [346]. The roadblock function was abolished by Bdp1 depletion, suggesting a pivotal role of this factor in TFIIIB stabilization [346]. Based on these reports, the observed complex stabilization conferred by addition of either HsBdp1 variant in TIRF experiments was unexpectedly low. All the above studies were based on ScBdp1, which is substantially shortened compared to HsBdp1. Nonetheless, the homologous N-terminal parts of the human and ScBdp1 are structurally highly similar [194–196,277] (Figure 67a, b).

The comparison between the two HsBdp1 variants used in this work demonstrates that the additional N- and C-terminal residues in Bdp1$_{ES}$ do not confer additional stability. HsBdp1$_{ES}$ is structurally similar to a truncated variant of ScBdp1 (amino acid residues 186–594, Figure 67a) that was confirmed to be fully functional in promoter directed transcription and resistant to heparin competition [269]. The shorter variant, HsBdp1$_S$, is not transcriptionally active [277]. However, the closest comparable truncated ScBdp1 variant (amino acid residues 263–464) formed

a heparin resistant TFIIIB complex [269]. Therefore, it is reasonable to assume similar binding properties for both variants.

As determined by the crystal structure of the U6P/TFIIIB complex, the high complex stability is created by several redundant protein-protein and protein-DNA interactions [277] (Figure 68a): the C-terminal lobe of HsTBP associates with the HsBrf2 cyclin domains and the convex side of HsTBP with the HsBrf2 C-terminal extension. On the opposite side of the complex, the N-terminal lobe of HsTBP interacts with the Bdp1 SANT-domain, which contact the end of the Brf2 C-terminal extension. The concave side of HsTBP, the Brf2 cyclin domain and the Bdp1 SANT domain and linker domain each contact at least two strands of the DNA duplex. The Bdp1 linker invades the minor groove of the DNA opposite of HsTBP, thus fully enclosing the DNA in the TFIIIB complex (Figure 68a).

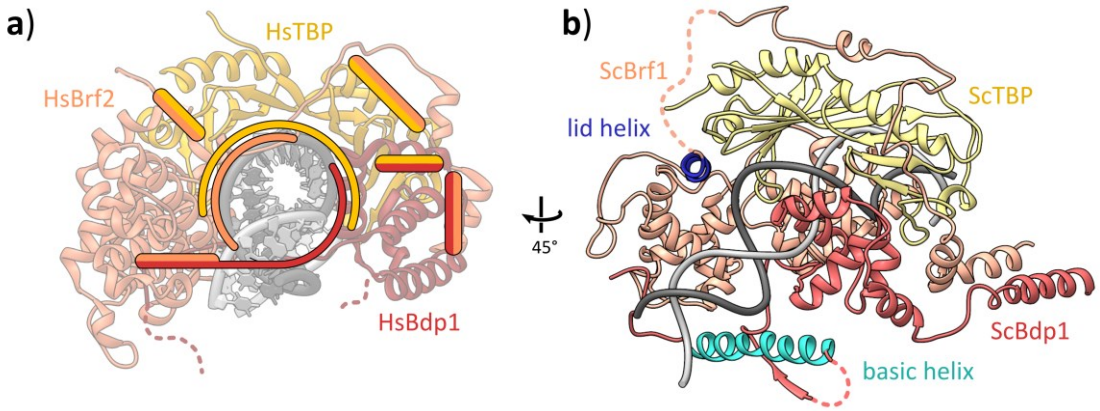

Figure 68: Stabilizing structural features of the human TFIIIB complex. a) Crystal structure of the human U6P/TFIIIB complex (PDB: 5N9G), highlighting the interaction sites between individual factors (dual colored bars) and envelopment of the DNA helix (colored circular outline). Dashed lines indicate the N- and C-term. extensions of HsBdp1. **b)** Structure model of *S. cerevisiae* DNA/TFIIIB complex (PDB: 6F40, only TFIIIB shown). The extended lid helix in ScBrf1 (blue) and basic helix in ScBdp1 (cyan) are highlighted as additional structural elements that enclose the DNA.

Recently emerged structures of the *S. cerevisiae* RNAP III PIC [194–196] revealed additional structural elements not seen in the human TFIIIB structure that further confine the DNA: The ScBrf1 lid helix (amino acid residues 286-304) extends longer than the corresponding structure in HsBrf2 and stabilizes the DNA upstream of the TATA-box and the Bdp1 basic helix (amino acid residues 293–312), which folds under the DNA near the Bdp1 linker (Figure 67, Figure 68b). A secondary structure prediction of the corresponding region in HsBdp1 indicates a separation of the basic helix structure due to the presence of two proline residues, potentially resulting in two shortened α-helical segments (Figure 67b). Hence, there is little structural evidence pointing towards an increased capability of $HsBdp1_{ES}$ to stabilize the ternary complex compared to $HsBdp1_{S}$.

In confocal smFRET experiments performed in solution with a 0 pN FC, which represent the experimental conditions most comparable to the TIRF measurements, the U6P/HsTBP/HsBrf2 and U6P/HsTBP/HsBrf2/$HsBdp1_{ES}$ complexes showed nearly identical bent state occupancy close to HF saturation (22%/78% vs. 11%/89%). Therefore, no major increase in complex stabilization can be inferred from these measurements. However, taking the measurement at higher forces into

consideration, HsBdp1 substantially increased the bent state occupancy a higher forces. Hence, the confocal experiments agree with the general consensus of the literature on the key role of Bdp1 as a stabilizing factor [189,191,269,270]. Why this is not reflected in TIRF experiments, is not clear. However, it might be a result from the use of sub-stoichiometric concentrations of both, HsBrf2 and HsBdp1 (1 nM compared to 10 nM HsTBP). By comparison, EMSAs with the human U6P/TFIIIB complex used 250 nM HsTBP, 350 nM HsBrf2 and 500 nM HsBdp1$_S$ [277]. However, a higher concentration of HsBrf2 or HsBdp1 in TIRF experiments generally resulted in a severe loss of analyzable traces.

8.1.5 Bending-angle differences between TIRF and confocal microscopy experiments

In confocal solution measurements, the FRET efficiency of the bent promoter DNA surprisingly changed from E = 0.39 for the U6P/HsTBP complex to $E \approx 0.72$ for the ternary U6P/HsTBP/HsBrf2 complex. A comparable change in FRET efficiency was not observed in the corresponding TIRF experiments.

If the observed increase in FRET efficiency corresponds to a conformational change in the promoter DNA, it would be introduced by HsBrf2 binding and not merely a shift in an already dynamic equilibrium, as observed for ScTBP binding to an H2B promoter [232]. In the study by Gietl *et al.,* the DNA/ScTBP complex fluctuated between an unbent, partially bent (E = 0.51) and fully bent state (E = 0.68) displaying a noticeable FRET efficiency density corresponding to the fully bent state in the histogram of DNA/ScTBP only. Addition of ScTFIIB stabilizes the dynamic equilibrium in the fully bent state [232]. In this work, the FRET efficiency distribution of the U6P/HsTBP complex, while broad, did not show any density at E = 0.72, the FRET efficiency measured for the bent ternary complex. Perhaps, binding of HsTBP to the U6P may only induce a partially bent state without the assistance of HsBrf2, explaining why only two conformations were observed in fluorescence traces in TIRF experiments. Still, this does not explain the identical FRET efficiency observed for all U6P/TFIIIB subcomplexes in TIRF experiments in combination with drastically increased bent state lifetime in the presence of HsBrf2 (and HsBdp1). It can be speculated that HsBrf2 can stabilize HsTBP at the promoter without inducing further DNA bending. The absence of an additional conformational change in the U6P/HsTBP/HsBrf2 complex in TIRF experiments compared to confocal measurements may be linked to the redox sensitive binding of HsBrf2. It was demonstrated that mutation of the redox sensitive cysteine C361 to alanine abolished the redox state-dependency of HsBrf2 binding, whereas a mutation of C361 to aspartate, mimicking the oxidized state, resulted in a 50-fold decreased binding affinity to the U6P/HsTBP complex [186]. The photo-stabilization-buffer used in TIRF experiments contains the ROX system trolox-trolox quinone, which has an estimated redox potential between -0.08 V to -0.50 V [394], whereas cysteine has a redox potential of -0.22 V [462]. Whether the redox potential of C361 in particular falls within the range of the ROX system is not trivial to determine, as the micro-environment of the residue can modify its redox potential [463]. The molecular pin resides in a local environment rich in positively charged amino acids that can stabilized the oxidized state of C361 [463] making it more susceptible to oxidation by trolox quinone [186]. This supports a scenario in which C361 is oxidized by the ROX system.

Gouge *et al.* demonstrated that artificial oxidation of HsBrf2 by H_2O_2 decreased the efficiency of ternary complex formation in EMSAs by approximately 80% [186]. This suggests a residual binding affinity of HsBrf2 for the U6P/HsTBP complex, even in its oxidized state, that may correspond to a partially bound state. This is congruent with results from pull-down experiments of the HsTBP/HsBrf2 complexes where no decrease in HsTBP-binding affinity of an oxidation mimicking mutant of HsBrf2 (C361D) could be detected in the absence of DNA [186]. Consequently, it can be speculated that the HsTBP/HsBrf2 complex forms in solution, binds to the U6P and induces a partially bent state while complete association is prevented by the oxidized C361 residue in the molecular pin.

The formation of a stable, partially bent complex may be attributed to the strong interaction of HsTBP/HsBrf2 even in solution and in the absence of DNA [185,186,262]. This hypothesis would further rationalize why only a minor complex stabilization was conferred by HsBdp1 in TIRF experiments. Even though ScBdp1 has been shown to form DNA/TFIIIB complexes with ScBrf1 lacking the first 164 amino acid, which includes the first cyclin domain. These complexes were competent for promoter directed transcription but not resistant to heparin [270]. Still, an ability of the redox sensing domain to specifically impair HsBdp1 association makes sense from a biological perspective, as Bdp1 binding likely commits the DNA/TFIIIB complex to transcription.

In confocal smFRET experiments, the reducing agent DTT was included in the sample buffer, as extended fluorophore stability is irrelevant for the fast transit through the confocal volume. This correlates with the observation of the assumedly fully bent U6P/HsTBP/HsBrf2 complex in confocal experiments only. Attempts were made to test the impact of reducing agent on the binding affinity in TIRF experiment, but addition of DTT or Tris-(2-carboxyethyl)-phosphine (TCEP) as reducing agent resulted in a severe increase of photo-blinking, rendering traces unreadable (data not shown). A promising approach to test whether a fully bent U6P/HsTBP/HsBrf2 complex can be detected in TIRF experiments is the use of a C361A mutant of HsBrf2 which showed full activity independent of the environmental redox state [186].

8.2 Comparison of force-dependent DNA binding by human RNAP II and III transcription factors

DNA origami-based force spectroscopy was employed to probe the effect of increasing promoter strain on formation of a bent promoter DNA complex in the presence of RNAP III- and RNAP II-specific initiation factor subassemblies. Overall, experiments demonstrated that TBP-binding is strongly affected by force. Additional initiation factors could enhance bent state formation against force with varying efficiency, which is summarized and discussed in the following section.

8.2.1 Influence of mechanical strain on TBP-induced DNA bending dynamics

In experiments probing the stability of the bent state under increasing strain on the promoter, HsTBP-induced bending of the U6P and MLP showed similar efficiency without force (P_{bent} 48% vs. 59%). However, application of 2.6 pN force decreased the bent state probability of HsTBP on the U6P to 21%, whereas a comparable value of 18% was reached upon application of 5.9 pN to the MLP. As discussed above, the MLP features an optimal consensus sequence, which is altered in

the critical 5' TATA motif in the U6P. Thus, the overall higher force resistance of the MLP/HsTBP complex agrees with the mechanical properties of the DNA.

It is interesting to note that the bent state probability of the U6P equalized at 21%, even at 6.3 pN force. It may be possible that the central FRET population observed in other FC experiments (discussed below) is also present in the U6P/HsTBP experiments and cannot be distinguished from the bent state population due to comparable FRET efficiencies (0.39 for U6P/HsTBP and 0.3–0.5 for the medium FRET population). In this case, the actual P_{bent} value at 6.3 pN force application may be considerably lower. In extension, this would also imply that the value measured for the U6P/HsTBP complex at 0 pN force showed less efficient binding. Hence, binding of HsTBP to the U6P would be less efficient than to the MLP, which is also in agreement with TIRF experiments.

In kinetic experiments employing TIRF microscopy, application of 6.3 pN force to the U6P affected both, bent state dwell time, which was reduced by 38%, and unbent state dwell time, which was increased by 24%. In contrast, for the MLP, only the unbent state dwell time increased by 56% and the bent state dwell time remained constant.

Force-dependent complex formation in combination with force independent dissociation was observed for DNA looping mediated by the *E. coli lac* repressor LacI [464]. The authors reasoned that the constant force in the 100 fN range applied to the DNA suppresses spontaneous conformational changes in the DNA induced by thermal fluctuation and thus reduces the occurrence of successful binding event. On the hand, forces applied to the DNA were not strong enough to remove the stably bound LacI [464]. This is in agreement with the generally observed stronger binding of HsTBP to the MLP.

Similar force-dependent dissociation was observed in a study that probed the effect of DNA stretching on the dissociation rates of two bacterial DNA bending proteins (HU, Fis). The authors reports a significant reduction in DNA binding times upon force application [465]. The authors attribute this effect to elastic response of DNA to resulting change in persistence length induced by DNA bending, which has been described by theoretical models [442,466].

A recent computational study modeled the force-dependency of dissociation kinetics for DNA/protein complexes [467]. Their findings suggest that an increased DNA bending angle results in a higher force sensitivity of the bound protein complex. In this work, the bent state lifetime of the comparatively more bent MLP/HsTBP is unaffected by force whereas the less bent U6P/HsTBP showed a decrease in bent state lifetime. This might be caused by the aforementioned partial binding of HsTBP to the U6P.

Overall, data obtained in DNA origami-based force experiments in this work agree with observation made for similar systems that used different techniques to apply force, which generally cannot detect the small conformational change induced in the DNA by a single TBP molecule. The DNA origami FC technique enables direct observation of individual binding events on strained DNA and thus makes force experiments accessible for new biological systems.

8.2.2 Stability of ternary U6 promoter and MLP complexes

In confocal FC experiments, the U6P/HsTBP/HsBrf2 and MLP/HsTBP/HsTFIIB both increased the bent state probability to similar degrees. With increasing force, the stabilization conferred by HsTFIIB was 61% higher as compared to HsBrf2 (P_{bent} 58% vs. 36%). However, this required a 10-fold molar excess of HsTFIIB compared to HsTFIIB, whereas equimolar concentrations on HsTBP and HsBrf2 were sufficient. Hence, HsBrf2 conveys considerably more force resistance to the U6P/HsTBP complex.

The major difference between both TFIIB-like factors is the C-terminal extension present in HsBrf2. As discussed above, this domain confers exceptional stability to the HsTBP/HsBrf2 complex even in solution [185,186,262] due to the large interaction surface with the convex side of HsTBP [186]. In contrast, reports of strong solution interaction for the homolog HsTFIIB in the RNAP II transcription system are scarce [260]. In fact, a recent study reported transient interactions of HsTFIIB with DNA-bound HsTBP in time-resolved single-molecule fluorescence experiments [468]. The cyclin core of HsTFIIB is sufficient for efficient binding to the MLP/HsTBP complex. In contrast, deletion of the cyclin domains of Brf2 prevents association with the DNA/TBP complex as detected in EMSAs, indicating that the core is required but not sufficient for high-affinity association [262]. In that regard, HsBrf2 is similar to ScBrf1, where a truncation of the C-terminal domain lead to extremely weak interaction with the DNA/ScTBP complex, only detectable via photochemical crosslinking [270,469–471]. Since an extended C-terminal domain is universally conserved among RNAP III related TFIIB-like factors [214], it can be speculated that this presents an evolutionary specialization towards increased complex stability.

Interestingly, Addition of HsTFIIB to the binary complex changed the FRET efficiency of the bent state from $E \approx 0.63$ to $E \approx 0.72$, which indicates a minor conformational change in the DNA also apparent in the MLP/HsTBP/HsTFIIA/HsTFIIB complex, but not the MLP/HsTBP/HsTFIIA complex. This relates to the stabilization of the fully bent state observed for ScTFIIB [232], even though the difference between the partially and fully bent state would be considerably smaller for the human RNAP II system compared to *S. cerevisiae* (E = 0.51 and E = 0.68). No dynamic equilibrium between the partially and fully bent state was noticed in the initial measurements of the MLP/HsTBP complex with TIRF microscopy. However, this state would fall within the variance of 0.63 FRET efficiency state and thus might not have been noticed if its occurrence rate is low. This seems likely as no obvious subpopulation corresponding to the $E \approx 0.72$ state can be detected in the FRET efficiency distributions of the MLP/HsTBP and MLP/HsTBP/HsTFIIA complexes from FC experiments. A much larger change between the partially and fully bent state may occur in the human RNAP III system, changing the bent state FRET efficiency from E = 0.39 to E = 0.72, which hints at the possibility that this presents a promoter specific trait.

HsTFIIA was included in experiments due to its binding site in DNA/HsTBP complex that overlaps with most of the HsBdp1 binding surface and also with the end of the C-terminal extension of HsBrf2 [277,472]. Addition of HsTFIIA to the MLP/HsTBP complex consistently resulted in a 10–15% higher bent state occupancy. Still, a 100-fold molar excess of HsTFIIA over HsTBP was required, which is considerably higher than reported elsewhere (e.g. 25 nM HsTBP/50 nM

HsTFIIA [473]). Consequently, the contribution of HsTFIIA to bent state stabilization must be considered to be low.

TFIIA is generally considered to be the second factor to bind to the promoter after TBP (or TFIID) in a classical step-wise promoter assembly model [152,474]. Consequently, DNA binding by TFIIA was reported to be highly inefficient in the absence of TBP (or TFIID) [468]. TFIIA has been demonstrated to stabilize TBP on the DNA [473] and to assist in correct directional orientation of TBP [217,234]. The latter effect could not be observed here, as no orientational isoforms of the DNA/HsTBP complex were detected for both promoter constructs. HsTFIIA has also been reported to further increase the bending angle of the DNA/HsTBP complex, based on ensemble FRET experiments [473], which was not reflected in the smFRET measurements conducted in this work and elsewhere [217].

In the context of TFIID-mediated initiation, TFIIA relieves inhibition conferred by a DNA-mimicking domain of TFIID subunit TAF1 that blocks the convex side of TBP from binding to the DNA [224]. Interestingly, TFIIA plays a major role in SNAPc-mediated snRNA transcription. TFIIA provides an additional layer of selectivity by blocking the interaction site on TBP that is also targeted by the C-terminal extension of Brf2, thereby preventing Brf2 binding to RNAP II transcribed snRNA promoter [260,475]. Both of these functions are coordinative and therefore likely do not require high stress resistance. Moreover, the coordinative function of TFIIA primarily seems to a play a role at TATA-less promoters such as RNAP II transcribed snRNA promoter or promoters that require TFIID.

8.2.3 Stability of quarternary U6 promoter and MLP complexes

In terms of minimal factor requirement, RNAP III is only reliant on TFIIIB for its recruitment to the promoter (which additionally requires SNAPc in humans). By comparison, the minimal RNAP II recruitment complex at TATA-box containing promoters consists only of TBP and TFIIB. This raises the question why a third factor evolved and is strictly required for transcription initiation in the RNAP III system.

In force experiments, complete HsTFIIIB was the only DNA-bound complex that was not affected by an application of medium force (2.6 pN) and only minor complex dissociation was detected for high forces (6.6 pN). This demonstrates a high degree of mechanical resilience compared to the MLP/HsTBP/HsTFIIA/HsTFIIB complex that utilizes similar binding surfaces but required higher protein concentrations to achieve equal or lower stabilization. This points towards a key role for HsBdp1 as a scaffolding factor to convey structural integrity to the TFIIIB complex. This idea is further supported by the observation, that ScBdp1 is not required for transcription with a pre-opened transcription bubble [189]. However, only single-round transcription is supported without ScBdp1, underlining its importance as a stabilizing factor. An ScTBP-ScBrf1 fusion protein is also able to initiate transcription on linear and supercoiled templates without Bdp1 [263].

Cloutier *et al.* proposed a kinetic trapping of DNA by ScTFIIIB, explaining the considerably increased lifetime of the DNA/TFIIIB complex compared to the DNA/ScTBP/ScBrf1 complex (95 min vs. 45 min) [271]. Recent structural data revealed the ‘headlock’ [194] conformation that TFIIIB imposes upon the bent DNA resulting in a fully encased DNA [194,195,277]. This cage-like

arrangement likely also confers superior mechanical stability through multiple interaction sites between factors. The redundant inter-molecular interaction discussed above (Figure 68) could help to prevent complex dissociation if one of the contacts is temporarily disengaged due to force application.

This correlates directly to the high transcription rates of RNAP III-transcribed genes, which are achieved by efficient initiation-elongation-termination-and-reinitiation cycles [435]. In particular, recycling of RNAP III using the same recruitment complex is critical [341–343,476]. Hence, the RNAP III-exclusive initiation factor Bdp1 plays a decisive role in the RNAP III transcription cycle as it allows the maintenance of a fully assembled DNA/TFIIIB complex between transcription rounds. This in turn requires tight regulation of PIC formation, e.g. via the redox controlled binding of HsBrf2 [186], as transcriptional regulation cannot take place at the level of elongation at these extremely short genes. In fact, kinase-dependent phosphorylation of HsBrf1 is utilized to facilitate TFIIIB dissociation during mitosis by disrupting the HsBrf1/HsBdp1 interaction and clear DNA for the replication machinery [477].

Furthermore, transcription complexes within chromatin are exposed to changes in the local DNA topography by nucleosomes [82–84,340,433]. This can be caused by inter-nucleosomes contacts mediated by the histone tail domains, which have recently been observed in experiments employing an alternative DNA origami-based force spectrometer design [95]. Stacking interactions within chromatin fibers are in the range of 3–4 pN [337,478]. In addition, transcription activity can generate forces up 30 pN [76–78,433].

At human snRNA promoters, a stably positioned nucleosome is typically positioned -150 bp relative to the TSS and allows cooperative binding of Oct-1 to the DSE and SNAPc to the PSE [258,479]. Hence, initiation factors at the promoter are situated at a DNA section that is topological constrained, on the upstream side by the -1 nucleosome and on the downstream side by a firmly associated transcribing RNAP. Before promoter escape, RNAPs generally build up torsional strain in a DNA scrunching mechanism that helps to break contact with the initiation complex [107,108]. In multiple round of transcription by RNAP III at the same gene locus, TFIIIB thus has to persist through the force generated by multiple promoter escape events [341,343,480]. Interestingly, abortive initiation by RNAP III seems to be highly efficient, leading to productive elongation after an average of three rounds of abortive transcript release [197]. Nevertheless, TFIIIB is likely to experience mechanical forces that must be compensated by the highly stable initiation complex. It can be further speculated that torsional strain through supercoiling accumulates from repeated rounds of transcription and cannot be released due to the nucleosomes surrounding the small transcriptional unit (Figure 69). Moreover, high template commitment in subsequent TFIIIB-directed reinitiation events suggests that RNAP III somehow maintains contact with the transcriptional unit after termination [341,343]. This mechanism of facilitated reinitiation would allow rapid reuse of the same TFIIIB complex (Figure 69). An alternative perspective is presented by a theoretical model that predicts a stabilizing effect of negative supercoiling on DNA/TBP complex stability [481]. In that case, continuous transcriptional activity of RNAP III and the resulting negative supercoiling in the upstream DNA could, in fact, help to maintain TFIIIB at the promoter.

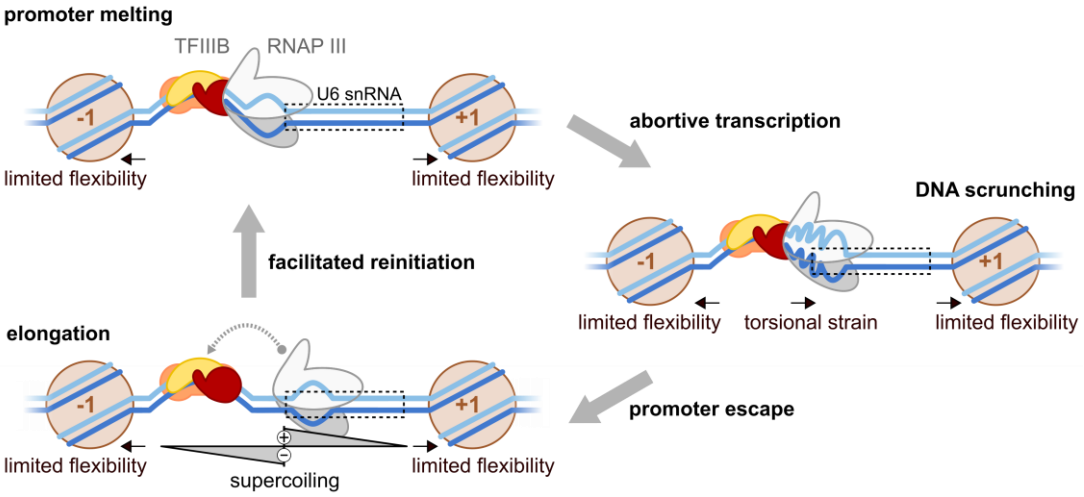

Figure 69: Model describing forces exerted on DNA by transcriptional activity at the U6 promoter. At the U6 snRNA promoter, the −1 nucleosome is firmly positioned close to the upstream promoter region, limiting DNA flexibility. DNA scrunching generates torsional strain that is used to drive promoter escape. Continuous transcription of the short U6 snRNA gene by RNAP III further generates torsional strain through negative (-) and positive (+) supercoiling in the upstream and downstream DNA, respectively. Facilitated reinitiation on the same transcription unit, potentially mediated by RNAPIII-TFIIIB contacts (dashed arrow), allow rapid reuse of TFIIIB complexes. The +1 nucleosome is positioned downstream of the gene body. Proteins and nucleic acids are color coded as follows: TBP (yellow), HsBrf2 (orange), Bdp1 (red), RNA polymerase II/III (grey), nucleosome (brown), template strand (blue) and non-template strand (light blue).

The situation is different at genes transcribed by RNAP II, where the gene body can be hundreds of base pairs in length. Here, rapid reinitiation does not seem to play a role due to the large physical distance between the TSS and termination site. Another point to consider is that RNAP III-transcribed gene bodies are generally nucleosome free [479], while a conserved +1 nucleosome is found at position +40 relative to the TSS in RNAP II transcribed genes [349,437]. The corresponding +1 nucleosome in RNAP III transcribed genes is usually found beyond the short gene body +220 bp downstream of the TSS [479].

The position of the +1 nucleosome does not show a strong sequence-dependency and its position appears to be flexible when nucleosomes are reconstituted on naked DNA *in vitro* [437]. Hence, it has been speculated that initiation factors situated at the promoter help to establish the position of the +1 nucleosome [320,482]. This might be especially relevant for RNAP II genes where the +1 nucleosome is found in close proximity to the TSS. In this case, initiation factors need to be stably attached at the promoter in order to avoid displacement by the nucleosome. Notably, the TAF1 component of TFIID extends approximately to the +30 position relative to the TSS [225] and can bind to adjacent nucleosomes [483].

In the context of the minimalistic RNAP II system analyzed here, HsTFIIA only conferred minor stabilization of the initial bent MLP/HsTBP complex. Instead, HsTFIIB acts as the initial stabilizing factor to secure HsTBP at the MLP. Interestingly, a recent study used TIRF microscopy to monitor the hierarchical assembly of individual fluorescently labeled human RNAP II transcription factors at the promoter and reported stable binding of HsTFIIA, whereas HsTFIIB only transiently interacted with the DNA (mean dwell time of 1.5 s) in the presence of HsTBP (or HsTFIID) [468]. While the confocal solution experiments conducted here only probed the presence of HsTBP at the promoter, the increased bent state fraction observed in the presence of HsTFIIB implies a

more stable binding than HsTFIIA, for which only minor bent state stabilization was observed. This difference is further emphasized by the higher force resistance conferred by HsTFIIB, which disagrees with a transient interaction (as seen for the transient U6P/HsTBP complex compared to stable MLP/HsTBP interaction). Nevertheless, the approach presented by Zhang and coworkers [468] could be used in future experiments in order to verify the presence of individual transcription factors at different assembly steps of the PIC.

In the confocal experiments only, an additive effect on complex stabilization with increasing force was observed for the combination of HsTFIIA and HsTFIIB (Figure 70a); i.e. the difference in P_{bent} between the MLP/HsTBP/HsTFIIA/HsTFIIB complex and MLP/HsTBP is approximately equal to the combined difference of its subcomplexes. This is in agreement with structural data that show no redundant or overlapping interaction sites within the MLP/HsTBP/HsTFIIA/HsTFIIB complex [52] (Figure 70b). In contrast, HsBdp1 considerably enhanced the bent state probability even though no stabilization is conferred by this factor alone in TIRF experiments.

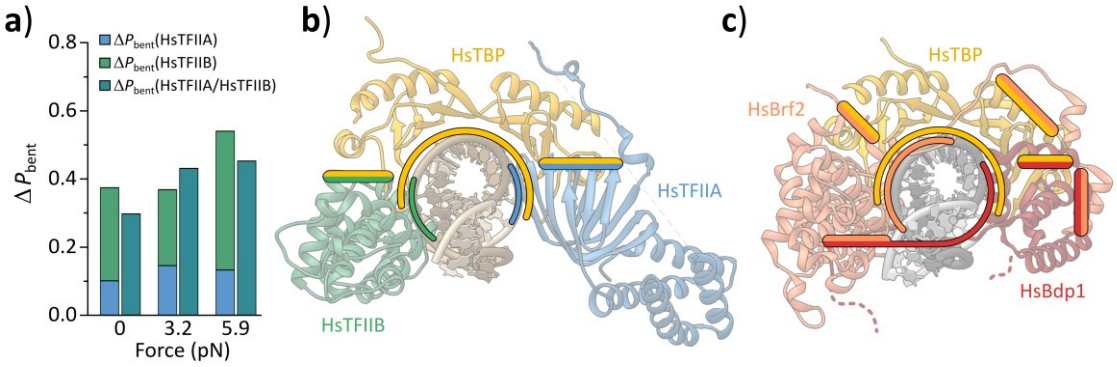

Figure 70: Contribution of individual RNAP II initiation factors to complex stabilization. a) The difference in bent state probability ΔP_{bent} of the MLP/HsTBP/HsTFIIA (blue), MLP/HsTBP/HsTFIIB (green) and MLP/HsTBP/HsTFIIA/HsTFIIB complexes, respectively and the MLP/HsTBP complex for all measured forces. **b)** Structure model of the human MLP/HsTBP/HsTFIIA/HsTFIIB complex (5IYB), highlighting the interaction sites between individual factors (dual colored bars) and envelopment of the DNA helix (colored circular outline). **c)** For comparison, the analogous model of the human TFIIIB complex is shown (Figure 68).

Taken together, the results presented in this work as well as in similar studies [94,95,465] indicate that mechanical forces acting on DNA might constitute a mechanism of gene regulation by locally modulating the binding of transcription factors. In this regard, the strain generated by DNA packaging, histone placement, action of the replication and transcription machinery and binding of regulatory proteins all contribute to the force landscape of chromatin. Thus, force presents an additional factor that shapes the efficiency of transcription on a chromatinized template.

8.2.4 The central FRET efficiency population in FC experiments

In all DNA origami FC experiments, a subpopulation with a FRET efficiency between 0.3–0.5 was observed (hereafter referred to as medium FRET (MF) population), or in the case of U6P/HsTBP samples, potentially overlapped the population that is specific to the bent U6P/HsTBP complex (E = 0.39). The population was i) not observed in experiments using the corresponding linear promoter fragment of the MLP (for the U6P and T6P, these population could not be fully discriminated) and ii) did not show a clear force-dependency as opposed to the HF population

corresponding to the TBP-induced bent state. Consequently, it was excluded from further analysis and only included in fits to improve the fitting quality.

The samples in which the MF population could not be unambiguously separated from the bent and unbent promoter DNA signal are the U6P/HsTBP and T6P/PfTBP/PfTFB1 complexes. For the U6P/HsTBP complex, the FRET efficiency of the bent state at $E = 0.39$ was verified using a short linear promote construct and a force-dependent decrease in peak area was observed when a force of 2.6 pN acted on the DNA. Hence, it is reasonable to assume that this population, at least in part, contains the bent state population. However, no further decrease of the peak area was observed when 6.6 pN force were applied to the promoter DNA. Thus, the remaining density at $E \approx 0.4$ in the 6.6 pN sample of the U6P/HsTBP complex may represent the unspecific MF population. For the T6P/PfTBP/PfTFB1 sample, the unbent and bent state population fully overlapped and thus did not allow proper fitting of a potential MF population.

One attempt to explain this phenomenon is dynamic averaging of bending-unbending dynamics faster than the time scale of one fluorescence burst from a molecule moving through the confocal volume. This could result in an apparent FRET efficiency in the range between unbent and fully bent state [385]. An analysis with the FRET-2CDE filter that uncovers sub-millisecond dynamics [385] showed a uniform distribution of all population centered around FRET-2CDE = 10, which represent the value for stable FRET efficiency across the burst (Figure 71a, Appendix Figure 77). Based on this analysis, it is unlikely that the MF population represent a dynamic averaging of the LF and HF state. However, the FRET-2CDE filter is only sensitive to dynamics slower than ≈10 ms^{-1} [385]. Thus, it cannot be formally excluded that the MF population represents transitions on a faster timescale. However, given the generally stable nature of most analyzed complexes, this scenario is not likely. Another explanation is provided by the tendency of DNA origami FCs to dimerize in solution [94]. Such dimers would not be detectable in *E*/*S* histograms due to the (on average) equal labeling with donor and acceptor fluorophores resulting in an identical stoichiometry value but twice the fluorescence intensity in each detection channel. This is consistent with the stoichiometry values of $S \approx 0.5$ found for all populations including the MF population (Appendix C.3, Figure 77).

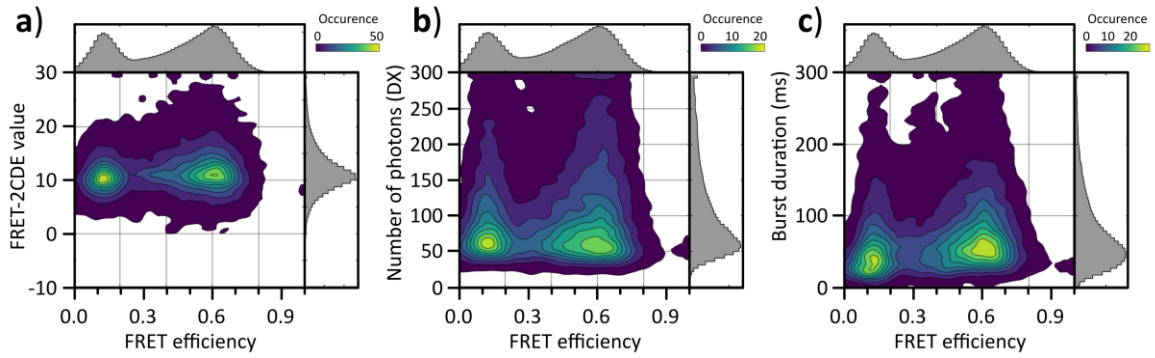

Figure 71: Burst analysis of the medium FRET efficiency population observed in DNA origami force clamp experiment. a) FRET-2CDE filter value, **b)** the number of photons per burst and **c)** the burst duration as a function of FRET efficiency were plotted for an exemplary dataset of a 0 pN MLP FC bound by HsTBP and HsTFIIA (corresponding to Figure 55b). Contours are smoothed to improve visibility.

Consequently, the MF population could arise from a mixture of one FC with an HsTBP-bound promoter and another with an empty promoter in a dimer configuration. Following this idea, the photon count of each burst for an exemplary measurement was evaluated but did not show a noticeable increase in photon count for the MF population (Figure 71b). The reducing agent DTT, which was included in the sample buffer as reducing agent, was shown to adversely affect dye stability and cause photo-blinking [389] raising the possibility that bursts were fragmented. A burst duration histogram of the exemplary measurement shows a mean burst duration of approximately 1–4 ms (Figure 71c), which is noticeably shorter than burst durations obtained in a study that employed DNA origami specifically to extend the observation time for DNA hairpin structures from 1–8 ms for short linear DNA to 8–40 ms for DNA origami coupled hairpins [484]. Judging from this, a fragmentation of fluorescence bursts through blinking induced by DTT offers an explanation for the reduced apparent burst duration.

In a previous study using the same DNA origami FC design, the separation between LF and HF populations in experiments probing MjTBP-induced DNA bending was not large enough to infer the presence of a similar MF population [94]. As this DNA origami design is not frequently used in other studies yet, the phenomenon observed here will have to be addressed in future applications to improve quantitative results obtained from force experiments. For this, an artificial fusion of two FCs using complementary linker DNA strands [485] provides a promising starting point to determine the effect of dimerization on apparent FRET efficiency.

8.2.5 Comparison of experimental and theoretical DNA bending probabilities

The probability to find the promoter DNA in the bent state in the presence of human RNAP II and RNAP III, as well as archaeal transcription initiation factors at different applied forces was compared to a theoretical model based on a two-state Boltzmann distribution (Chapter 6.7.3). In this framework, the distance change Δw between the 5’ and 3’ ends of the dsDNA promoter segment upon unbent–bent state transition is calculated according to a two-dimensional geometric model in which the stiff, rod-like dsDNA upstream and downstream of the TATA-box pivots around its center (Figure 72a). This simplification is overall in agreement with the DNA conformation seen in structural models using long promoter DNA constructs and only neglect the minor lateral displacement of the TATA-box DNA [224,225] (Figure 72a).

The end-to-end distance change Δw represents the work performed by HsTBP when the DNA is bent against the applied force. For nearly all FC experiments, a fit of the F/P_{bent} plot with the two-state Boltzmann distribution resulted in a Δw = 1.1 nm. This value deviates considerably from the theoretical value derived from the geometric bending model for the 55 bp U6P ($\Delta w_{theoretical}$ = 4.76 nm), 51 bp SSV T6 promoter ($\Delta w_{theoretical}$ = 2.76 nm) and 35 bp MLP ($\Delta w_{theoretical}$ = 2.47 nm). Notably, this was also observed in the DNA origami FC experiments with MjTBP by Nickels *et al.* [94].

Three potential sources of this error are identifiable that may contribute to the substantial difference (factor 2–4) between observed and predicted values.

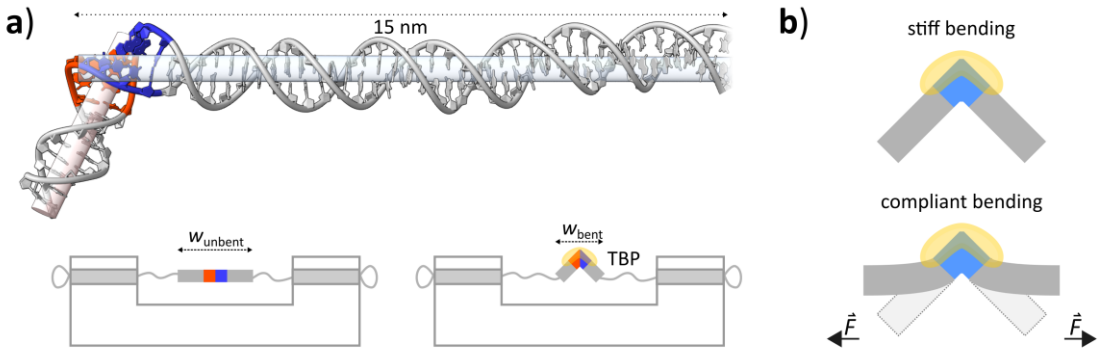

Figure 72: Comparison of the geometric model for DNA bending with structural data. a) Structure model of a long promoter DNA construct with a TBP-induced bent (human TFIID/TFIIA complex, PDB: 5FUR, proteins are not shown). The upstream half (orange) and downstream half (blue) of the TATA-box are highlighted. The DNA upstream and downstream of the TATA-box are approximated as stiff rods. The schematic depiction of the DNA origami FC illustrates DNA bending against force and the resulting change in promoter end to end distance ($w_{unbent} - w_{bent}$). **b)** Possible model for the behavior of TATA-box flanking DNA in the TBP-induced bent state. Without force, DNA behaves as seen in the structure model. Under force application, DNA may adopt are more curved structure, resulting in less end-to-end distance change.

(i) The bent state probability may be incorrect. P_{bent} was extracted directly from the relative fit area of the HF population. Fits were performed on data of three technical replicates with low standard deviations (Appendix Figure 76) and thus do not explain the observed differences. A fixed source of error is represented by the MF population observed in most FC experiments, which was excluded from analysis as well as calculation of relative fit areas. As deconvolution of the exact size of the MF was not possible for all samples, a fixed fit area was chosen as a compromise. Thus, the MF population may subtract from the fit area of the HF and/or LF population in a non-symmetric manner and thus bias the P_{bent}. However, the MF population only accounted for up to 21% of the total fit area in any given experiment and does not explain the observed factor 2–4 difference in measured and predicted Δw values. In addition, transmission electron microscopy experiments showed that for around 23% of imaged particles, the lateral posts of the origami body are badly resolved. This could either be caused by a different orientation
of the DNA origami structure on the EM grid or indicate structural defects, which could result in a reduced force of the ssDNA spring. Similar to the MF population, the minor fraction of potentially lower force FCs does not account for the rather large difference in theoretical and measured Δw values.

(ii) The geometric model may not adequately describe the conformational changes in the DNA. This would agree with the calculated DNA end-to-end distance change of $\Delta w = 1.1$ nm for all measured DNA constructs compared to the predicted 2.47–4.76 nm, depending on the promoter construct. Based on structural data as well as mechanical properties of dsDNA, treating the two halves of the promoter DNA upstream and downstream of center of the bent TATA-box as rigid rods is reasonable and complies with the generally acknowledged persistence length of dsDNA of 50 nm [486]. However, substantially reduced persistence lengths of 10–20 nm have been reported for DNA fragments <100 bp. This phenomenon was attributed to spontaneous unpairing of single bases which affects short DNAs comparatively more than longer DNAs [487]. A local decrease in persistence length is further supported by studies that characterized the force-dependent

unbinding of the high-mobility group B protein, a DNA bending chromatin factor, and found that binding of this protein increases local DNA flexibility [488,489]. Potentially, a similar effect invoked by TBP is observed here, causing the TATA-box-flanking DNA to buckle under force application, which results only in a small local kink in agreement with Δ*w* = 1.1 nm (Figure 72).

(iii) The force of the ssDNA spring calculated based on the extensible freely jointed chain model (exFJC, Chapter 6.4) may not be correct. A crucial difference of the DNA origami FC compared to other force sensing techniques is that force is not directly applied by an external source. On the one hand, this presents an advantage as noise from long linker DNAs is omitted [93]. On the other hand, forces cannot be manipulated and thus evaluated *in situ*, which is typically employed for calibration and feedback regulation in magnetic and optical trapping devices [86]. Thus, forces are predicted based on models for polymer behavior such as the exFJC model introduced by Smith *et al.* [380], which was adopted by Nickels *et al*. to calculate the force applied by the entropic spring in their DNA origami FC design [94]. Within the context of the exFJC model it is assumed that the ssDNA chain behaves like an ideal polymer at low forces [94]. However, two factors may substantially alter the properties of the ssDNA and thus lead to non-ideal behavior.

First, the concentration of mono- and bivalent solvent ions can drastically change the elastic behavior of the ssDNA chain [490]. In their study, McIntosh *et al.* determined ion concentrations for K^+ (3.5 M) and Mg^{2+} (50 mM) at which ideal polymer behavior of ssDNA is observed. At lower ion concentrations, electrostatic repulsion of the backbone phosphates within the ssDNA chain lead to increased rigidity [491], thus effectively decreasing the generated force. The buffer used for measurements with human initiation factors contained only 15 mM $MgCl_2$ and 60 mM KCl and therefore, lower forces than predicted by the exFJC model are expected. Still, this does not explain why the same Δ*w* value was calculated for experiments with MjTBP, which were performed at high salt concentrations (1 M Na^+, 1.5 M K^+) and should consequently yield lower P_{bent} values corresponding to higher effective forces. According to work by Huguet *et al.*, ssDNA at low salt concentrations may be more appropriately described by the worm-like-chain model generally used for dsDNA [491].

Secondly, formation of secondary structures (e.g. DNA hairpins) within the ssDNA spring was neglected in the model used here, but has been shown previously to affect the entropic behavior of ssDNA [492]. Secondary structures effectively reduce the contour length of the ssDNA chain and thus increase the force. Moreover, the parameters used in the exFJC model (Chapter 6.4) are taken from a study by Smith *et al*. who measured the elastic response of λ phage genomic ssDNA [380]. These parameters represent an average over the secondary structure specific to λ DNA and are thus not universally transferrable to ssDNA with a different sequence. This could be accounted for by calculating the specific secondary structures formed in the spring region of the M13mp18-based FC scaffold by computational simulations [493]. Alternatively, the scaffold DNA could be modified to only include poly-mononucleotides (e.g. poly-dT) in the spring region that do not form secondary structures and are therefore more predictable in modeling approaches, which has already been proposed by Nickels and co-workers [94].

Low salt concentrations and secondary structure formation affect the entropic force of the ssDNA spring in opposing ways. However, low salt concentration also suppresses secondary structure

formation due to internal electrostatic repulsion [494], similar to how increasing Mg^{2+} ion concentrations stabilize the stacked conformers of the HJ. This could indicate that the force-decreasing influence of weak electrostatic screening at low salt concentrations dominates the behavior of the ssDNA in the experiments conducted here and would fit with the observed Δ*w* values compared to the model.

All of the above phenomena are likely to contribute to some degree to the observed discrepancy between theoretical and measured Δ*w* values. Determining the exact influence of each factor will require more in depth characterization of the properties of the DNA origami FC aided by quantitative computational simulations [495].

8.3 The role of TFB2 in transcription initiation

The genome of *S. acidocaldarius* encodes three TFB paralogs [296], of which only SaTFB1 and SaTFB3 have been characterized. SaTFB1 is the housekeeping factor used for most transcription under standard growth conditions [111,297,298]. SaTFB2 is transcribed in a cell cycle-dependent manner, but its effect on transcription is thus far unknown. The impact of SaTFB2 on formation of a bent promoter DNA complex with SaTBP was analyzed with confocal smFRET measurements to analyze its role in transcription initiation complex formation.

This study confirmed that promoter DNA bending in *S. acidocaldarius* is strictly dependent on the interaction of both, SaTBP and SaTFB1, which has been reported by a previous study [232]. In contrast, a combination of SaTBP and SaTFB2 has no effect on the promoter DNA conformation. These data suggest that SaTFB2, in the context of T6P-directed transcription, does not function as a basal transcription factor that can stabilize the T6P/SaTBP complex.

A sequence alignment of SaTFB1 and SaTFB2 revealed low conservation of DNA interacting amino acids in the N-terminal cyclin domain of SaTFB2 that contacts the DNA downstream of the TATA-box. In archaea, structural data and chemical crosslinking experiments demonstrated that TFB interacts with a 10 bp DNA segment directly downstream of the TATA-box [53,121,126,496], which is often enriched in adenine nucleotides [497]. In eukaryotes, binding of HsBrf2 is modulated by the TD motif 3–4 downstream of the TATA-box that is primarily recognized by arginine 110 in the N-terminal cyclin fold of HsBrf2 [186]. Sequence changes in the TD motif as well as alanine substitution of R110 each resulted in reduced ternary complex formation in EMSAs (50–70% decrease) [186]. Therefore, the sequence alterations in the N-terminal cyclin domain of SaTFB2 may reduce its DNA-binding affinity and thus impair DNA/SaTBP/SaTFB2 complex formation at the T6P.

Direct interactions between TBP and TFB are critical for DNA/TBP/TFB complex stabilization [232]. To analyze whether the interface to SaTBP is altered in SaTFB2 compared to SaTFB1, the conservation of amino acid residues that are known to be involved in TBP-TFB contacts was determined for both proteins (Figure 73a). Four of the 13 TBP-contacting residues of TFB in the crystal structure of *P. woesei* are considerably altered in SaTFB2 [123]. The threonine 171 and arginine 191 residues in *P. woesei* TFB are extremely conserved among all TFIIB-like factors and mediate contacts with two equally conserved glutamate residues in the C-terminal stirrup loop of TBP [200]. The positively charged R191 is changed to a negatively charged glutamate in SaTFB2

and the polar T171 is altered to a hydrophobic leucine. Likewise, the positively charged R164 and K183 are replaced by uncharged glutamines (Figure 73b). The C-terminal stirrup of TBP, together with α-helix H1' (Figure 12), is the main contributor to the specific protein-protein contacts at its interface with TFB [121].

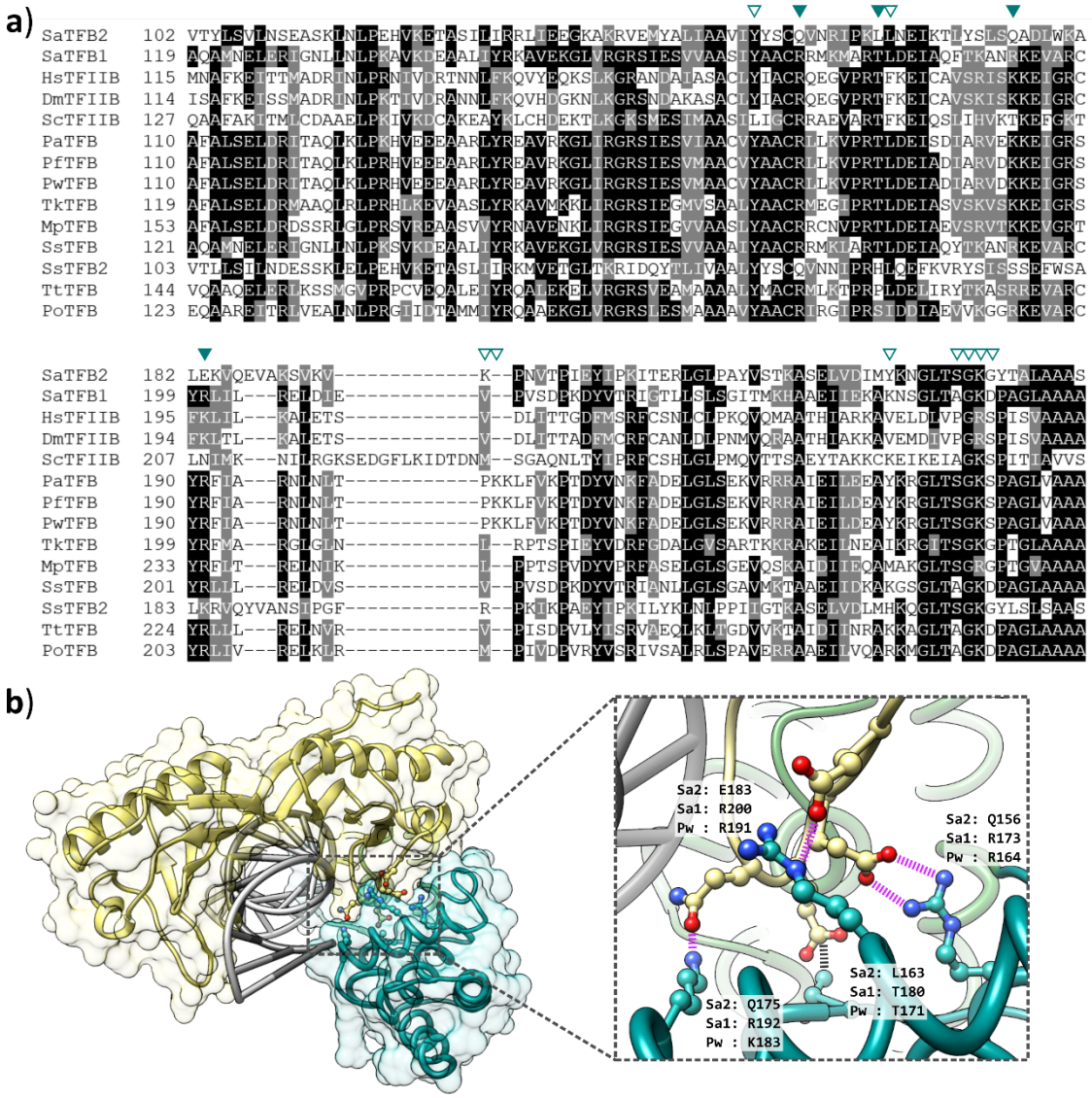

Figure 73: Comparison of TBP-contacting residues of SaTFB1 and SaTFB2. a) Multiple sequence alignment of archaeal and eukaryotic TFB/TFIIB N-terminal cyclin domains (PRALINE webservice). Highly conserved residues are shaded black, residues with chemical properties similar to the consensus residue of a column are shaded gray. Filled triangles indicate highly conserved residues involved in TFB-TBP contacts according to [123] that are not conserved in SaTFB2, empty triangles indicate conserved TFB-TBP contacts that are also conserved in SaTFB2 or TFB-TBP contacts that show low conservation across the alignment. Dm (*Drosophila melanogaster*), Pa (*Pyrococcus abyssi*), Pw (*Pyrococcus woesei*), Tk (*Thermococcus kodakarensis*), Mp (*Methanobacterium paludis*), Tt (*Thermoproteus tenax*), Po (*Pyrodictium occultum*). **b)** The crystal structure of the *P. woesei* DNA/TBP/TFB complex (PDB: 1AIS) was used as a reference for mapping specific residue interactions at the TBP-TFB interface; TBP (yellow), TFB N-terminal cyclin (teal). TFB residues marked with a filled triangle in a) and their interaction partners in TBP are shown as ball-and-stick models. In the close-up, ionic interactions (pink lines) and hydrophobic interaction (black lines) are shown for the *P. woesei* structure (Pw) with the corresponding residues in SaTFB2 (Sa2) and SaTFB1 (Sa1) listed adjacent.

Mutational analysis in archaeal and eukaryotic TBP demonstrated that specific residue substitutions abrogated TFIIB recruitment and transcriptional activity [232,498]. For example, an alanine substitution of R173 and C174 in SaTFB1 abolished DNA/SaTBP/SaTFB1 complex formation in EMSAs [232]. Similarly, an alanine substitution of R164 in ScTBP, which contacts the TFIIB residue corresponding to R173 in SaTFB1 displayed a 100-fold decrease in DNA/TBP/TFIIB complex formation [498]. Hence, changes in chemical properties of these critical interfacing residues can dramatically change binding behavior. The fact these changes in chemical properties determined for SaTFB2 are not present in the canonical initiation factor SaTFB1 suggest that SaTFB2 has a reduced affinity for SaTBP.

Hence, the disruptive effect of SaTFB2 on T6P/SaTBP/SaTFB1 complex formation could be caused by SaTFB2 competing for the SaTFB1 binding interface in the T6P/SaTBP complex. Binding of SaTFB2 would not stabilize the complex due to defects in the SaTBP/SaTFB2 interface resulting in subsequent complex dissociation. In agreement with this idea, a decrease of the bent state population was observed for samples containing SaTBP, SaTFB1 and SaTFB2. This effect was dependent on SaTFB2 concentration and required a six-fold molar excess of SaTFB2 compared to SaTFB1 to reduce the bent promoter fraction by half, relative to the conditions without SaTFB2 (from 56% to 27%). The required surplus of SaTFB2 can be attributed to the above predicted reduced affinity of SaTFB2 for the T6P/SaTBP complex compared to SaTFB2. It can be speculated that the charge reversal resulting from the R200E change in SaTFB2, which likely results in direct proximity of two negatively charged glutamates at the SaTBP/SaTFB2 interface helps to destabilize the DNA/SaTBP interaction and thereby accelerates complex dissociation. Whether SaTFB2 acts by simply competing with SaTFB1 for T6P/TBP complex binding and subsequent SaTBP dissociation occurs due to the lack of a stabilizing interface needs to be determined in future experiments. A systematic mutational analysis of both, DNA- and TBP-contacting residues in SaTFB2 could shed light on their individual effect on complex stabilization.

In this regard, SaTFB2 behaves drastically different compared to other euryarchaeal TFB paralogs that were characterized in previous studies. The two TFB paralogs, PfTFB1 and PfTFB2, encoded by *P. furiosus* are both transcriptionally active. However, PfTFB2 lacks the conserved B-reader domain involved in DNA melting and is thus less efficient in initiating transcription, which was confirmed by swapping the B-reader domains of PfTFB1 and PfTFB2 [292]. Similarly, the closely related *Thermococcus kodakarensis* also encodes two TFB paralogs that both support transcription *in vitro* [499].

In contrast, the inability of SaTFB2 to support even early PIC-formation steps and its negative contribution to canonical T6P/SaTBP/SaTFB1 initiation suggest a regulatory role for SaTFB2 as an inhibitor of transcription. This hypothesis is supported by studies that demonstrated the neofunctionalization of *S. solfataricus* (Ss) TFB3 [299,500]. SsTFB3 acts as an activator of genes involved in UV-induced DNA damage response. SsTFB3 only contains the N-terminal Zn-ribbon and linker region found in canonical TFBs and is missing the two cyclin domains. Instead, a coiled-coil motif is present at the C-terminus of SsTFB3. The Zn-ribbon and coiled coil are essential for the activator function of TFB3 [299]. SsTFB1 as well as SaTFB1 are unusual in that their Zn-ribbon

domain only contains two instead of four cysteine residues as found in most archaeal TFB [501], whereas all four are conserved in the Zn-ribbon of their respective TFB3 [500]. The authors thus speculate that SsTFB1 and SsTFB3 cooperate for initiation, using the canonical Zn-ribbon of SsTFB3 and other domains of SsTFB1 and proposed that the role of SsTFB3 as DNA damage-response regulator is evolutionarily conserved [299,500]. Additionally, a recent study that analyzed evolutionary rates in archaeal gene families determined that neofunctionalization of paralogs is highly abundant among archaeal TFB-family proteins [502].

In order to determine, whether SaTFB2 acts as a global competitor to SaTFB1, total intracellular concentrations of both proteins must be determined. However, since SaTFB2 was required in six-fold molar excess compared to SaTFB1 in the above smFRET experiments to efficiently decrease bent state formation, a local gene-specific role seems more likely. The genome-wide localization of SaTFB2 could be determined via chromatin immunoprecipitation and subsequent sequencing of isolated DNAs (ChIP-Seq).

Taken together, the smFRET experiments conducted here could demonstrate that SaTFB2 can function as an inhibitor to canonical SaTFB1-dependent PIC formation. The amino acids sequence analysis provides first evidence for functional differences between SaTFB1 and SaTFB2 that point towards a role of SaTFB2 as a gene-specific transcriptional regular.

8.4 Mechanism of TFB-RF1-mediated TFB recruitment

The effect of PfTFB-RF1 on PfTBP/PfTFB1 promoter DNA bending was probed using a smFRET promoter bending assay. Initiation at a native *pf1089* promoter strictly required PfTFB-RF1 to yield a bent DNA complex. This is overall in agreement with results by Ochs *et al*. who reported strongly reduced *in vitro* transcription efficiency for this promoter without PfTFB-RF1 [285]. An analysis with the FRET-2CDE Filter did not identify fast conformational changes, suggesting the residual activation of this promoter occurs only at higher temperature that could not be maintained in smFRET assays and was thus not detected.

In contrast, exchanging the native *pf1089* promoter BRE for a *P. furiosus* consensus BRE abolished the requirement for PfTFB-RF1. In this case PfTBP and PfTFB1 are sufficient to form a bent complex. Addition of equimolar concentrations of PfTFB-RF1 increased the efficiency of bent state formation by 50 % to identical level as the native promoter after addition of PfTFB-RF1. For both promoters, 18% of DNAs remained in the unbent state after addition of PfTFB-RF1, indicating that no saturating protein concentrations were used. Compared to the complex without PfTFB-RF1, no change in FRET efficiency was detected for the bent complex, suggesting no alteration in DNA bending angle.

This is supported by the crystal structure of *P. horikoshii* PH1061, an ArsR-like transcriptional regulator of unknown function that bears 77% sequence identity to PfTFB-RF1 [289]. Interestingly, the distance between recognition helices in this homolog is not suitable for DNA-binding. Consequently, SELEX experiments did not yield a compatible target sequence suggesting it presents a closed conformation that requires activation [289]. Thus, PfTFB-RF1 likely has a slightly modified structural arrangement that allows DNA binding it its native state, or PfTFB1 is sufficient to induce the necessary conformational change. The structure also suggests that PfTFB-RF1 – due

to its small size – cannot simultaneously interact with both, its target site and the TATA-box. Consequently, conformational changes that might be induced by PfTFB-RF1 binding can most likely not be monitored by the promoter DNA bending-assay.

Bacterial ArsR-like transcriptional regulators are mostly involved in stress response to critical levels of metal ions (reviewed in [503]). While some archaeal ArsR-type regulators are also involved in metalloregulatory processes [504–506], their functional repertoire seems to be more diverse (reviewed in [281]); e.g. MsvR, an ArsR-like regulator of *Methanothermobacter thermautothrophicus* is a cellular redox sensor that, similar to HsBrf2, employs a cysteine residue to modify its binding capability and controls genes involved in oxidative stress response [507]. Likewise, SurR, a redox-responsive ArsR-like regulator encoded in the genomes of *P. furiosus* and *Thermococcus kodakarensis*, activates or represses transcription by binding to two SBS sequence elements upstream and downstream of the TATA-box [508,509]. Cooperative binding of SurR to two SBSs directly adjacent to the TATA-box of the FNOR1 promoter strongly represses transcription, whereas binding to a more distal upstream SBS (-18 relative to the TATA box) at the FNOR2 promoter enhances transcription [509]. The activator function of SurR could therefore be related to the mechanism employed by PfTFB-RF1.

PfTFB-RF1 dependent gene activation is highly conserved within the *Thermococcales*, as genome analysis of identified the *pf1089/tfb-rf1* operon in 28 out of 35 organisms and 14 organisms with both, the *pf1089*/*tfb-rf1* and *pf101*1/*pf1012* operon [288]. A similar activation mechanism has been reported for the *S. solfataricus* araS promoter, that contains a weak BRE and an upstream ara-box element [510]. *In vivo* reporter assays demonstrated that efficient transcription of the araS promoter strictly depends on the presence of this upstream element, while mutation of the BRE to a consensus sequence allowed ara-box independent transcription. In the closely related *S. acidocaldarius*, promoter bending is strictly dependent on both, SaTBP and SaTFB1. In this context it would be interesting to explore, whether facilitated TFB recruitment as regulatory mechanism is only present in archaea that rely on both factors for bent state formation.

A study from Ding *et al.* showed that in *Methanococcus maripaludis*, the *fla* operon is regulated by EarA, a factor that supports binding of TFB to a non-canonical BRE. EarA-independent expression of the fla operon was reported upon mutation of the BRE to a more consensus-like sequence [511]. *M. maripaludis* belongs to the *Methanococcales* including for example *M. jannaschii* that requires only TBP for this step. This indicates that facilitated TFB-recruitment might be a universal regulatory mechanism.

Kinetic experiments at room temperature showed that PfTFB-RF1 affects complex assembly two-fold: i) by accelerating bent state formation and ii) by shifting the equilibrium towards higher bent state ratios. Surprisingly, complex formation was faster at the native pf1089 promoter, hinting at a competition between canonical PfTFB1 binding and PfTFB-RF1-mediated recruitment. Potentially, PfTFB1/PfTFB-RF1 complexes in solution are prevented from binding to stably bound PfTBP/PfTFB1 complexes at the P_{con}, which cannot occur at the P_{nat} due to the weak BRE. Thereby, free PfTFB1/PfTFB-RF1 complex would reduce the effective concentration of PfTFB-RF in solution. This could be addressed in future experiments using fluorescently labelled proteins to monitor factor interactions without DNA.

In conclusion, the characterization of PfTFB-RF1-mediated PfTFB1 recruitment could provide novel insights into the kinetics of factors binding, uncovering an increased association rate at a weaker BRE. Furthermore, no conformational changes in the promoter DNA could be detected, strongly implying that PfTFB-RF1 acts as a static secondary binding platform for PfTFB1, supporting the mechanism proposed by Ochs *et al*.

8.5 Influence of force on DNA bending induced by archaeal transcription factors

Similar to the measurements with eukaryotic transcription factors, the DNA-bending induced by the transcription factors TBP and TFB of the archaeal organisms *M. jannaschii* and *P. furiosus* was probed in confocal smFRET experiments using the DNA origami FC technique. A critical difference between both systems is the requirement of MjTBP only for DNA bending, whereas PfTBP and PfTFB1 are required simultaneously to establish a bent promoter complex.

Data for T6P/MjTBP showed a decrease in P_{bent} from 56% to 21% for increasing forces from 0 pN to 6.2 pN. A highly similar decrease in P_{bent} was observed when comparable forces were used for the T6P/PfTBP/PfTFB complex. Here, the bent state dropped from 66% to 37%. Hence, a complex formation of the two-factor system PfTBP/PfTFB displays similar efficiency and force resistance as MjTBP alone. A potential additive effect of MjTFB on T6P/MjTBP complex stabilization was not tested in this work, but it has been previously shown that this factor does not promote bent state formation nor influence the DNA conformation [232].

The force-dependent binding of MjTBP to the T6P was also measured by Nickels *et al.* [94] (Figure 74). Overall, the reference data show less efficient binding at low forces but indicates a higher force resistance, although forces above 6.2 pN were not tested in this work. Several factors (conditions used here vs. conditions used by Nickels *et al.*) can influence this behavior spanning the difference in protein concentration used (50 µM vs. 1 µM, different preparations), sample temperature (23 °C vs. 35 °C) and different salt concentration (1 M NaCl + 1.5 M KAc vs. 1 M NaCl). In particular, salt concentration has been shown to affect binding of MjTBP, increasing bent state stability with increasing concentration of monovalent ions [232].

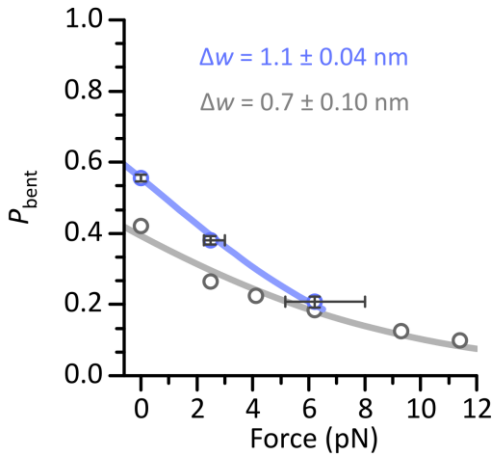

Figure 74: Comparison of force-dependent DNA-bending by *M. jannaschii* TBP between independent studies. The data generated in this study (purple) and by Nickels *et al*. (gray) [94] using an identical FC design are compared. The fit with a two-state Boltzmann distribution is shown as a solid line and the calculated end-to-end distance change Δ*w* of the double-stranded promoter DNA is indicated by color. The x-axis error results from the variance of the single-nucleotide length and the y-axis error is derived via error propagation from the Gaussian fit.

On the other hand, high salt concentrations may increase the force applied by the entropic spring by screening repulsive negative charges of the DNA backbone. This may artificially decrease the stiffness of the ssDNA spring and thus lead to higher forces (Chapter 8.2.5). Further research will which of these factors dominate the T6P/MjTBP interaction in either study will require.

Gietl *et al*. analyzed the different DNA-binding modes demonstrated by *S. acidocaldarius* (TBP/TFB required) and *M. jannaschii* [232]. Their findings show that hydrophobic interactions are the main driving force of TBP/DNA-interaction in hyperthermophilic archaea. High intracellular salt concentrations found in methanogens (up to 1 M K^+ [512]) such as *M. jannaschii* as well as high temperature stabilize hydrophobic interactions and thus present adaptation to extreme environmental conditions [513,514]. In *P. woesei*, high salt concentrations have also been shown to stabilize TBP/DNA interactions by mediating salt bridges between anionic TBP residues and the DNA backbone [515]. This was demonstrated for a glutamic acid (E12) that is highly conserved among archaeal TBPs, but not eukaryotic TBPs [515]. Mutagenesis to alanine prevents incorporation of stabilizing cations into the TBP/DNA interface and resulted in reduced affinity at high salt concentrations [515]. DNA-interactions of *P. furiosus* initiation factors were only measured at 250 mM NaCl based on established experimental conditions [127]. However, these could potentially be further increased by using higher salt concentrations.

Histone proteins in archaea form tight interactions, resulting in continuous stacks of nucleosomes [350,351] up to 300 bp in length [350]. Disruption of these extended structures by site-directed mutagenesis resulted in impaired gene regulation and slower adaptation to new growth conditions [351]. In the euryarchaeon *T. kodakarensis*, histone proteins can also form extended structures that assemble in distinct DNA regions and nucleosome free regions were detected around promoter regions and TSS of genes [372]. Nucleoid-associated proteins like Cren7 and Sul7 in *S. solfataricus* can compact DNA by introducing stiff bends in the DNA that can resist forces up to 3.5 pN [85]. Furthermore, a reduced transcription rates of histone-bound DNA was reported for *P. furiosus* [371]. The diminishing effect was amplified for transcription of circular DNA templates compared to linear DNA, suggesting that topological changes introduced by nucleosome assembly, nucleoid-associated proteins well as transcriptional activity can accumulate in constraint DNA regions and affect transcription.

Interestingly, *M. jannaschii* encodes one of the few archaeal histone isoforms (MJ1647) featuring eukaryote-like C-terminal extensions that were shown to be crucial for DNA binding and the formation of higher-order structures [516]. It can be speculated that the high affinity of MjTBP to DNA without the need for additional stabilization presents an evolutionary response to the novel interplay of histones and DNA that in eukaryotes are enable by histone-tail interactions and can project additional forces on the coupled DNA [517]. This idea is further supported by the emergence of the MjTBP recruitment factor MjPtr2, which has been reported to facilitate binding of MjTBP to weak TATA-boxes even when histones are added at saturating concentrations [374]. Still, transcriptional control by histones can take place in *M. jannaschii* as demonstrated by the histone assembly upstream of the *rb2* gene, which has been shown to block formation of PICs and thereby reduce transcription rates [374]. This hints towards a co-evolution of archaeal histones and the transcriptional machinery. Interestingly, structural modeling of the histones encoded by

Heimdallarchaeota of the ASGARD clade, which are evolutionary closer to modern eukaryotes [518], show that the LC 3 histones contain tails similar in length and sequence composition to the extensions of eukaryotic histone subunit H4, potentially presenting a link to modern eukaryotic histones [364].
The force landscape of archaeal chromatin is practically unexplored. Experiments conducted in this work could demonstrate that forces on DNA can influence archaeal transcription factor binding and thereby influence gene regulation.

8.6 Conclusion and outlook

In this work, smFRET experiments were used to characterize the stepwise assembly of human TFIIIB complex. HsTBP transiently binds the promoter DNA in a single step, inducing a relatively small bending angle, which may present a partially bent intermediate. Binding of reduced HsBrf2 induces further bending and stabilizes the complex in the fully bent conformation. HsBdp1 enters the complex as the final components that interconnects all subunits, completely encasing the DNA. This was highlighted in DNA origami-based force measurements, where human TFIIIB conferred superior force resistance compared to a combination of TFIIA and TFIIB that share no overlapping interfaces. In the context of the RNAP III transcription cycle, this allows maintenance of a fully assembled initiation complex that can be reused repeatedly by RNAP III throughout multiple reinitiation events [342,343]. Future experiments could address TFIIIB stability in the wider genetic context of snRNA transcription. Here, interaction with the adjoining factors SNAPc and Oct-1, as well as experiments using reconstituted nucleosomes [339] could provide further insight into RNAP II and RNAP III transcription mechanisms, due to the overlapping functionality and involved factors for this gene class [260,261].
The single-molecule approach employed in this work allowed direct observation of the fast binding dynamics and to distinguish between partially and fully bent complexes, revealing intricate details of the assembly pathway that could not be deduced from static crystal structures [186,277] and thus led to a more complete picture of TFIIIB-directed transcription initiation.
While experiments with DNA origami FCs demonstrated that the model used for force calculation likely requires further refinement [495], the more important aspects are the new possibilities this method opens for the analysis of protein-DNA interactions. Force measurements with DNA-distorting proteins were thus far limited to systems that introduce drastic conformational changes in the DNA such as loops [464] or multiple bends [465]. The DNA origami design introduced by Nickels *et al.* makes single-molecule force spectroscopy accessible to small conformational changes induced by single proteins [94]. In this work, experiments with human and archaeal transcription initiation factors further extended the scope of this approach by demonstrating its applicability to complex multi-protein systems.
For the *S. acidocaldarius* transcription system, smFRET experiments could provide first evidence for its disruptive effect on canonical PIC formation. Changes in key residues at the SaTBP/SaTFB1 interface were shown previously to abolish complex formation [232], and similar or more unfavorable interactions sites are present at the SaTBP/SaTFB2 interface. Further insight on the involved mechanism could be gained from time-resolved smFRET experiments with fluorescently

labeled proteins to monitor the stepwise binding of individual factors, similar to the approach utilized by Zhang *et al.* [468]. However, complex formation was highly inefficient at room temperature (data not shown), and will require the use of a heating system for microscope samples [232].

For the *P. furiosus* transcription system, analysis of PfTFB-RF1 mediated PfTFB1 recruitment to promoters with strong and weak BREs presented results that agree with previous biochemical studies [285,288]. Hence, PfTFB-RF1 can support PfTFB binding to the promoter by presenting an additional interaction site to compensate for weak DNA/PfTFB1 interactions. Curiously, measurements that follow the complex assembly over time indicate an accelerated rate of bent state formation at the P_{nat}, while the same equilibrium bent state occupancy is reached for both promoters. Thus, it can be speculated that canonical P_{con}/PfTBP/PfTFB1 complex formation somehow interferes with PfTFB-RF1 mediated recruitment of PfTFB1. Microscale thermophoresis could be employed to determine binding constants of all involved factors and gain further insight into this conundrum.

Experiments performed in this work could highlight gene-regulatory molecular features and mechanisms that are conserved among archaeal and eukaryotic transcription systems. Binding of TBP to the promoter is regulated in many archaeal species by concerted interaction with TFB, as demonstrated for the *P. furiosus* and *S. acidocaldarius* transcription systems. Similarly, non-optimal binding sites such as the weak BRE of the *pf1089* promoter or the non-consensus TATA-box of the U6 snRNA promoter allows for multiple control steps in the initiation process by additional factors such as TFB-RF1 and SNAPc. TFIIB-like factors are specialized adapter proteins that confer RNAP specificity. In archaea, paralogs of these factors have emerged that regulate differential gene expression as predicted for SaTFB2, enabling adaptation to environmental changes. In analogy, higher eukaryotes have evolved two distinct variants of Brf-proteins, of which Brf2 regulates a subset of genes in response to oxidative stress. Emergence of specialized domains such as the C-terminal extension that is present in Brf-proteins but not TFB and TFIIB present further adaption to specialized RNAP functionality. Hence, the RNAP III-specific factor Bdp1 likely evolved as a stabilizing scaffold of the core TBP/Brf1/2 complex to support the high transcriptional output of RNAP III. Taken together, the mechanisms studied here all directly modulate the stability of the initial DNA/TBP/TFIIB-life factor complex that is at the very heart of transcription initiation and thus allow direct control over this central process.

9 References

[1] S. Mohapatra, C.-T. Lin, X.A. Feng, A. Basu, T. Ha, Single-Molecule Analysis and Engineering of DNA Motors., Chem. Rev. 120 (2020) 36–78.

[2] L. Bacic, A. Sabantsev, S. Deindl, Recent advances in single-molecule fluorescence microscopy render structural biology dynamic, Curr. Opin. Struct. Biol. 65 (2020) 61–68.

[3] E. Monachino, L.M. Spenkelink, A.M. van Oijen, Watching cellular machinery in action, one molecule at a time, J. Cell Biol. 216 (2017) 41–51.

[4] A.A. Deniz, T.A. Laurence, G.S. Beligere, M. Dahan, A.B. Martin, D.S. Chemla, P.E. Dawson, P.G. Schultz, S. Weiss, Single-molecule protein folding: Diffusion fluorescence resonance energy transfer studies of the denaturation of chymotrypsin inhibitor 2, Proc. Natl. Acad. Sci. 97 (2000) 5179–5184.

[5] H. Frauenfelder, S. Sligar, P. Wolynes, The energy landscapes and motions of proteins, Science (80-.). 254 (1991) 1598–1603.

[6] S. Hohng, R. Zhou, M.K. Nahas, J. Yu, K. Schulten, D.M.J. Lilley, T. Ha, Fluorescence-force spectroscopy maps two-dimensional reaction landscape of the holliday junction, Science. 318 (2007) 279–283.

[7] H. Miller, Z. Zhou, J. Shepherd, A.J.M. Wollman, M.C. Leake, Single-molecule techniques in biophysics: A review of the progress in methods and applications, Reports Prog. Phys. 81 (2018) 024601.

[8] A. Meller, L. Nivon, E. Brandin, J. Golovchenko, D. Branton, Rapid nanopore discrimination between single polynucleotide molecules, Proc. Natl. Acad. Sci. U. S. A. 97 (2000) 1079–1084.

[9] M. Rief, M. Gautel, F. Oesterhelt, J.M. Fernandez, H.E. Gaub, Reversible unfolding of individual titin immunoglobulin domains by AFM, Science (80-.). 276 (1997) 1109–1112.

[10] A. Ashkin, J.M. Dziedzic, J.E. Bjorkholm, S. Chu, Observation of a single-beam gradient force optical trap for dielectric particles, in: Opt. Angular Momentum, CRC Press, 2016: pp. 196–198.

[11] Z. Farka, M.J. Mickert, M. Pastucha, Z. Mikušová, P. Skládal, H.H. Gorris, Advances in Optical Single-Molecule Detection: En Route to Supersensitive Bioaffinity Assays, Angew. Chemie - Int. Ed. 59 (2020) 10746–10773.

[12] N.C. Shaner, G.G. Lambert, A. Chammas, Y. Ni, P.J. Cranfill, M.A. Baird, B.R. Sell, J.R. Allen, R.N. Day, M. Israelsson, M.W. Davidson, J. Wang, A bright monomeric green fluorescent protein derived from Branchiostoma lanceolatum, Nat. Methods. 10 (2013) 407–409.

[13] M.H. Ulbrich, E.Y. Isacoff, Subunit counting in membrane-bound proteins, Nat. Methods. 4 (2007) 319–321.

[14] I. Nikič, T. Plass, O. Schraidt, J. Szymański, J. a G. Briggs, C. Schultz, E. a. Lemke, Minimal tags for rapid dual-color live-cell labeling and super-resolution microscopy, Angew. Chemie - Int. Ed. 53 (2014) 2245–2249.

[15] A. Gust, L. Jakob, D. Zeitler, A. Bruckmann, K. Kramm, S. Willkomm, P. Tinnefeld, G. Meister, D. Grohmann, Site-specific labelling of native mammalian proteins for single-molecule FRET measurements, ChemBioChem. (2018) 1–5.

[16] A. Gust, A. Zander, A. Gietl, P. Holzmeister, S. Schulz, B. Lalkens, P. Tinnefeld, D. Grohmann, A starting point for fluorescence-based single-molecule measurements in biomolecular research., Molecules. 19 (2014) 15824–65.

[17] S.M.J.L. van den Wildenberg, B. Prevo, E.J.G. Peterman, A brief introduction to single-molecule fluorescence methods, in: Methods Mol. Biol., Humana Press Inc., 2018: pp. 93–113.

[18] P. Holzmeister, G.P. Acuna, D. Grohmann, P. Tinnefeld, Breaking the concentration limit of optical single-molecule detection., Chem. Soc. Rev. 43 (2014) 1014–28.

[19] M. Böhmer, J. Enderlein, Fluorescence Spectroscopy of Single Molecules under Ambient

Conditions: Methodology and Technology, ChemPhysChem. 4 (2003) 792–808.
[20] G.P. Acuna, F.M. Möller, P. Holzmeister, S. Beater, B. Lalkens, P. Tinnefeld, Fluorescence enhancement at docking sites of DNA-directed self-assembled nanoantennas, Science (80-.). 338 (2012) 506–510.
[21] A. Kinkhabwala, Z. Yu, S. Fan, Y. Avlasevich, K. Müllen, W.E. Moerner, Large single-molecule fluorescence enhancements produced by a bowtie nanoantenna, Nat. Photonics. 3 (2009) 654–657.
[22] S. Nie, D.T. Chiu, R.N. Zare, Probing individual molecules with confocal fluorescence microscopy, Science (80-.). 266 (1994) 1018–1021.
[23] H.J. Levene, J. Korlach, S.W. Turner, M. Foquet, H.G. Craighead, W.W. Webb, Zero-mode waveguides for single-molecule analysis at high concentrations, Science (80-.). 299 (2003) 682–686.
[24] B. Okumus, T.J. Wilson, D.M.J. Lilley, T. Ha, Vesicle encapsulation studies reveal that single molecule ribozyme heterogeneities are intrinsic., Biophys. J. 87 (2004) 2798–2806.
[25] T. Funatsu, Y. Harada, M. Tokunaga, K. Saito, T. Yanagida, Imaging of single fluorescent molecules and individual ATP turnovers by single myosin molecules in aqueous solution., Nature. 374 (1995) 555–559.
[26] A.A. Deniz, M. Dahan, J.R. Grunwell, T. Ha, A.E. Faulhaber, D.S. Chemla, S. Weiss, P.G. Schultz, Single-pair fluorescence resonance energy transfer on freely diffusing molecules: Observation of Förster distance dependence and subpopulations, Proc. Natl. Acad. Sci. U. S. A. 96 (1999) 3670–3675.
[27] D. Axelrod, Cell-substrate contacts illuminated by total internal reflection fluorescence, J. Cell Biol. 89 (1981) 141–145.
[28] T. Förster, Energiewanderung und Fluoreszenz, Naturwissenschaften. 33 (1946) 166–175.
[29] L. Stryer, R.P. Haugland, Energy transfer: a spectroscopic ruler, Proc. Natl. Acad. Sci. U. S. A. 58 (1967) 719–26.
[30] A. Muschielok, J. Andrecka, A. Jawhari, F. Brückner, P. Cramer, J. Michaelis, A nano-positioning system for macromolecular structural analysis., Nat. Methods. 5 (2008) 965–71.
[31] T. Ha, T. Enderle, D.F. Ogletree, D.S. Chemla, P.R. Selvin, S. Weiss, Probing the interaction between two single molecules: Fluorescence resonance energy transfer between a single donor and a single acceptor, Proc. Natl. Acad. Sci. U. S. A. 93 (1996) 6264–6268.
[32] E. Lerner, T. Cordes, A. Ingargiola, Y. Alhadid, S.Y. Chung, X. Michalet, S. Weiss, Toward dynamic structural biology: Two decades of single-molecule Förster resonance energy transfer, Science (80-.). 359 (2018) eaan1133.
[33] J. Choi, R. Grosely, E. V. Puglisi, J.D. Puglisi, Expanding single-molecule fluorescence spectroscopy to capture complexity in biology, Curr. Opin. Struct. Biol. 58 (2019) 233–240.
[34] M. Sustarsic, A.N. Kapanidis, Taking the ruler to the jungle: Single-molecule FRET for understanding biomolecular structure and dynamics in live cells, Curr. Opin. Struct. Biol. 34 (2015) 52–59.
[35] M. Dimura, T.O. Peulen, C.A. Hanke, A. Prakash, H. Gohlke, C.A. Seidel, Quantitative FRET studies and integrative modeling unravel the structure and dynamics of biomolecular systems, Curr. Opin. Struct. Biol. 40 (2016) 163–185.
[36] J. Hohlbein, L. Aigrain, T.D. Craggs, O. Bermek, O. Potapova, P. Shoolizadeh, N.D.F. Grindley, C.M. Joyce, A.N. Kapanidis, Conformational landscapes of DNA polymerase i and mutator derivatives establish fidelity checkpoints for nucleotide insertion, Nat. Commun. 4 (2013) 1–11.
[37] Y. Santoso, C.M. Joyce, O. Potapova, L. Le Reste, J. Hohlbein, J.P. Torella, N.D.F. Grindley, A.N. Kapanidis, Conformational transitions in DNA polymerase I revealed by single-molecule FRET, Proc. Natl. Acad. Sci. U. S. A. 107 (2010) 715–720.
[38] H. Yardimci, X. Wang, A.B. Loveland, I. Tappin, D.Z. Rudner, J. Hurwitz, A.M. Van Oijen, J.C.

Walter, Bypass of a protein barrier by a replicative DNA helicase, Nature. 492 (2012) 205–209.
[39] D. Duzdevich, M.D. Warner, S. Ticau, N.A. Ivica, S.P. Bell, E.C. Greene, The dynamics of eukaryotic replication initiation: Origin specificity, licensing, and firing at the single-molecule level, Mol. Cell. 58 (2015) 483–494.
[40] C.E. Aitken, J.D. Puglisi, Following the intersubunit conformation of the ribosome during translation in real time, Nat. Struct. Mol. Biol. 17 (2010) 793–800.
[41] S.C. Blanchard, R.L. Gonzalez, H.D. Kim, S. Chu, J.D. Puglisi, tRNA selection and kinetic proofreading in translation, Nat. Struct. Mol. Biol. 11 (2004) 1008–1014.
[42] J. Der Wen, L. Lancaster, C. Hodges, A.C. Zeri, S.H. Yoshimura, H.F. Noller, C. Bustamante, I. Tinoco, Following translation by single ribosomes one codon at a time, Nature. 452 (2008) 598–603.
[43] N. Caliskan, V.I. Katunin, R. Belardinelli, F. Peske, M. V. Rodnina, Programmed -1 frameshifting by kinetic partitioning during impeded translocation, Cell. 157 (2014) 1619–1631.
[44] F. Werner, D. Grohmann, Evolution of multisubunit RNA polymerases in the three domains of life., Nat. Rev. Microbiol. 9 (2011) 85–98.
[45] J.R. Warner, The economics of ribosome biosynthesis in yeast, Trends Biochem. Sci. 24 (1999) 437–440.
[46] B.J. Greber, E. Nogales, The Structures of Eukaryotic Transcription Pre-initiation Complexes and Their Functional Implications, in: Subcell. Biochem., NLM (Medline), 2019: pp. 143–192.
[47] J. Griesenbeck, H. Tschochner, D. Grohmann, Structure and Function of RNA Polymerases and the Transcription Machineries, Subcell. Biochem. 83 (2017) 225–270.
[48] A. Mazumder, A.N. Kapanidis, Recent Advances in Understanding σ70-Dependent Transcription Initiation Mechanisms, J. Mol. Biol. 431 (2019) 3947–3959.
[49] D.F. Browning, S.J.W. Busby, Local and global regulation of transcription initiation in bacteria, Nat. Rev. Microbiol. 14 (2016) 638–650.
[50] C. Mejía-Almonte, S.J.W. Busby, J.T. Wade, J. van Helden, A.P. Arkin, G.D. Stormo, K. Eilbeck, B.O. Palsson, J.E. Galagan, J. Collado-Vides, Redefining fundamental concepts of transcription initiation in bacteria, Nat. Rev. Genet. (2020) 1–16.
[51] C. Plaschka, M. Hantsche, C. Dienemann, C. Burzinski, J. Plitzko, P. Cramer, Transcription initiation complex structures elucidate DNA opening, Nature. 533 (2016) 353–358.
[52] Y. He, C. Yan, J. Fang, C. Inouye, R. Tjian, I. Ivanov, E. Nogales, Near-atomic resolution visualization of human transcription promoter opening, Nature. 533 (2016) 359–365.
[53] J. Nagy, D. Grohmann, A.C.M. Cheung, S. Schulz, K. Smollett, F. Werner, J. Michaelis, Complete architecture of the archaeal RNA polymerase open complex from single-molecule FRET and NPS, Nat. Commun. 6 (2015) 6161.
[54] K. Kramm, C. Engel, D. Grohmann, Transcription initiation factor TBP: old friend new questions., Biochem. Soc. Trans. 47 (2019) 411–423.
[55] P. Cramer, A Tale of Chromatin and Transcription in 100 Structures, Cell. 159 (2014) 985–994.
[56] S. Osman, P. Cramer, Structural Biology of RNA Polymerase II Transcription: 20 Years On, (2020) 1–34.
[57] M.H. Larson, R. Landick, S.M. Block, Single-Molecule Studies of RNA Polymerase: One Singular Sensation, Every Little Step It Takes, Mol. Cell. 41 (2011) 249–262.
[58] J. Michaelis, B. Treutlein, Single-molecule studies of RNA polymerases, Chem. Rev. 113 (2013) 8377–8399.
[59] M. Dangkulwanich, T. Ishibashi, L. Bintu, C. Bustamante, Molecular Mechanisms of Transcription through Single-Molecule Experiments, Chem. Rev. 114 (2014) 3203–3223.
[60] K. Kramm, U. Endesfelder, D. Grohmann, A Single-Molecule View of Archaeal Transcription,

J. Mol. Biol. 431 (2019) 4116–4131.
[61] S. Brasselet, W.E. Moerner, Fluorescence Behavior of Single-Molecule pH-Sensors, Single Mol. 1 (2000) 17–23.
[62] P.F. Aramendía, R. Martín Negri, E. San Román, Temperature dependence of fluorescence and photoisomerization in symmetric carbocyanines. Influence of medium viscosity and molecular structure, J. Phys. Chem. 98 (1994) 3165–3173.
[63] H. Hwang, H. Kim, S. Myong, Protein induced fluorescence enhancement as a single molecule assay with short distance sensitivity, Proc. Natl. Acad. Sci. U. S. A. 108 (2011) 7414–7418.
[64] N. Karedla, A.I. Chizhik, I. Gregor, A.M. Chizhik, O. Schulz, J. Enderlein, Single-Molecule Metal-Induced Energy Transfer (smMIET): Resolving Nanometer Distances at the Single-Molecule Level, ChemPhysChem. 15 (2014) 705–711.
[65] J.R. Lakowicz, Principles of fluorescence spectroscopy, 2006.
[66] U. Noomnarm, R.M. Clegg, Fluorescence lifetimes: Fundamentals and interpretations, Photosynth. Res. 101 (2009) 181–194.
[67] T. Förster, Zwischenmolekulare Energiewanderung und Fluoreszenz, Ann. Phys. 437 (1948) 55–75.
[68] T. Förster, Experimentelle und theoretische Untersuchung des zwischenmolekularen Übergangs von Elektronenanregungsenergie, Zeitschrift Fur Naturforsch. - Sect. A J. Phys. Sci. 4 (1949) 321–327.
[69] I. Medintz, N. Hildebrandt, FRET-Förster resonance energy transfer: from theory to applications, (2013).
[70] T. Förster, Transfer Mechanisms of Electronic Excitation Energy, Radiat. Res. Suppl. 2 (1960) 326.
[71] B. Ambrose, M. Willmott, T. Johnston-Wood, R.A. Shaw, J.G. Hill, T.D. Craggs, Below the FRET Limit: A New Quantitative Single-Molecule Tool for Measuring Short-Range (0-3 NM) Biomolecular Conformations, Biophys. J. 118 (2020) 615a.
[72] T. Förster, Fluoreszenz organischer Verbindungen, Vandenhoeck & Ruprecht, 1982.
[73] L. Stryer, Fluorescence Energy Transfer as a Spectroscopic Ruler, Annu. Rev. Biochem. 47 (1978) 819–846.
[74] L. Le Reste, J. Hohlbein, K. Gryte, A.N. Kapanidis, Characterization of dark quencher chromophores as nonfluorescent acceptors for single-molecule FRET, Biophys. J. 102 (2012) 2658–2668.
[75] M.L. Martin-Fernandez, C.J. Tynan, S.E.D. Webb, A “pocket guide” to total internal reflection fluorescence., J. Microsc. 252 (2013) 16–22.
[76] H. Yin, M.D. Wang, K. Svoboda, R. Landick, S.M. Block, J. Gelles, Transcription against an applied force, Science (80-.). 270 (1995) 1653–1657.
[77] M.D. Wang, M.J. Schnitzer, H. Yin, R. Landick, J. Gelles, S.M. Block, Force and velocity measured for single molecules of RNA polymerase, Science (80-.). 282 (1998) 902–907.
[78] E.A. Galburt, S.W. Grill, A. Wiedmann, L. Lubkowska, J. Choy, E. Nogales, M. Kashlev, C. Bustamante, Backtracking determines the force sensitivity of RNAP II in a factor-dependent manner, Nature. 446 (2007) 820–823.
[79] B. Maier, D. Bensimon, V. Croquette, Replication by a single DNA polymerase of a stretched single-stranded DNA, Proc. Natl. Acad. Sci. U. S. A. 97 (2000) 12002–12007.
[80] G.J.L. Wulte, S.B. Smith, M. Young, D. Keller, C. Bustamante, Single-molecule studies of the effect of template tension on T7 DNA polymerase activity, Nature. 404 (2000) 103–106.
[81] D.H. Goldman, C.M. Kaiser, A. Milin, M. Righini, I. Tinoco, C. Bustamante, Mechanical force releases nascent chain-mediated ribosome arrest in vitro and in vivo, Science (80-.). 348 (2015) 457–460.
[82] J.M. Eeftens, S. Bisht, J. Kerssemakers, M. Kschonsak, C.H. Haering, C. Dekker, Real-time detection of condensin-driven <scp>DNA</scp> compaction reveals a multistep binding

mechanism, EMBO J. 36 (2017) 3448–3457.
[83] R.A. Keenholtz, T. Dhanaraman, R. Palou, J. Yu, D. D'amours, J.F. Marko, Oligomerization and ATP stimulate condensin-mediated DNA compaction, Sci. Rep. 7 (2017) 1–13.
[84] M. Ganji, I.A. Shaltiel, S. Bisht, E. Kim, A. Kalichava, C.H. Haering, C. Dekker, Real-time imaging of DNA loop extrusion by condensin, Science (80-.). 360 (2018) 102–105.
[85] R.P.C. Driessen, H. Meng, G. Suresh, R. Shahapure, G. Lanzani, U.D. Priyakumar, M.F. White, H. Schiessel, J. Van Noort, R.T. Dame, Crenarchaeal chromatin proteins Cren7 and Sul7 compact DNA by inducing rigid bends, Nucleic Acids Res. 41 (2013) 196–205.
[86] K.C. Neuman, A. Nagy, Single-molecule force spectroscopy: optical tweezers, magnetic tweezers and atomic force microscopy, Nat. Methods. 5 (2008) 491–505.
[87] T. Strick, J.F. Allemand, V. Croquette, D. Bensimon, Twisting and stretching single DNA molecules, Prog. Biophys. Mol. Biol. 74 (2000) 115–140.
[88] K.C. Neuman, E.A. Abbondanzieri, R. Landick, J. Gelles, S.M. Block, Ubiquitous Transcriptional Pausing Is Independent of RNA Polymerase Backtracking, Cell. 115 (2003) 437–447.
[89] K.M. Herbert, A. La Porta, B.J. Wong, R.A. Mooney, K.C. Neuman, R. Landick, S.M. Block, Sequence-Resolved Detection of Pausing by Single RNA Polymerase Molecules, Cell. 125 (2006) 1083–1094.
[90] J.W. Shaevitz, E.A. Abbondanzieri, R. Landick, S.M. Block, Backtracking by single RNA polymerase molecules observed at near-base-pair resolution, Nature. 426 (2003) 684–687.
[91] E.A. Abbondanzieri, W.J. Greenleaf, J.W. Shaevitz, R. Landick, S.M. Block, Direct observation of base-pair stepping by RNA polymerase, Nature. 438 (2005) 460–465.
[92] C.O. Mejean, A.W. Schaefer, E.A. Millman, P. Forscher, E.R. Dufresne, Multiplexed force measurements on live cells with holographic optical tweezers, Opt. Express. 17 (2009) 6209.
[93] M.T. Woodside, S.M. Block, Reconstructing folding energy landscapes by single-molecule force spectroscopy, Annu. Rev. Biophys. 43 (2014) 19–39.
[94] P.C. Nickels, B. Wünsch, P. Holzmeister, W. Bae, L.M. Kneer, D. Grohmann, P. Tinnefeld, T. Liedl, Molecular force spectroscopy with a DNA origami–based nanoscopic force clamp, Science. 354 (2016) 305–307.
[95] J.J. Funke, P. Ketterer, C. Lieleg, S. Schunter, P. Korber, H. Dietz, Uncovering the forces between nucleosomes using DNA origami, Sci. Adv. 2 (2016) e1600974.
[96] H. Gu, W. Yang, N.C. Seeman, DNA scissors device used to measure mutS binding to dna mis-pairs, J. Am. Chem. Soc. 132 (2010) 4352–4357.
[97] W. Shen, M.F. Bruist, S.D. Goodman, N.C. Seeman, A Protein-Driven DNA Device That Measures the Excess Binding Energy of Proteins That Distort DNA, Angew. Chemie Int. Ed. 43 (2004) 4750–4752.
[98] N.C. Seeman, Nucleic acid junctions and lattices, J. Theor. Biol. 99 (1982) 237–247.
[99] P.W.K. Rothemund, Folding DNA to create nanoscale shapes and patterns, Nature. 440 (2006) 297–302.
[100] S.M. Douglas, H. Dietz, T. Liedl, B. Högberg, F. Graf, W.M. Shih, Self-assembly of DNA into nanoscale three-dimensional shapes., Nature. 459 (2009) 414–8.
[101] B. Wünsch, Fluoreszenz- und streuungsbasierte Einzelmolekülmikroskopie an DNA-Origami-Nanostrukturen, Technischen Universität Carolo-Wilhelmina zu Braunschweig, 2018.
[102] P. Wang, T.A. Meyer, V. Pan, P.K. Dutta, Y. Ke, The Beauty and Utility of DNA Origami, Chem. 2 (2017) 359–382.
[103] K.S. Murakami, S. Masuda, E.A. Campbell, O. Muzzin, S.A. Darst, Structural basis of transcription initiation: An RNA polymerase holoenzyme-DNA complex, Science (80-.). 296 (2002) 1285–1290.
[104] K.S. Murakami, S. Masuda, S.A. Darst, Crystallographic Analysis of Thermus aquaticus RNA

Polymerase Holoenzyme and a Holoenzyme/Promoter DNA Complex, Methods Enzymol. 370 (2003) 42–53.

[105] B. Bae, A. Feklistov, A. Lass-Napiorkowska, R. Landick, S.A. Darst, Structure of a bacterial RNA polymerase holoenzyme open promoter complex, Elife. 4 (2015).

[106] A.J. Carpousis, J.D. Gralla, Cycling of ribonucleic acid polymerase to produce oligonucleotides during initiation in vitro at the lac UV5 promoter, Biochemistry. 19 (1980) 3245–3253.

[107] A.N. Kapanidis, E. Margeat, S.O. Ho, E. Kortkhonjia, S. Weiss, R.H. Ebright, Initial transcription by RNA polymerase proceeds through a DNA-scrunching mechanism., Science. 36 (2006) 3809–3823.

[108] A. Revyakin, C. Liu, R.H. Ebright, T.R. Strick, Abortive initiation and productive initiation by RNA polymerase involve DNA scrunching, Science. 314 (2006) 1139–43.

[109] K.L. Henderson, L.C. Felth, C.M. Molzahn, I. Shkel, S. Wang, M. Chhabra, E.F. Ruff, L. Bieter, J.E. Kraft, M.T. Record, Mechanism of transcription initiation and promoter escape by E. coli RNA polymerase, Proc. Natl. Acad. Sci. U. S. A. 114 (2017) E3032–E3040.

[110] F. Blombach, E. Salvadori, T. Fouqueau, J. Yan, J. Reimann, C. Sheppard, K.L. Smollett, S. V. Albers, C.W.M. Kay, K. Thalassinos, F. Werner, Archaeal TFEα/β is a hybrid of TFIIE and the RNA polymerase III subcomplex hRPC62/39., Elife. 4 (2015) e08378.

[111] S.A. Qureshi, S.D. Bell, S.P. Jackson, Factor requirements for transcription in the Archaeon Sulfolobus shibatae., EMBO J. 16 (1997) 2927–36.

[112] W. Hausner, J. Wettach, C. Hethke, M. Thomm, Two transcription factors related with the eucaryal transcription factors TATA-binding protein and transcription factor IIB direct promoter recognition by an archaeal RNA polymerase., J. Biol. Chem. 271 (1996) 30144–8.

[113] B.L. Hanzelka, T.J. Darcy, J.N. Reeve, TFE, an archaeal transcription factor in Methanobacterium thermoautotrophicum related to eucaryal transcription factor TFIIEα, J. Bacteriol. 183 (2001) 1813–1818.

[114] S.D. Bell, A.B. Brinkman, J. Van Der Oost, S.P. Jackson, The archaeal TFIIEα homologue facilitates transcription initiation by enhancing TATA-box recognition, EMBO Rep. 2 (2001) 133–138.

[115] S.A. Qureshi, P. Baumann, T. Rowlands, B. Khoo, S.P. Jackson, Cloning and functional analysis of the TATA binding protein from Sulfolobus shibatae, Nucleic Acids Res. 23 (1995) 1775–1781.

[116] T. Rowlands, P. Baumann, S.P. Jackson, The TATA-binding protein: a general transcription factor in eukaryotes and archaebacteria., Science. 264 (1994) 1326–9.

[117] C. Ouzounis, C. Sander, TFIIB, an Evolutionary Link between the Transcription Machineries of Archaebacteria and Eukaryotes, 71 (1992) 189–190.

[118] T. Fouqueau, F. Blombach, G. Cackett, A.E. Carty, D.M. Matelska, S. Ofer, S. Pilotto, D.K. Phung, F. Werner, The cutting edge of archaeal transcription, Emerg. Top. Life Sci. 2 (2018) 517–533.

[119] A.M. Gehring, J.E. Walker, T.J. Santangelo, Transcription regulation in archaea, J. Bacteriol. 198 (2016) 1906–1917.

[120] F. Blombach, K.L. Smollett, D. Grohmann, F. Werner, Molecular Mechanisms of Transcription Initiation—Structure, Function, and Evolution of TFE/TFIIE-Like Factors and Open Complex Formation, J. Mol. Biol. 428 (2016) 2592–2606.

[121] O. Littlefield, Y. Korkhin, P.B. Sigler, The structural basis for the oriented assembly of a TBP/TFB/promoter complex, Proc. Natl. Acad. Sci. U. S. A. 96 (1999) 13668–13673.

[122] M. Horikoshi, C. Bertuccioli, R. Takada, J. Wang, T. Yamamoto, R.G. Roeder, Transcription factor TFIID induces DNA bending upon binding to the TATA element., Proc. Natl. Acad. Sci. U. S. A. 89 (1992) 1060–1064.

[123] P.F. Kosa, G. Ghosh, B.S. DeDecker, P.B. Sigler, The 2.1-Å crystal structure of an archaeal preinitiation complex: TATA-box-binding protein/transcription factor (II)B core/TATA-box.,

Proc. Natl. Acad. Sci. U. S. A. 94 (1997) 6042–7.
[124] S.D. Bell, P.L. Kosa, P.B. Sigler, S.P. Jackson, Orientation of the transcription preinitiation complex in archaea., Proc. Natl. Acad. Sci. U. S. A. 96 (1999) 13662–7.
[125] W. Hausner, G. Frey, M. Thomm, Control regions of an archaeal gene: A TATA box and an initiator element promote cell-free transcription of the tRNAVal gene of Methanococcus vannielii, J. Mol. Biol. 222 (1991) 495–508.
[126] M.B. Renfrow, N. Naryshkin, L.M. Lewis, H.T. Chen, R.H. Ebright, R.A. Scott, Transcription Factor B Contacts Promoter DNA Near the Transcription Start Site of the Archaeal Transcription Initiation Complex, J. Biol. Chem. 279 (2004) 2825–2831.
[127] D. Kostrewa, M.E. Zeller, K.-J. Armache, M. Seizl, K. Leike, M. Thomm, P. Cramer, RNA polymerase II-TFIIB structure and mechanism of transcription initiation, Nature. 462 (2009) 323–30.
[128] F. Werner, R.O.J. Weinzierl, A recombinant RNA polymerase II-like enzyme capable of promoter-specific transcription., Mol. Cell. 10 (2002) 635–46.
[129] F. Werner, R.O.J. Weinzierl, Direct modulation of RNA polymerase core functions by basal transcription factors., Mol. Cell. Biol. 25 (2005) 8344–55.
[130] S. Grünberg, M.S. Bartlett, S. Naji, M. Thomm, Transcription Factor E Is a Part of Transcription Elongation Complexes, J. Biol. Chem. 282 (2007) 35482–35490.
[131] D. Grohmann, J. Nagy, A. Chakraborty, D. Klose, D. Fielden, R.H. Ebright, J. Michaelis, F. Werner, The initiation factor TFE and the elongation factor Spt4/5 compete for the RNAP clamp during transcription initiation and elongation., Mol. Cell. 43 (2011) 263–74.
[132] S. Dexl, R. Reichelt, K. Kraatz, S. Schulz, D. Grohmann, M. Bartlett, M. Thomm, Displacement of the transcription factor B reader domain during transcription initiation, Nucleic Acids Res. 46 (2018) 10066–10081.
[133] A. Vannini, P. Cramer, Conservation between the RNA Polymerase I, II, and III Transcription Initiation Machineries, Mol. Cell. 45 (2012) 439–446.
[134] P. Bucher, Weight matrix descriptions of four eukaryotic RNA polymerase II promoter elements derived from 502 unrelated promoter sequences, J. Mol. Biol. 212 (1990) 563–578.
[135] T. Lagrange, A.N. Kapanidis, H. Tang, D. Reinberg, R.H. Ebright, New core promoter element in RNA polymerase II-dependent transcription: sequence-specific DNA binding by transcription factor IIB, Genes Dev. 12 (1998) 34–44.
[136] W. Deng, S.G.E. Roberts, Core promoter elements recognized by transcription factor IIB., Biochem. Soc. Trans. 34 (2006) 1051–3.
[137] V. Haberle, A. Stark, Eukaryotic core promoters and the functional basis of transcription initiation, Nat. Rev. Mol. Cell Biol. 19 (2018) 621–637.
[138] F.T. Tsai, P.B. Sigler, Structural basis of preinitiation complex assembly on human pol II promoters., EMBO J. 19 (2000) 25–36.
[139] D.B. Nikolov, H. Chen, E.D. Halay, A.A. Usheva, K. Hisatake, D.K. Lee, R.G. Roeder, S.K. Burley, Crystal structure of a TFIIB-TBP-TATA-element ternary complex, Nature. 377 (1995) 119–128.
[140] J.J. Kang, D.T. Auble, J.A. Ranish, S. Hahn, Analysis of the yeast transcription factor TFIIA: distinct functional regions and a polymerase II-specific role in basal and activated transcription., Mol. Cell. Biol. 15 (1995) 1234–1243.
[141] S. Tan, Y. Hunziker, D.F. Sargent, T.J. Richmond, Crystal structure of a yeast TFIIA/TBP/DNA complex, Nature. 381 (1996) 127–51.
[142] J.H. Geiger, S. Hahn, S. Lee, P.B. Sigler, Crystal structure of the yeast TFIIA/TBP/DNA complex., Science. 272 (1996) 830–6.
[143] H.T. Chen, S. Hahn, Binding of TFIIB to RNA polymerase II: Mapping the binding site for the TFIIB zinc ribbon domain within the preinitiation complex, Mol. Cell. 12 (2003) 437–447.
[144] D.A. Bushnell, K.D. Westover, R.E. Davis, R.D. Kornberg, Structural Basis of Transcription:

An RNA Polymerase II-TFIIB Cocrystal at 4.5 Angstroms, Science (80-.). 303 (2004) 983–988.

[145] Y. Li, P.M. Flanagan, H. Tschochner, R.D. Kornberg, RNA polymerase II initiation factor interactions and transcription start site selection, Science (80-.). 263 (1994) 805–807.

[146] Y. Ohkuma, S. Hashimoto, C.K. Wang, M. Horikoshi, R.G. Roeder, Analysis of the role of TFIIE in basal transcription and TFIIH-mediated carboxy-terminal domain phosphorylation through structure-function studies of TFIIE-alpha., Mol. Cell. Biol. 15 (1995) 4856–4866.

[147] Y. Ohkuma, R.G. Roeder, Regulation of TFIIH ATPase and kinase activities by TFIIE during active initiation complex formation, Nature. 368 (1994) 160–163.

[148] H.T. Chen, L. Warfield, S. Hahn, The positions of TFIIF and TFIIE in the RNA polymerase II transcription preinitiation complex, Nat. Struct. Mol. Biol. 14 (2007) 696–703.

[149] P. Čabart, A. Újvári, M. Pal, D.S. Luse, Transcription factor TFIIF is not required for initiation by RNA polymerase II, but it is essential to stabilize transcription factor TFIIB in early elongation complexes, Proc. Natl. Acad. Sci. U. S. A. 108 (2011) 15786–15791.

[150] J. Fishburn, S. Hahn, Architecture of the Yeast RNA Polymerase II Open Complex and Regulation of Activity by TFIIF, Mol. Cell. Biol. 32 (2012) 12–25.

[151] Q. Yan, R.J. Moreland, J.W. Conaway, R.C. Conaway, Dual roles for transcription factor IIF in promoter escape by RNA polymerase II, J. Biol. Chem. 274 (1999) 35668–35675.

[152] Y. He, J. Fang, D.J. Taatjes, E. Nogales, Structural visualization of key steps in human transcription initiation, Nature. 495 (2013) 481–486.

[153] C. Dienemann, B. Schwalb, S. Schilbach, P. Cramer, Promoter Distortion and Opening in the RNA Polymerase II Cleft, Mol. Cell. 73 (2019) 97-106.e4.

[154] E. Compe, C.M. Genes, C. Braun, F. Coin, J.M. Egly, TFIIE orchestrates the recruitment of the TFIIH kinase module at promoter before release during transcription, Nat. Commun. 10 (2019) 1–14.

[155] T.K. Kim, R.H. Ebright, D. Reinberg, Mechanism of ATP-dependent promoter melting by transcription factor IIH, Science (80-.). 288 (2000) 1418–1421.

[156] S. Grünberg, L. Warfield, S. Hahn, Architecture of the RNA polymerase II preinitiation complex and mechanism of ATP-dependent promoter opening., Nat. Struct. Mol. Biol. 19 (2012) 788–96.

[157] J. Fishburn, E. Tomko, E. Galburt, S. Hahn, Double-stranded DNA translocase activity of transcription factor TFIIH and the mechanism of RNA polymerase II open complex formation, Proc. Natl. Acad. Sci. U. S. A. 112 (2015) 3961–3966.

[158] E. Ly, A.E. Powell, J.A. Goodrich, J.F. Kugel, Release of Human TFIIB from Actively Transcribing Complexes Is Triggered upon Synthesis of 7- and 9-nt RNAs, J. Mol. Biol. 432 (2020) 4049–4060.

[159] C. Engel, S. Neyer, P. Cramer, Distinct Mechanisms of Transcription Initiation by RNA Polymerases I and II, Annu. Rev. Biophys. 47 (2018) 425–446.

[160] C. Blattner, S. Jennebach, F. Herzog, A. Mayer, A.C.M. Cheung, G. Witte, K. Lorenzen, K.-P. Hopfner, A.J.R. Heck, R. Aebersold, P. Cramer, Molecular basis of Rrn3-regulated RNA polymerase I initiation and cell growth, Genes Dev. 25 (2011) 2093–105.

[161] S. Naidu, J.K. Friedrich, J. Russell, J.C.B.M. Zomerdijk, TAF1B is a TFIIB-like component of the basal transcription machinery for RNA polymerase I, Science. 333 (2011) 1640–2.

[162] B.A. Knutson, S. Hahn, Yeast Rrn7 and human TAF1B are TFIIB-related RNA polymerase I general transcription factors., Science. 333 (2011) 1637–40.

[163] J. Keener, C.A. Josaitis, J.A. Dodd, M. Nomura, Reconstitution of Yeast RNA Polymerase I Transcription in Vitro from Purified Components, J. Biol. Chem. 273 (1998) 33795–33802.

[164] M. Pilsl, C. Crucifix, G. Papai, F. Krupp, R. Steinbauer, J. Griesenbeck, P. Milkereit, H. Tschochner, P. Schultz, Structure of the initiation-competent RNA polymerase I and its implication for transcription, Nat. Commun. 7 (2016) 12126.

[165] C. Engel, J. Plitzko, P. Cramer, RNA polymerase I-Rrn3 complex at 4.8 Å resolution., Nat.

Commun. 7 (2016) 12129.
[166] J.S. Steffan, D.A. Keys, J.A. Dodd, M. Nomura, The role of TBP in rDNA transcription by RNA polymerase I in Saccharomyces cerevisiae: TBP is required for upstream activation factor-dependent recruitment of core factor, Genes Dev. 10 (1996) 2551–2563.
[167] J.S. Steffan, D.A. Keys, L. Vu, M. Nomura, Interaction of TATA-binding protein with upstream activation factor is required for activated transcription of ribosomal DNA by RNA polymerase I in Saccharomyces cerevisiae in vivo, Mol. Cell. Biol. 18 (1998) 3752–61.
[168] P. Aprikian, B. Moorefield, R.H. Reeder, New model for the yeast RNA polymerase I transcription cycle, Mol. Cell. Biol. 21 (2001) 4847–4855.
[169] C. Engel, T. Gubbey, S. Neyer, S. Sainsbury, C. Oberthuer, C. Baejen, C. Bernecky, P. Cramer, Structural Basis of RNA Polymerase I Transcription Initiation, Cell. 169 (2017) 120-131.e22.
[170] Y. Sadian, F. Baudin, L. Tafur, B. Murciano, R. Wetzel, F. Weis, C.W. Müller, Molecular insight into RNA polymerase I promoter recognition and promoter melting, Nat. Commun. 10 (2019) 5543.
[171] Y. Sadian, L. Tafur, J. Kosinski, A.J. Jakobi, R. Wetzel, K. Buczak, W.J. Hagen, M. Beck, C. Sachse, C.W. Müller, Structural insights into transcription initiation by yeast RNA polymerase I, EMBO J. 36 (2017) 2698–2709.
[172] M. Pilsl, C. Engel, Structural basis of RNA polymerase I pre-initiation complex formation and promoter melting, Nat. Commun. 11 (2020) 1–10.
[173] G.J. Bedwell, F.D. Appling, S.J. Anderson, D.A. Schneider, Efficient transcription by RNA polymerase I using recombinant core factor, Gene. 492 (2012) 94–99.
[174] H. Khatter, M.K. Vorländer, C.W. Müller, RNA polymerase I and III: similar yet unique, Curr. Opin. Struct. Biol. 47 (2017) 88–94.
[175] E. Landrieux, N. Alic, C. Ducrot, J. Acker, M. Riva, C. Carles, A subcomplex of RNA polymerase III subunits involved in transcription termination and reinitiation, EMBO J. 25 (2006) 118–128.
[176] N.A. Hoffmann, A.J. Jakobi, M. Moreno-Morcillo, S. Glatt, J. Kosinski, W.J.H.H. Hagen, C. Sachse, C.W. Müller, Molecular structures of unbound and transcribing RNA polymerase III, Nature. 528 (2015) 231–236.
[177] R. Carter, G. Drouin, The Increase in the number of subunits in eukaryotic RNA polymerase III relative to RNA polymerase II Is due to the permanent recruitment of general transcription factors, Mol. Biol. Evol. 27 (2010) 1035–1043.
[178] G. Peyroche, P. Milkereit, N. Bischler, H. Tschochner, P. Schultz, A. Sentenac, C. Carles, M. Riva, The recruitment of RNA polymerase I on rDNA is mediated by the interaction of the A43 subunit with Rrn3., EMBO J. 19 (2000) 5473–82.
[179] A. López-De-León, M. Librizzi, K. Puglia, I.M. Willis, PCF4 encodes an RNA polymerase III transcription factor with homology to TFIIB, Cell. 71 (1992) 211–220.
[180] Z. Wang, R.G. Roeder, Structure and function of a human transcription factor TFIIIB subunit that is evolutionarily conserved and contains both TFIIB- and high-mobility-group protein 2-related domains, Proc. Natl. Acad. Sci. U. S. A. 92 (1995) 7026–7030.
[181] G.A. Kassavetis, B. Bartholomew, J.A. Blanco, T.E. Johnson, E.P. Geiduschek, Two essential components of the Saccharomyces cerevisiae transcription factor TFIIIB: Transcription and DNA-binding properties, Proc. Natl. Acad. Sci. U. S. A. 88 (1991) 7308–7312.
[182] G.A. Kassavetis, S.T. Nguyen, R. Kobayashi, A. Kumar, E.P. Geiduschek, M. Pisano, Cloning, expression, and function of TFC5, the gene encoding the B" component of the Saccharomyces cerevisiae RNA polymerase III transcription factor TFIIIB., Proc. Natl. Acad. Sci. U. S. A. 92 (1995) 9786–90.
[183] L. Schramm, P.S. Pendergrast, Y. Sun, N. Hernandez, Different human TFIIIB activities direct RNA polymerase III transcription from TATA-containing and TATA-less promoters, Genes Dev. 14 (2000) 2650–2663.
[184] M. Teichmann, Z. Wang, R.G. Roeder, A stable complex of a novel transcription factor IIB-

related factor, human TFIIIB50, and associated proteins mediate selective transcription by RNA polymerase III of genes with upstream promoter elements., Proc. Natl. Acad. Sci. U. S. A. 97 (2000) 14200–5.

[185] P. Cabart, S. Murphy, BRFU, a TFIIB-like factor, is directly recruited to the TATA-box of polymerase III small nuclear RNA gene promoters through its interaction with TATA-binding protein., J. Biol. Chem. 276 (2001) 43056–64.

[186] J. Gouge, K. Satia, N. Guthertz, M. Widya, A.J. Thompson, P. Cousin, O. Dergai, N. Hernandez, A. Vannini, Redox Signaling by the RNA Polymerase III TFIIB-Related Factor Brf2, Cell. 163 (2015) 1375–1387.

[187] N. James Faresse, D. Canella, V. Praz, J. Michaud, D. Romascano, N. Hernandez, Genomic Study of RNA Polymerase II and III SNAPc-Bound Promoters Reveals a Gene Transcribed by Both Enzymes and a Broad Use of Common Activators, PLoS Genet. 8 (2012) e1003028.

[188] A.J. Oler, R.K. Alla, D.N. Roberts, A. Wong, P.C. Hollenhorst, K.J. Chandler, P.A. Cassiday, C.A. Nelson, C.H. Hagedorn, B.J. Graves, B.R. Cairns, Human RNA polymerase III transcriptomes and relationships to Pol II promoter chromatin and enhancer-binding factors, Nat. Struct. Mol. Biol. 17 (2010) 620–628.

[189] G.A. Kassavetis, A minimal RNA polymerase III transcription system, EMBO J. 18 (1999) 5042–5051.

[190] K.A. Tatosyan, D. V. Stasenko, A.P. Koval, I.K. Gogolevskaya, D.A. Kramerov, TATA-like boxes in RNA polymerase iii promoters: Requirements for nucleotide sequences, Int. J. Mol. Sci. 21 (2020).

[191] G.A. Kassavetis, B.R. Braun, L.H. Nguyen, E.P. Geiduschek, S. cerevisiae TFIIIB is the transcription initiation factor proper of RNA polymerase III, while TFIIIA and TFIIIC are assembly factors., Cell. 60 (1990) 235–45.

[192] G. Male, A. von Appen, S. Glatt, N.M.I. Taylor, M. Cristovao, H. Groetsch, M. Beck, C.W. Müller, Architecture of TFIIIC and its role in RNA polymerase III pre-initiation complex assembly, Nat. Commun. 6 (2015) 7387.

[193] A. Orioli, C. Pascali, A. Pagano, M. Teichmann, G. Dieci, RNA polymerase III transcription control elements: Themes and variations, Gene. 493 (2012) 185–194.

[194] M.K. Vorländer, H. Khatter, R. Wetzel, W.J.H.H. Hagen, C.W. Müller, Molecular mechanism of promoter opening by RNA polymerase III, Nature. 553 (2018) 295–300.

[195] G. Abascal-Palacios, E.P. Ramsay, F. Beuron, E. Morris, A. Vannini, Structural basis of RNA polymerase III transcription initiation, Nature. 553 (2018) 301–306.

[196] Y. Han, C. Yan, S. Fishbain, I. Ivanov, Y. He, Structural visualization of RNA polymerase III transcription machineries, Cell Discov. 4 (2018) 40.

[197] P. Bhargava, G.A. Kassavetis, Abortive initiation by Saccharomyces cerevisiae RNA polymerase III, J. Biol. Chem. 274 (1999) 26550–26556.

[198] B. Brindefalk, B.H. Dessailly, C. Yeats, C. Orengo, F. Werner, A.M. Poole, Evolutionary history of the TBP-domain superfamily, Nucleic Acids Res. 41 (2013) 2832–2845.

[199] F. Blombach, D. Grohmann, Same same but different: The evolution of TBP in archaea and their eukaryotic offspring, Transcription. 8 (2017) 162–168.

[200] C.N.J. Ravarani, T. Flock, S. Chavali, M. Anandapadamanaban, M.M. Babu, S. Balaji, Molecular determinants underlying functional innovations of TBP and their impact on transcription initiation, Nat. Commun. 11 (2020) 1–16.

[201] A.D. Basehoar, S.J. Zanton, B.F. Pugh, Identification and Distinct Regulation of Yeast TATA Box-Containing Genes, Cell. 116 (2004) 699–709.

[202] J.L. Kim, D.B. Nikolov, S.K. Burley, Co-crystal structure of TBP recognizing the minor groove of a TATA element, Nature. 365 (1993) 520–527.

[203] G.A. Patikoglou, J.L. Kim, L. Sun, S.H. Yang, T. Kodadek, S.K. Burley, TATA element recognition by the TATA box-binding protein has been conserved throughout evolution., Genes Dev. 13 (1999) 3217–30.

[204] Y. Kim, J.H. Geiger, S. Hahn, P.B. Sigler, Crystal structure of a yeast TBP/TATA-box complex, Nature. 365 (1993) 512–520.
[205] C. Millán-Pacheco, V.M. Capistrán, N. Pastor, On the consequences of placing amino groups at the TBP-DNA interface. Does TATA really matter?, J. Mol. Recognit. 22 (2009) 453–64.
[206] P.L. Privalov, A.I. Dragan, C. Crane-Robinson, The cost of DNA bending, Trends Biochem. Sci. 34 (2009) 464–470.
[207] L. Savinkova, I. Drachkova, T. Arshinova, P. Ponomarenko, M. Ponomarenko, N. Kolchanov, An Experimental Verification of the Predicted Effects of Promoter TATA-Box Polymorphisms Associated with Human Diseases on Interactions between the TATA Boxes and TATA-Binding Protein, PLoS One. 8 (2013) e54626.
[208] C.R. Wobbe, K. Struhl, Yeast and human TATA-binding proteins have nearly identical DNA sequence requirements for transcription in vitro., Mol. Cell. Biol. 10 (1990) 3859–67.
[209] J.V. Spencer, K.M. Arndt, A TATA Binding Protein Mutant with Increased Affinity for DNA Directs Transcription from a Reversed TATA Sequence In Vivo, Mol. Cell. Biol. 22 (2002) 8744–8755.
[210] K.M. Masters, K.M. Parkhurst, M.A. Daugherty, L.J. Parkhurst, Native human TATA-binding protein simultaneously binds and bends promoter DNA without a slow isomerization step or TFIIB requirement, J. Biol. Chem. 278 (2003) 31685–31690.
[211] R.F. Delgadillo, J.D.E. Whittington, L.K. Parkhurst, L.J. Parkhurst, The TATA-binding protein core domain in solution variably bends TATA sequences via a three-step binding mechanism, Biochemistry. 48 (2009) 1801–1809.
[212] J.D.E. Whittington, R.F. Delgadillo, T.J. Attebury, L.K.L.J. Parkhurst, M.A. Daugherty, L.K.L.J. Parkhurst, TATA-binding protein recognition and bending of a consensus promoter are protein species dependent, Biochemistry. 47 (2008) 7264–7273.
[213] K.M. Parkhurst, R.M. Richards, M. Brenowitz, L.J. Parkhurst, Intermediate species possessing bent DNA are present along the pathway to formation of a final TBP-TATA complex., J. Mol. Biol. 289 (1999) 1327–41.
[214] S.H.C. Duttke, Evolution and diversification of the basal transcription machinery, Trends Biochem. Sci. 40 (2015) 127–129.
[215] Z.S. Juo, G.A. Kassavetis, J. Wang, E.P. Geiduschek, P.B. Sigler, Crystal structure of a transcription factor IIIB core interface ternary complex, Nature. 422 (2003) 534–539.
[216] A. Butryn, J.M. Schuller, G. Stoehr, P. Runge-Wollmann, F. Förster, D.T. Auble, K.-P. Hopfner, Structural basis for recognition and remodeling of the TBP:DNA:NC2 complex by Mot1, Elife. 4 (2015) 1–22.
[217] G. Heiss, E. Ploetz, L. Voith von Voithenberg, R. Viswanathan, S. Glaser, P. Schluesche, S. Madhira, M. Meisterernst, D.T. Auble, D.C. Lamb, Conformational changes and catalytic inefficiency associated with Mot1-mediated TBP-DNA dissociation., Nucleic Acids Res. (2019).
[218] P. Schluesche, G. Stelzer, E. Piaia, D.C. Lamb, M. Meisterernst, NC2 mobilizes TBP on core promoter TATA boxes., Nat. Struct. Mol. Biol. 14 (2007) 1196–1201.
[219] J.D. Parvin, P.A. Sharp, DNA topology and a minimal set of basal factors for transcription by RNA polymerase II, Cell. 73 (1993) 533–540.
[220] R. Donczew, S. Hahn, Mechanistic Differences in Transcription Initiation at TATA-Less and TATA-Containing Promoters, Mol. Cell. Biol. 38 (2017) 1–14.
[221] D.M. Eisenmann, C. Dollard, F. Winston, SPT15, the gene encoding the yeast TATA binding factor TFIID, is required for normal transcription initiation in vivo, Cell. 58 (1989) 1183–1191.
[222] E. Martinez, C.M. Chiang, H. Ge, R.G. Roeder, TATA-binding protein-associated factor(s) in TFIID function through the initiator to direct basal transcription from a TATA-less class II promoter., EMBO J. 13 (1994) 3115–26.
[223] V.R. Yella, M. Bansal, DNA structural features of eukaryotic TATA-containing and TATA-less

promoters, FEBS Open Bio. 7 (2017) 324–334.
[224] R.K. Louder, Y. He, J.R. López-Blanco, J. Fang, P. Chacón, E. Nogales, Structure of promoter-bound TFIID and model of human pre-initiation complex assembly, Nature. 531 (2016) 1–16.
[225] A.B. Patel, R.K. Louder, B.J. Greber, S. Grünberg, J. Luo, J. Fang, Y. Liu, J. Ranish, S. Hahn, E. Nogales, Structure of human TFIID and mechanism of TBP loading onto promoter DNA, Science (80-.). 362 (2018).
[226] T. Baptista, S. Grünberg, N. Minoungou, M.J.E. Koster, H.T.M. Timmers, S. Hahn, D. Devys, L. Tora, SAGA Is a General Cofactor for RNA Polymerase II Transcription., Mol. Cell. 68 (2017) 130-143.e5.
[227] G. Papai, A. Frechard, O. Kolesnikova, C. Crucifix, P. Schultz, A. Ben-Shem, Structure of SAGA and mechanism of TBP deposition on gene promoters, Nature. 577 (2020) 1–6.
[228] E. Nogales, A.B. Patel, R.K. Louder, Towards a mechanistic understanding of core promoter recognition from cryo-EM studies of human TFIID, Curr. Opin. Struct. Biol. 47 (2017) 60–66.
[229] M. Anandapadamanaban, C. Andresen, S. Helander, Y. Ohyama, M.I. Siponen, P. Lundström, T. Kokubo, M. Ikura, M. Moche, M. Sunnerhagen, High-resolution structure of TBP with TAF1 reveals anchoring patterns in transcriptional regulation, Nat. Struct. Mol. Biol. 20 (2013) 1008–1014.
[230] L. Larivière, S. Geiger, S. Hoeppner, S. Röther, K. Sträßer, P. Cramer, Structure and TBP binding of the Mediator head subcomplex Med8–Med18–Med20, Nat. Struct. Mol. Biol. 13 (2006) 895–901.
[231] J. Soutourina, Transcription regulation by the Mediator complex, Nat. Rev. Mol. Cell Biol. 19 (2018) 262–274.
[232] A. Gietl, P. Holzmeister, F. Blombach, S. Schulz, L.V. von Voithenberg, D.C. Lamb, F. Werner, P. Tinnefeld, D. Grohmann, Eukaryotic and archaeal TBP and TFB/TF(II)B follow different promoter DNA bending pathways., Nucleic Acids Res. 42 (2014) 6219–31.
[233] S.A. Dexl, Functional interactions of the Transcription Factor B during transcription initiation in Pyrococcus furiosus Dissertation, Universität Regensburg, 2016.
[234] A.R. Kays, A. Schepartz, Virtually unidirectional binding of TBP to the AdMLP TATA box within the quaternary complex with TFIIA and TFIIB, Chem. Biol. 7 (2000) 601–610.
[235] R.H. Blair, J.A. Goodrich, J.F. Kugel, Single-molecule fluorescence resonance energy transfer shows uniformity in TATA binding protein-induced DNA bending and heterogeneity in bending kinetics, Biochemistry. 51 (2012) 7444–7455.
[236] A.R. Hieb, A. Gansen, V. Böhm, J. Langowski, The conformational state of the nucleosome entry–exit site modulates TATA box-specific TBP binding, Nucleic Acids Res. 42 (2014) 7561–7576.
[237] J. Segall, T. Matsui, R.G. Roeder, Multiple factors are required for the accurate transcription of purified genes by RNA polymerase III., J. Biol. Chem. 255 (1980) 11986–91.
[238] X. Liu, D.A. Bushnell, D. Wang, G. Calero, R.D. Kornberg, Structure of an RNA polymerase II-TFIIB complex and the transcription initiation mechanism., Science. 327 (2010) 206–9.
[239] S.A. Qureshi, S.P. Jackson, Sequence-specific DNA binding by the S. shibatae TFIIB homolog, TFB, and its effect on promoter strength, Mol. Cell. 1 (1998) 389–400.
[240] I. Ha, S. Roberts, E. Maldonado, X. Sun, L.U. Kim, M. Green, D. Reinberg, Multiple functional domains of human transcription factor IIB: Distinct interactions with two general transcription factors and RNA polymerase II, Genes Dev. 7 (1993) 1021–1032.
[241] S. Malik, K. Hisatake, H. Sumimoto, M. Horikoshi, R.G. Roeder, Sequence of general transcription factor TFIIB and relationships to other initiation factors, Proc. Natl. Acad. Sci. U. S. A. 88 (1991) 9553–9557.
[242] I. Pinto, D.E. Ware, M. Hampsey, The yeast SUA7 gene encodes a homolog of human transcription factor TFIIB and is required for normal start site selection in vivo, Cell. 68

(1992) 977–988.
[243] S. Malik, D.K. Lee, R.G. Roeder, Potential RNA polymerase II-induced interactions of transcription factor TFIIB., Mol. Cell. Biol. 13 (1993) 6253–6259.
[244] S. Lee, S. Hahn, Model for binding of transcription factor TFIIB to the TBP-DNA complex, Nature. 376 (1995) 609–612.
[245] T.S. Pardee, C.S. Bangur, A.S. Ponticelli, The N-terminal region of yeast TFIIB contains two adjacent functional domains involved in stable RNA polymerase II binding and transcription start site selection, J. Biol. Chem. 273 (1998) 17859–17864.
[246] G.A. Kassavetis, E.P. Geiduschek, Transcription factor TFIIIB and transcription by RNA polymerase III, Biochem. Soc. Trans. 34 (2006) 1082–1087.
[247] C.S. Bangur, T.S. Pardee, A.S. Ponticelli, Mutational analysis of the D1/E1 core helices and the conserved N-terminal region of yeast transcription factor IIB (TFIIB): identification of an N-terminal mutant that stabilizes TATA-binding protein-TFIIB-DNA complexes., Mol. Cell. Biol. 17 (1997) 6784–6793.
[248] E.J. Cho, S. Buratowski, Evidence that transcription factor IIB is required for a post-assembly step in transcription initiation, J. Biol. Chem. 274 (1999) 25807–25813.
[249] S. Sainsbury, J. Niesser, P. Cramer, Structure and function of the initially transcribing RNA polymerase II-TFIIB complex, Nature. 493 (2013) 437–440.
[250] S. Schulz, A. Gietl, K. Smollett, P. Tinnefeld, F. Werner, D. Grohmann, TFE and Spt4/5 open and close the RNA polymerase clamp during the transcription cycle., Proc. Natl. Acad. Sci. U. S. A. 113 (2016) E1816-25.
[251] A.C. Schier, D.J. Taatjes, Structure and mechanism of the RNA polymerase II transcription machinery, Genes Dev. 34 (2020) 465–488.
[252] M. Hantsche, P. Cramer, Conserved RNA polymerase II initiation complex structure, Curr. Opin. Struct. Biol. 47 (2017) 17–22.
[253] C. Engel, J. Plitzko, P. Cramer, RNA polymerase I-Rrn3 complex at 4.8 Å resolution, Nat. Commun. 7 (2016) 12129.
[254] O. Harismendy, C.G. Gendrel, P. Soularue, X. Gidrol, A. Sentenac, M. Werner, O. Lefebvre, Genome-wide location of yeast RNA polymerase III transcription machinery, EMBO J. 22 (2003) 4738–4747.
[255] G. Dieci, R. Percudani, S. Giuliodori, L. Bottarelli, S. Ottonello, TFIIIC-independent in vitro transcription of yeast tRNA genes, J. Mol. Biol. 299 (2000) 601–613.
[256] V. Mittal, M.A. Cleary, W. Herr, N. Hernandez, The Oct-1 POU-specific domain can stimulate small nuclear RNA gene transcription by stabilizing the basal transcription complex SNAPc., Mol. Cell. Biol. 16 (1996) 1955–1965.
[257] E. Ford, M. Strubin, N. Hernandez, The Oct-1 POU domain activates snRNA gene transcription by contacting a region in the SNAP(c) largest subunit that bears sequence similarities to the Oct-1 coactivator OBF-1, Genes Dev. 12 (1998) 3528–3540.
[258] X. Zhao, P.S. Pendergrast, N. Hernandez, A Positioned Nucleosome on the Human U6 Promoter Allows Recruitment of SNAPc by the Oct-1 POU Domain, Mol. Cell. 7 (2001) 539–549.
[259] R.W. Henry, C.L. Sadowski, R. Kobayashi, N. Hernandez, A TBP–TAF complex required for transcription of human snRNA genes by RNA polymerases II and III, Nature. 374 (1995) 650–653.
[260] O. Dergai, P. Cousin, J. Gouge, K. Satia, V. Praz, T. Kuhlman, P. Lhôte, A. Vannini, N. Hernandez, Mechanism of selective recruitment of RNA polymerases II and III to snRNA gene promoters., Genes Dev. 32 (2018) 711–722.
[261] O. Dergai, N. Hernandez, How to Recruit the Correct RNA Polymerase? Lessons from snRNA Genes, Trends Genet. 35 (2019) 457–469.
[262] A. Saxena, B. Ma, L. Schramm, N. Hernandez, Structure-Function Analysis of the Human TFIIB-Related Factor II Protein Reveals an Essential Role for the C-Terminal Domain in RNA

Polymerase III Transcription, Mol. Cell. Biol. 25 (2005) 9406–9418.
[263] G.A. Kassavetis, E. Soragni, R. Driscoll, E.P. Geiduschek, Reconfiguring the connectivity of a multiprotein complex: Fusions of yeast TATA-binding protein with Brf1, and the function of transcription factor IIIB, Proc. Natl. Acad. Sci. U. S. A. 102 (2005) 15406–15411.
[264] P. Hu, K. Samudre, S. Wu, Y. Sun, N. Hernandez, CK2 Phosphorylation of Bdp1 Executes Cell Cycle-Specific RNA Polymerase III Transcription Repression, Mol. Cell. 16 (2004) 81–92.
[265] A. Ishiguro, G. a Kassavetis, E.P. Geiduschek, Essential roles of Bdp1, a subunit of RNA polymerase III initiation factor TFIIIB, in transcription and tRNA processing., Mol. Cell. Biol. 22 (2002) 3264–75.
[266] H.-L. Hu, C.-C. Wu, J.-C. Lee, H.-T. Chen, A Region of Bdp1 Necessary for Transcription Initiation That Is Located within the RNA Polymerase III Active Site Cleft, Mol. Cell. Biol. 35 (2015) 2831–2840.
[267] S.M.A. Shah, A. Kumar, E.P. Geiduschek, G.A. Kassavetis, Alignment of the B'' subunit of RNA polymerase III transcription factor IIIB in its promoter complex, J. Biol. Chem. 274 (1999) 28736–28744.
[268] T. Colbert, S. Hahn, A yeast TFIIB-related factor involved in RNA polymerase III transcription, Genes Dev. 6 (1992) 1940–1949.
[269] A. Kumar, G.A. Kassavetis, E.P. Geiduschek, M. Hambalko, C.J. Brent, Functional dissection of the B" component of RNA polymerase III transcription factor IIIB: a scaffolding protein with multiple roles in assembly and initiation of transcription., Mol. Cell. Biol. 17 (1997) 1868–1880.
[270] G.A. Kassavetis, C. Bardeleben, A. Kumar, E. Ramirez, E.P. Geiduschek, Domains of the Brf component of RNA polymerase III transcription factor IIIB (TFIIIB): functions in assembly of TFIIIB-DNA complexes and recruitment of RNA polymerase to the promoter., Mol. Cell. Biol. 17 (1997) 5299–5306.
[271] T.E. Cloutier, M.D. Librizzi, A.K.M.M. Mollah, M. Brenowitz, I.M. Willis, Kinetic trapping of DNA by transcription factor IIIB, Proc. Natl. Acad. Sci. U. S. A. 98 (2001) 9581–9586.
[272] N. Verma, A.M. Hurlburt, A. Wolfe, M.K. Kim, Y.S. Kang, J.J. Kang, W.E. Stumph, Bdp1 interacts with SNAPc bound to a U6, but not U1, snRNA gene promoter element to establish a stable protein-DNA complex, FEBS Lett. 592 (2018) 2489–2498.
[273] I. Brun, A. Sentenac, M. Werner, Dual role of the C34 subunit of RNA polymerase III in transcription initiation, EMBO J. 16 (1997) 5730–5741.
[274] J.C. Andrau, A. Sentenac, M. Werner, Mutagenesis of yeast TFIIIB70 reveals C-terminal residues critical for interaction with TBP and C34, J. Mol. Biol. 288 (1999) 511–520.
[275] M. Werner, N. Chaussivert, I.M. Willis, A. Sentenac, Interaction between a complex of RNA polymerase III subunits and the 70-kDa component of transcription factor IIIB., J. Biol. Chem. 268 (1993) 20721–4.
[276] P. Hu, S. Wu, N. Hernandez, A minimal RNA polymerase III transcription system from human cells reveals positive and negative regulatory roles for CK2, Mol. Cell. 12 (2003) 699–709.
[277] J. Gouge, N. Guthertz, K. Kramm, O. Dergai, G. Abascal-Palacios, K. Satia, P. Cousin, N. Hernandez, D. Grohmann, A. Vannini, Molecular mechanisms of Bdp1 in TFIIIB assembly and RNA polymerase III transcription initiation, Nat. Commun. 8 (2017) 130.
[278] F. Canganella, J. Wiegel, Anaerobic Thermophiles, Life. 4 (2014) 77–104.
[279] C. Baker-Austin, M. Dopson, Life in acid: pH homeostasis in acidophiles, Trends Microbiol. 15 (2007) 165–171.
[280] A. Oren, Halophilic archaea on Earth and in space: growth and survival under extreme conditions, Philos. Trans. R. Soc. A Math. Phys. Eng. Sci. 372 (2014) 20140194.
[281] L. Lemmens, H.R. Maklad, I. Bervoets, E. Peeters, Transcription Regulators in Archaea: Homologies and Differences with Bacterial Regulators, J. Mol. Biol. 431 (2019) 4132–4146.
[282] M. Martinez-Pastor, P.D. Tonner, C.L. Darnell, A.K. Schmid, Transcriptional Regulation in

Archaea: From Individual Genes to Global Regulatory Networks, Annu. Rev. Genet. 51 (2017) 143–170.

[283] E. Pérez-Rueda, S.C. Janga, Identification and genomic analysis of transcription factors in archaeal genomes exemplifies their functional architecture and evolutionary origin, Mol. Biol. Evol. 27 (2010) 1449–1459.

[284] M. Ouhammouch, R.E. Dewhurst, W. Hausner, M. Thomm, E.P. Geiduschek, Activation of archaeal transcription by recruitment of the TATA-binding protein., Proc. Natl. Acad. Sci. U. S. A. 100 (2003) 5097–102.

[285] S.M. Ochs, S. Thumann, R. Richau, M.T. Weirauch, T.M. Lowe, M. Thomm, W. Hausner, Activation of archaeal transcription mediated by recruitment of transcription factor B., J. Biol. Chem. 287 (2012) 18863–71.

[286] K. Teufel, F. Pfeifer, Interaction of transcription activator GvpE with TATA-box-binding proteins of Halobacterium salinarum, Arch. Microbiol. 192 (2010) 143–149.

[287] E. Peeters, R. Willaert, D. Maes, D. Charlier, Ss-LrpB from Sulfolobus solfataricus condenses about 100 base pairs of its own operator DNA into globular nucleoprotein complexes, J. Biol. Chem. 281 (2006) 11721–11728.

[288] R. Reichelt, K.M.A. Ruperti, M. Kreuzer, S. Dexl, M. Thomm, W. Hausner, The Transcriptional Regulator TFB-RF1 Activates Transcription of a Putative ABC Transporter in Pyrococcus furiosus, Front. Microbiol. 9 (2018) 838.

[289] U. Okada, N. Sakai, M. Yao, N. Watanabe, I. Tanaka, Structural analysis of the transcriptional regulator homolog protein from Pyrococcus horikoshii OT3, Proteins Struct. Funct. Bioinforma. 63 (2006) 1084–1086.

[290] D. Grohmann, F. Werner, Recent advances in the understanding of archaeal transcription, Curr. Opin. Microbiol. 14 (2011) 328–334.

[291] S. Turkarslan, D.J. Reiss, G. Gibbins, W.L. Su, M. Pan, J.C. Bare, C.L. Plaisier, N.S. Baliga, Niche adaptation by expansion and reprogramming of general transcription factors, Mol. Syst. Biol. 7 (2011).

[292] M. Micorescu, S. Grünberg, A. Franke, P. Cramer, M. Thomm, M. Bartlett, Archaeal transcription: Function of an alternative transcription factor B from Pyrococcus furiosus, J. Bacteriol. 190 (2008) 157–167.

[293] R. Hidese, R. Nishikawa, L. Gao, M. Katano, T. Imai, S. Kato, T. Kanai, H. Atomi, T. Imanaka, S. Fujiwara, Different roles of two transcription factor B proteins in the hyperthermophilic archaeon Thermococcus kodakarensis, Extremophiles. 18 (2014) 573–588.

[294] A. Kaur, P.T. Van, C.R. Busch, C.K. Robinson, M. Pan, W.L. Pang, D.J. Reiss, J. Diruggiero, N.S. Baliga, Coordination of frontline defense mechanisms under severe oxidative stress, Mol. Syst. Biol. 6 (2010).

[295] P. Seitzer, E.G. Wilbanks, D.J. Larsen, M.T. Facciotti, A Monte Carlo-based framework enhances the discovery and interpretation of regulatory sequence motifs, BMC Bioinformatics. 13 (2012) 1–16.

[296] L. Chen, K. Brügger, M. Skovgaard, P. Redder, Q. She, E. Torarinsson, B. Greve, M. Awayez, A. Zibat, H.P. Klenk, R.A. Garrett, The genome of Sulfolobus acidocaldarius, a model organism of the Crenarchaeota, J. Bacteriol. 187 (2005) 4992–4999.

[297] Q. She, R.K. Singh, F. Confalonieri, Y. Zivanovic, G. Allard, [...], J. Van Der Oost, The complete genome of the crenarchaeon Sulfolobus solfataricus P2, Proc. Natl. Acad. Sci. U. S. A. 98 (2001) 7835–7840.

[298] S.D. Bell, S.P. Jackson, The role of transcription factor B in transcription initiation and promoter clearance in the archaeon Sulfolobus acidocaldarius, J. Biol. Chem. 275 (2000) 12934–12940.

[299] X. Feng, M. Sun, W. Han, Y.X. Liang, Q. She, A transcriptional factor B paralog functions as an activator to DNA damage-responsive expression in archaea, Nucleic Acids Res. 46 (2018) 7085–7096.

[300] F. Schult, T.N. Le, A. Albersmeier, B. Rauch, P. Blumenkamp, C. van der Does, A. Goesmann, J. Kalinowski, S.-V.V. Albers, B. Siebers, C. Van Der Does, A. Goesmann, J. Kalinowski, S.-V.V. Albers, B. Siebers, Effect of UV irradiation on Sulfolobus acidocaldarius and involvement of the general transcription factor TFB3 in the early UV response, Nucleic Acids Res. 46 (2018) 7179–7192.
[301] D. Götz, S. Paytubi, S. Munro, M. Lundgren, R. Bernander, M.F. White, Responses of hyperthermophilic crenarchaea to UV irradiation., Genome Biol. 8 (2007) R220.
[302] L.F. Bischof, M.F. Haurat, L. Hoffmann, A. Albersmeier, J. Wolf, A. Neu, T.K. Pham, S.P. Albaum, T. Jakobi, S. Schouten, M. Neumann-Schaal, P.C. Wright, J. Kalinowski, B. Siebers, S.V. Albers, Early response of Sulfolobus acidocaldarius to nutrient limitation, Front. Microbiol. 10 (2019) 3201.
[303] M. Lundgren, R. Bernander, Genome-wide transcription map of an archaeal cell cycle, Proc. Natl. Acad. Sci. U. S. A. 104 (2007) 2939–2944.
[304] B. van Steensel, E.E.M. Furlong, The role of transcription in shaping the spatial organization of the genome, Nat. Rev. Mol. Cell Biol. 20 (2019) 327–337.
[305] R.D. Kornberg, Chromatin structure: a repeating unit of histones and DNA., Science. 184 (1974) 868–71.
[306] K. Luger, A.W. Mäder, R.K. Richmond, D.F. Sargent, T.J. Richmond, Crystal structure of the nucleosome core particle at 2.8 Å resolution, Nature. 389 (1997) 251–260.
[307] J.O. Thomas, R.D. Kornberg, An octamer of histones in chromatin and free in solution, Proc. Natl. Acad. Sci. U. S. A. 72 (1975) 2626–2630.
[308] B.D. Strahl, C.D. Allis, The language of covalent histone modifications, Nature. 403 (2000) 41–45.
[309] T. Jenuwein, C.D. Allis, Translating the histone code, Science (80-.). 293 (2001) 1074–1080.
[310] S.B. Rothbart, B.D. Strahl, Interpreting the language of histone and DNA modifications, Biochim. Biophys. Acta - Gene Regul. Mech. 1839 (2014) 627–643.
[311] T. Schalch, S. Duda, D.F. Sargent, T.J. Richmond, X-ray structure of a tetranucleosome and its implications for the chromatin fibre, Nature. 436 (2005) 138–141.
[312] K. Luger, M.L. Dechassa, D.J. Tremethick, New insights into nucleosome and chromatin structure: An ordered state or a disordered affair?, Nat. Rev. Mol. Cell Biol. 13 (2012) 436–447.
[313] R.C. Allshire, H.D. Madhani, Ten principles of heterochromatin formation and function, Nat. Rev. Mol. Cell Biol. 19 (2018) 229–244.
[314] J.R. Dixon, S. Selvaraj, F. Yue, A. Kim, Y. Li, Y. Shen, M. Hu, J.S. Liu, B. Ren, Topological domains in mammalian genomes identified by analysis of chromatin interactions, Nature. 485 (2012) 376–380.
[315] C. Hou, L. Li, Z.S. Qin, V.G. Corces, Gene Density, Transcription, and Insulators Contribute to the Partition of the Drosophila Genome into Physical Domains, Mol. Cell. 48 (2012) 471–484.
[316] J. Dekker, E. Heard, Structural and functional diversity of Topologically Associating Domains, FEBS Lett. 589 (2015) 2877–2884.
[317] M. Kong, E.E. Cutts, D. Pan, F. Beuron, T. Kaliyappan, C. Xue, E.P. Morris, A. Musacchio, A. Vannini, E.C. Greene, Human Condensin I and II Drive Extensive ATP-Dependent Compaction of Nucleosome-Bound DNA, Mol. Cell. (2020).
[318] D. Dorsett, Cohesin: Genomic insights into controlling gene transcription and development, Curr. Opin. Genet. Dev. 21 (2011) 199–206.
[319] F. Müller, L. Tora, Chromatin and DNA sequences in defining promoters for transcription initiation., Biochim. Biophys. Acta. 1839 (2014) 118–28.
[320] K. Struhl, E. Segal, Determinants of nucleosome positioning, Nat. Struct. Mol. Biol. 20 (2013) 267–273.
[321] R. V. Chereji, D.J. Clark, Major Determinants of Nucleosome Positioning, Biophys. J. 114

(2018) 2279–2289.
[322] D. Levens, L. Baranello, F. Kouzine, Controlling gene expression by DNA mechanics: emerging insights and challenges, Biophys. Rev. 8 (2016) 259–268.
[323] B. Fierz, M.G. Poirier, Biophysics of Chromatin Dynamics, Annu. Rev. Biophys. 48 (2019) 321–345.
[324] Y. Gruenbaum, R. Foisner, Lamins: Nuclear intermediate filament proteins with fundamental functions in nuclear mechanics and genome regulation, Annu. Rev. Biochem. 84 (2015) 131–164.
[325] S.S. Teves, S. Henikoff, DNA torsion as a feedback mediator of transcription and chromatin dynamics, Nucleus. 5 (2014) 211–218.
[326] M.T.J. Van Loenhout, M. V. De Grunt, C. Dekker, Dynamics of DNA supercoils, Science (80-.). 338 (2012) 94–97.
[327] R.J. Davenport, G.J. Wuite, R. Landick, C. Bustamante, Single-molecule study of transcriptional pausing and arrest by E. coli RNA polymerase., Science. 287 (2000) 2497–500.
[328] H.Y. Wu, S.H. Shyy, J.C. Wang, L.F. Liu, Transcription generates positively and negatively supercoiled domains in the template., Cell. 53 (1988) 433–40.
[329] J. Ma, L. Bai, M.D. Wang, Transcription under torsion, Science (80-.). 340 (2013) 1580–1583.
[330] J. Ma, M. Wang, Interplay between DNA supercoiling and transcription elongation, Transcription. 5 (2014) e28636.
[331] P. Nelson, Transport of torsional stress in DNA, Proc. Natl. Acad. Sci. U. S. A. 96 (1999) 14342–14347.
[332] P. Tessarz, T. Kouzarides, Histone core modifications regulating nucleosome structure and dynamics, Nat. Rev. Mol. Cell Biol. 15 (2014) 703–708.
[333] G.D. Bowman, M.G. Poirier, Post-translational modifications of histones that influence nucleosome dynamics, Chem. Rev. 115 (2015) 2274–2295.
[334] M. Tyagi, N. Imam, K. Verma, A.K. Patel, Chromatin remodelers: We are the drivers!!, Nucleus. 7 (2016) 388–404.
[335] C.L. Woodcock, A.I. Skoultchi, Y. Fan, Role of linker histone in chromatin structure and function: H1 stoichiometry and nucleosome repeat length, Chromosom. Res. 14 (2006) 17–25.
[336] C.Y. Zhou, S.L. Johnson, N.I. Gamarra, G.J. Narlikar, Mechanisms of ATP-Dependent Chromatin Remodeling Motors, Annu. Rev. Biophys. 45 (2016) 153–181.
[337] M. Kruithof, F.T. Chien, A. Routh, C. Logie, D. Rhodes, J. Van Noort, Single-molecule force spectroscopy reveals a highly compliant helical folding for the 30-nm chromatin fiber, Nat. Struct. Mol. Biol. 16 (2009) 534–540.
[338] W. Li, P. Chen, J. Yu, L. Dong, D. Liang, J. Feng, J. Yan, P.Y. Wang, Q. Li, Z. Zhang, M. Li, G. Li, FACT Remodels the Tetranucleosomal Unit of Chromatin Fibers for Gene Transcription, Mol. Cell. 64 (2016) 120–133.
[339] S. Kilic, S. Felekyan, O. Doroshenko, I. Boichenko, M. Dimura, H. Vardanyan, L.C. Bryan, G. Arya, C.A.M. Seidel, B. Fierz, Single-molecule FRET reveals multiscale chromatin dynamics modulated by HP1α, Nat. Commun. 9 (2018) 235.
[340] F. Kouzine, D. Levens, L. Baranello, DNA topology and transcription, Nucl. (United States). 5 (2014).
[341] G. Dieci, A. Sentenac, Facilitated recycling pathway for RNA polymerase III, Cell. 84 (1996) 245–252.
[342] G. Dieci, M.C. Bosio, B. Fermi, R. Ferrari, Transcription reinitiation by RNA polymerase III, Biochim. Biophys. Acta - Gene Regul. Mech. 1829 (2013) 331–341.
[343] R. Ferrari, C. Rivetti, J. Acker, G. Dieci, Distinct roles of transcription factors TFIIIB and TFIIIC in RNA polymerase III transcription reinitiation, Proc. Natl. Acad. Sci. U. S. A. 101 (2004)

13442–13447.
[344] J.L. Goodier, H. Fan, R.J. Maraia, A carboxy-terminal basic region controls RNA polymerase III transcription factor activity of human La protein., Mol. Cell. Biol. 17 (1997) 5823–5832.
[345] R.J. Maraia, D.J. Kenan, J.D. Keene, Eukaryotic transcription termination factor La mediates transcript release and facilitates reinitiation by RNA polymerase III., Mol. Cell. Biol. 14 (1994) 2147–2158.
[346] K. Roy, J. Gabunilas, A. Gillespie, D. Ngo, G.F. Chanfreau, Common genomic elements promote transcriptional and DNA replication roadblocks., Genome Res. 26 (2016) 1363–1375.
[347] D. Donze, R.T. Kamakaka, R.K.-T.E. journal, undefined 2001, RNA polymerase III and RNA polymerase II promoter complexes are heterochromatin barriers in Saccharomyces cerevisiae, 20 (2001) 520–531.
[348] G.-C. Yuan, Y.-J. Liu, M.F. Dion, M.D. Slack, L.F. Wu, S.J. Altschuler, O.J. Rando, Genome-scale identification of nucleosome positions in S. cerevisiae., Science. 309 (2005) 626–30.
[349] D.E. Schones, K. Cui, S. Cuddapah, T.-Y.Y. Roh, A. Barski, Z. Wang, G. Wei, K. Zhao, Dynamic Regulation of Nucleosome Positioning in the Human Genome, Cell. 132 (2008) 887–898.
[350] F. Mattiroli, S. Bhattacharyya, P.N. Dyer, A.E. White, K. Sandman, B.W. Burkhart, K.R. Byrne, T. Lee, N.G. Ahn, T.J. Santangelo, J.N. Reeve, K. Luger, Structure of histone-based chromatin in Archaea, Science. 357 (2017) 609–612.
[351] S. Bhattacharyya, F. Mattiroli, K. Luger, Archaeal DNA on the histone merry-go-round, FEBS J. 285 (2018) 3168–3174.
[352] S.L. Pereira, R.A. Grayling, R. Lurz, J.N. Reeve, Archaeal nucleosomes, Proc. Natl. Acad. Sci. U. S. A. 94 (1997) 12633–12637.
[353] M. Lawrence, S. Daujat, R. Schneider, Lateral Thinking: How Histone Modifications Regulate Gene Expression, Trends Genet. 32 (2016) 42–56.
[354] R.P.C. Driessen, R.T. Dame, Nucleoid-associated proteins in Crenarchaea, in: Biochem. Soc. Trans., Portland Press, 2011: pp. 116–121.
[355] R.P.C. Driessen, R.T. Dame, Structure and dynamics of the crenarchaeal nucleoid, in: Biochem. Soc. Trans., Portland Press, 2013: pp. 321–325.
[356] S.D. Bell, C.H. Botting, B.N. Wardleworth, S.P. Jackson, M.F. White, The interaction of Alba, a conserved archaeal chromatin protein, with Sir2 and its regulation by acetylation, Science (80-.). 296 (2002) 148–151.
[357] N. Laurens, R.P.C. Driessen, I. Heller, D. Vorselen, M.C. Noom, F.J.H. Hol, M.F. White, R.T. Dame, G.J.L. Wuite, Alba shapes the archaeal genome using a delicate balance of bridging and stiffening the DNA, Nat. Commun. 3 (2012).
[358] B.N. Wardleworth, R.J.M. Russell, S.D. Bell, G.L. Taylor, M.F. White, Structure of Alba: An archaeal chromatin protein modulated by acetylation, EMBO J. 21 (2002) 4654–4662.
[359] H. Xue, R. Guo, Y. Wen, D. Liu, L. Huang, An abundant DNA binding protein from the hyperthermophilic archaeon Sulfolobus shibatae affects DNA supercoiling in a temperature-dependent fashion, J. Bacteriol. 182 (2000) 3929–3933.
[360] A.K. Efremov, Y. Qu, H. Maruyama, C.J. Lim, K. Takeyasu, J. Yan, Transcriptional repressor TrmBL2 from Thermococcus kodakarensis forms filamentous nucleoprotein structures and competes with histones for DNA binding in a salt- and DNA supercoiling-dependent manner, J. Biol. Chem. 290 (2015) 15770–15784.
[361] S. Wierer, P. Daldrop, M. Ud Din Ahmad, W. Boos, M. Drescher, W. Welte, R. Seidel, TrmBL2 from Pyrococcus furiosus Interacts Both with Double-Stranded and Single-Stranded DNA, PLoS One. 11 (2016) e0156098.
[362] X. Luo, U. Schwarz-Linek, C.H. Botting, R. Hensel, B. Siebers, M.F. White, CC1, a novel crenarchaeal DNA binding protein, J. Bacteriol. 189 (2007) 403–409.
[363] E. Peeters, R.P.C.C. Driessen, F. Werner, R.T. Dame, The interplay between nucleoid organization and transcription in archaeal genomes, Nat. Rev. Microbiol. 13 (2015) 333–

341.
[364] T.J. Sanders, C.J. Marshall, T.J. Santangelo, The Role of Archaeal Chromatin in Transcription, J. Mol. Biol. 431 (2019) 4103–4115.
[365] J. Cao, Q. Wang, T. Liu, N. Peng, L. Huang, Insights into the post-translational modifications of archaeal Sis10b (Alba): lysine-16 is methylated, not acetylated, and this does not regulate transcription or growth, Mol. Microbiol. 109 (2018) 192–208.
[366] R. Lurz, M. Grote, J. Dijk, R. Reinhardt, B. Dobrinski, Electron microscopic study of DNA complexes with proteins from the Archaebacterium *Sulfolobus acidocaldarius*, EMBO J. 5 (1986) 3715–3721.
[367] C. Jelinska, M.J. Conroy, C.J. Craven, A.M. Hounslow, P.A. Bullough, J.P. Waltho, G.L. Taylor, M.F. White, Obligate heterodimerization of the archaeal Alba2 protein with Alba1 provides a mechanism for control of DNA Packaging, Structure. 13 (2005) 963–971.
[368] M.A. Pritchett, S.P. Wilkinson, E.P. Geiduschek, M. Ouhammouch, Hybrid Ptr2-like activators of archaeal transcription, Mol. Microbiol. 74 (2009) 582–593.
[369] T.J. Sanders, M. Lammers, C.J. Marshall, J.E. Walker, E.R. Lynch, T.J. Santangelo, TFS and Spt4/5 accelerate transcription through archaeal histone-based chromatin, Mol. Microbiol. (2018) 0–3.
[370] Y. Xie, J.N. Reeve, Transcription by an archaeal RNA polymerase is slowed but not blocked by an archaeal nucleosome, J. Bacteriol. 186 (2004) 3492–3498.
[371] D. Soares, I. Dahlke, W.T. Li, K. Sandman, C. Hethke, M. Thomm, J.N. Reeve, Archaeal histone stability, DNA binding, and transcription inhibition above 90°C, Extremophiles. 2 (1998) 75–81.
[372] H. Maruyama, J.C. Harwood, K.M. Moore, K. Paszkiewicz, S.C. Durley, H. Fukushima, H. Atomi, K. Takeyasu, N.A. Kent, An alternative beads-on-a-string chromatin architecture in *Thermococcus kodakarensis*, EMBO Rep. 14 (2013) 711–717.
[373] N. Nalabothula, L. Xi, S. Bhattacharyya, J. Widom, J.P. Wang, J.N. Reeve, T.J. Santangelo, Y.N. Fondufe-Mittendorf, Archaeal nucleosome positioning in vivo and in vitro is directed by primary sequence motifs, BMC Genomics. 14 (2013) 1–13.
[374] S.P. Wilkinson, M. Ouhammouch, E.P. Geiduschek, Transcriptional activation in the context of repression mediated by archaeal histones, Proc. Natl. Acad. Sci. U. S. A. 107 (2010) 6777–6781.
[375] K. Gupta, A.A. Watson, T. Baptista, E. Scheer, A.L. Chambers, C. Koehler, J. Zou, I. Obong-Ebong, E. Kandiah, A. Temblador, A. Round, E. Forest, P. Man, C. Bieniossek, E.D. Laue, E.A. Lemke, J. Rappsilber, C. V. Robinson, D. Devys, L. Tora, I. Berger, Architecture of TAF11/TAF13/TBP complex suggests novel regulation properties of general transcription factor TFIID, Elife. 6 (2017).
[376] F. Schult, Function of the TFIIB homologs TFB2 and TFB3 as alternative general transcription factors in Sulfolobus acidocaldarius, Universität Duisburg-Essen, 2020.
[377] S. Preus, S.L. Noer, L.L. Hildebrandt, D. Gudnason, V. Birkedal, iSMS: single-molecule FRET microscopy software, Nat. Methods. 12 (2015) 593–594.
[378] W. Schrimpf, A. Barth, J. Hendrix, D.C. Lamb, PAM: A Framework for Integrated Analysis of Imaging, Single-Molecule, and Ensemble Fluorescence Data, Biophys. J. 114 (2018) 1518–1528.
[379] E. Gasteiger, C. Hoogland, A. Gattiker, S. Duvaud, M.R. Wilkins, R.D. Appel, A. Bairoch, Protein Analysis Tools on the ExPASy Server 571 571 From: The Proteomics Protocols Handbook Protein Identification and Analysis Tools on the ExPASy Server, n.d.
[380] S.B. Smith, Y. Cui, C. Bustamante, Overstretching B-DNA: the elastic response of individual double-stranded and single-stranded DNA molecules., Science. 271 (1996) 795–9.
[381] G.S. Manning, The Persistence Length of DNA Is Reached from the Persistence Length of Its Null Isomer through an Internal Electrostatic Stretching Force, Biophys. J. 91 (2006) 3607–3616.

[382] D.N. Mastronarde, Automated electron microscope tomography using robust prediction of specimen movements, J. Struct. Biol. 152 (2005) 36–51.
[383] J. Zivanov, T. Nakane, B.O. Forsberg, D. Kimanius, W.J.H. Hagen, E. Lindahl, S.H.W. Scheres, New tools for automated high-resolution cryo-EM structure determination in RELION-3, Elife. 7 (2018).
[384] M.A. Geeves, D.S. Pearson, Kinetics: Relaxation Methods, in: Encycl. Biophys., Springer Berlin Heidelberg, Berlin, Heidelberg, 2013: pp. 1207–1212.
[385] T.E. Tomov, R. Tsukanov, R. Masoud, M. Liber, N. Plavner, E. Nir, Disentangling subpopulations in single-molecule FRET and ALEX experiments with photon distribution analysis, Biophys. J. 102 (2012) 1163–1173.
[386] A.N. Kapanidis, T.A. Laurence, N.K. Lee, E. Margeat, X. Kong, S. Weiss, Alternating-laser excitation of single molecules., Acc. Chem. Res. 38 (2005) 523–33.
[387] S.H. Behrens, D.G. Grier, The charge of glass and silica surfaces, J. Chem. Phys. 115 (2001) 6716–6721.
[388] I. Rasnik, S. a Mckinney, T. Ha, Nonblinking and long- lasting single-molecule fluorescence imaging, Nat. Method. 3 (2006) 891–893.
[389] C.E. Aitken, R.A. Marshall, J.D. Puglisi, An oxygen scavenging system for improvement of dye stability in single-molecule fluorescence experiments., Biophys. J. 94 (2008) 1826–1835.
[390] R. Zondervan, F. Kulzer, S.B. Orlinskii, M. Orrit, Photoblinking of rhodamine 6G in poly(vinyl alcohol): Radical dark state formed through the triplet, J. Phys. Chem. A. 107 (2003) 6770–6776.
[391] T. Ha, T. Enderle, D.S. Chemla, P.R. Selvin, S. Weiss, Quantum jumps of single molecules at room temperature, Chem. Phys. Lett. 271 (1997) 1–5.
[392] J. Widengren, P. Schwïlle, Characterization of photoinduced isomerization and back-isomerization of the cyanine dye cy5 by fluorescence correlation spectroscopy, J. Phys. Chem. A. 104 (2000) 6416–6428.
[393] T. Ha, P. Tinnefeld, Photophysics of fluorescent probes for single-molecule biophysics and super-resolution imaging, Annu. Rev. Phys. Chem. 63 (2012) 595–617.
[394] T. Cordes, J. Vogelsang, P. Tinnefeld, On the mechanism of trolox as antiblinking and antibleaching reagent, J. Am. Chem. Soc. 131 (2009) 5018–5019.
[395] I. Rasnik, S. a McKinney, T. Ha, Nonblinking and long-lasting single-molecule fluorescence imaging., Nat. Methods. 3 (2006) 891–893.
[396] J. Vogelsang, R. Kasper, C. Steinhauer, B. Person, M. Heilemann, M. Sauer, P. Tinnefeld, A Reducing and Oxidizing System Minimizes Photobleaching and Blinking of Fluorescent Dyes, Angew. Chemie Int. Ed. 47 (2008) 5465–5469.
[397] J.E. Bronson, J. Fei, J.M. Hofman, R.L. Gonzalez, C.H. Wiggins, Learning Rates and States from Biophysical Time Series: A Bayesian Approach to Model Selection and Single-Molecule FRET Data, Biophys. J. 97 (2009) 3196–3205.
[398] OBIS Laser Family Datasheet, 2015.
[399] Pubchem database: glycerol, National Center for Biotechnology information, (2020).
[400] Pubchem database: silicon dioxide, National Center for Biotechnology information, (2020).
[401] K. Takamura, H. Fischer, N.R. Morrow, Physical properties of aqueous glycerol solutions, J. Pet. Sci. Eng. 98–99 (2012) 50–60.
[402] X. Li, L. Liu, J. Zhao, J. Tan, Optical properties of sodium chloride solution within the spectral range from 300 to 2500 nm at room temperature, Appl. Spectrosc. 69 (2015) 635–640.
[403] https://www.ahf.de/produkte/, Online catalogue AHF Analysentechnik, (n.d.).
[404] A. Schwacha, N. Kleckner, Identification of double holliday junctions as intermediates in meiotic recombination, Cell. 83 (1995) 783–791.
[405] R. Holliday, A mechanism for gene conversion in fungi, Genet. Res. 5 (1964) 282–304.
[406] H. Potter, D. Dressler, On the mechanism of genetic recombination: electron microscopic

observation of recombination intermediates, Proc. Natl. Acad. Sci. U. S. A. 73 (1976) 3000–3004.
[407] S. Uphoff, S.J. Holden, L. Le Reste, J. Periz, S. Van De Linde, M. Heilemann, A.N. Kapanidis, Monitoring multiple distances within a single molecule using switchable FRET, Nat. Methods. 7 (2010) 831–836.
[408] M. Karymov, D. Daniel, O.F. Sankey, Y.L. Lyubchenko, Holliday junction dynamics and branch migration: Single-molecule analysis, Proc. Natl. Acad. Sci. U. S. A. 102 (2005) 8186–8191.
[409] S.A. McKinney, A.D.J. Freeman, D.M.J. Lilley, T. Ha, Observing spontaneous branch migration of Holliday junctions one step at a time, Proc. Natl. Acad. Sci. U. S. A. 102 (2005) 5715–5720.
[410] S.A. McKinney, A.-C. Déclais, D.M.J. Lilley, T. Ha, Structural dynamics of individual Holliday junctions., Nat. Struct. Biol. 10 (2003) 93–7.
[411] C. Joo, S.A. McKinney, D.M.J. Lilley, T. Ha, Exploring rare conformational species and ionic effects in DNA Holliday junctions using single-molecule spectroscopy, J. Mol. Biol. 341 (2004) 739–751.
[412] R. Zhou, O. Yang, A.C. Déclais, H. Jin, G.H. Gwon, A.D.J. Freeman, Y. Cho, D.M.J. Lilley, T. Ha, Junction resolving enzymes use multivalency to keep the Holliday junction dynamic, Nat. Chem. Biol. 15 (2019) 269–275.
[413] D.M.J. Lilley, Holliday junction-resolving enzymes—structures and mechanisms, FEBS Lett. 591 (2017) 1073–1082.
[414] A.C. Déclais, D.M. Lilley, New insight into the recognition of branched DNA structure by junction-resolving enzymes, Curr. Opin. Struct. Biol. 18 (2008) 86–95.
[415] T. Shida, H. Iwasaki, A. Saito, Y. Kyogoku, H. Shinagawa, Analysis of substrate specificity of the RuvC Holliday junction resolvase with synthetic Holliday junctions, J. Biol. Chem. 271 (1996) 26105–26109.
[416] J. Litke, Y. Li, L. Nocka, I. Mukerji, Probing the Ion Binding Site in a DNA Holliday Junction Using Förster Resonance Energy Transfer (FRET), Int. J. Mol. Sci. 17 (2016) 366.
[417] R.M. Clegg, A.I. Murchie, D.M. Lilley, The solution structure of the four-way DNA junction at low-salt conditions: a fluorescence resonance energy transfer analysis, Biophys. J. 66 (1994) 99–109.
[418] J. Nowakowski, P.J. Shim, G.S. Prasad, C.D. Stout, G.F. Joyce, Crystal structure of an 82-nucleotide RNA-DNA complex formed by the 10- 23 DNA enzyme, Nat. Struct. Biol. 6 (1999) 151–156.
[419] M. Ortiz-Lombardia, A. Gonzalez, R. Eritja, J. Aymami, F. Azorin, M. Coll, Crystal structure of a DNA Holliday junction, Nat. Struct. Biol. 6 (1999) 913–917.
[420] B.F. Eichman, J.M. Vargason, B.H.M. Mooers, P.S. Ho, The Holliday junction in an inverted repeat DNA sequence: Sequence effects on the structure of four-way junctions, Proc. Natl. Acad. Sci. U. S. A. 97 (2000) 3971–3976.
[421] K. Okamoto, Y. Sako, State transition analysis of spontaneous branch migration of the Holliday junction by photon-based single-molecule fluorescence resonance energy transfer, Biophys. Chem. 209 (2016) 21–27.
[422] S. Hohng, C. Joo, T. Ha, Single-molecule three-color FRET, Biophys. J. 87 (2004) 1328–1337.
[423] C. Buranachai, S.A. McKinney, T. Ha, Single molecule nanometronome, Nano Lett. 6 (2006) 496–500.
[424] S.A. McKinney, C. Joo, T. Ha, Analysis of Single-Molecule FRET Trajectories Using Hidden Markov Modeling, Biophys. J. 91 (2006) 1941–1951.
[425] G. Bonnet, O. Krichevsky, A. Libchaber, Kinetics of conformational fluctuations in DNA hairpin-loops, Proc. Natl. Acad. Sci. U. S. A. 95 (1998) 8602–8606.
[426] R.J. Grainger, A.I.H. Murchie, D.M.J. Lilley, Exchange between stacking conformers in a four-way DNA junction, Biochemistry. 37 (1998) 23–32.

[427] A. Gietl, P. Holzmeister, D. Grohmann, P. Tinnefeld, DNA origami as biocompatible surface to match single-molecule and ensemble experiments, Nucleic Acids Res. 40 (2012) e110–e110.
[428] F.E. Kemmerich, M. Swoboda, D.J. Kauert, M.S. Grieb, S. Hahn, F.W. Schwarz, R. Seidel, M. Schlierf, Simultaneous Single-Molecule Force and Fluorescence Sampling of DNA Nanostructure Conformations Using Magnetic Tweezers, Nano Lett. 16 (2016) 381–386.
[429] W. Wang, L.M. Nocka, B.Z. Wiemann, D.M. Hinckley, I. Mukerji, F.W. Starr, Holliday Junction Thermodynamics and Structure: Coarse-Grained Simulations and Experiments, Sci. Rep. 6 (2016).
[430] K.M. Parkhurst, L.J. Parkhurst, Kinetic Studies by Fluorescence Resonance Energy Transfer Employing a Double-Labeled Oligonucleotide: Hybridization to the Oligonucleotide Complement and to Single-Stranded DNA, Biochemistry. 34 (1995) 285–292.
[431] M.D. Librizzi, M. Brenowitz, I.M. Willis, The TATA element and its context affect the cooperative interaction of TATA-binding protein with the TFIIB-related factor, TFIIIB70, J. Biol. Chem. 273 (1998) 4563–4568.
[432] G.A. Kassavetis, D.L. Riggs, R. Negri, L.H. Nguyen, E.P. Geiduschek, Transcription factor IIIB generates extended DNA interactions in RNA polymerase III transcription complexes on tRNA genes., Mol. Cell. Biol. 9 (1989) 2551–66.
[433] F. Kouzine, A. Gupta, L. Baranello, D. Wojtowicz, K. Ben-Aissa, J. Liu, T.M. Przytycka, D. Levens, Transcription-dependent dynamic supercoiling is a short-range genomic force, Nat. Struct. Mol. Biol. 20 (2013) 396–403.
[434] K. Kramm, T. Schröder, J. Gouge, A.M. Vera, K. Gupta, F.B. Heiss, T. Liedl, C. Engel, I. Berger, A. Vannini, P. Tinnefeld, D. Grohmann, DNA origami-based single-molecule force spectroscopy elucidates RNA Polymerase III pre-initiation complex stability., Nat. Commun. 11 (2020) 2828.
[435] A.G. Arimbasseri, K. Rijal, R.J. Maraia, Comparative overview of RNA polymerase II and III transcription cycles, with focus on RNA polymerase III termination and reinitiation, Taylor and Francis Inc., 2013.
[436] Y. Hasegawa, K. Struhl, J. Lieb, K. Struhl, Promoter-specific dynamics of TATA-binding protein association with the human genome, Genome Res. 29 (2019) 1939–1950.
[437] Y. Zhang, Z. Moqtaderi, B.P. Rattner, G. Euskirchen, M. Snyder, J.T. Kadonaga, X.S. Liu, K. Struhl, Intrinsic histone-DNA interactions are not the major determinant of nucleosome positions in vivo, Nat. Struct. Mol. Biol. 16 (2009) 847–852.
[438] J. Wu, K.M. Parkhurst, R.M. Powell, M. Brenowitz, L.J. Parkhurst, DNA Bends in TATA-binding Protein·TATA Complexes in Solution Are DNA Sequence-dependent, J. Biol. Chem. 276 (2001) 14614–14622.
[439] J. Wu, K.M. Parkhurst, R.M. Powell, L.J. Parkhurst, DNA Sequence-dependent Differences in TATA-binding Protein-induced DNA Bending in Solution Are Highly Sensitive to Osmolytes, J. Biol. Chem. 276 (2001) 14623–14627.
[440] K. Yokomori, M.P. Zeidler, J.L. Chen, C.P. Verrijzer, M. Mlodzik, R. Tjian, Drosophila TFIIA directs cooperative DNA binding with TBP and mediates transcriptional activation, Genes Dev. 8 (1994) 2313–2323.
[441] P. Schluesche, G. Heiss, M. Meisterernst, D.C. Lamb, Dynamics of TBP binding to the TATA box, in: J. Enderlein, Z.K. Gryczynski, R. Erdmann (Eds.), International Society for Optics and Photonics, 2008: p. 68620E.
[442] J. Yan, J.F. Marko, Effects of DNA-distorting proteins on DNA elastic response, Phys. Rev. E - Stat. Physics, Plasmas, Fluids, Relat. Interdiscip. Top. 68 (2003) 12.
[443] T.D. Brock, K.M. Brock, R.T. Belly, R.L. Weiss, Sulfolobus: A new genus of sulfur-oxidizing bacteria living at low pH and high temperature, Arch. Mikrobiol. 84 (1972) 54–68.
[444] G. Fiala, K.O. Stetter, Pyrococcus furiosus sp. nov. represents a novel genus of marine heterotrophic archaebacteria growing optimally at 100°C, Arch. Microbiol. 145 (1986) 56–

61.
[445] W.J. Jones, J.A. Leigh, F. Mayer, C.R. Woese, R.S. Wolfe, Methanococcus jannaschii sp. nov., an extremely thermophilic methanogen from a submarine hydrothermal vent, Arch. Microbiol. 136 (1983) 254–261.
[446] W.-D. Reiter, P. Palm, W. Zillig, Analysis of transcription in the archaebacterium Sulfolobus indicates that archaebacterial promoters are homologous to eukaryotic pol II promoters, Nucleic Acids Res. 16 (1988) 1–19.
[447] F. Grünberger, R. Reichelt, B. Bunk, C. Spröer, J. Overmann, R. Rachel, D. Grohmann, W. Hausner, Next Generation DNA-Seq and Differential RNA-Seq Allow Re-annotation of the Pyrococcus furiosus DSM 3638 Genome and Provide Insights Into Archaeal Antisense Transcription., Front. Microbiol. 10 (2019) 1603.
[448] Z.S. Juo, T.K. Chiu, P.M. Leiberman, I. Baikalov, A.J. Berk, R.E. Dickerson, How proteins recognize the TATA box, J. Mol. Biol. 261 (1996) 239–254.
[449] D. Strahs, D. Barash, X. Qian, T. Schlick, Sequence-dependent solution structure and motions of 13 TATA/TBP (TATA-box binding protein) complexes, Biopolymers. 69 (2003) 216–243.
[450] S.F. Tolić-Nørrelykke, M.B. Rasmussen, F.S. Pavone, K. Berg-Sørensen, L.B. Oddershede, Stepwise bending of DNA by a single TATA-box binding protein, Biophys. J. 90 (2006) 3694–3703.
[451] J.M. Cox, M.M. Hayward, J.F. Sanchez, L.D. Gegnas, S. Van Der Zee, J.H. Dennis, P.B. Sigler, A. Schepartz, Bidirectional binding of the TATA box binding protein to the TATA box, Proc. Natl. Acad. Sci. U. S. A. 94 (1997) 13475–13480.
[452] A.M. Domitrovich, G.R. Kunkel, Multiple, dispersed human U6 small nuclear RNA genes with varied transcriptional efficiencies., Nucleic Acids Res. 31 (2003) 2344–52.
[453] C. Notredame, D.G. Higgins, J. Heringa, T-coffee: A novel method for fast and accurate multiple sequence alignment, J. Mol. Biol. 302 (2000) 205–217.
[454] T.L. Bailey, M. Boden, F.A. Buske, M. Frith, C.E. Grant, L. Clementi, J. Ren, W.W. Li, W.S. Noble, MEME Suite: Tools for motif discovery and searching, Nucleic Acids Res. 37 (2009) W202–W208.
[455] H. Faiger, M. Ivanchenko, T.E. Haran, Nearest-neighbor non-additivity versus long-range non-additivity in TATA-box structure and its implications for TBP-binding mechanism, Nucleic Acids Res. 35 (2007) 4409–4419.
[456] J.G. Nadeau, D.M. Crothers, Structural basis for DNA bending, Proc. Natl. Acad. Sci. U. S. A. 86 (1989) 2622–2626.
[457] D.B. Nikolov, H. Chen, E.D. Halay, A. Hoffmann, R.G. Roeder, S.K. Burley, Crystal structure of a human TATA box-binding protein/TATA element complex, Proc. Natl. Acad. Sci. U. S. A. 93 (1996) 4862–4867.
[458] B. Hellenkamp, S. Schmid, O. Doroshenko, O. Opanasyuk, R. Kühnemuth, S. Rezaei Adariani, B. Ambrose, M. Aznauryan, A. Barth, V. Birkedal, M.E. Bowen, H. Chen, T. Cordes, T. Eilert, C. Fijen, C. Gebhardt, M. Götz, G. Gouridis, E. Gratton, T. Ha, P. Hao, C.A. Hanke, A. Hartmann, J. Hendrix, L.L. Hildebrandt, V. Hirschfeld, J. Hohlbein, B. Hua, C.G. Hübner, E. Kallis, A.N. Kapanidis, J.-Y. Kim, G. Krainer, D.C. Lamb, N.K. Lee, E.A. Lemke, B. Levesque, M. Levitus, J.J. McCann, N. Naredi-Rainer, D. Nettels, T. Ngo, R. Qiu, N.C. Robb, C. Röcker, H. Sanabria, M. Schlierf, T. Schröder, B. Schuler, H. Seidel, L. Streit, J. Thurn, P. Tinnefeld, S. Tyagi, N. Vandenberk, A.M. Vera, K.R. Weninger, B. Wünsch, I.S. Yanez-Orozco, J. Michaelis, C.A.M. Seidel, T.D. Craggs, T. Hugel, Precision and accuracy of single-molecule FRET measurements—a multi-laboratory benchmark study, Nat. Methods. 15 (2018) 669–676.
[459] S. Kalinin, T. Peulen, S. Sindbert, P.J. Rothwell, S. Berger, T. Restle, R.S. Goody, H. Gohlke, C.A.M. Seidel, A toolkit and benchmark study for FRET-restrained high-precision structural modeling, Nat. Methods. 9 (2012) 1218–1225.
[460] E. Ploetz, E. Lerner, F. Husada, M. Roelfs, S. Chung, J. Hohlbein, S. Weiss, T. Cordes, Förster

resonance energy transfer and protein-induced fluorescence enhancement as synergetic multi-scale molecular rulers, Sci. Rep. 6 (2016) 33257.
[461] M.D. Librizzi, R.D. Moir, M. Brenowitz, I.M. Willis, Expression and purification of the RNA polymerase III transcription specificity factor IIIB70 from Saccharomyces cerevisiae and its cooperative binding with TATA-binding protein, J. Biol. Chem. 271 (1996) 32695–32701.
[462] S. Vasdev, V.D. Gill, P.K. Singal, Modulation of oxidative stress-induced changes in hypertension and atherosclerosis by antioxidants, Exp. Clin. Cardiol. 11 (2006) 206–216.
[463] M. Lo Conte, K.S. Carroll, The redox biochemistry of protein sulfenylation and sulfinylation, J. Biol. Chem. 288 (2013) 26480–26488.
[464] Y.-F. Chen, J.N. Milstein, J.-C. Meiners, Femtonewton entropic forces can control the formation of protein-mediated DNA loops., Phys. Rev. Lett. 104 (2010) 048301.
[465] B. Xiao, H. Zhang, R.C. Johnson, J.F. Marko, Force-driven unbinding of proteins HU and Fis from DNA quantified using a thermodynamic Maxwell relation, Nucleic Acids Res. 39 (2011) 5568–5577.
[466] J.F. Marko, E.D. Siggia, Driving proteins off DNA using applied tension, Biophys. J. 73 (1997) 2173–2178.
[467] K. Dahlke, J. Zhao, C.E. Sing, E.J. Banigan, Force-Dependent Facilitated Dissociation Can Generate Protein-DNA Catch Bonds, Biophys. J. 117 (2019) 1085–1100.
[468] Z. Zhang, B.P. English, J.B. Grimm, S.A. Kazane, W. Hu, A. Tsai, C. Inouye, C. You, J. Piehler, P.G. Schultz, L.D. Lavis, A. Revyakin, R. Tjian, Rapid dynamics of general transcription factor TFIIB binding during preinitiation complex assembly revealed by single-molecule analysis, Genes Dev. 30 (2016) 2106–2118.
[469] T. Colbert, S. Lee, G. Schimmack, S. Hahn, Architecture of Protein and DNA Contacts within the TFIIIB-DNA Complex, Mol. Cell. Biol. 18 (1998) 1682–1691.
[470] G.A. Kassavetis, A. Kumar, E. Ramirez, E.P. Geiduschek, Functional and Structural Organization of Brf, the TFIIB-Related Component of the RNA Polymerase III Transcription Initiation Complex, Mol. Cell. Biol. 18 (1998) 5587–5599.
[471] O. Schröder, G.O. Bryant, E.P. Geiduschek, A.J. Berk, G.A. Kassavetis, A common site on TBP for transcription by RNA polymerases II and III, EMBO J. 22 (2003) 5115–5124.
[472] M. Bleichenbacher, S. Tan, T.J. Richmond, Novel interactions between the components of human and yeast TFIIA/TBP/DNA complexes, J. Mol. Biol. 332 (2003) 783–793.
[473] A.R. Hieb, W.A. Halsey, M.D. Betterton, T.T. Perkins, J.F. Kugel, J.A. Goodrich, TFIIA Changes the Conformation of the DNA in TBP/TATA Complexes and Increases their Kinetic Stability, J. Mol. Biol. 372 (2007) 619–632.
[474] M.C. Thomas, C.-M.M. Chiang, The general transcription machinery and general cofactors, Crit. Rev. Biochem. Mol. Biol. 41 (2006) 105–178.
[475] T.C. Kuhlman, H. Cho, D. Reinberg, N. Hernandez, The general transcription factors IIA, IIB, IIF, and IIE are required for RNA polymerase II transcription from the human U1 small nuclear RNA promoter., Mol. Cell. Biol. 19 (1999) 2130–41.
[476] P. Čabart, J.H. Lee, I.M. Willis, Facilitated recycling protects human RNA polymerase III from repression by Maf1 in vitro, J. Biol. Chem. 283 (2008) 36108–36117.
[477] J.A. Fairley, P.H. Scott, R.J. White, TFIIIB is phosphorylated, disrupted and selectively released from tRNA promoters during mitosis in vivo., EMBO J. 22 (2003) 5841–50.
[478] H. Meng, K. Andresen, J. Van Noort, Quantitative analysis of single-molecule force spectroscopy on folded chromatin fibers, Nucleic Acids Res. 43 (2015) 3578–3590.
[479] A.S. Helbo, F.D. Lay, P.A. Jones, G. Liang, K. Grønbæk, Nucleosome Positioning and NDR Structure at RNA Polymerase III Promoters, Sci. Rep. 7 (2017) 1–11.
[480] G. Dieci, A. Sentenac, Detours and shortcuts to transcription reinitiation, 2003.
[481] J.D. Kahn, Topological effects of the TATA box binding protein on minicircle DNA and a possible thermodynamic linkage to chromatin remodeling., Biochemistry. 39 (2000) 3520–4.

[482] M. Radman-Livaja, O.J. Rando, Nucleosome positioning: How is it established, and why does it matter?, Dev. Biol. (n.d.).
[483] M. Vermeulen, K.W. Mulder, S. Denissov, W.W.M.P. Pijnappel, F.M.A. van Schaik, R.A. Varier, M.P.A. Baltissen, H.G. Stunnenberg, M. Mann, H.T.M. Timmers, Selective anchoring of TFIID to nucleosomes by trimethylation of histone H3 lysine 4., Cell. 131 (2007) 58–69.
[484] R. Tsukanov, T.E. Tomov, R. Masoud, H. Drory, N. Plavner, M. Liber, E. Nir, Detailed Study of DNA Hairpin Dynamics using Single-Molecule Fluorescence Assisted by DNA Origami. DNA Origami and motors View project Detailed Study of DNA Hairpin Dynamics Using Single-Molecule Fluorescence Assisted by DNA Origami, Artic. J. Phys. Chem. B. (2013).
[485] Z. Zhao, Y. Liu, H. Yan, Organizing DNA origami tiles into larger structures using preformed scaffold frames, Nano Lett. 11 (2011) 2997–3002.
[486] C. Bustamante, J.F. Marko, E.D. Siggia, S. Smith, Entropic elasticity of λ-phage DNA, Science (80-.). 265 (1994) 1599–1600.
[487] C. Yuan, H. Chen, X.W. Lou, L.A. Archer, DNA bending stiffness on small length scales, Phys. Rev. Lett. 100 (2008) 018102.
[488] M.J. McCauley, M.C. Williams, Optical tweezers experiments resolve distinct modes of DNA-protein binding, Biopolymers. 91 (2009) 265–282.
[489] M.J. McCauley, E.M. Rueter, I. Rouzina, L.J. Maher, M.C. Williams, Single-molecule kinetics reveal microscopic mechanism by which High-Mobility Group B proteins alter DNA flexibility, Nucleic Acids Res. 41 (2013) 167–181.
[490] D.B. McIntosh, O.A. Saleh, Salt species-dependent electrostatic effects on ssDNA elasticity, Macromolecules. 44 (2011) 2328–2333.
[491] J.M. Huguet, C. V. Bizarro, N. Forns, S.B. Smith, C. Bustamante, F. Ritort, Single-molecule derivation of salt dependent base-pair free energies in DNA, Proc. Natl. Acad. Sci. U. S. A. 107 (2010) 15431–15436.
[492] A. Bosco, J. Camunas-Soler, F. Ritort, Elastic properties and secondary structure formation of single-stranded DNA at monovalent and divalent salt conditions, Nucleic Acids Res. 42 (2014) 2064–2074.
[493] J.S. Schreck, T.E. Ouldridge, F. Romano, P. Šulc, L.P. Shaw, A.A. Louis, J.P.K. Doye, DNA hairpins destabilize duplexes primarily by promoting melting rather than by inhibiting hybridization, Nucleic Acids Res. 43 (2015) 6181–6190.
[494] D.B. McIntosh, G. Duggan, Q. Gouil, O.A. Saleh, Sequence-dependent elasticity and electrostatics of single-stranded DNA: Signatures of base-stacking, Biophys. J. 106 (2014) 659–666.
[495] M.C. Engel, F. Romano, A.A. Louis, J.P.K. Doye, Measuring internal forces in single-stranded DNA: Application to a DNA force clamp, (2020) 1–53.
[496] M.S. Bartlett, M. Thomm, E.P. Geiduschek, Topography of the Euryarchaeal Transcription Initiation Complex, J. Biol. Chem. 279 (2004) 5894–5903.
[497] K. Smollett, F. Blombach, R. Reichelt, M. Thomm, F. Werner, A global analysis of transcription reveals two modes of Spt4/5 recruitment to archaeal RNA polymerase, Nat. Microbiol. 2 (2017) 17021.
[498] M. Lee, K. Struhl, A severely defective TATA-binding protein-TFIIB interaction does not preclude transcriptional activation in vivo., Mol. Cell. Biol. 17 (1997) 1336–45.
[499] T.J. Santangelo, L.L. Čuboňová, C.L. James, J.N. Reeve, TFB1 or TFB2 Is Sufficient for Thermococcus kodakaraensis Viability and for Basal Transcription in Vitro, J. Mol. Biol. 367 (2007) 344–357.
[500] S. Paytubi, M.F. White, The crenarchaeal DNA damage-inducible transcription factor B paralogue TFB3 is a general activator of transcription, Mol. Microbiol. 72 (2009) 1487–1499.
[501] V. Dixit, E. Bini, M. Drozda, P. Blum, Mercury inactivates transcription and the generalized transcription factor TFB in the archaeon Sulfolobus solfataricus, Antimicrob. Agents

Chemother. 48 (2004) 1993–1999.
[502] C. Petitjean, K.S. Makarova, Y.I. Wolf, E. V. Koonin, Extreme deviations from expected evolutionary rates in archaeal protein families, Genome Biol. Evol. 9 (2017) 2791–2811.
[503] L.S. Busenlehner, M.A. Pennella, D.P. Giedroc, The SmtB/ArsR family of metalloregulatory transcriptional repressors: structural insights into prokaryotic metal resistance, FEMS Microbiol. Rev. 27 (2003) 131–143.
[504] G. Wang, S.P. Kennedy, S. Fasiludeen, C. Rensing, S. DasSarma, Arsenic Resistance in Halobacterium sp. Strain NRC-1 Examined by Using an Improved Gene Knockout System, J. Bacteriol. 186 (2004) 3187–3194.
[505] J. Schelert, M. Drozda, V. Dixit, A. Dillman, P. Blum, Regulation of mercury resistance in the crenarchaeote Sulfolobus solfataricus, J. Bacteriol. 188 (2006) 7141–7150.
[506] C. Baker-Austin, A.E. Mark, D. Ae, M. Wexler, A.R. Gary, S. Ae, A. Stemmler, A.E. Barry, P. Rosen, A.E. Philip, L. Bond, R.G. Sawers, A. Stemmler, Á.B.P. Rosen, P.L. Bond, M. Dopson, Extreme arsenic resistance by the acidophilic archaeon “Ferroplasma acidarmanus” Fer1, Extremophiles. 11 (2007) 425–434.
[507] E.A. Karr, The methanogen-specific transcription factor MsvR regulates the fpaA-rlp-rub oxidative stress operon adjacent to msvR in Methanothermobacter thermautotrophicus, J. Bacteriol. 192 (2010) 5914–5922.
[508] H. Yang, G.L. Lipscomb, A.M. Keese, G.J. Schut, M. Thomm, M.W.W. Adams, B.C. Wang, R.A. Scott, SurR regulates hydrogen production in Pyrococcus furiosus by a sulfur-dependent redox switch, Mol. Microbiol. 77 (2010) 1111–1122.
[509] R. Hidese, K. Yamashita, K. Kawazuma, T. Kanai, H. Atomi, T. Imanaka, S. Fujiwara, Gene regulation of two ferredoxin:NADP+ oxidoreductases by the redox-responsive regulator SurR in Thermococcus kodakarensis, Extremophiles. 21 (2017) 903–917.
[510] N. Peng, Q. Xia, Z. Chen, Y.X. Liang, Q. She, An upstream activation element exerting differential transcriptional activation on an archaeal promoter, Mol. Microbiol. 74 (2009) 928–939.
[511] Y. Ding, A. Berezuk, C.M. Khursigara, K.F. Jarrell, Bypassing the need for the transcriptional activator eara through a spontaneous deletion in the BRE portion of the fla operon promoter in Methanococcus maripaludis, Front. Microbiol. 8 (2017).
[512] G.D. Sprott, K.M. Shaw, K.F. Jarrell, Ammonia/potassium exchange in methanogenic bacteria., J. Biol. Chem. 259 (1984) 12602–8.
[513] P.K. Nandi, D.R. Robinson, The Effects of Salts on the Free Energies of Nonpolar Groups in Model Peptides, J. Am. Chem. Soc. 94 (1972) 1308–1315.
[514] J.A. Schellman, Temperature, stability, and the hydrophobic interaction, Biophys. J. 73 (1997) 2960–2964.
[515] S. Bergqvist, R. O’Brien, J.E. Ladbury, Site-specific cation binding mediates TATA binding protein-DNA interaction from a hyperthermophilic archaeon., Biochemistry. 40 (2001) 2419–25.
[516] W.T. Li, K. Sandman, S.L. Pereira, J.N. Reeve, MJ1647, an open reading frame in the genome of the hyperthermophile methanococcus jannaschii, encodes a very thermostable archaeal histone with a C-terminal extension, Extremophiles. 4 (2000) 43–51.
[517] J.J. Funke, P. Ketterer, C. Lieleg, S. Schunter, P. Korber, H. Dietz, Uncovering the Forces between Nucleosomes using a DNA Origami Force Spectrometer, Biophys. J. 112 (2017) 166a.
[518] K. Zaremba-Niedzwiedzka, E.F. Caceres, J.H. Saw, Di. Bäckström, L. Juzokaite, E. Vancaester, K.W. Seitz, K. Anantharaman, P. Starnawski, K.U. Kjeldsen, M.B. Stott, T. Nunoura, J.F. Banfield, A. Schramm, B.J. Baker, A. Spang, T.J.G. Ettema, Asgard archaea illuminate the origin of eukaryotic cellular complexity, Nature. 541 (2017) 353–358.

Danksagung

An dieser Stelle möchte ich allen Menschen danken, die mich beim Erstellen dieser Dissertation unterstützt haben.

Besonderer Dank gilt Prof. Dr. Dina Grohmann für die großartige Betreuung dieser Arbeit, angeregten Diskussionen und Unterstützung. Ihre Energie und Enthusiasmus für Wissenschaft haben mich stets motiviert.

Des Weiteren möchte ich allen Kollaborationspartnern danken, ohne deren Hilfe diese Arbeit nicht möglich gewesen wäre:

Vielen Dank an Dr. Winfried Hausner für die wertvollen Ratschläge und die angenehme Zusammenarbeit bei den *P. furiosus* Projekten.

Des Weiteren danke ich Prof. Dr. Philip Tinnefeld und Tim Schröder für ihre Unterstützung bei den DNA Origami Messungen und insbesondere die geduldigen und vor allem Biotechnologen-tauglichen Erklärungen zu den physikalischen Grundlagen.

Prof. Dr. Alessandro Vannini und Dr. Jerome Gouge danke ich für die humanen Transkriptions-faktoren und interessanten Einblicke in die Strukturbiologie.

Vielen Dank an Prof. Dr. Herbert Tschochner und Michael Pilsl für die auf sich genommen Mühen und Unterstützung, auch wenn Pol I und ich am Ende doch keine Freunde geworden sind.

des Weiteren danke ich dem SFB 960 und allen beteiligten für die Unterstützung dieser Arbeit und das exzellente Umfeld für wissenschaftlichen Austausch.

Vielen Dank an alle Mitglieder des Boards der Graduiertenakademie RNA Biologie: Prof. Dr. Thomas Dresselhaus, Prof. Dr. Joachim Griesenbeck, Prof. Dr. Christoph Engel, Dr. Jan Medenbach sowie Kinga Ai, Carolin Apfel und meine Mit-Doktorandenvertreter Christina Braun und Dr. Kristina Straub. Die Zusammenarbeit mit euch hat mir immer sehr viel Freude bereitet.

Des Weiteren möchte ich mich herzlich bei allen Mitgliedern des Lehrstuhls für Mikrobiologie für die großartige Zeit bedanken. Das Arbeitsklima war immer sehr angenehm und entspannt, und neben dem Laborstress haben die gemütlichen Kaffeerunden für Ausgleich gesorgt.

Besonders danke ich meinen Kollegen Dr. Sarah Willkomm, Elisabeth Wöhrle, Benji Moissl, Felix Grünberger und Henri Michel sowie den früheren Mitarbeitern Dr. Leonhard Jakob, Dr. Adrian Zander und Alexander Gust für die gute Zusammenarbeit und interessanten Diskussion über wissenschaftliche, und vor allem auch nicht-wissenschaftliche, Themen. Ihr habt mich immer zum Durchhalten motiviert, auch wenn mal wieder nichts funktioniert hat. Des Weiteren danke ich insbesondere allen Studenten des Lehrstuhls, die meine Popkultur Referenzen verstanden haben.

Ein riesiges Dankeschön geht an meine Freunde in Regensburg und daheim im Norden (was in Bayern eben der Norden ist), die mich immer aufgebaut und für geistige Erholung gesorgt haben. Ohne die gemeinsamen Spiele- und Trash-Movie Abende und Sushi Gelage hätte ich die Zeit nicht annähernd so sehr genossen.

Zu guter Letzt möchte ich meiner Familie für konstante moralische Unterstützung danken, auch wenn es meist nur auf Entfernung war. Vielen Dank für eure Geduld und Hilfe in allen Lebenslagen. Ihr habt mich immer motiviert diese Arbeit bis zum Ende durchzuziehen und nie den Kopf hängen zu lassen und dafür danke ich euch von ganzem Herzen.

List of abbreviations

2CDE	Two channel kernel-based density estimator
a.u.	Arbitrary unit
Bdp1	B double prime (historically B'')
$Bdp1_{ES}$	Bdp1 variant constituting amino acid residues (130–484)
$Bdp1_{S}$	Bdp1 variant constituting amino acid residues (241–396)
BRE	B recognition element /B responsive element
Brf	B related factor
CE	Core element
CF	Core factor
CRE	Core recognition element
C-term.	Carboxyl-terminal
CTF	Contrast transfer function
dsDNA	Double-stranded DNA
DSE	Distal sequence element
DTT	Dithiothreitol
EDTA	Ethylenediaminetetraacetic acid
EMCCD	Electron multiplying charge-coupled device
EMSA	Electrophoretic mobility shift assay
FC	Force clamp
FCS	Fluorescence correlation spectroscopy
FRET	Förster resonance energy transfer
HF	High FRET efficiency
HJ	Holliday junction
HMM	Hidden Markov Model
Hs(protein name)	*Homo sapiens* (protein name)
Iso I	Isoform I
Iso II	Isoform II
LF	Low FRET efficiency
MF	Medium FRET efficiency
Mj(protein name)	*Methanocaldococcus jannaschii* (protein name)
MLP	Adenovirus major late promoter
mPEG	Methoxi-polyethylene glycol
mRNA	Messenger RNA
N-term.	Amino-terminal
NTS	Non-template strand
PBS	Phosphate buffered saline
P_{con}	pf1089 promoter with a *Pyrococcus furiosus* consensus BRE sequence
PEG	polyethylene glycol
Pf(protein name)	*Pyrococcus furiosus* (protein name)
PIC	Pre-initiation complex
P_{nat}	Native *pf1089* promoter
PS	Photo-stabilization
PSE	Proximal sequence element
PSF	Point-spread function
RNA	Ribonucleic acid
RNAP	RNA polymerase
s.e.	Standard error
Sa(protein name)	*Sulfolobus acidocaldarius* (protein name)
Sc(protein name)	*Saccharomyces cerevisiae* (protein name)

SNAPc	Small nuclear RNA activation protein complex
snRNA	Small nuclear RNA
Ss(protein name)	*Saccharolobus solfataricus* (protein name)
ssDNA	Single-stranded DNA
T6P	SSV T6 promoter
TBP	TATA-binding protein
TBS	Tris-buffered saline
TCEP	Tris-(2-carboxyethyl)-phosphine
TF	Transcription factor
TFB-RF1	TFB recruitment factor 1
TIRF	Total inter reflection fluorescence
tRNA	Transfer RNA
TS	Template strand
U6P	U6 snRNA promoter
UAF	Upstream activating factor

List of figures

Figure 1: Concepts of molecular heterogeneity. 15
Figure 2: Simplified Jablonski diagram. 19
Figure 3: The spectral overlap integral *J*. 20
Figure 4: The orientation factor κ^2. 21
Figure 5: Principles of Förster resonance energy transfer. 22
Figure 6: Principles of total internal reflection fluorescence microscopy. 24
Figure 7: Comparison of TIRF microscope geometries. 25
Figure 8: Principles of confocal fluorescence microscopy. 26
Figure 9: Principles of DNA origami. 27
Figure 10: The DNA origami force clamp. 28
Figure 11: Transcription initiation complex assembly in bacteria, archaea and eukaryotes. 31
Figure 12: Structural conservation of TBP. 34
Figure 13: Structural conservation of TFIIB-like factors. 36
Figure 14: Preparation of doubly labelled promoter DNA for DNA origami force clamps. 56
Figure 15: Enzymatic digestion of force clamp scaffold DNA. 57
Figure 16: Freely jointed chain model of single-stranded DNA. 58
Figure 17: Force-extension calculation for DNA origami force clamps. 60
Figure 18: Confocal single-molecule fluorescence microscopy. 62
Figure 19: Pulsed interleaved excitation. 63
Figure 20: PIE channel definition and burst search in PAM. 65
Figure 21: Determination of correction factors for confocal smFRET data. 67
Figure 22: Working principle of the FRET-2CDE filter. 70
Figure 23: Total internal reflection fluorescence (TIRF) microscopy. 72
Figure 24: Flow chamber assembly. 74
Figure 25: Mechanisms of photo-stabilization. 75
Figure 26: Determination of correction factors for wide-field smFRET experiments. 78
Figure 27: Dwell time analysis of dynamic FRET traces using a hidden Markov model. 80
Figure 28: Photographs of the home-build TIRF microscope setup. 81
Figure 29: Layout of the home-built TIRF microscope setup. 82
Figure 30: Construction plan of the laser-mount. 83
Figure 31: Assembly of post-mounted optical components. 83
Figure 32: Construction plan of the prims- and lense-mounts. 84
Figure 33: Total internal reflection at the prism/sample interface. 85
Figure 34: Construction plan of the beam blocker assembly. 86
Figure 35: Emission detection channels for ALEX experiments. 87
Figure 36: Sequence and structure of a synthetic DNA Holliday junction. 89
Figure 37: Experimental setup for smFRET analysis of DNA Holliday junction dynamics. 90
Figure 38: Magnesium dependent conformational dynamics of DNA Holliday junctions. 91
Figure 39: Kinetics of isoform I–isoform II conformational dynamics. 93

Figure 40: Comparison of Holliday junction conformer kinetics between independent studies. 93
Figure 41: Variability in conformational dynamics of DNA Holliday junctions. 94
Figure 42: Transition state dynamics of DNA Holliday junctions. 95
Figure 43: Domain organization of human TFIIIB subunits. 97
Figure 44: Structural features of the human TFIIIB complex. 98
Figure 45: Experimental setup and smFRET TFIIIB promoter bending assays using TIRF microscopy. 99
Figure 46: Analysis of immobilized U6 promoter/HsTFIIIB subcomplexes under equilibrium conditions. 101
Figure 47: Analysis of immobilized U6 promoter/HsTFIIIB subcomplexes after washing. 103
Figure 48: Control experiments for smFRET analysis of human TFIIIB components. 105
Figure 49: Analysis of dynamics in smFRET time traces of human TFIIIB subcomplexes. 106
Figure 50: Experimental setup for DNA origami based single-molecule force measurements. 108
Figure 51: Structure comparison of RNAP II and III initiation factor complexes. 109
Figure 52: Comparison of U6 promoter and MLP DNA origami force clamps to linear double-stranded promoters. 110
Figure 53: Comparison of TBP-induced DNA bending for linear double-stranded DNA promoters and DNA origami force clamps. 111
Figure 54: Force-dependency of TFIIIB subcomplex assembly at the U6 promoter. 113
Figure 55: Force-dependency of RNAP II initiation factor assembly at the MLP. 114
Figure 56: Force-dependency of HsTBP-induce DNA bending dynamics at the U6 promoter. 117
Figure 57: Force-dependency of MLP/HsTBP DNA-bending dynamics analyzed with TIRF microscopy. 118
Figure 58: Force-dependency of HsTBP/MLP association and dissociation kinetics analyzed via confocal microscopy. 119
Figure 59: Sequence conservation of *Sulfolobus acidocaldarius* TFB1 and TFB2. 122
Figure 60: Effects of SaTFB1 and SaTFB2 on promoter DNA bending. 123
Figure 61: Structural features of the *Pyrococcus furiosus* DNA/TBP/TFB1 complex and TFB-RF1. 124
Figure 62: Initiation factor and regulator assembly in the *Pyrococcus furiosus* transcription system. 126
Figure 63: Kinetics of PfTFB-RF1 facilitated TFB recruitment. 127
Figure 64: Comparison of a linear double stranded SSV T6 promoter to a DNA origami force clamp. 129
Figure 65: Force-dependency of promoter DNA bending by archaeal transcription initiation factors. 130
Figure 66: Sequence alignment of the promoter regions of human U6 snRNA genes. 133
Figure 67: Domain organization of human and *S. cerevisiae* Bdp1. 136
Figure 68: Stabilizing structural features of the human TFIIIB complex. 137
Figure 69: Model describing forces exerted on DNA by transcriptional activity at the U6 promoter. 144
Figure 70: Contribution of individual RNAP II initiation factors to complex stabilization. 145

Figure 71: Burst analysis of the medium FRET efficiency population observed in DNA origami force clamp experiment. 146
Figure 72: Comparison of the geometric model for DNA bending with structural data. 148
Figure 73: Comparison of TBP-contacting residues of SaTFB1 and SaTFB2. 151
Figure 74: Comparison of force-dependent DNA-bending by *M. jannaschii* TBP between independent studies. 155
Figure 75: FRET efficiency histograms with standard deviation for TIRF experiments with human TFIIIB subcomplexes. 199
Figure 76: FRET efficiency histograms with standard deviation for force measurements with human RNAP II and III transcription factors. 202
Figure 77: *E*/*S* histograms and FRET-2CDE values for force measurements with human RNAP II and III transcription factors. 203
Figure 78: FRET efficiency histograms with standard deviation for measurements with *Sulfolobus acidocaldarius* transcription factors. 204
Figure 79: FRET efficiency histograms with standard deviation for measurements with *Pyrococcus furiosus* transcription factors. 205
Figure 80: FRET efficiency histograms with standard deviation for force measurements with archaeal transcription factors. 207

List of tables

Table 1: List of chemicals and reagents. 44
Table 2: Composition of buffers. 45
Table 3: List of used proteins. 48
Table 4: Sequences and modifications of oligonucleotides. 49
Table 5: List of expendable items. 50
Table 6: List of electronic devices. 51
Table 7: List of optical components and devices integrated in the MicroTime 200 confocal fluorescence microscope. 52
Table 8: List of optical components and devices used in the construction of the home-built prism TIRF microscope setup. 52
Table 9: List of software. 54
Table 10: Composition of a 15% denaturing TBE-PAGE gel. 56
Table 11: Composition of a 1% TAEM agarose gel. 57
Table 12: Temperature ramp for the annealing of DNA origami force clamps. 58
Table 13: Parameters of DNA origami force clamps. 61
Table 14: Amino acid sequences of proteins used in experiments. 192
Table 15: Nucleotide sequences of M13mp18-derived DNA origami scaffolds. 195
Table 16: Molecule counts and fitting errors for measurements with DNA Holliday junctions. 197
Table 17: Molecule/trace counts for Holliday junction dynamics analysis. 197
Table 18: Molecule counts and fitting errors for TIRF measurements with human TFIIIB subcomplexes. 198
Table 19: Dwell times calculation for U6P/TBP and U6P/TBP/Bdp1 subcomplexes. 199
Table 20: Molecule counts and fitting errors for force measurements with human TFIIIB subcomplexes. 200
Table 21: Molecule counts and fitting errors for force measurements with human RNAP II transcription factors 201
Table 22: Kinetic data parameters from force measurements with U6P/TBP and MLP/TBP complexes. 203
Table 23: Molecule counts and fitting errors for measurements with *Sulfolobus acidocaldarius* transcription factors. 204
Table 24: Molecule counts and fitting errors for confocal smFRET measurements with *Pyrococcus furiosus* transcription factors. 205
Table 25: Molecule counts and fitting errors for force measurements with archaeal transcription initiation factors. 206

Appendix

A Protein sequences

Table 14: Amino acid sequences of proteins used in experiments. Proteins are listed in alphabetical order.

Name Organism Uniprot ID	**Amino acid sequence**
Bdp1 *Homo sapiens* A6H8Y1	MFRRARLSVKPNVRPGVGARGSTASNPQRGRESPRPPDPATDSA SKPAEPTDVPTVDFGGAEPQEKAPRSSTEKTGGDNDVEESSRSS STVSQRRKRISSTSSLVKSSVSVPSESHPLSTINQEAPQPTATS TKEKQPCSDRYRIYKAQKLREMLKEELRKEKKQWKNKYAINESQ RPPDRSKMTMRDFIYYLPDNNPMTSSLEQEKKTEKPSTPVQTRE QEGKSTPNAEDNEMEEETDDGPLLVPRVKVAEDGSIILDEESLT VEVLRTKGPCVVEENDPIFERGSTTTYSSFRKNYYSKPWSNKET DMFFLAISMVGTDFSMIGQLFPHRARIEIKNKFKREEKTNGWRI DKAFQEKRPFDFDFFAHLLQKVLAEEEKRKQKSVKNHSLKEKKS TKPRKNVKVKKVACEGVNNDPDESMSSRISDTERSQKDAQTVEE ESLTLSREDAEQVALEVDLNQKKRRRKKQDGANELGVNNLLENA TVQAGPSKGEKHKNKCQAIRPELKEGECSKEQMLSCTQNIDGIV GFASTEKVEKRTDPILSLSNQQDATSVATESSESSTSDLPSFEV GIRALCEVNNAEGSCIEERNVDLKNNSLEIDQTENVKPMLRGRF QRPKPNLSRAGKKSVLSQGKTESESKNSHSKTSVEKNHVEKDKM NTLDILRMETTERENPEAETVSVLGEKNCLQEGSQLKALRPVQV RGRLQKPKPNAGKAAERKEILISQEEIGANVEKNENESCADRDT PQHMEDQSRKDFEEEDVILQPEKNDSFQNVQPDEPKVLNECLSV QENNKANKLNQVPILRTRFQKPKPNIGRGTGRREISSKEEVLEK ILVSGEMAAALRETVRLDTSPKEMVPAEINTKEMQSDLKETGRR AISPREKILDVIDDTIEMETGLKAMGREICLREKTPEVIDATEE IDKDLEEAGRREISPQKNGPEEVKPLGEVETDLKATGNESSPRE KTPEVTDATEEIDKNLEETGRRKISPRENGPEEVKPVDEMETDL NATGRESSPREKTPEVIDATEEIDLEETEREVSPQENGLEEVKP LGEMETDLKATGRDSFPRGKTPEVIDAIEEIEIDLEETEREISP QENGLEEVKPLGEMQTDLKATGREISPREKTPEVIDATEEIDKD LEETGRREISPEENGPEEVKPVDEMETDLKTTGREGSSREKTRE VIDAAEVIETDLEETEREISPQENGPEEVKPVGKMETDLKEIRE EISQREKVLAEFSAIREKEIDLKETGKRDIPIMEKVSGKMAVVE EMEADLKETGKENFRERGSEEICVTEEKVAELKQTGKTDISPRE NELEETSTSRQTDTHLMQSGSNDFSAVPSLDIQNISSEVLSMMH TPVEEKRNSEKEVSSHFSHFKISSQTHESDKTEVQGIQSPDVPE QFSDINLSKSLPQEQKPLEIKPAPFVRSRFKRPKPNLARAALKR ETTESEKYIYEKKSETKKMETIVMQENNEQTDTLPSQHDEASLM ISREKDTLGHRNEEAVILPCTQTERNLSPSNSCEPKEESQSAPV QKNDSVVSVGTNNVNTFQQEMKESVIQTARQVRGRLQRPRPNIR KTGQRQIVDKGEAKGIIKEGRTILPKDETEKKVLTVSNSQIETE IEVPSSAVPEHRMYENQSQVVLVENLHVNKTNETIRHENKPYVP SSAQMTRRKFQKAKPNLGRAHSKKEEPVLEKVTTDQSKEGKPED HLLQKGASNTQLLLKEKAELLTSLEVSARKDCVGSKESALAKID AELEEVGPSRRVGEETVGDNSPSSVVEEQYLNKLTSCPQPLNET SYSKIALDGKTTISSTSEYERNRGERRSHKKFKPNVTRGRGSKR VRGKTSKKEPRASKAMLVTLRASQEEDDDADDFESDYEEESYHL APEEVNKAPVFVPVGLRSPEPVSAQIEETMEELEITVNVPDVGC IAVVEHELPNTDVTTEEMKQEENLSVPFEMTTSEHIQDEPGTND GSTEAAITLLTMGDLVLQSEISSEQGDVGVCIIPHVHSKDKSHI PSSLDNVNHKIVHECQELSSPVITTSPASFEENKIVLEEQSSRE EISLMEKVKENATPTRNTISKVTSNLRIRSRLAKPKPNLEKTLG TNRLDDYQEVSSLCVTKGAEMETQRETEKNASKATELENKNLGP VTTAENKDQSKLACVHGIKGTSISSEVNLTERNENQEESSQEVH MLSVAPVASSETGPCTLGLDRGLGENSVEEPQIKDSKGDSVLTL PVPEYTPTSIPEVQQENIINPQDLTVNLVANVPQDGEDEQAFIL TLVEIPANAVEEFTDATAQFMPNPLLPAPILVKSVNTEERGDMS ICLPATSVGQDAMGLSISGRDNSKKPPDNLDLVSRKRFQCRLDK NDHIPPAKKRSLTLRDDCQEYTTEVHSKELTNVFEETGESHKGQ

DIFLTSGSTLTTPEPQRQQVEAAFQSRGSRSPDACMDKNVPQLP
QDEMIVSDKEERTDAAPKSQQMDSRTSSSKASLSRPGRRPLGFL
SLICSKNSLESDEPMQVHSKKRLKPLIPGLRKKLKRSNPFNESQ
EKNRESSDLLPSPSVITTQSENISSSATQVSCDQPLLKEGYKSA
QKRAPQGEATTVSEYFFNDIFIEVDETE

Brf2
Homo sapiens
Q9HAW0

MPGRGRCPDCGSTELVEDSHYSQSQLVCSDCGCVVTEGVLTTTF
SDEGNLREVTYSRSTGENEQVSRSQQRGLRRVRDLCRVLQLPPT
FEDTAVAYYQQAYRHSGIRAARLQKKEVLVGCCVLITCRQHNWP
LTMGAICTLLYADLDVFSSTYMQIVKLLGLDVPSLCLAELVKTY
CSSFKLFQASPSVPAKYVEDKEKMLSRTMQLVELANETWLVTGR
HPLPVITAATFLAWQSLQPADRLSCSLARFCKLANVDLPYPASS
RLQELLAVLLRMAEQLAWLRVLRLDKRSVVKHIGDLLQHRQSLV
RSAFRDGTAEVETREKEPPGWGQGQGEGEVGNNSLGLPQGKRPA
SPALLLPPCMLKSPKRICPVPPVSTVTGDENISDSEIEQYLRTP
QEVRDFQRAQAARQAATSVPNPP

TBP
homo sapiens
P20226

MDQNNSLPPYAQGLASPQGAMTPGIPIFSPMMPYGTGLTPQPIQ
NTNSLSILEEQQRQQQQQQQQQQQQQQQQQQQQQQQQQQQQQQQ
QQQQQQQAVAAAAVQQSTSQQATQGTSGQAPQLFHSQTLTTAPL
PGTTPLYPSPMTPMTPITPATPASESSGIVPQLQNIVSTVNLGC
KLDLKTIALRARNAEYNPKRFAAVIMRIREPRTTALIFSSGKMV
CTGAKSEEQSRLAARKYARVVQKLGFPAKFLDFKIQNMVGSCDV
KFPIRLEGLVLTHQQFSSYEPELFPGLIYRMIKPRIVLLIFVSG
KVVLTGAKVRAEIYEAFENIYPILKGFRKTT

TBP
Pyrococcus furiosus
P62000

MVDMSKVKLRIENIVASVDLFAQLDLEKVLDLCPNSKYNPEEFP
GIICHLDDPKVALLIFSSGKLVVTGAKSVQDIERAVAKLAQKLK
SIGVKFKRAPQIDVQNMVFSGDIGREFNLDVVALTLPNCEYEPE
QFPGVIYRVKEPKSVILLFSSGKIVCSGAKSEADAWEAVRKLLR
ELDKYGLLEEEEEEL

TBP
Methanocaldococcus jannaschii
Q57930

MKIMEPEIKIVNVVVSTKIGDNIDLEEVAMILENAEYEPEQFPG
LVCRLSVPKVALLIFRSGKVNCTGAKSKEEAEIAIKKIIKELKD
AGIDVIENPEIKIQNMVATADLGIEPNLDDIALMVEGTEYEPEQ
FPGLVYRLDDPKVVVLIFGSGKVVITGLKSEEDAKRALKKILDT
IKEVQEL

TBP
Sulfolobus acidocaldarius
Q9UWN7

MIPDEIPYKAVVNIENIVATVTLDQTLDLYAMERSVPNVEYDPD
QFPGLIFRLESPKITSLIFKSGKMVVTGAKSTDELIKAVKRIIK
TLKKYGMQLTGKPKIQIQNIVASANLHVIVNLDKAAFLLENNMY
EPEQFPGLIYRMDEPRVVLLIFSSGKMVITGAKREDEVHKAVKK
IFDKLVELDCVKPVEEEELEF

TFB1
Pyrococcus furiosus
P61998

MNKQKVCPACESAELIYDPERGEIVCAKCGYVIEENIIDMGPEW
RAFDASQRERRSRTGAPESILLHDKGLSTEIGIDRSLSGLMREK
MYRLRKWQSRLRVSDAAERNLAFALSELDRITAQLKLPRHVEEE
AARLYREAVRKGLIRGRSIESVMAACVYAACRLLKVPRTLDEIA
DIARVDKKEIGRSYRFIARNLNLTPKKLFVKPTDYVNKFADELG
LSEKVRRRAIEILDEAYKRGLTSGKSPAGLVAAALYIASLLEGE
KRTQREVAEVARVTEVTVRNRYKELVEKLKIKVPIA

TFB
Methanocaldococcus jannaschii
Q58192

MVWLMEALKTKENETTKEKKLTTKVEKSEKKEENVREEEIVCPI
CGSKEVVKDYERAEIVCAKCGCVIKEKLFDIGPEWRAFDHEQKI
KRCRVGAPMTYSVDYNEPIIIKENGEIKVVKIGELIDKIIENSE
NIRREGILEIAKCKGIEVIAFNSNYKFKFMPVSEVSRHPVSEMF
EIVVEGNKKVRVTRSHSVFTIRDNEVVPIRVDELKVGDILVLAK
ELPNIEEDIEIDKKFSKILGYIIAEGYYDDKKIVLSYDYNEKEF
INETIDYFKSLNSDITIYSKDLNIQIEVKNKKIINLLKKLRVKN
KRIPSIIFKSPYEIKKSFIDGIFNGKDAKVFVSKELAEDVIFLL
LQIKENATINKKSINDIEVYEVRRITNIYTNRKLEKLINSDFIF
LKIKEINKVEPTSGYAYDLTVPNAENFVAGFGGFVLHNTIHDKG
LSTVIDWRNKDSYGKDLSANKRAQLYRLRKWQRRIRVSDAAERN
LAFALSELDRITSKLGLPRHVRENAAIIYRGAVEKGLIRGRSIE

GVVAAAIYAACRRCRVPRTLDEIAEASRVDRKEIGRTYRFLARE
LNIKLTPTNPIDYVPRFASELGLPGEVESKAIQILQQAAEKGLT
SGRGPTGVAAAAIYIASVLLGCRRTQREVAEVAGVTEVTIRNRY
KELTEHLDIDVTL

TFB1
Sulfolobus acidocaldarius
Q9UWN6

MVEQSKVPSSSLCPPDKIIFDEERGEYICTETGEVIEERIIDQG
PEWRAFTPEEKEKRSRVGGPLNQTIHDMGISTVIDWKDKDAMGR
SLDPKRRLEVLRWRKWQIRTRIQSSIDRNLAQAMNELERIGNLL
NLPKAVKDEAALIYRKAVEKGLVRGRSIESVVAASIYAACRRMK
MARTLDEIAQFTKANRKEVARCYRLILRELDIEVPVSDPKDYVT
RIGTLLSLSGITMKHAAEIIEKAKNSGLTAGKDPAGLAAAAIYI
AALLNDERRTQKEIAQVAGVTEVTVRNRYKELTQELKIQIPSQ

TFB2
Sulfolobus acidocaldarius
Q4J949

MKCKICGSESLIFDRERGIYVCINCASVDDEPLIDQGPEWRAYT
TEDKVERERTGSPLTAKVHDFGITTKIGYTKIKDRIKVHKLRLM
QNKIRVSARERKLVTYLSVLNSEASKLNLPEHVKETASILIRRL
IEEGKAKRVEMYALIAAVIYYSCQVNRIPKLLNEIKTLYSLSQA
DLWKALEKVQEVAKSVKVKPNVTPIEYIPKITERLGLPAYVSTK
ASELVDIMYKNGLTSGKGYTALAAASVYLISTLMDVKKTQKEIA
DSLSITEVTIRNRYREIIKAFDIEVKL

TFB-RF1
Pyrococcus furiosus
Q8U1W6

MEEIKEIMKSHTLGNPVRLGIMIYLFPRRRAPFSHIQKALDLTP
GNLDSHIKVLEKHGFVRTYKVIADRPRTMVEITDYGMEETRKFL
SHLKTVIDAIHF

TFIIA (single chain variant)
Homo sapiens

Fusion of construct of:
TFIIAγ (residues 2–103, F81 mutated to V)
TFIIAαβ (residues 2–58)
TFIIAαβ (residues 327–376)

AYQLYRNTTLGNSLQESLDELIQSQQITPQLALQVLLQFDKAIN
AALAQRVRNRVNFRGSLNTYRFCDNVWTFVLNDVEVREVTELIK
VDKVKIVACDGKNTANSANTNTVPKLYRSVIEDVINDVRDIFLD
DGVDEQVLMELKTLWENKLMQSRAVDGELFDTENVVVCQYDKIH
RSKNKWKFHLKDGIMNLNGRDYIFSKAIGDAEW

TFIIAαβ
Homo sapiens
P52655

MANSANTNTVPKLYRSVIEDVINDVRDIFLDDGVDEQVLMELKT
LWENKLMQSRAVDGFHSEEQQLLLQVQQQHQPQQQQHHHHHHHQ
QAQPQQTVPQQAQTQQVLIPASQQATAPQVIVPDSKLIQHMNAS
NMSAAATAATLALPAGVTPVQQILTNSGQLLQVVRAANGAQYIF
QPQQSVVLQQQVIPQMQPGGVQAPVIQQVLAPLPGGISPQTGVI
IQPQQILFTGNKTQVIPTTVAAPTPAQAQITATGQQQPQAQPAQ
TQAPLVLQVDGTGDTSSEEDEDEEEDYDDDEEEDKEKDGAEDGQ
VEEEPLNSEDDVSDEEGQELFDTENVVVCQYDKIHRSKNKWKFH
LKDGIMNLNGRDYIFSKAIGDAEW

TFIIAγ
Homo sapiens
P52657

MAYQLYRNTTLGNSLQESLDELIQSQQITPQLALQVLLQFDKAI
NAALAQRVRNRVNFRGSLNTYRFCDNVWTFVLNDVEFREVTELI
KVDKVKIVACDGKNTGSNTTE

TFIIB
Homo sapiens
Q00403

MASTSRLDALPRVTCPNHPDAILVEDYRAGDMICPECGLVVGDR
VIDVGSEWRTFSNDKATKDPSRVGDSQNPLLSDGDLSTMIGKGT
GAASFDEFGNSKYQNRRTMSSSDRAMMNAFKEITTMADRINLPR
NIVDRTNNLFKQVYEQKSLKGRANDAIASACLYIACRQEGVPRT
FKEICAVSRISKKEIGRCFKLILKALETSVDLITTGDFMSRFCS
NLCLPKQVQMAATHIARKAVELDLVPGRSPISVAAAAIYMASQA
SAEKRTQKEIGDIAGVADVTIRQSYRLIYPRAPDLFPTDFKFDT
PVDKLPQL

B DNA origami scaffolds

Table 15: Nucleotide sequences of M13mp18-derived DNA origami scaffolds. The multiple-cloning site framed by the BamHI (yellow) and HindIII (orange) restriction site used to clone the three different promoter sequence is shown. The complementary strand and the TATA-box region (blue) indicate the double stranded promoter region. The common part of all scaffolds, downstream of the HindIII site (indicated by ···) is given below.

SSV T6 promoter(T6P) scaffold | total length: 7283 nt

```
5′-GGATCCTTCGGACCGAAAGCGCGACCATCGCCGGAGATTGGAGTAAAGTTTAAATACTGACTAAAAGCTT ···
        3′-GCCTGGCTTTCGCGCTGGTAGCGGCCTCTAACCTCATTTCAAATTTATGAC
```

Adenovirus major late promoter (MLP) scaffold | total length: 7267 nt

```
5′-GGATCCTATGACTGCTTCGCGCCCGAACCCCCTTTTTATAGGCGCCCTAAAGCTT ···
                  3′-GCGGGCTTGGGGGAAAAATATCCGCGGGATTTCGAA
```

U6 snRNA promoter (U6P) scaffold | total length: 7285 nt

```
5′-GGATCCTATGATCAAGGGTTACTCTAACACCTATTTTAAGCCCTTCAATCAAATCATCTTGGTCCGAAGCTT ···
           3′-AGTTCCCAATGAGATTGTGGATAAAATTCGGGAAGTTAGTTTAGTAGAACCAGGC
```

Common M13mp18 scaffold sequence (downstream of HindIII site)

```
··· 5′-GGCACTGGCCGTCGTTTTACAACGTCGTGACTGGGAAAACCCTGGCGTTACCCAACTTAATCGCCTTGCAGCACATCCCCC
TTTCGCCAGCTGGCGTAATAGCGAAGAGGCCCGCACCGATCGCCCTTCCCAACAGTTGCGCAGCCTGAATGGCGAATGGCGCTTTGCC
TGGTTTCCGGCACCAGAAGCGGTGCCGGAAAGCTGGCTGGAGTGCGATCTTCCTGAGGCCGATACTGTCGTCGTCCCCTCAAACTGGC
AGATGCACGGTTACGATGCGCCCATCTACACCAACGTGACCTATCCCATTACGGTCAATCCGCCGTTTGTTCCCACGGAGAATCCGAC
GGGTTGTTACTCGCTCACATTTAATGTTGATGAAAGCTGGCTACAGGAAGGCCAGACGCGAATTATTTTTGATGGCGTTCCTATTGGT
TAAAAAATGAGCTGATTTAACAAAAATTTAATGCGAATTTTAACAAAATATTAACGTTTACAATTTAAATATTTGCTTATACAATCTT
CCTGTTTTTGGGGCTTTTCTGATTATCAACCGGGGTACATATGATTGACATGCTAGTTTTACGATTACCGTTCATCGATTCTCTTGTT
TGCTCCAGACTCTCAGGCAATGACCTGATAGCCTTTGTAGATCTCTCAAAAATAGCTACCCTCTCCGGCATTAATTTATCAGCTAGAA
CGGTTGAATATCATATTGATGGTGATTTGACTGTCTCCGGCCTTTCTCACCCTTTTGAATCTTTACCTACACATTACTCAGGCATTGC
ATTTAAAATATATGAGGGTTCTAAAAATTTTTATCCTTGCGTTGAAATAAAGGCTTCTCCCGCAAAAGTATTACAGGGTCATAATGTT
TTTGGTACAACCGATTTAGCTTTATGCTCTGAGGCTTTATTGCTTAATTTTGCTAATTCTTTGCCTTGCCTGTATGATTTATTGGATG
TTAATGCTACTACTATTAGTAGAATTGATGCCACCTTTTCAGCTCGCGCCCCAAATGAAAATATAGCTAAACAGGTTATTGACCATTT
GCGAAATGTATCTAATGGTCAAACTAAATCTACTCGTTCGCAGAATTGGGAATCAACTGTTATATGGAATGAAACTTCCAGACACCGT
ACTTTAGTTGCATATTTAAAACATGTTGAGCTACAGCATTATATTCAGCAATTAAGCTCTAAGCCATCCGCAAAAATGACCTCTTATC
AAAAGGAGCAATTAAAGGTACTCTCTAATCCTGACCTGTTGGAGTTTGCTTCCGGTCTGGTTCGCTTTGAAGCTCGAATTAAAACGCG
ATATTTGAAGTCTTTCGGGCTTCCTCTTAATCTTTTTGATGCAATCCGCTTTGCTTCTGACTATAATAGTCAGGGTAAAGACCTGATT
TTTGATTTATGGTCATTCTCGTTTTCTGAACTGTTTAAAGCATTTGAGGGGGATTCAATGAATATTTATGACGATTCCGCAGTATTGG
ACGCTATCCAGTCTAAACATTTTACTATTACCCCCTCTGGCAAAACTTCTTTTGCAAAAGCCTCTCGCTATTTTGGTTTTTATCGTCG
TCTGGTAAACGAGGGTTATGATAGTGTTGCTCTTACTATGCCTCGTAATTCCTTTTGGCGTTATGTATCTGCATTAGTTGAATGTGGT
ATTCCTAAATCTCAACTGATGAATCTTTCTACCTGTAATAATGTTGTTCCGTTAGTTCGTTTTATTAACGTAGATTTTTCTTCCCAAC
GTCCTGACTGGTATAATGAGCCAGTTCTTAAAATCGCATAAGGTAATTCACAATGATTAAAGTTGAAATTAAACCATCTCAAGCCCAA
TTTACTACTCGTTCTGGTGTTTCTCGTCAGGGCAAGCCTTATTCACTGAATGAGCAGCTTTGTTACGTTGATTTGGGTAATGAATATC
CGGTTCTTGTCAAGATTACTCTTGATGAAGGTCAGCCAGCCTATGCGCCTGGTCTGTACACCGTTCATCTGTCCTCTTTCAAAGTTGG
TCAGTTCGGTTCCCTTATGATTGACCGTCTGCGCCTCGTTCCGGCTAAGTAACATGGAGCAGGTCGCGGATTTCGACACAATTTATCA
GGCGATGATACAAATCTCCGTTGTACTTTGTTTCGCGCTTGGTATAATCGCTGGGGGTCAAAGATGAGTGTTTTAGTGTATTCTTTTG
CCTCTTTCGTTTTAGGTTGGTGCCTTCGTAGTGGCATTACGTATTTTACCCGTTTAATGGAAACTTCCTCATGAAAAAGTCTTTAGTC
CTCAAAGCCTCTGTAGCCGTTGCTACCCTCGTTCCGATGCTGTCTTTCGCTGCTGAGGGTGACGATCCCGCAAAAGCGGCCTTTAACT
CCCTGCAAGCCTCAGCGACCGAATATATCGGTTATGCGTGGGCGATGGTTGTTGTCATTGTCGGCGCAACTATCGGTATCAAGCTGTT
TAAGAAATTCACCTCGAAAGCAAGCTGATAAACCGATACAATTAAAGGCTCCTTTTGGAGCCTTTTTTTTGGAGATTTTCAACGTGAA
AAAATTATTATTCGCAATTCCTTTAGTTGTTCCTTTCTATTCTCACTCCGCTGAAACTGTTGAAAGTTGTTTAGCAAAATCCCATACA
GAAAATTCATTTACTAACGTCTGGAAAGACGACAAAACTTTAGATCGTTACGCTAACTATGAGGGCTGTCTGTGGAATGCTACAGGCG
TTGTAGTTTGTACTGGTGACGAAACTCAGTGTTACGGTACATGGGTTCCTATTGGGCTTGCTATCCCTGAAAATGAGGGTGGTGGCTC
TGAGGGTGGCGGTTCTGAGGGTGGCGGTTCTGAGGGTGGCGGTACTAAACCTCCTGAGTACGGTGATACACCTATTCCGGGCTATACT
TATATCAACCCTCTCGACGGCACTTATCCGCCTGGTACTGAGCAAAACCCCGCTAATCCTAATCCTTCTCTTGAGGAGTCTCAGCCTC
TTAATACTTTCATGTTTCAGAATAATAGGTTCCGAAATAGGCAGGGGGCATTAACTGTTTATACGGGCACTGTTACTCAAGGCACTGA
```

CCCCGTTAAAACTTATTACCAGTACACTCCTGTATCATCAAAAGCCATGTATGACGCTTACTGGAACGGTAAATTCAGAGACTGCGCT
TTCCATTCTGGCTTTAATGAGGATTTATTTGTTTGTGAATATCAAGGCCAATCGTCTGACCTGCCTCAACCTCCTGTCAATGCTGGCG
GCGGCTCTGGTGGTGGTTCTGGTGGCGGCTCTGAGGGTGGTGGCTCTGAGGGTGGCGGTTCTGAGGGTGGCGGCTCTGAGGGAGGCGG
TTCCGGTGGTGGCTCTGGTTCCGGTGATTTTGATTATGAAAAGATGGCAAACGCTAATAAGGGGGCTATGACCGAAAATGCCGATGAA
AACGCGCTACAGTCTGACGCTAAAGGCAAACTTGATTCTGTCGCTACTGATTACGGTGCTGCTATCGATGGTTTCATTGGTGACGTTT
CCGGCCTTGCTAATGGTAATGGTGCTACTGGTGATTTTGCTGGCTCTAATTCCCAAATGGCTCAAGTCGGTGACGGTGATAATTCACC
TTTAATGAATAATTTCCGTCAATATTTACCTTCCCTCCCTCAATCGGTTGAATGTCGCCCTTTTGTCTTTGGCGCTGGTAAACCATAT
GAATTTTCTATTGATTGTGACAAAATAAACTTATTCCGTGGTGTCTTTGCGTTTCTTTTATATGTTGCCACCTTTATGTATGTATTTT
CTACGTTTGCTAACATACTGCGTAATAAGGAGTCTTAATCATGCCAGTTCTTTTGGGTATTCCGTTATTATTGCGTTTCCTCGGTTTC
CTTCTGGTAACTTTGTTCGGCTATCTGCTTACTTTTCTTAAAAAGGGCTTCGGTAAGATAGCTATTGCTATTTCATTGTTTCTTGCTC
TTATTATTGGGCTTAACTCAATTCTTGTGGGTTATCTCTCTGATATTAGCGCTCAATTACCCTCTGACTTTGTTCAGGGTGTTCAGTT
AATTCTCCCGTCTAATGCGCTTCCCTGTTTTTATGTTATTCTCTCTGTAAAGGCTGCTATTTTCATTTTTGACGTTAAACAAAAAATC
GTTTCTTATTTGGATTGGGATAAATAATATGGCTGTTTATTTTGTAACTGGCAAATTAGGCTCTGGAAAGACGCTCGTTAGCGTTGGT
AAGATTCAGGATAAAATTGTAGCTGGGTGCAAAATAGCAACTAATCTTGATTTAAGGCTTCAAAACCTCCCGCAAGTCGGGAGGTTCG
CTAAAACGCCTCGCGTTCTTAGAATACCGGATAAGCCTTCTATATCTGATTTGCTTGCTATTGGGCGCGGTAATGATTCCTACGATGA
AAATAAAAACGGCTTGCTTGTTCTCGATGAGTGCGGTACTTGGTTTAATACCCGTTCTTGGAATGATAAGGAAAGACAGCCGATTATT
GATTGGTTTCTACATGCTCGTAAATTAGGATGGGATATTATTTTTCTTGTTCAGGACTTATCTATTGTTGATAAACAGGCGCGTTCTG
CATTAGCTGAACATGTTGTTTATTGTCGTCGTCTGGACAGAATTACTTTACCTTTTGTCGGTACTTTATATTCTCTTATTACTGGCTC
GAAAATGCCTCTGCCTAAATTACATGTTGGCGTTGTTAAATATGGCGATTCTCAATTAAGCCCTACTGTTGAGCGTTGGCTTTATACT
GGTAAGAATTTGTATAACGCATATGATACTAAACAGGCTTTTTCTAGTAATTATGATTCCGGTGTTTATTCTTATTTAACGCCTTATT
TATCACACGGTCGGTATTTCAAACCATTAAATTTAGGTCAGAAGATGAAATTAACTAAAATATATTTGAAAAAGTTTTCTCGCGTTCT
TTGTCTTGCGATTGGATTTGCATCAGCATTTACATATAGTTATATAACCCAACCTAAGCCGGAGGTTAAAAAGGTAGTCTCTCAGACC
TATGATTTTGATAAATTCACTATTGACTCTTCTCAGCGTCTTAATCTAAGCTATCGCTATGTTTTCAAGGATTCTAAGGGAAAATTAA
TTAATAGCGACGATTTACAGAAGCAAGGTTATTCACTCACATATATTGATTTATGTACTGTTTCCATTAAAAAAGGTAATTCAAATGA
AATTGTTAAATGTAATTAATTTTGTTTTCTTGATGTTTGTTTCATCATCTTCTTTTGCTCAGGTAATTGAAATGAATAATTCGCCTCT
GCGCGATTTTGTAACTTGGTATTCAAAGCAATCAGGCGAATCCGTTATTGTTTCTCCCGATGTAAAAGGTACTGTTACTGTATATTCA
TCTGACGTTAAACCTGAAAATCTACGCAATTTCTTTATTTCTGTTTTACGTGCAAATAATTTTGATATGGTAGGTTCTAACCCTTCCA
TTATTCAGAAGTATAATCCAAACAATCAGGATTATATTGATGAATTGCCATCATCTGATAATCAGGAATATGATGATAATTCCGCTCC
TTCTGGTGGTTTCTTTGTTCCGCAAAATGATAATGTTACTCAAACTTTTAAAATTAATAACGTTCGGGCAAAGGATTTAATACGAGTT
GTCGAATTGTTTGTAAAGTCTAATACTTCTAAATCCTCAAATGTATTATCTATTGACGGCTCTAATCTATTAGTTGTTAGTGCTCCTA
AAGATATTTTAGATAACCTTCCTCAATTCCTTTCAACTGTTGATTTGCCAACTGACCAGATATTGATTGAGGGTTTGATATTTGAGGT
TCAGCAAGGTGATGCTTTAGATTTTTCATTTGCTGCTGGCTCTCAGCGTGGCACTGTTGCAGGCGGTGTTAATACTGACCGCCTCACC
TCTGTTTTATCTTCTGCTGGTGGTTCGTTCGGTATTTTTAATGGCGATGTTTTAGGGCTATCAGTTCGCGCATTAAAGACTAATAGCC
ATTCAAAAATATTGTCTGTGCCACGTATTCTTACGCTTTCAGGTCAGAAGGGTTCTATCTCTGTTGGCCAGAATGTCCCTTTTATTAC
TGGTCGTGTGACTGGTGAATCTGCCAATGTAAATAATCCATTTCAGACGATTGAGCGTCAAAATGTAGGTATTTCCATGAGCGTTTTT
CCTGTTGCAATGGCTGGCGGTAATATTGTTCTGGATATTACCAGCAAGGCCGATAGTTTGAGTTCTTCTACTCAGGCAAGTGATGTTA
TTACTAATCAAAGAAGTATTGCTACAACGGTTAATTTGCGTGATGGACAGACTCTTTTACTCGGTGGCCTCACTGATTATAAAAACAC
TTCTCAGGATTCTGGCGTACCGTTCCTGTCTAAAATCCCTTTAATCGGCCTCCTGTTTAGCTCCCGCTCTGATTCTAACGAGGAAAGC
ACGTTATACGTGCTCGTCAAAGCAACCATAGTACGCGCCCTGTAGCGGCGCATTAAGCGCGGCGGGTGTGGTGGTTACGCGCAGCGTG
ACCGCTACACTTGCCAGCGCCCTAGCGCCCGCTCCTTTCGCTTTCTTCCCTTCCTTTCTCGCCACGTTCGCCGGCTTTCCCCGTCAAG
CTCTAAATCGGGGGCTCCCTTTAGGGTTCCGATTTAGTGCTTTACGGCACCTCGACCCCAAAAAACTTGATTTGGGTGATGGTTCACG
TAGTGGGCCATCGCCCTGATAGACGGTTTTTCGCCCTTTGACGTTGGAGTCCACGTTCTTTAATAGTGGACTCTTGTTCCAAACTGGA
ACAACACTCAACCCTATCTCGGGCTATTCTTTTGATTTATAAGGGATTTTGCCGATTTCGGAACCACCATCAAACAGGATTTTCGCCT
GCTGGGGCAAACCAGCGTGGACCGCTTGCTGCAACTCTCTCAGGGCCAGGCGGTGAAGGGCAATCAGCTGTTGCCCGTCTCACTGGTG
AAAAGAAAAACCACCCTGGCGCCCAATACGCAAACCGCCTCTCCCCGCGCGTTGGCCGATTCATTAATGCAGCTGGCACGACAGGTTT
CCCGACTGGAAAGCGGGCAGTGAGCGCAACGCAATTAATGTGAGTTAGCTCACTCATTAGGCACCCCAGGCTTTACACTTTATGCTTC
CGGCTCGTATGTTGTGTGGAATTGTGAGCGGATAACAATTTCACACAGGAAACAGCTATGACCATGATTACGAATTCGAGCTCGGTAC
CCGG

C Extended data

This section lists additional data corresponding to figures in the results section that were omitted due to space constraints in figures.

C.1 Measurements with DNA Holliday junctions

Table 16: Molecule counts and fitting errors for measurements with DNA Holliday junctions. FRET efficiency histograms calculated from FRET efficiency traces of Holliday junctions at different $MgCl_2$ concentrations (corresponding to Figure 38) were fitted with a Gaussian distribution. The number of video frames N_F (resulting from N_M molecules) used to calculate each histogram, the coefficient of determination of the fit R^2, the mean FRET efficiencies E (± s.e. of the fit) and the full width half-maximum (FWHM) (± s.e. of the fit) of each Gaussian are listed. *Value was fixed for the fit.

[$MgCl_2$] (mM)	N_M (molecules)	N_F (frames)	E_1 E_2	s.e. E_1 s.e. E_2	$FWHM_1$ $FWHM_2$	s.e. $FWHM_1$ s.e. $FWHM_2$	R^2
0	166	47589	0.468	0.001	0.240	0.003	0.9939
			-	-	-	-	
10	213	62235	0.333	0.004	0.252	0.009	0.9821
			0.671	0.005	0.272	0.011	
20	307	111026	0.337	0.004	0.249	0.009	0.9721
			0.716	0.003	0.228	0.011	
50	279	89288	0.294	0.004	0.214	0.009	0.9556
			0.712	0.004	0.204	0.008	
100	316	91363	0.293	0.003	0.196	0.006	0.9759
			0.729	0.003	0.195	0.007	
200	297	108206	0.304	0.003	0.191	0.006	0.9765
			0.749	0.003	0.122	0.002	

Table 17: Molecule/trace counts for Holliday junction dynamics analysis. Dynamic FRET efficiency traces were fitted with a 2-state (corresponding to Figure 39 and Figure 41) or 4-state Hidden Markov Modell model (corresponding to Figure 42) to determine the dwell time in isoform I or II and the open conformation. The number of traces N_T, dwell times N_t and the coefficient of determination $R^2$of the mono-exponential fit are listed.

[$MgCl_2$] (mM)	N_T (traces)	N_t (dwell times)	R^2	N (dwell times)	R^2	N (transitions)
		Isoform I	Isoform I	Isoform II	Isoform II	4-step HMM
10	213	8700	0.9998	9164	0.9999	884
20	307	6891	0.9991	7699	0.9999	924
50	279	6483	0.9981	6891	0.9981	859
100	316	7716	0.9912	7642	0.9963	748
200	297	5188	0.9936	5265	0.9909	334

C.2 Analysis of human TFIIIB with TIRF microscopy

Table 18: Molecule counts and fitting errors for TIRF measurements with human TFIIIB subcomplexes. FRET efficiency histograms calculated from dynamic and static FRET efficiency traces (corresponding to Figure 45, Figure 46, Figure 47 and Figure 48) were fitted with a Gaussian distribution. The number of molecules N_M used to calculate each histogram, the coefficient of determination R^2, the mean FRET efficiencies E (± s.e. of the fit) and the peak area A (± s.e. of the fit) of each Gaussian are listed. *Value was fixed for the fit.

Sample (equilibrium condition or after washing)	Traces	N_M (molecules)	E_1 E_2	s.e. E_1 s.e. E_2	A_1 A_2	s.e. A_1 s.e. A_2	R^2
U6P	static	263	0.1165	0.0003			0.9984
U6P/TBP	dynamic	155	0.115 0.404	0.001 0.002	0.0080 0.0169	0.0002 0.0003	0.9937
U6P/TBP	static	158	0.112 0.37	0.001 0.04	0.0202 0.0053	0.001 0.001	0.9964
U6P/TBP/Brf2	dynamic	29	0.110 0.356	0.003 0.004	0.008 0.016	0.001 0.001	0.9617
U6P/TBP/Brf2	static	264	0.106 0.411	0.001 0.003	0.008 0.0169	0.0002 0.0004	0.9886
U6P/TBP/Brf2/Bdp1$_{ES}$	dynamic	21	0.127 0.39	0.003 0.01	0.011 0.015	0.001 0.001	0.9481
U6P/TBP/Brf2/Bdp1$_{ES}$	static	302	0.115 0.450	0.001 0.002	0.0056 0.0194	0.0001 0.0002	0.9948
U6P/TBP/Brf2/Bdp1$_S$	dynamic	2	0.106 0.411	0.001 0.003	0.0081 0.0169	0.0002 0.0004	0.9886
U6P/TBP/Brf2/Bdp1$_S$	static	9	0.118 0.402	0.001 0.003	0.0094 0.0155	0.0003 0.0009	0.9819
U6P/TBP + wash	dynamic	16	0.128 0.415	0.003 0.003	0.0088 0.0161	0.0004 0.0013	0.9796
U6P/TBP + wash	static	475	0.1157 0.4*	0.0003	0.023 0.0021	0.0002 0.0003	0.9992
U6P/TBP/Brf2 + wash	dynamic	13	0.151 0.433	0.009 0.003	0.005 0.020	0.001 0.001	0.9724
U6P/TBP/Brf2 + wash	static	315	0.112 0.394	0.001 0.003	0.0122 0.0128	0.0002 0.0003	0.9938
U6P/TBP/Brf2/Bdp1$_{ES}$ + wash	dynamic	6	0.153 0.417	0.003 0.002	0.0062 0.0190	0.0004 0.0.001	0.9784
U6P/TBP/Brf2/Bdp1$_{ES}$ + wash	static	356	0.106 0.440	0.001 0.003	0.0102 0.0149	0.0002 0.0003	0.9950
U6P/TBP/Brf2/Bdp1S + wash	dynamic	8	0.133 0.371	0.004 0.003	0.007 0.018	0.001 0.001	0.9692
U6P/TBP/Brf2/Bdp1S + wash	static	618	0.1167 0.4126	0.0004 0.0009	0.0119 0.0130	0.0001 0.0002	0.9983
U6P/TBP/Bdp1$_{ES}$	dynamic	40	0111 0.381	0.002 0.002	0.0058 0.0189	0.0003 0.0004	0.9868
U6P/TBP/Bdp1$_{ES}$ + wash	static	193	0.1116 0.4*	0.0004	0.0228 0.0025	0.0002 0.0004	0.9985
U6P/TBP/Bdp1$_S$	dynamic	122	0.103 0.373	0.001 0.001	0.0066 0.0183	0.0002 0.0002	0.9967
U6P/TBP/Bdp1$_S$ + wash	static	210	0.1051 0.4*	0.0004	0.0233 0.002	0.0003 0.001	0.9975
U6P/Brf2	static	97	0.1252	0.0009			0.9960
U6P/Bdp1$_{ES}$	static	125	0.1304	0.0003			0.9986
U6P/Bdp1$_S$	static	129	0.1002	0.0002			0.9994

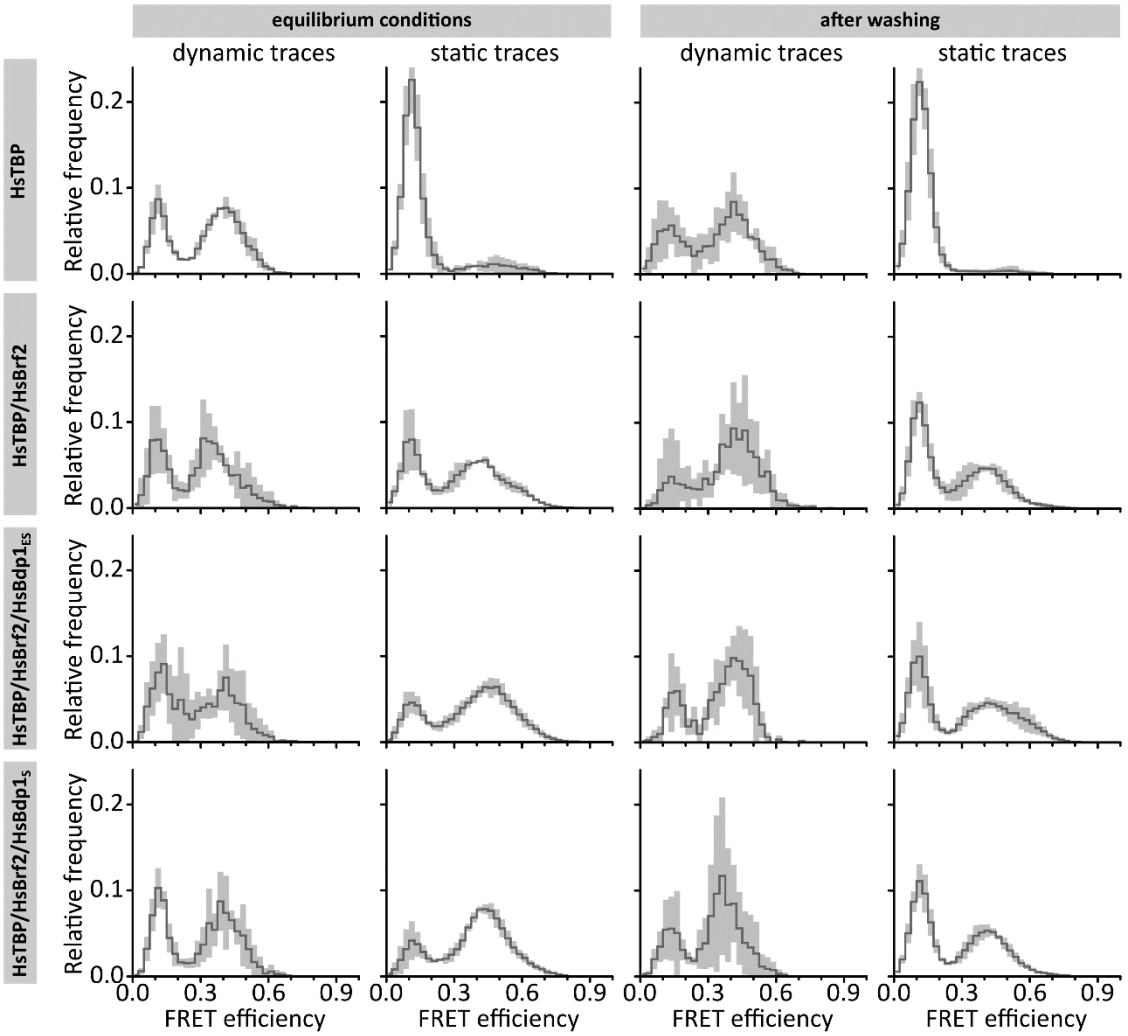

Figure 75: FRET efficiency histograms with standard deviation for TIRF experiments with human TFIIIB subcomplexes. FRET efficiency histograms of measurement with a short linear U6 promoter and human TFIIIB subunits (corresponding to Figure 46 and Figure Figure 47). Histograms show the mean FRET efficiency (solid line) and standard deviation (gray area) of three technical replicates.

Table 19: Dwell times calculation for U6P/TBP and U6P/TBP/Bdp1 subcomplexes. Data for U6P/HsTBP complexes were obtained in TIRF microscopy measurements (corresponding to Figure 49). Data were fitted with a mono-exponential decay function to determine dwell times in the unbent and bent state. The number of dwell times N_t (resulting from N_M molecules) used to calculate the dwell time in each state and the coefficient of determination of the fit R^2 are listed.

Sample	N_M (molecules)	State	N_t (dwell times)	R^2
U6P/TBP	155	unbent	1133	0.9998
		bent	966	0.9876
U6P/TBP/Bdp1$_{ES}$	40	unbent	258	0.9584
		bent	267	0.9991
U6P/TBP/Bdp1$_S$	144	unbent	1140	0.9838
		bent	1202	0.9998

C.3 Force measurements with human RNAP II and III transcription factors

Table 20: Molecule counts and fitting errors for force measurements with human TFIIIB subcomplexes. FRET efficiency histograms calculated from dynamic and static FRET efficiency traces (corresponding to Figure 52, Figure 53 and Figure 54) were fitted with one, two or three Gaussian distributions. The number of molecules N_M used to calculate each histogram, the coefficient of determination of the fit R^2, the mean FRET efficiencies E (± s.e. of the fit) and the peak area A (± s.e. of the fit) of each Gaussian are listed. * Value was fixed for the fit.

Sample	Force (pN)	N_M (molecules)	E_1 E_2 E_3	s.e. E_1 s.e. E_2 s.e. E_3	A_1 A_2 A_3	s.e. A_1 s.e. A_3 s.e. A_3	R^2
U6P	0	25170	0.145 - -	0.002 - -			0.9608
U6P	2.6	25960	0.148 - -	0.002 - -			0.9819
U6P	6.3	49120	0.145 - -	0.002 - -			0.9849
U6P/TBP	0	31961	0.142 0.39* -	0.002 - -			0.9920
U6P/TBP	2.6	26820	0.1385 0.39* -	0.0014 - -	0.0203 0.0054	0.0004 0.0007 -	0.9930
U6P/TBP	6.3	10178	0.1296 0.39* -	0.0012 - -	0.0205 0.0053 -	0.0004 0.0006 -	0.9947
U6P/TBP/Brf2	0	33693	0.16* 0.454 0.765	- 0.012 0.003	0.0043 0.006* 0.0151	0.0004 - 0.0004	0.9717
U6P/TBP/Brf2	2.6	44296	0.154 0.454 0.748	0.003 0.012 0.003	0.0094 0.004* 0.0121	0.0003 - 0.0003	0.9763
U6P/TBP/Brf2	6.3	45829	0.150 0.389 0.707	0.002 0.011 0.005	0.0137 0.004* 0.0078	0.0003 - 0.0003	0.9926
U6P/TBP/Brf2/Bdp1$_{ES}$	0	30453	*0.16 0.472 0.784	- 0.014 0.002	0.002* 0.006* 0.0168	- - 0.0004	0.9829
U6P/TBP/Brf2/Bdp1$_{ES}$	2.6	25724	0.16* 0.497 0.758	- 0.010 0.003	0.0030 0.004* 0.0186	0.0003 - 0.0003	0.9946
U6P/TBP/Brf2/Bdp1$_{ES}$	6.3	48274	0.15* 0.392 0.6748	- 0.008 0.0013	0.0039 0.004* 0.0173	0.0002 - 0.0002	0.9966

Table 21: Molecule counts and fitting errors for force measurements with human RNAP II transcription factors FRET efficiency histograms (corresponding to Figure 52, Figure 53 and Figure 55) were fitted with one, two or three Gaussian distributions. The number of molecules N_M used to calculate each histogram, the coefficient of determination of the fit R^2, the mean FRET efficiencies E (± s.e. of the fit) and the peak are A (± s.e. of the fit) of each Gaussian are listed. * Value was fixed for the fit.

Sample	Force (pN)	N_M (molecules)	E_1 E_2 E_3	s.e. E_1 s.e. E_2 s.e. E_3	A_1 A_2 A_3	s.e. A_1 s.e. A_3 s.e. A_3	R^2
MLP	0	27729	0.1348 - -	0.0015 - -	-	-	0.9917
MLP	3.2	40289	0.1493 - -	0.0014 - -	-	-	0.9926
MLP	5.9	33930	0.1431 - -	0.0014 - -	-	-	0.9905
MLP/TBP	0	26187	0.119 0.37 0.638	0.004 0.02 0.004	0.0087 0.004* 0.0127	0.0004 - 0.0004	0.9856
MLP/TBP	3.2	48743	0.097 0.305 0.586	0.0013 0.007 0.002	0.0126 0.004* 0.0095	0.0002 - 0.0002	0.9962
MLP/TBP	5.9	37981	0.128 0.4* 0.670	0.0012 - 0.007	0.0179 0.004* 0.0038	0.0003 - 0.0003	0.9984
MLP/TBP/TFIIA	0	33217	0.125 0.372 0.594	0.004 0.008 0.002	0.0065 0.004* 0.0148	0.0003 - 0.0003	0.9904
MLP/TBP/TFIIA	3.2	27514	0.130 0.361 0.615	0.0010 0.007 0.0013	0.0089 0.004* 0.0122	0.0002 . 0.0002	0.9974
MLP/TBP/TFIIA	5.9	24865	0.131 0.364 0.60*	0.002 0.008 -	0.0147 0.004* 0.0066	0.0003 - 0.0003	0.9895
MLP/TBP/TFIIB	0	36027	0.12* 0.466 0.742	- 0.011 0.002	0.0028 0.004* 0.0182	0.0002 - 0.0003	0.9904
MLP/TBP/TFIIB	3.2	59994	0.124 0.429 0.702	0.009 0.013 0.003	0.0096 0.004* 0.0133	0.0007 - 0.0004	0.9879
MLP/TBP/TFIIB	5.9	35307	0.13* 0.40* 0.660	- - 0.007	0.0089 0.004* 0.0125	0.0003 - 0.0003	0.9880
MLP/TBP/TFIIA/TFIIB	0	37846	0.13* 0.465 0.721	- 0.012 0.002	0.0021 0.006 0.0117	0.0004 - 0.0004	0.9922
MLP/TBP/TFIIA/TFIIB	3.2	29419	0.126 0.380 0.673	0.008 0.012 0.002	0.0029 0.004* 0.0183	0.0003 - 0.0003	0.9901
MLP/TBP/TFIIA/TFIIB	5.9	20817	0.126 0.38 0.667	0.003 0.04 0.005	0.0079 0.004* 0.0134	0.0004 - 0.0005	0.9826

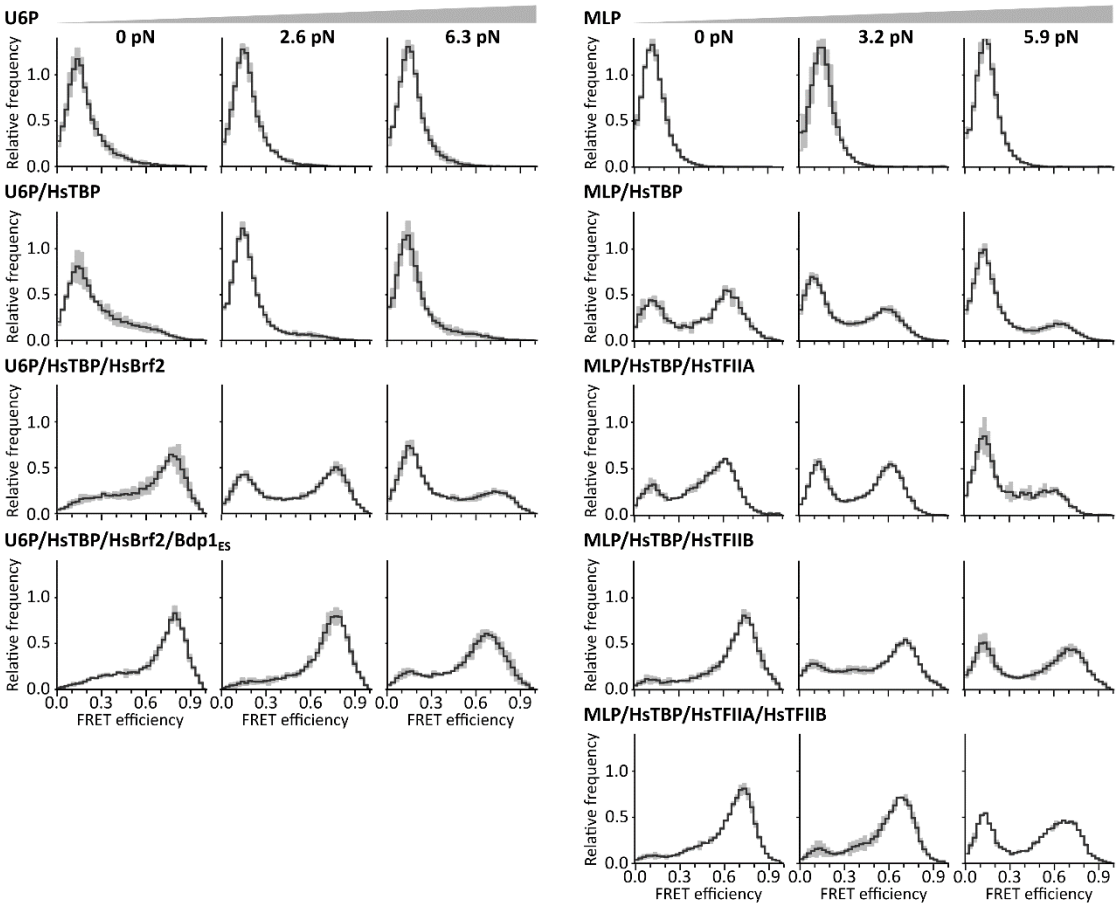

Figure 76: FRET efficiency histograms with standard deviation for force measurements with human RNAP II and III transcription factors. FRET efficiency histograms of measurement with a U6P and MLP DNA origami FC without proteins (upper row, corresponding to Figure 52) and human RNAP II and III transcription initiation factors (corresponding to Figure 54 and Figure 55). Histograms show the mean FRET efficiency (solid line) and standard deviation (gray area) of three technical replicates. Adapted from [434].

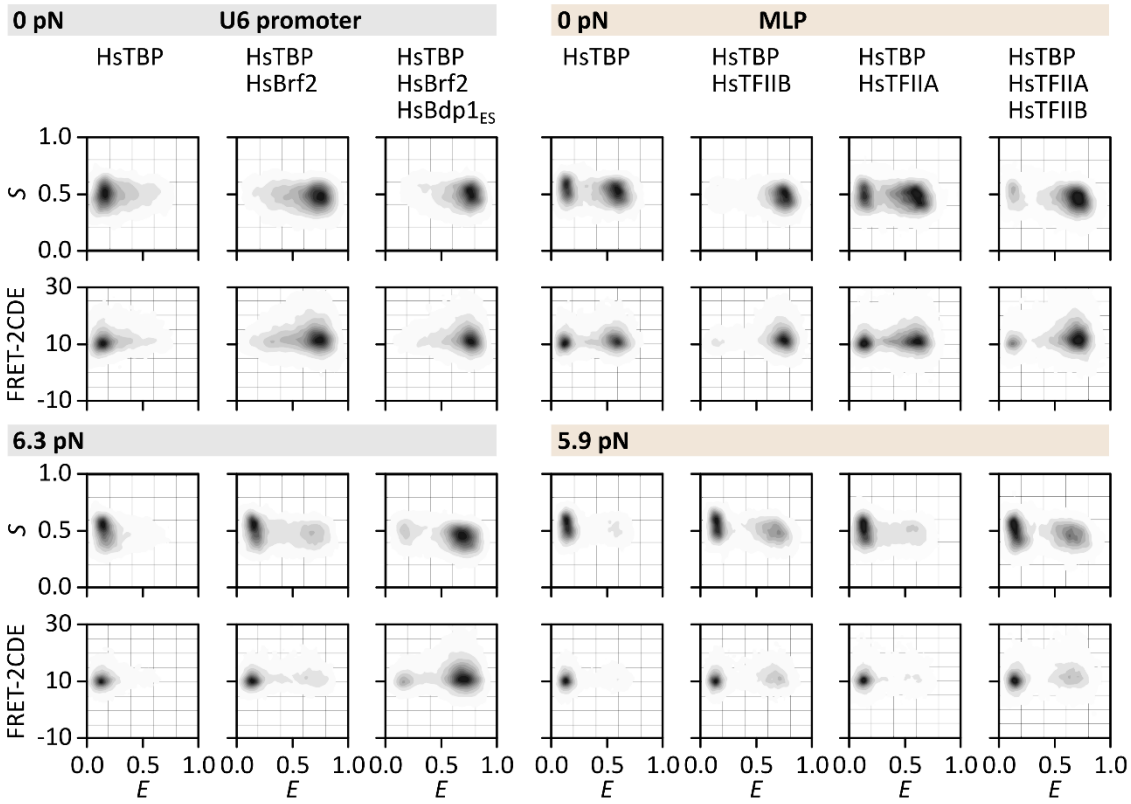

Figure 77: *E/S* histograms and FRET-2CDE values for force measurements with human RNAP II and III transcription factors. Representative histograms showing the stoichiometry factor *S* and the FRET-2CDE value as a function of FRET efficiency *E* for measurements with U6P and MLP DNA origami force clamps at 0 pN and 5.9 pN or 6.3 pN (corresponding to Figure 54 and Figure 55). The relative occurrence is indicated by grayscale from white (low) to black (high).

Table 22: Kinetic data parameters from force measurements with U6P/TBP and MLP/TBP complexes. Data for U6P/HsTBP complexes were obtained in TIRF microscopy measurements (corresponding to Figure 56) and data for MLP/HsTBP complexes were obtained from confocal smFRET time-course experiments (corresponding to Figure 58). Data were fitted with mono-exponential decay functions to determine dwell times in the unbent and bent state. The number of dwell times N_t and/or number of molecules N_M, the coefficient of determination of the fit R^2, the decay constant τ (± s.e. of the fit) and the y-axis offset y_0 (± s.e. of the fit) of each fit are listed. * Value was fixed for the fit.

Sample	Force (pN)	N (molecules)	N_t (dwell times) unbent state bent state	τ (s)	s.e. τ (s)	y_0	s.e. y_0	R^2
U6P/TBP	0	419	1091 1159	0.214 0.54	0.005 0.02			0.9986 0.9965
U6P/TBP	6.3	435	956 857	0.347 0.261	0.004 0.006			0.9970 0.9965
MLP/TBP	0	56851		170	30	0.526	0.012	0.9276
MLP/TBP	5.9	64111		230	36	0.728	0.005	0.8703

C.4 Measurements with *Sulfolobus acidocaldarius* transcription factors

Table 23: Molecule counts and fitting errors for measurements with *Sulfolobus acidocaldarius* transcription factors. FRET efficiency histograms (corresponding to Figure 60) were fitted with one or two Gaussian distributions. The number molecules N_M used to calculate each histogram, the coefficient of determination of the fit R^2, the mean FRET efficiencies E (± s.e. of the fit) and the peak are A (± s.e. of the fit) of each Gaussian are listed. * Value was fixed for the fit.

Sample	N_M (molecules)	E_1 E_2	s.e. E_1 s.e. E_2	A_1 A_2	s.e. A_1 s.e. A_3	R^2
T6P/TBP	11606	0.190	0.002			0.9908
T6P/TBP/TFB1	15272	0.193 0.51 3	0.005 0.006	0.1132 0.0139	0.0006 0.0006	0.9895
T6P/TBP/TFB1/3xTFB2	25325	0.190 0.500	0.004 0.008	0.0136 0.0126	0.0006 0.0006	0.9931
T6P/TBP/TFB1/6xTFB2	21517	0.19* 0.495	- 0.006	0.0186 0.0068	0.0003 0.0003	0.9959
T6P/TBP/TFB2	29784	0.187	0.002			0.9916

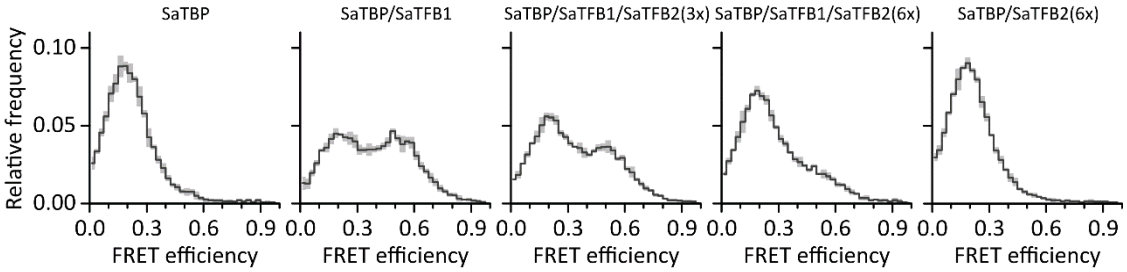

Figure 78: FRET efficiency histograms with standard deviation for measurements with *Sulfolobus acidocaldarius* transcription factors. FRET efficiency histograms of measurements with short linear SSV T6 promoter DNA and *S. acidocaldarius* initiation factors (corresponding to Figure 60). Histograms show the mean FRET efficiency (solid line) and standard deviation (gray area) of three technical replicates.

C.5 Measurements with *Pyrococcus furiosus* transcription factors

Table 24: Molecule counts and fitting errors for confocal smFRET measurements with *Pyrococcus furiosus* transcription factors. FRET efficiency histograms (corresponding to Figure 61) were fitted with one or two Gaussian distributions. The number of molecules N_M used to calculate each histogram, the coefficient of determination of the fit R^2, the mean FRET efficiencies E (± s.e. of the fit) and the peak are A (± s.e. of the fit) of each Gaussian are listed. * Value was fixed for the fit.

Sample	N_M (molecules)	E_1 E_2	s.e. E_1 s.e. E_2	A_1 A_2	s.e. A_1 s.e. A_3	R^2
P_{con}	9514	0.321	0.004			0.9527
Pc_{on}/TBP	7871	0.345	0.003			0.9769
P_{con}/TBP/TFB1	6882	0.330 0.660	0.009 0.006	0.0113 0.0132	0.007 0.0007	0.9608
P_{con}/TBP/TFB1/TFB-RF1	2250	0.35* 0.657	- 0.004	0.0039 0.0206	0.0006 0.0006	0.9964
Pnat	6438	0.348	0.003			0.9787
P_{nat}/TBP	5248	0.335	0.004			0.9642
P_{nat}/TBP/TFB1	10013	0.374-	0.001			0.9670
P_{nat}/TBP/TFB/1TFB-RF1	4523	0.37* 0.651	- 0.002	0.0045 0.0200	0.0005 0.0004	0.9999
P_{con}/TFB1	4671	0.347-	0.004			0.9684
P_{con}/TFB-RF1	5348	0.342	0.004			0.9696
P_{con}/TFB1/TFB-RF1	6629	0.331-	0.013-			0.9562
P_{nat}/TFB1	8963	0.335-	0.004			0.9642
P_{nat}/TFB-RF1	2211	0.330	0.003			0.9789
P_{nat}/TFB1/TFB-RF1	2142	0.371	0.004			0.9682
T6P/TBP/TFB1	2599	0.194 0.473	0.006 0.012	0.0138 0.0112	0.0010 0.0010	0.9792
T6P/TBP/TFB1/TFB-RF1	4213	0.186 0.450	0.005 0.012	0.0137 0.0113	0.0009 0.0010	0.9839

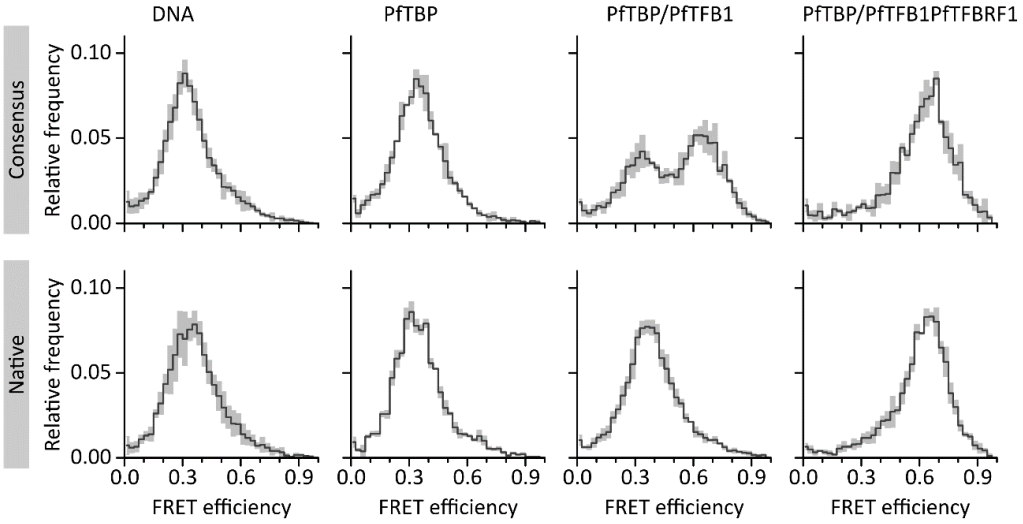

Figure 79: FRET efficiency histograms with standard deviation for measurements with *Pyrococcus furiosus* transcription factors. FRET efficiency histograms of measurements with the P_{nat}, P_{con} and T6P and P. *furiosus* initiation factors (corresponding to Figure 61). Histograms show the mean FRET efficiency (solid line) and standard deviation (gray area) of three technical replicates.

C.6 Force measurements with archaeal transcription factors

Table 25: Molecule counts and fitting errors for force measurements with archaeal transcription initiation factors. FRET efficiency histograms (corresponding to Figure 64 and Figure 65) were fitted with one, two or three Gaussian distributions. The number of molecules N_M used to calculate each histogram, the coefficient of determination of the fit R^2, the mean FRET efficiencies E (± s.e. of the fit) and the peak are A (± s.e. of the fit) of each Gaussian are listed. * Value was fixed for the fit.

Sample	Force (pN)	N_M (molecules)	E_1 E_2 E_3	s.e. E_1 s.e. E_2 s.e. E_3	A_1 A_2 A_3	s.e. A_1 s.e. A_3 s.e. A_3	R^2
T6P	0	6040	0.1929 - -	0.0007 - -			0.9943
T6P	2.5	7320	0.2025 - -	0.0012 - -			0.9877
T6P	6.2	2712	0.2055 - -	0.0014 - -			0.9839
T6P/MjTBP	0	16091	E1 0.204 E2 0.442 E3 0.624	0.002 0.008 0.002	0.0968 0.003* 0.01212	0.0003 - 0.0003	0.9898
T6P/MjTBP	2.5	14938	E1 0.199 E2 0.393 E3 0.590	0.002 0.010 0.004	0.0135 0.003 0.0083	0.0003 - 0.0003	0.9902
T6P/MjTBP	6.2	16053	E1 0.191 E2 0.355 E3 0.583	0.002 0.016 0.014	0.0172 0.003* 0.0045	0.0004 - 0.0004	0.9963
T6P/PfTBP/PfTFB1	0	22974	E1 0.206 E2 0.517 -	0.004 0.002 -	0.0084 0.0163 -	0.0003 0.0004 -	0.9927
T6P/PfTBP/PfTFB1	2.5	19250	E1 0.208 E2 0.509 -	0.002 0.003 -	0.0113 0.0137 -	0.0003 0.0003 -	0.9895
T6P/PfTBP/PfTFB1	6.2	44401	E1 0.195 E2 0.492 -	0.002 0.009 -	0.0158 0.0090 -	0.0003 0.0003 -	0.9918

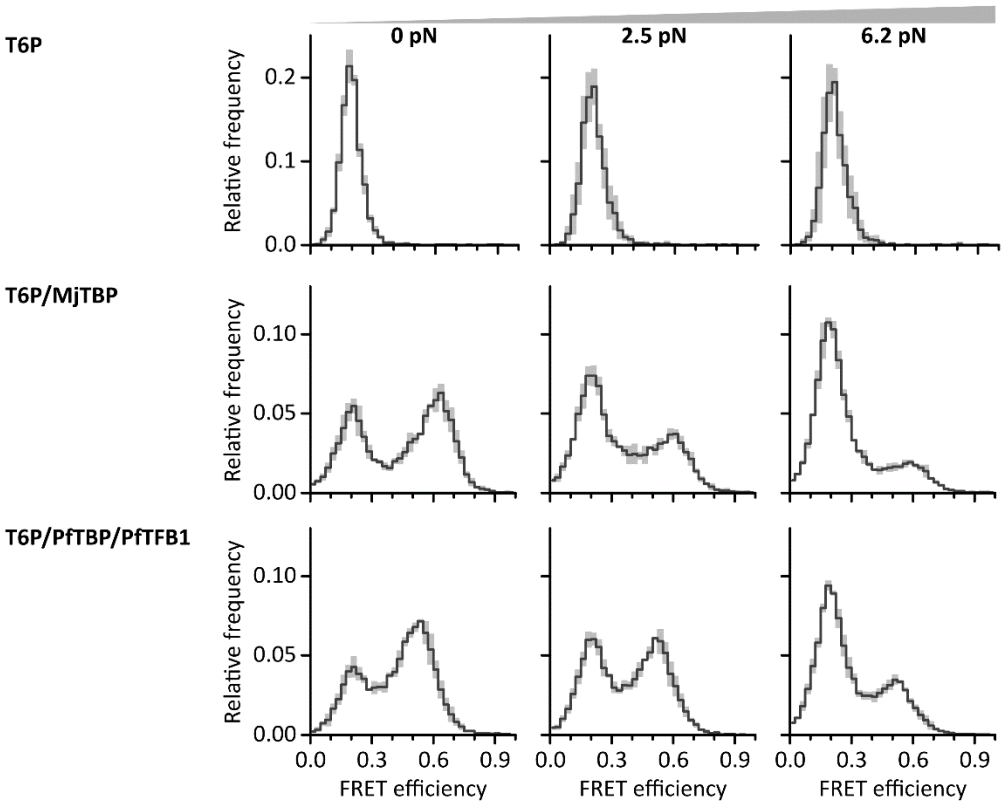

Figure 80: FRET efficiency histograms with standard deviation for force measurements with archaeal transcription factors. FRET efficiency histograms of measurements with T6P DNA origami FCs and *M. jannaschii* or *P. furiosus* initiation factors (corresponding to Figure 64 and Figure 65). Histograms show the mean FRET efficiency (solid line) and standard deviation (gray area) of three technical replicates